

Optical Kerr Gate
for
Eliciting Axial Emitter Profiles
- Design, Realization and Application -

D I S S E R T A T I O N

zur Erlangung des akademischen Grades
doctor rerum naturalium (Dr. rer. nat.)

vorgelegt dem Rat der Physikalisch-Astronomischen Fakultät
der Friedrich-Schiller-Universität Jena



seit 1558

von
Dipl.-Phys. **Christian Karras**
geboren am 24.05.1986 in Meiningen

Gutachter:

1. Gutachter: Prof. Dr. Herbert Stafast
*Leibniz Institut für Photonische Technologien, Jena
und Friedrich-Schiller-Universität Jena*
2. Gutachter: Prof. Dr. Christian Spielmann
*Institut für Optik und Quantenelektronik
der Friedrich-Schiller-Universität Jena*
3. Gutachter: Prof. Dr. Patrick Nürnberger
*Fakultät für Chemie und Biochemie
der Ruhr-Universität Bochum*

Tag der Disputation: 05. September 2016

Sorgen sind für Leute, die nicht improvisieren können

T.v.Doorn

Zusammenfassung

Für eine funktionelle Schichtanalyse der Retina ist eine markerfreie molekülspezifische Diagnostik mit einer axialen Auflösung von wenigen μm nötig. Die kleine numerische Apertur für die Abbildung der Autofluoreszenz des Augenhintergrundes und die geringe zulässige Strahlungsbelastung der Retina begrenzen den Einsatz konventioneller Fluoreszenzmikroskopietechniken.

Gegenstand dieser Arbeit ist eine alternative Methode. Mit ihr soll aus dem Laufzeitunterschied des Lichtes aus verschiedenen Schichten deren Position ermittelt werden. Diese Methode ist bereits aus der Atmosphärenforschung bekannt (LIDAR, light detection and ranging). Die Schichtposition ist dabei im zeitaufgelösten Signal nach einer Laserpulsanregung kodiert.

Bei einer geforderten Ortsauflösung von $10\ \mu\text{m}$ (Dicke der Retinaschichten: $20 - 50\ \mu\text{m}$) benötigt man eine Zeitauflösung von $10^{-13}\ \text{s}$ bei der Anregung und der Detektion. Diese Auflösung lässt sich durch Abtasten des Lichtsignals mit einem schnellen Transmissionsschalter nach Femtosekunden (fs)-Laserspulsanregung realisieren.

Der im Rahmen der vorliegenden Arbeit ermittelte optimale Schaltprozess ist optisches Kerrschalten (OKG). Es wurde der Zusammenhang zwischen den linear und nichtlinear optischen Eigenschaften des Schaltmaterials und der Effizienz bzw. der Zeitauflösung beim Schalten spektral breiter Signale analysiert. Ein aus dem Vergleich der optischen Eigenschaften und der Schaltleistung (Effizienz und Zeitauflösung) verschiedener Materialien abgeleitetes optimiertes Bewertungskriterium für OKG berücksichtigt die dispersionsbedingte Begrenzung der Schalteffizienz und die schaltpulsinduzierte Signalabschwächung. Für moderate Schaltintensitäten, die mit kommerziellen fs-Laseroszillatoren realisierbar sind ($500\ \text{GW}/\text{cm}^2 < I_G < 700\ \text{GW}/\text{cm}^2$) zeigt $\text{SiO}_2\text{-Al}_2\text{O}_3\text{-La}_2\text{O}_3$ (SAL)-Glas die besten Schalteigenschaften mit Effizienzen $\eta > 50\ \%$ und Schaltzeiten im Bereich von $150\ \text{fs}$ über einen breiten Spektralbereich.

Das entwickelte Abbildungssystem basiert auf Parabolspiegeln und garantiert eine dispersionsoptimierte Abbildung der Lumineszenz aus dem Schichtsystem in das OKG. Das abgeleitete Kriterium zur Bestimmung der Ortsauflösung berücksichtigt das Signal-zu-Rauschverhältnis (SNR). Hierbei sind Analogien zur Mikroskopie nützlich.

Verschiedene Schichtstrukturen (dünne isolierte Schichten mit unterschiedlichem zeitlichen Emissionsverhalten sowie dicke Schichten) dienten zur Erprobung der Messmethode und des Auswertungssystems. Die Genauigkeit der Positionsbestimmung der Schichten beträgt $\Delta\Delta z = 2\ \mu\text{m}$. Zudem wurde ein signifikanter Zusammenhang zwischen der Ortsauflösung und dem SNR gefunden. Die erreichte Ortsauflösung liegt zwischen $\Delta z = 22\ \mu\text{m}$ und $\Delta z = 40\ \mu\text{m}$. Simulationen weisen darauf hin, dass bei großem SNR die Ortsauflösung unabhängig vom zeitlichen Emissionsverhalten der Schichtlumineszenz ist. Bekannte Methoden aus der Bildverarbeitung dienten zur Rekonstruktion der dicken Emitterstrukturen aus dem zeitaufgelösten Messsignal. Die gemessene Auflösung ist bereits ausreichend, um Fluorophorverteilungen in der Retina tiefenaufgelöst zu vermessen. Durch eine weitere Optimierung des Systems lässt sich die Auflösung jedoch noch steigern.

Bei einem Testsystem, Cadmiumsulfid(CdS)-Nanostrukturen, zeigte sich erstmals der zeitliche Aufbau von stimulierter Emission zwischen $0.1\ \text{ps}$ und $5\ \text{ps}$ als Funktion der Anregungsfluenz. Das komplexe spektral-zeitliche Emissionsverhalten dieser Strukturen ist eine Folge von gekoppelten Relaxationsprozessen nach fs-Laseranregung.

Contents

1	Introduction	1
2	State of the art for axially resolved emitter determination	4
2.1	Time-of-flight measurements compared to other methods	4
2.2	State-of-the-art of gating techniques	5
3	Physical basics of ultrafast gating	8
3.1	Light matter interaction	8
3.1.1	General mechanism	8
3.1.2	The refractive index	8
3.1.3	Relation between the refractive index and microscopic properties	10
3.1.4	Absorption and band structure of solids	10
3.1.5	Fresnel reflection and transmission of a slab	11
3.1.6	Luminescence of photo excited material	12
3.2	Ultrashort laser pulses	14
3.2.1	Spatial and temporal profile	14
3.2.2	Impact of the material parameters	15
3.2.3	Optical Kerr gating (OKG)	16
4	Experimental setups	19
4.1	The laser system	19
4.2	Signal detection	19
4.3	Imaging System	20
4.3.1	Design of the imaging system	20
4.3.2	Alignment of the off-axis parabola telescope	21
4.3.3	Extinction ratio of the polarizers	21
4.4	Sample preparation and chemical characterization of the investigated Kerr media	21
4.5	Setups for measuring the linear and nonlinear optical properties . . .	22
4.5.1	Linear absorption and transmission measurements	22
4.5.2	Characterization of the nonlinear refractive index	22
4.6	Optical Kerr gating setups	23
4.6.1	Two-color optical Kerr gating setup	23
4.6.2	White light optical Kerr gating setup	24
4.6.3	Setup for Kerr gating of axially distributed emission	25
5	Important setup parameters	28
5.1	Laser pulse duration and emission spectra	28
5.2	Spot widths	30
5.3	Extinction ratio of the polarizers	31
5.4	Characterization of the imaging system	32

6	Material evaluation for optical Kerr gating	34
6.1	State-of-the-art of gating materials and their selection	35
6.2	Linear and nonlinear properties of selected gating materials	37
6.2.1	Wavelength dependent linear absorption and refraction	38
6.2.2	Estimate of the Urbach and the band gap energies	39
6.2.3	Nonlinear refraction of the materials	41
6.2.4	Discussion of the microscopic material properties	44
6.3	Material properties and OKG	47
6.3.1	Absorption	47
6.3.2	Refraction	49
6.4	Broad-band OKG performance	52
6.5	Efficiency analysis using two-color OKG	56
6.5.1	Qualitative comparison of the materials	56
6.5.2	Quantitative analysis of the transient absorption	58
6.6	The optimum gating material	60
7	Detection of axially distributed emitters	63
7.1	Spatial and temporal relations in the time-of-flight method	63
7.2	Axially distributed scattering	65
7.3	Identifying the axial distribution of thin layers showing a finite temporal response	67
7.3.1	Emission of a single CdS nanostructure layer	67
7.3.2	Interpretation of the CdS ensemble emission	69
7.3.3	Emission from a stacked CdS nanostructure system	70
7.3.4	Data analysis	72
7.3.5	Identifying the layers of the stacked CdS system	76
7.3.6	Nanostructure density of the layers	80
7.4	The temporal response of thick distributed emitter layers	80
7.4.1	Delay time dependent signal of the fluorophore	81
7.4.2	Evaluation of the thermalization time constant τ_r , the fluorophore concentration and the temporal resolution	81
7.4.3	Retrieval of the emitter distribution	83
8	Summary	85
9	Conclusion and outlook	88
	List of abbreviations and symbols	90
	Appendix	94
	Bibliography	111
	List of Figures	134
	List of Tables	139

Chapter 1

Introduction

The continuously increasing human life expectancy and growing prosperity correlate with an increase of certain diseases. Diabetes mellitus typ II or age-related macular degeneration (AMD) are only two examples of what is afflicting the modern industrial society more and more [1, 2]. Consequently novel highly sophisticated diagnostic techniques are required for early treatment of these diseases in order to improve life quality.

Even at an early stage, these diseases are related to metabolic changes, which are particularly pronounced in the human retina [3, 4]. Hence, a promising diagnostic approach is to map molecules that play a crucial role in cell metabolism such as hydrogenated nicotinamide adenine dinucleotide (NADH) [5]. Due to its characteristic auto-fluorescence signal, mapping of NADH in the human retina via fluorescence lifetime imaging (FLIM) has evolved to a powerful tool for the diagnosis of metabolic disorders. In addition, this technique is successfully applied to detect other metabolically important fluorophores such as flavin adenine dinucleotide (FAD) or flavin mononucleotide (FMN) [6–12] and to examine the human skin [13]. The major drawback of FLIM is its limitation to image two dimensions, i.e. lateral fluorophore distributions. In order to improve diagnostics, it is desired to resolve the axial fluorophore distribution.

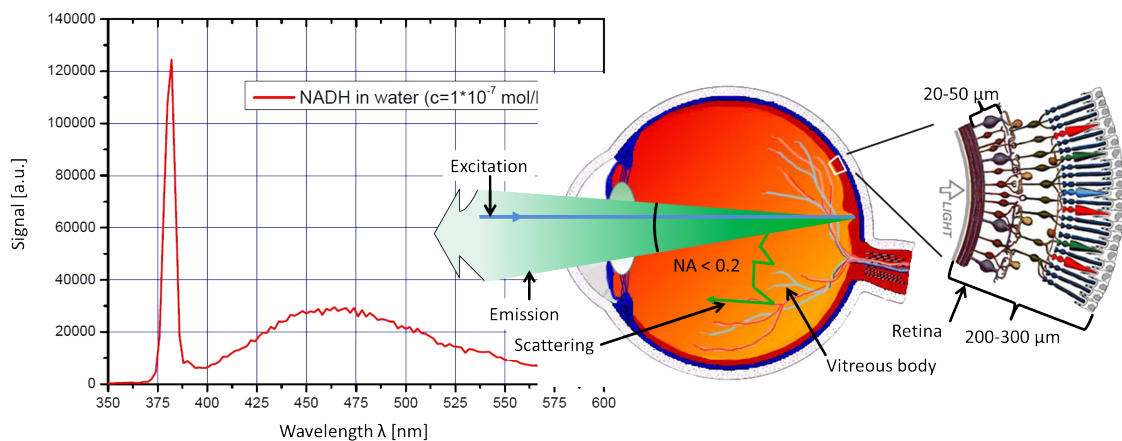


Fig. 1.1: Excitation of the NADH auto-fluorescence in the fundus of the human eye and the NADH emission spectrum (Spectrum from [14], scheme from [15])

Fluorescence excitation of constituents of the human retina is limited to weak pulse fluences in order to prevent photo-damage. Additionally, the light has to be detected at a low numerical aperture of $NA < 0.2$, due to the geometry of the eye ball (fig. 1.1). Furthermore the signal may be affected by scattering of the vitreous

body. This limits the application of well-established techniques, such as multiphoton fluorescence microscopy or confocal microscopy.

An alternative approach is to deduce the axial fluorophore distribution by measuring the difference in the propagation time (time-of-flight, ToF) of light emitted by the different layers. The spatial information of the system is then decoded in the temporal signal of the luminescence upon short pulse excitation. In this way the demand for large numerical apertures and/or high light intensities is evaded. Although the ToF method has been exploited comprehensively in order to investigate axial structures using scattered light (diffuse reflection or Raman scattering, cf. subsect. 2.2), its application to measure the axial fluorophore distribution is new. A first approach was recently presented by Gräfe et al. [16].

As a potential diagnostic tool using the auto-fluorescence of the human retina, a spatial resolution down to a few microns is necessary (fig. 1.1). This correlates to a temporal resolution in the 100 fs range. Concomitantly, the diagnostic system should be capable of detecting single photons, since the auto-fluorescence signal is very weak. Single photon detection is a well-established method and already applied in fundus imaging techniques. The temporal resolution of the detection is, however, limited to several tens of picoseconds [8, 17]. Therefore the combination of single photon detection and an ultrafast light gate is an obvious approach in order to provide sensitivity and time resolution. Light controlled switches were shown to be capable of providing the required time resolution [18]. The design of a gate which comprises a large efficiency and the desired temporal resolution is, however, challenging.

As a second challenge it is *a priori* unclear how a complex temporal response function of the fluorophores will limit the spatial resolution. This might be particularly critical at the 100 fs time range in which vibrational relaxation of excited molecules upon laser irradiation tends to delay the fluorescence onset.

The present work addresses the critical issues mentioned above by investigating the optical gating technique such that the ToF method may become applicable to functional investigations of the retina. In this context, the work structures in two major parts:

Design, optimization and evaluation of the optical gate. Although optical gating is well established, its potential application as a diagnostic tool for investigating thin fluorescing layers (as in the human retina) poses tremendous requirements on the light gate:

- **Fast:** The time resolution has to be in the 100 fs range.
- **Efficiency:** The temporally integrated auto-fluorescence signal (life time $\tau_F > 300$ ps) is already weak. Filtering the emission onset by a fast gating (gating time $\tau_{Gate} \approx 100$ fs) reduces the detectable signal to some few photons per excitation pulse. Thus gating of single photons has to be possible. Additionally, the signal out of the gate needs to be sufficiently suppressed (low background).

In addition, highly efficient gating will evade tight focusing of the gate and the signal pulses and thus may enable switching of a wide field signal.

- **Broad-band:** Fluorescence of e.g. NADH ranges from $\lambda_{em} = 400$ nm to $\lambda_{em} = 600$ nm [14]. Consequently, the gate should support broad-band switch-

ing. The same applies to the imaging system for routing the signal light from the sample to the gate.

- **High repetition rate:** Optical gating at high repetition rates (MHz) is necessary in order to enable short measurement times and significant noise suppression. As a consequence efficient gating should be possible at pulse intensities which are available by commercial fs-oscillators (high repetition rate).

Therefore all optical gating is revisited. Optical Kerr gating (OKG) is identified to be the most suited gating technique. The OKG performance substantially depends on the gating material. Hence a comprehensive experimental material study is performed. In this context the optical parameters of the materials are characterized and evaluated with respect to common literature. The impact of selected optical material properties on the OKG performance is analyzed and a novel figure of merit is established. Additionally, a well suited optical system for imaging the sample emission into the OKG is designed and characterized.

Investigation of the influence of the emitter response onto the axial resolution As a second critical issue, the influence of the temporal emission characteristics onto the spatial resolution is investigated using selected testing samples. The spatial and temporal coupling are disentangled by detecting the temporal signal of:

- thin distinctly stacked layers (thickness $d < 1 \mu\text{m}$), showing a very fast time response (thin scattering layers),
- thin distinctly stacked layers ($d < 1 \mu\text{m}$), showing a more complex time response (cadmium sulfide nanowire emission),
- thick stacked layers ($d > 80 \mu\text{m}$), showing a slow complex time response (fluorescence signal of Coumarin 153 solution).

The effect of the temporal material response on the axial resolution is deduced. In this context analogies to microscopy are discussed.

The discrimination between thin and thick layer measurements is adequate, since NADH is known to show distinct local concentration peaks in the retina [19, 20]. Hence applying the results from the thin layer measurements should be suited for functional analysis of the retina. Investigating the effect of thick (continuous) distributions on the time signal ensures a more general application of the detection system.

One testing sample consists of cadmium sulfide (CdS) nanowires. These are promising candidates for highly efficient integrated laser sources. The results of the present work reveal novel expertise regarding the ultrafast processes in this material system at room temperature. This finding demonstrates the broad applicability of the selected, designed and tested ultrafast optical switch in combination with the low dispersion imaging system.

Chapter 2

State of the art for axially resolved emitter determination

2.1 Time-of-flight measurements compared to other methods

In this section the Time-of-Flight (ToF) method is compared to other techniques that can be used in order to realize depth resolved fluorescence detection.

Using the ToF method, the spatial distance between two objects (such as two emitter layers or a reference point and a layer) is determined by measuring the propagation time of a short light pulse. Hence the axial emitter distribution is encoded in the temporal characteristics of a detected signal (below called "time trace"). The method is equivalent to the "Light detection and ranging" method (LIDAR), which is commonly used in automotive industry, velocity measurements, astronomic distance measurements and more [21, 22]. The spatial resolution of this technique is limited by the temporal resolution of the ToF system, i.e. by the used pulse duration (cf. chap. 7). A temporal resolution of $\Delta t = 50$ fs for instance correlates to an axial resolution of $\Delta z = 7.5 \mu\text{m}$ (in air, eq.(7.1)).

Competitive techniques are, however, existing and the most important methods are elucidated briefly below.

Confocal microscopy Confocal microscopy (CFM) is a widely used technique in order to achieve high axial and lateral resolutions [23, 24]. It is generally applied to enhance the quality of microscopic images. In CFM the emitted fluorescence is collimated by an objective and focused through a pinhole. Only light originating from the focal plane of the objective is properly focused through the pinhole, blocking light from deeper or shallower layers. The resolution of this system is limited by diffraction. Thus, depth resolutions below $1 \mu\text{m}$ are possible. However, the axial resolution Δz strongly depends on the numerical aperture (NA) of the objective as well as the wavelength λ and the refractive index n_0 [25]:

$$\Delta z(FWHM) = \frac{0.88\lambda}{n_0 - \sqrt{n_0^2 - NA^2}} \quad (2.1)$$

A high resolution (small Δz) requires large numerical apertures. At small NA values the resolution diminishes dramatically. For example a NA as low as 0.1 (typical for human eye), Δz amounts to $90 \mu\text{m}$ ($\lambda = 500$ nm, $n = 1$). Hence, the axial resolution of ToF can be much better than that of CFM for low NA applications. Even for

a numerical aperture of $NA = 0.2$ (ultimate maximum for human eye), the depth resolution amounts to $\Delta z \approx 20 \mu\text{m}$.

Optical coherence tomography Another commonly used technology for depth resolved imaging is optical coherence tomography (OCT) [26]. OCT enables fast axial structure analysis via an interferometric technique. The light, which is scattered back from different layers produces different interferograms, when used in one reflecting arm of a Michelson like interferometer. Using OCT, an axial resolution $\Delta z < 1 \mu\text{m}$ can be achieved, if a white light source is used. The big disadvantage of this technique, compared to the ToF method, is its insensitivity to fluorescence, as only scattered light produces a proper interferogram. Hence only structural, but no functional information can be achieved.

Self-interference of fluorescence microscopy (SIFM) Probably the most competitive technique to ToF is self-interference microscopy [27]. Here, a phase mask is inserted between the objective and the tube lens of a microscope. Due to self interference of the emission, the depth information is enciphered within an interference pattern at the image plane. This technology enables the fast three dimensional functional information acquisition of a test sample, featuring a depth resolution of just a few micrometers.

This method, however, shows large disadvantages compared to the ToF method. First of all, the periodicity of the interference pattern limits the maximum depth ranges to a few hundred microns [27], while the maximum depth range of the ToF method is theoretically infinity. Additionally the signal-to-noise ratio (SNR) declines when a low numerical aperture is used or only a few photons are available (weak fluorescence signal). The SNR correlates strongly with the depth resolution of SIFM. De Groot et al. [27] for example have mentioned that the depth resolution of their setup decreases to $13 \mu\text{m}$, if a numerical aperture of 0.09 would be used.

Finally, due to the interferometric approach, SIFM strongly depends on the phase of the fluorescence signal. If light travels through inhomogeneous and scattering material (such as the vitreous body for *in vivo* retina measurements), the phase will be changed statistically, even for low scattering. This should lower the SNR and consequently the depth resolution. In contrast, measuring the propagation time via ToF should not be affected by scattering, if it is not too strong.

2.2 State-of-the-art of gating techniques

For a ToF based system showing axial resolutions of only some few μm , a detection system with high temporal resolution down to $\Delta t = 100 \text{ fs}$ is necessary. This can only be achieved by all optical gating, since the fastest electronic detectors show temporal resolutions of $\Delta t > 20 \text{ ps}$ [28]. Even the temporal resolution of modern streak cameras is limited to $\Delta t > 200 \text{ fs}$ [29]. Those, furthermore, are not capable of detecting single photons. Using optical gating techniques allows the temporal resolution to be determined by the pump pulse duration, hence being in the range of $\Delta t \approx 50 \text{ fs}$ and below. In this section selected gating techniques will be elucidated with respect to their gating performance.

Cascaded transient absorption and reflection At a cascaded switch, based on transient absorption or reflection, the signal light is switched by two processes. The first one opens the gate, the second one closes it. The unique feature of this technique is its adjustable gate width, since the optical path between the "open" and "close" process can be varied easily. The opening component could for instance be realized by a pumped gain material [30], a strong transient reflection change of a thin film [31, 32] or a semiconductor saturable absorber mirror [33]. On the other hand, transient absorption realized by seeded free carrier absorption in semiconductors [33, 34] or organic materials [35] may be used to close the gate. Since free carrier effects are not very wavelength selective, the gate could be operated at a broad spectral range [33, 36, 37].

The maximum change in transient absorption or reflection were reported to amount to approximately 95 % [35, 38]. Therefore, the background signal would be in the range of several per cent by applying this technique. Furthermore the constant excitation of electrons into the conduction band of the gating material may result in the generation of defect centers leading to photo darkening [39], decreasing the transparency of the gate.

Nonlinear lens An induced spatial modulation, such as a deflection [40] or (de)-focusing [41, 42] of a signal beam by a strong pulse as a result of a nonlinear refractive index modification (sect. 3.1.2) can also be used for gating.

A sufficiently large index modification requires, however, a large gate pulse intensity and hence a tight focusing of the gate and the signal beams. This is correlated to a large divergence of the beams. Thus, the shift (deflection [40]) or the change ((de)focus [43]) of the signal spot is much smaller than its spot size in the far field behind the gate. This results in a very small efficiency.

Optical parametric processes Gating techniques based on parametric processes (sum frequency generation, SFG [44–46] and optical parametric amplification, OPA [16, 47, 48]) were used in order to investigate the temporal behavior of a fluorescence signal in the past decades. Thereby the fluorescence signal is superposed with a gate pulse in a nonlinear crystal, such as lithium iodate (LiIO_3) [49]. From the time trace of the fluorescence only the part overlaying with the gate pulse is frequency shifted (SFG) or amplified (OPA). The parametric processes are very fast such that temporal resolutions down to $\Delta t = 33$ fs have been reported [46]. SFG is basically background free due to the availability of very good spectral filters. Its efficiency, however, is below 1 %, making its application difficult for very weak fluorescence signals, particularly in case of single photons [50, 51].

In contrast the OPA process is very efficient due to the amplification. Gain factors of the fluorescence in the range of 10^5 were reported [16]. This method has already been used in order to investigate axially distributed fluorophores. Pulse energies above $100 \mu\text{J}$ were, however, necessary, prohibiting the use of fs-oscillators for high repetition rate measurements. Additionally this method was reported to suffer from a large background due to self phase modulation [16, 48]. Furthermore it is not clear, if the OPA process can be applied to gating of single photons.

Both the SFG and the OPA processes require phase matching [50]. This basically limits the broad band suitability for these techniques. Broad band SFG requires either angular scanning [46] or a very complex optical setup [45].

Kerr gating A linearly polarized intense light pulse (gate pulse) can induce transient birefringence in a material (gating material) due to the nonlinear refractive index. This affects the polarization of a signal field when propagating through the gate material. If the signal is polarized linearly, its polarization may be rotated, which can be observed by a cross polarizer setup. For a very fast nonlinear material response the polarization rotation will only be observed when the signal trace and the gate pulse overlap. Consequently, observing the transmission through the cross polarizer setup as a function of the delay time between the gate pulse and the signal allows to deduce the temporal signal structure. This technique is known as optical Kerr gating (OKG) [52, 53].

During the past decades OKG evolved to a well established technique. It was applied to ultrafast fluorescence analysis [18, 54–61], even in combination with imaging [62, 63] or to pulse characterization [64]. It was used also for temporal imaging of turbid media [65, 66] or ballistic photons through scattering media [67]. Three dimensional imaging based on observing scattering light via the time-of-flight method using OKG has been reported [68–70]. Furthermore, OKG was successfully employed as a temporal filter in order to suppress self-emission in plasma imaging [71] or fluorescence in resonance Raman measurements [72–75]. Even for three dimensional Raman imaging of biological tissue the OKG technique is exploited [76–78]. The spatial resolution in these works was, however, limited to several hundred μm due to the use of a slow gate material. Three dimensional fluorescence imaging using the OKG technique, however, has not been reported, yet.

The OKG process is inherently phase matched. Hence no wavelength specific gating is expected in the first place. Furthermore its temporal resolution should generally be governed by the gate pulse duration, if a suitable gating material is used (sects. 6.1 and 3.2.3). A temporal resolution down to $\Delta t = 100$ fs was observed over a broad spectral range [18].

The background in OKG arises from non-gated light leaking through the cross polarizer setup (sect. 3.2.3) only. Hence efficient background suppression is possible for sufficiently large extinction ratios of the polarizers.

The maximum gated amplitude of the signal amounts to 100 % when using common gating materials (sects. 3.2.3 and 6.1). Even though, gating efficiencies up to 4000 % were reported in amplifying media [79]. Since the transient birefringence depends on the gate pulse intensity only, the gating of very weak signals down to the single photon level should be possible without loss of generality.

Preliminary conclusion Evaluating the advantages and disadvantages of the described gating techniques, optical Kerr gating is the most suitable candidate to satisfy the above described tremendous requirements for the gating process. On the one hand it is very fast. Even though the reported gating times are shorter for parametric processes. But this is attributed to the respective experimental conditions. For suitable media (sect. 6.1) no material related limitation of the OKG time (down to the 10 fs range) is obvious. The OKG process seems not to require a minimum signal amplitude and its gating efficiency is much larger compared to the other presented gating mechanisms, except of optical parametric amplification. In addition OKG requires no phase matching, which would limit the spectral bandwidth of the gate and does not suffer from a large background due to self phase modulation. The background of OKG is only determined by the polarizers.

Chapter 3

Physical basics of ultrafast gating

In the following chapter the major physical effects are elucidated that form the foundation for the experiments and the discussion of this thesis. In the first section general effects regarding light matter interaction are presented. Subsequently substantial aspects of ultrashort pulse propagation are explained. Particular focus is on the polarization rotation by the optical Kerr effect.

3.1 Light matter interaction

3.1.1 General mechanism

The electric field $\vec{E}(\omega)$ of a light wave of frequency ω induces a polarization \vec{P} in a material. This leads to a modified field within the material (electric displacement field \vec{D}), which can be expressed by the electric susceptibility χ [80]:

$$\vec{D} = \epsilon_0 \vec{E} + \vec{P} = \epsilon_0 \vec{E} + \epsilon_0 \chi \vec{E} = (1 + \chi) \epsilon_0 \vec{E} = \left(1 + \chi^{(1)} + \chi^{(2)} \vec{E} + \chi^{(3)} |\vec{E}|^2 + \dots \right) \epsilon_0 \vec{E}, \quad (3.1)$$

where ϵ_0 is the vacuum permittivity.

In general the electric susceptibility $\chi(\omega) = \chi_r(\omega) + i\chi_i(\omega)$ is a complex value and a function of the frequency ω (or the wavelength λ) of the electric field.

For weak fields the influence of the higher χ terms is negligible and the relation (3.1) is approximately linear in \vec{E} . In the presence of strong electric fields (high light intensities) the terms $\chi^{(2)}$, $\chi^{(3)}$ etc. in (3.1) cannot be neglected. Physical effects related to $\chi^{(2)}$ or $\chi^{(3)}$ are known as second- or third-order effects. The focus of the present work lies on $\chi^{(1)}$ or $\chi^{(3)}$. Effects arising from $\chi^{(2)}$ require special experimental conditions that are not part of this thesis (phase matching or special material symmetry). Larger orders of χ ($\chi^{(4)}$ and higher) are negligible at the used intensities.

The electric susceptibility χ is a tensor with its rank depending on the order of the nonlinearity. Particularly $\chi^{(3)}$ is a fourth-rank tensor. In isotropic materials, which are in the focus of the present work, $\chi^{(3)}$ possesses 21 nonzero elements, of which only three are independent [81].

3.1.2 The refractive index

The light induced polarization of the material affects the propagation of light. This is characterized by a material property, which is known as "refractive index" $\tilde{n} = n + ik$.

In the linear case \tilde{n} is related to $\chi^{(1)}$ by $\tilde{n}^2(\omega) = 1 + \chi^{(1)}(\omega)$ [80]. The correlation between n and λ (and consequently ω) can be modeled empirically by the Sellmeier equation. Different mathematical structures are common for this equation [82–84]. Two of them will be used in the present work:

$$n^2(\lambda) = C_0 + \sum_i \frac{A_i \lambda^2}{\lambda^2 - B_i} \quad (3.2)$$

$$n^2(\lambda) = C_0 + \sum_i \frac{\tilde{A}_i}{\lambda^2 - B_i} \quad (3.3)$$

C_0 , A_i and B_i are the empirical Sellmeier coefficients.

The refractive index n is a scale for the speed at which light of a given wavelength λ travels through a material. In the case of a wave packet (pulse, cf. sect. 3.2) the group velocity differs from the velocity of each particular spectral component (phase velocity). The refractive index "experienced" by the wave packet (light pulse) is the group refractive index [85]:

$$n_g = n - \lambda \frac{dn}{d\lambda} \quad (3.4)$$

From the series expansion of eq. (3.1) follows the dependence of the refractive index from the electric field. Particularly, the third order term causes an intensity dependence of n [86]:

$$n(I) \approx n_0 + n_2 I = n_0 + n_2^F \langle E^2 \rangle, \quad (3.5)$$

with n_0 being the linear part of the refractive index arising from $\chi^{(1)}$ and n_2 being the nonlinear part arising from $\chi^{(3)}$. I is the intensity of the incident light. The dispersion of $\chi^{(3)}$ is not considered in the present work. The two different expressions for the nonlinear extension of the refractive index n_2 and n_2^F refer to the nonlinear refractive index with respect to the intensity and the average electrical field, respectively. The former is typically given in SI units and mostly used in this thesis. The latter is very common in literature and generally given in cgs units. The relationships between both indices is given by:

$$n_2 [cm^2/W] = \frac{10^{-8}}{9\epsilon_0 c n_0} n_2^F [esu], \quad (3.6)$$

with c being the vacuum speed of light.

For linearly polarized light, n_2 is only related to the $\chi_{xxxx}^{(3)}$ component of the susceptibility tensor [86]. It is important to note that the electronic polarization is only one possible mechanism modifying the refractive index as a function of the intensity. n can also be affected by molecular orientation (in liquids), Raman induced processes or free carrier absorption [86]. Since the present work focuses on the index modification in amorphous solids at fairly small intensities (sect. 6.5.2), these effects are insignificant. Other possible index modifications such as thermal refractive index modification or electrostriction do only occur at longer time scales than those investigated in this work.

Whereas some of these mechanisms (e.g. the free carrier modification) may lead to a scalar index modification, the electronically induced one is considered to be a vectorial effect [87–89]. Thus it can cause nonlinear birefringence.

3.1.3 Relation between the refractive index and microscopic properties

Investigating the microscopic scale the global polarization \vec{P} arises from the summation of the individual molecular (atomic) polarizations. In analogy to the series expansion of the macroscopic polarization, the molecular polarization can as well be decomposed into a linear and higher order parts. The linear part is characterized by the molar polarizability α_m (in cgs unit system). It is related to the linear refractive index by the Lorentz-Lorenz relation [90] (cgs units):

$$\alpha_m = \frac{3V_m}{4\pi N_A} \frac{n_0^2 - 1}{n_0^2 + 2} = \frac{3M_m}{4\pi\rho N_A} \frac{n_0^2 - 1}{n_0^2 + 2}, \quad (3.7)$$

with N_A being the Avogadro constant, V_m the molar volume, ρ the material density and M_m the molar mass. The frequency dependence and complex characteristic of n results from resonant coupling between the electric field (light wave) and the electrons at a given frequency ω_0 .

The nonlinear part that causes the third order term in eq. (3.1) is characterized by the hyperpolarizability γ . It is related to n_2 by [91]:

$$n_2 = \frac{20f^4\pi^2}{cn_0^2} N_m \gamma = \frac{20f^4\pi^2}{cn_0^2} \sum_i N_{m,i} \gamma_i, \quad (3.8)$$

where N is the number density of molecules and f is the local-field correction factor and given as $f = (n_0^2 + 2)/3$. If the material is a mixture, its n_2 value can be estimated by the weighted average of the hyperpolarizabilities of its constituents (last term in eq.(3.8)).

3.1.4 Absorption and band structure of solids

The imaginary part of \tilde{n} refers to the absorption of the light. It is particularly strong at the resonance frequency ω_0 (sect. 3.1.3). In this case the photon energy E_{Ph} of the light fits the energetic difference between two energy levels of the material with at least the lower one being occupied by electrons. This process is known as photo excitation. The correlation between the frequency or the wavelength and E_{Ph} of the light is given by:

$$E_{Ph} = \hbar\omega = \frac{hc}{\lambda}, \quad (3.9)$$

with $h = 2\pi\hbar$ being the Planck constant.

In a solid, the many different energy levels form quasi continuous energy bands. The energetically highest band that is still occupied at zero temperature is called valence band (VB). Bands of higher energies are called conduction bands (CBs). In dielectrics or semiconductors the VB and the CB are separated by a band gap energy E_{Gap} and the CB is empty at zero temperature. Only a few electronic levels

(Urbach levels [92] or energy levels caused by impurities) are present within the band gap.

Consequently absorption in dielectrics and semiconductors becomes dominant, if the photon energy exceeds the band gap energy E_{Gap} . For $E_{Ph} < E_{Gap}$ the absorption is generally very weak. The imaginary part of the nonlinear refractive index can, however, cause multiphoton absorption. In this case two or more photons are absorbed simultaneously. Like the nonlinear refractive index modification (eq. (3.5)) this process is only significant for high intensities. Yet, if a weak light field (signal field I_S) overlaps with a strong field (gate field I_G) single photon absorption from I_S assisted by I_G is possible, even if the photon energies of both fields each are smaller than E_{Gap} . In this work, this effect will be referred to as "combined multi photon absorption" (CMPA). The different absorption mechanisms are summarized in fig. 3.1a (left). In the presence of CMPA and linear absorption the intensity attenuation of the signal field along the light propagation axis z is [86]:

$$\frac{dI_S}{dz} = -(\alpha_k I_G^{k-1} + \alpha_{PD}) I_S, \quad (3.10)$$

where k is the order of the CMPA. α_k and α_{PD} are the absorption coefficients characterizing the CMPA and the linear absorption, respectively. The intensity of the signal behind a sample of thickness d is given by:

$$I_S = I_0 e^{-(\alpha_{PD}d + \alpha_k (I_G(1-R_F))^{k-1} d_{eff})}. \quad (3.11)$$

where R_F is the material's Fresnel reflection for wavelength of the gate pulse (subsect. 3.1.5). d_{eff} is the interaction distance of the two fields inside the material (sect. 6.3).

The gate and the signal fields are typically functions of space and time. Their temporal overlap can be characterized by a delay time t_D . The spatial overlap is considered to be constant. Hence the energy transmission (which is measured by a detector) of the signal field behind the sample is:

$$T(t_D) = \frac{\int_{-\infty}^{\infty} \int_{-\infty}^{\infty} I_S(t, t_D, r) dr dt}{\mathcal{E}_0}, \quad (3.12)$$

where \mathcal{E}_0 is the transmitted energy in the absence of any absorption.

3.1.5 Fresnel reflection and transmission of a slab

When a light wave in medium 1 enters a medium 2 the refractive index changes from n_1 to n_2 ($n_1 \neq n_2$) and Fresnel reflection occurs. The reflection coefficient R depends on n_1 , n_2 , the polarization of the light wave and the angle of incidence. At normal incidence and only weak absorption the reflection coefficient can be calculated by:

$$R_F = \left(\frac{n_1 - n_2}{n_1 + n_2} \right)^2. \quad (3.13)$$

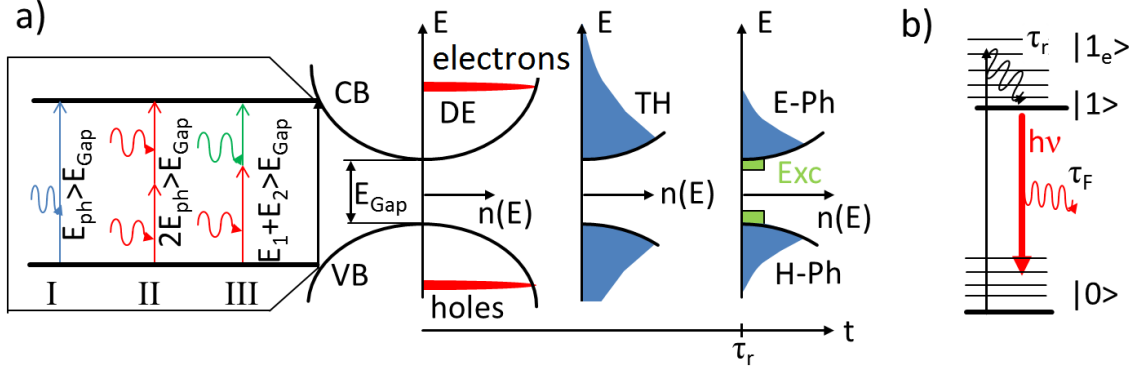


Fig. 3.1: a) Carrier dynamics in a solid upon irradiation: left: electron-hole pair generation in the conduction band (CB) and the valence band (VB), respectively: I) single photon absorption, II) two photon absorption, III) combined two photon absorption; right: relaxation process: thermal disequilibrium (DE), thermalization (TH), electron-phonon interaction (E-Ph), hole-phonon interaction (H-Ph) and exciton (Exc) generation b) Excitation of molecules: (right, $|0\rangle$: electronic ground state, $|1\rangle$: excited electronic state, $|1_e\rangle$: excited vibrational state of $|1\rangle$). τ_r and τ_F are the different relaxation time constants (cf. text)

The reflection and transmission of a coplanar slab are given by:

$$\begin{aligned}
 R_{Slab} &= R_F + R_F \cdot (1 - R_F)^2 \cdot e^{-2\alpha \cdot d} + R_F^3 \cdot (1 - R_F)^2 \cdot e^{-4\alpha \cdot d} + \dots \\
 T_{Slab} &= (1 - R_F)^2 \cdot e^{-\alpha \cdot d} + (1 - R_F)^2 \cdot R_F^2 \cdot e^{-3\alpha \cdot d} + (1 - R_F)^3 \cdot R_F^4 \cdot e^{-5\alpha \cdot d} + \dots,
 \end{aligned}
 \tag{3.14}$$

with α being the linear absorption coefficient of the slab and d its thickness.

3.1.6 Luminescence of photo excited material

Linear or nonlinear light absorption in semiconductors leads to excited electrons in the CB and excited holes in the VB. These are at first in thermal disequilibrium, due to the selection rules of the optical transition. A fast energy redistribution amongst themselves leads to a thermal equilibrium of both, the hot electrons and holes. This process is known as thermalization. It occurs on the 100 fs time scale [33, 93] and is not related to an energy transfer between the carriers and the lattice. Interaction with phonons, which happens on the 100 fs - 1000 fs time scale leads to a cooling of the electron and the hole ensembles in the CB and the VB, respectively (fig. 3.1a).

The thermalized electrons in the CB can bind to holes in the VB. Such carrier pairs are called excitons. Depending on their binding energy excitons are classified in "Frenkel" (strong binding) and "Wannier-Mott" (loose binding) excitons [94]. The excitonic energy levels are typically located inside the band gap. At large carrier densities, additional effects, such as band filling or band gap renormalization may occur [94, 95]. The recombination of thermalized electrons and holes (excitons or free carriers) can cause emission of light which is known as luminescence. It is characterized by a time constant τ_F . Of course, the highly excited electrons in the CB can directly recombine with holes in the VB. Since the thermalization and exciton formation is, however, much faster than the electron hole recombination the direct recombination of highly excited carriers is unlikely.

Photo excitation of molecules (such as dissolved fluorophores) by visible light generally causes the population of upper vibrational states $|1_e\rangle$ of an excited electronic energy state $|1\rangle$. Due to interactions with other molecules or the solvent matrix the excited molecules relax towards the energetic level $|1\rangle$ forming a Boltzmann distribution over the vibrational rotational levels of the electronically excited state. This is known as vibrational relaxation [96]. The relaxation of the molecules from an excited electronic state $|1\rangle$ to the ground state $|0\rangle$ (or vibrational states belonging to $|0\rangle$) can cause luminescence (time constant τ_F). The electronic relaxation is generally much slower than the vibrational relaxation amounting to at least several picoseconds in condensed matter (fig. 3.1b).

The luminescence is either fluorescence or phosphorescence, depending on whether the multiplicity of the electronic spin is conserved or not during the radiative relaxation. For the present work, only fluorescence is relevant.

In the present work, both processes, the electron (hole) relaxation in the CB (VB) in solids (thermalization, phonon interaction and exciton formation) and the vibrational relaxation of molecules are modeled by a single decay, characterized by a time constant τ_r (fig. 3.1a, b). Due to this simplified assumption both systems (solids and molecules) can be analyzed equivalently. The dynamics of carrier concentration or excited molecules can be described by solving the set of rate equations (exemplary for molecules):

$$\begin{aligned}\frac{dN_{1e}}{dt} &= -\frac{1}{\tau_r}N_{1e} \\ \frac{dN_1}{dt} &= \frac{1}{\tau_r}N_{1e} - \frac{1}{\tau_F}N_1,\end{aligned}\tag{3.15}$$

where an initial excited molecule concentration of N_{1e}^0 in the state $|1_e\rangle$ due to the laser pulse excitation is assumed. It is pointed out that besides the radiative relaxation characterized by τ_F , also non-radiative processes may occur (e.g. internal conversion, intersystem crossing). They are not considered in this work, since only emission is detected. Those transitions reduce both, the quantum yield η_F and the measured emission lifetime τ_F . For efficient fluorophores (such as Coumarin 153) they are basically negligible [97]. When detecting the auto-fluorescence of NADH, however, those transitions are responsible for the short emission life time ($\tau_F \approx 500$ ps [8, 98]) and the small quantum yield ($\eta_F = 0.019$ [99]).

The emission power of the fluorescence signal $S_F(t)$ is proportional to $N_1(t)$. Solving (3.15) leads to the time dependent concentration in $|1\rangle$:

$$S_F(t) \propto N_1(t) = \frac{N_{1e}^0/\tau_r}{1/\tau_r - 1/\tau_F} \left[e^{-(1/\tau_F)(t-t_0)} - e^{-(t-t_0)/\tau_r} \right],\tag{3.16}$$

with t_0 being the time at which the molecules are excited into the state $|1_e\rangle$.

In addition to the simple fluorescence, amplified spontaneous emission (ASE) may occur. In this case a population inversion between the $|1\rangle$ and the $|0\rangle$ level is necessary. ASE causes a higher peak power of the fluorescence $S_F(t)$ but a shorter emission time τ_F [85].

3.2 Ultrashort laser pulses

The large intensities that are necessary in order to observe nonlinear effects are achieved by the use of ultrashort laser pulses. These are created by the coherent superposition of different spectral components. Assuming a slowly varying envelope approximation, the electric field of a pulse is given by [51]:

$$\vec{E}(\vec{r}, t) = \frac{1}{2} \vec{A}(\vec{r}, t) e^{i(\omega_0 t - k(\omega_0)z)} + c.c., \quad (3.17)$$

with $\vec{A}(\vec{r}, t)$ being the envelope function of the pulse and $k(\omega_0) = nk_0$ the wave vector in the material at the central frequency ω_0 of the pulse.

3.2.1 Spatial and temporal profile

In this work, the temporal profile of envelope \vec{A} in eq.(3.17) is considered to be Gaussian in space and time. Consequently, the intensity of the pulses is Gaussian as well. Due to the spectral coupling, the pulse duration $\Delta\tau_P$ is related to a minimum bandwidth of the pulses $\Delta\omega$. The correlation between $\Delta\omega$ and its $\Delta\tau_P$ (full width half maximum, FWHM) for the bandwidth limited case is [51]:

$$\frac{\Delta\omega}{2\pi} \tau_P = \frac{c\Delta\lambda\Delta\tau_P}{\lambda_0^2} = 0.441 \quad (3.18)$$

The spatial profile of laser beams is also modeled by Gaussians [80]. This follows from the Maxwell equations and is true for short laser pulses, since all spectral components may be considered separately in a first approximation.

In this context the spatio-temporal intensity profile is given by

$$I(t, r) = I_0 e^{-(\sqrt{2}r/w)^2} e^{-(2\sqrt{\ln 2}t/\Delta\tau_P)^2}, \quad (3.19)$$

with w being the $1/e^2$ beam radius and I_0 is the pulse peak intensity.

The correlation between peak pulse intensity I_0 , the peak pulse power P_0 , the peak pulse fluence F_0 and the pulse energy \mathcal{E} is given by:

$$I_0 = \frac{2 P_0}{\pi w^2} = \sqrt{\frac{4 \ln 2}{\pi}} \frac{F_0}{\Delta\tau_P} = \sqrt{\frac{16 \ln 2}{\pi^3}} \frac{\mathcal{E}}{w^2 \Delta\tau_P}. \quad (3.20)$$

In the Gaussian beam model the beam radius at a distance z from the focal plane is given by:

$$w(z) = w_0 \sqrt{1 + \left(\frac{z}{z_R}\right)^2}, \quad (3.21)$$

with w_0 being the beam radius in the focal plane. z_R is the Rayleigh length. It marks the distance at which the area of the spot has doubled and is calculated by:

$$z_R = \frac{\pi w_0^2}{\lambda}. \quad (3.22)$$

Although the Rayleigh length and hence the focal spot size of a short pulse varies for the different spectral components, this effect is negligible in the present work.

When focusing a Gaussian beam by a lens with focal length f , which is placed in the plane of w_0 , the spot size w_{foc} in the focus of the lens is given by [80]:

$$w_{foc} = \frac{f\lambda}{\pi w_0}. \quad (3.23)$$

3.2.2 Impact of the material parameters

If a short pulse travels through a dispersive material with a nonlinear refractive index n_2 , pulse and beam distortions can take place due to its high intensity and the broad spectrum. The dispersion leads to different phase velocities of the pulse's spectral components. The mutual shift of those causes a broadening of the pulse duration, known as chirp. Assuming a bandwidth limited pulse, the pulse duration will have extended by the factor of $\sqrt{2}$ within the dispersion length, which is defined as:

$$L_D = \frac{\Delta\tau_P^2}{4 \ln 2 k''}, \quad k'' = \frac{\lambda_0^3}{2\pi c^2} \frac{d^2 n}{d\lambda_0^2}, \quad (3.24)$$

with $\Delta\tau_P$ being the bandwidth limited pulse duration and λ_0 being the central wavelength of the Gaussian pulse [51].

Additionally, the intensity dependent nonlinear refractive index will cause a modification of the phase factor in eq.(3.17). On the one hand this affects the transverse coordinate of the pulse, causing self (de)focusing. This effect can be characterized by a critical power P_{cr} , where self focusing exceeds diffraction [81] and catastrophic self-focusing becomes possible. P_{cr} is given by:

$$P_{cr} = \frac{\pi(0.61)^2 \lambda_0^2}{8n_0 n_2}, \quad (3.25)$$

with n_0 and n_2 being the linear and the nonlinear refractive indices, respectively. In case of a high laser pulse peak power $P_0 \gg P_{cr}$, the distance for critical beam collapsing ("self-focusing" distance) is given by:

$$d_{sf} = \frac{2n_0 w_0^2}{\lambda_0} \frac{1}{\sqrt{P_0/P_{cr}}}, \quad (3.26)$$

where w_0 is the $1/e^2$ radius of the laser beam (material at the focal region of the laser beam).

Besides the spatial modulation, the nonlinear refractive index will as well cause a temporal modulation of the pulse. This will, however, lead to spectral broadening. The spectral broadening becomes critical above the nonlinear interaction length L_{NL} [51]:

$$L_{NL} = \frac{1}{k_0 n_2 I_0}. \quad (3.27)$$

On the other hand it causes self-steepening, since the center of the pulse travels with a different velocity than the front and the rear parts. The characteristic length for

self steepening is much larger than L_{NL} and the effect is insignificant for the present work [81].

3.2.3 Optical Kerr gating (OKG)

General analysis

In optical Kerr gating (OKG), a strong linearly polarized pulse (gate pulse) causes a transient birefringence of a material with nonlinear refractive index n_2 . This will modify the polarization of a signal wave as it propagates through the material simultaneously with the gate pulse. The polarization modification can be detected by an analyzer. For most effective gating, the initial polarization of the signal should be linear and rotated about 45° with respect to the gate pulse polarization.

Due to the complex interplay between the material parameters (dispersion and nonlinearities) as well as diffraction effects, the propagation analysis of a short pulse is a problem that requires advanced numerical analysis. For the present work most effects are, however, negligible. The thicknesses of the investigated OKG samples are for instance much smaller than the Rayleigh length z_R or the dispersion length L_D . The effect of self focusing only plays a minor role (sect. 6.5.2). Therefore a simplified model assuming plane waves is used to model the Kerr gating effect.

In this framework, the energy transmission of the optical gate is given by:

$$\mathcal{E}(t_D) = \pi \int_{-\infty}^{+\infty} \int_0^{+\infty} I_S(r, t) r \underbrace{\left(1 - \cos \phi_{nl}(r, t - t_D) \right)}_G dr dt, \quad (3.28)$$

with $I_S(r, t)$ being the intensity of the signal field. ϕ_{nl} is the nonlinear phase shift that is imprinted onto the signal by the gate pulse. The temporal frame of reference is the coordinate system of the signal. Thus the delay time t_D is the temporal distance between the gate pulse and the signal as the signal enters the OKG medium. In eq. (3.28), G is defined to be the gating function for OKG. Additionally cylindrical symmetry was assumed for both, the signal and the gate fields. In this work the maximum energy transmission of a gated signal is defined as the gating efficiency η . The detailed derivation of eq.(3.28) is given in appendix A.

If ϕ_{nl} is small (weak gate pulse intensity approximation) and $\phi_{nl}(r, t) = \phi_{nl}(r)\phi_{nl}(t)$ (which is valid for a Gaussian gate pulse) eq.(3.28) transfers to a second order cross correlation:

$$\mathcal{E}(t_D) = \pi I_{S,0} \int_0^{+\infty} I_{S,r}(r) r \frac{\phi_{nl}^2(r)}{2} dr \int_{-\infty}^{+\infty} I_{S,t} \frac{\phi_{nl}^2(t - t_D)}{2} dt, \quad (3.29)$$

with $I_{S,0}$, $I_{S,r}$ and $I_{S,t}$ being the amplitude, the spatial and temporal intensity profiles (both normalized with respect to the amplitude) of the signal field. Hence the temporal structure of the phase ϕ_{nl} that is imprinted onto the signal determines the

gating time. In the absence of temporal walk-off (sect. 6.3.2) and very fast response times, it is given by:

$$\phi_{nl}(r, t - t_D) = \int_{z=0}^{z=d} k_0 \Delta n(I(t, r)) dz = k_0 n_2 I_G(r, t - t_D) d, \quad (3.30)$$

with d being the sample thickness and I_G being the gate pulse intensity (eq.(3.19)).

It is particularly emphasized that for Gaussian shaped gate and signal functions (FWHM: τ_G and τ_S) the gated signal is again Gaussian with a FWHM value of:

$$\Delta\tau_{OKG} = \sqrt{\Delta\tau_S^2 + 0.5\Delta\tau_G^2} = \Delta\tau_{cc}. \quad (3.31)$$

It is noted that for efficient OKG, an imprinted phase of $\phi_{nl} \geq \pi$ is necessary. Inserting the nonlinear interaction length (3.27) into (3.30) the OKG sample thickness for efficient gating should be:

$$d > \frac{\pi\lambda_S}{\lambda_G} L_{NL}, \quad (3.32)$$

with λ_S and λ_G being the wavelengths of the signal and the gate pulses (central wavelength for the latter). Generally the required thickness exceeds L_{NL} . In particular when the signal wavelength is shorter than the gate pulse wavelength, the spectral distortion of the gate should, however, not be critical [51].

Spatial relations between gate and signal pulse

The relation between the spot widths of the gate pulse and the signal also affects the gating efficiency of OKG. In order to acquire a satisfying gating efficiency, a proper overlap between the gate and the signal is necessary.

The transmitted energy in case of a weak gate pulse intensity is given by (cf. appendix A):

$$\mathcal{E}(w_S, w_G) = A \frac{w_S^2}{1 + 2\frac{w_S^2}{w_G^2}} \quad (3.33)$$

where A is a factor containing the temporal behavior and w_G and w_S being the $1/e^2$ radii of the gate and the signal beams. The maximum theoretical energy transmission $\mathcal{E}_t(w_S, w_G) = \eta_w$ as a function of the spot size relation w_S/w_G is depicted in fig. 3.2. If the gate pulse spot is twice as large as the signal pulse spot in diameter (or radius), the gating efficiency reduces by 30 %.

Fast gating of slow signals

An energy detector temporally integrates an incident signal for several ns [100]. Hence, the finite extinction ratio r_ϵ of the polarizers causes a background in optical Kerr gating, particularly, if the gate is used to analyze signals with time constants much longer than the gating time.

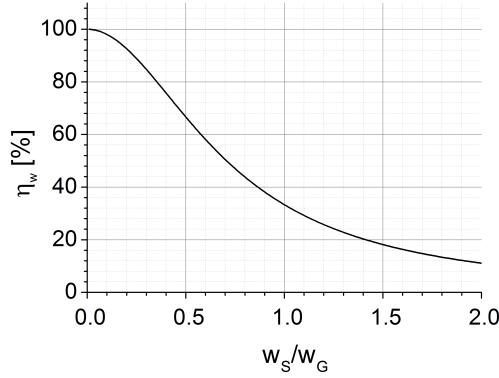


Fig. 3.2: Efficiency η_w of the OKG as a function of the spot width ratio w_s/w_G (weak gating intensity)

The "transmission-to-background" ratio (TBR) of the OKG is defined by (cf. appendix B):

$$TBR = \frac{T}{B} = \frac{\eta_{eff} \Delta\tau_G}{r_\epsilon \tau_F}, \quad (3.34)$$

where η is the gating efficiency and $\Delta\tau_G$ and τ_F are the gate pulse duration and the signal time constant, respectively. Obviously, the TBR scales with the ratio of the time constants $\Delta\tau_G/\tau_F$, which in case of gating a molecular fluorescence will be in the range of 1 : 10000 (order of magnitude).

Likewise it is possible to estimate the number of gated photons n_P to be:

$$n_P = \frac{1.57 \eta_{eff} F_{ex} w_0^2 \lambda_S \Delta\tau_G}{hc \tau_F}. \quad (3.35)$$

Here F_{ex} is the excitation fluence of the signal, η_{eff} is the effective efficiency of the system (a product of the gating efficiency, the transmission of the imaging system and the quantum efficiency of the fluorescence), λ_S the signal wavelength, w_0 the spot radius of the excitation, h is the Planck constant, c the vacuum speed of light and $\tau_{G,S}$ the gate and the signal time constant, respectively.

Equation (3.35) is an estimate for the theoretical limit of the OKG. For a given setup (i.e. given fluorophore, given maximum excitation fluence and given lateral resolution) it defines the minimum possible gating duration $\Delta\tau_G$, which is necessary to at least detect one fluorescence photon. Note that eq. (3.35) is an estimate, assuming a rectangular gate function and an exponential decay. Using the more realistic Gaussian gate function and an emission characteristic which includes a build-up as presented in eq. (3.16) leads to a more complex correlation (eq. (B.8) in appendix B).

The propagation of the signal light through scattering material (such as the vitreous body in the human eye) will cause a blurring of the gated signal, due to the longer propagation time of scattered photons [67], hence causing a loss of temporal resolution. Nevertheless, gating of both, ballistic and scattered light should work equally well. Thus, in contrast to interference based methods for examining the axial distribution the detection efficiency should not be affected by scattering, if it is not too large (i.e. no light passes the scattering material anymore).

Chapter 4

Experimental setups

4.1 The laser system

In this chapter the applied experimental setups will be described. For all experiments, except for those considering the linear material characterization, an amplified femtosecond (fs) laser system was used (Mantis Oscillator and Legend Elite amplifier, both from Coherent Inc.), emitting pulses at $f_{rep} = 1$ kHz repetition rate and a central wavelength of $\lambda_L = 800$ nm. For the two-color OKG experiments, the white light OKG experiments and the experiments regarding the axially distributed fluorescence, the amplified fs laser pulses were coupled into an optical parametric amplifier (OPA, Coherent Opera Solo) in order to generate the pulses at central wavelengths of $\lambda_{ex} = 440$ nm and $\lambda_S = 530$ nm. All setup parameters are summarized in chapter 5.

4.2 Signal detection

Laser pulse energies The energy of the laser pulses were measured using a photodiode (PD 10, read out with a Pulsar 2 system, both from Ophir Inc.).

Laser spectra, white light continuum measurements and two-color OKG The spectra of the laser pulses were measured using a Ocean optics USB4000 spectrometer. For the two-color OKG experiment the transmitted signal, scattered from a scattering disc was also observed by this spectrometer.

Spot size measurements A beam profile camera (Ophir Spiricon SP620U) was used for the spot size and beam shape measurements.

Detection system for the axially resolved measurements:

- **Axially distributed scattering:** The gated light was focused (lens with $f = 50$ mm focal length) onto a photomultiplier (PMT, Hamamatsu H6780-20), which was read out by an oscilloscope (Lecroy Waverunner X64).
- **CdS nanostructure emission and characterization of the gating system:** The gated light was coupled into a spectrograph (Andor SR303i-B, fiber coupled), including a cooled CCD camera ($T = -18$ °C) in combination with a microchannel plate (MCP, Andor i-Star, maximum gain: 255) using a lens with a focal length of $f = 50$ mm. For the CdS double layer measurements

a band pass filter (Brightline 550/88 nm) was used in order to suppress the excitation light. For the measurements regarding the characterization of the gating system (sect. 4.6.3, paragraph "Characterization of the gating system") the CCD signal was spectrally integrated.

- **Coumarin153 fluorescence:** A software based lock-in technique was applied in order to suppress large background due to leakage of the polarizers (subsect. 3.2.3). Therefore, the gate beam was modulated by a light chopper ($f_{\text{chop}} = 13$ Hz). The gated signal was measured using a photo multiplier tube (PMT, Hamamatsu H6780-20). Additionally a part of the gating pulse was observed by a home built silicon photo diode (reference). Trains of 5000 subsequent pulses per delay were recorded by reading out the detectors with an oscilloscope (Lecroy Waverunner X64). The data sets were sent to a computer and numerically integrated for each pulse. Subsequently, the reference data set was digitized to 0 and 1 (gate pulse switched "on" and "off") and multiplied with the (integrated) pulse train of the gated signal. The result was Fourier transformed and the first element of the transformed array was used as measure for the signal. This procedure was repeated five times per delay. The delay scan was repeated 5 times. The data processing was done using LabView2011 from National instruments. A stack of dichroic filters (Brightline 550/88 nm fluorescence filter, 3rd millenium 630SP and Thorlabs FES0750-1) was used in order to block gate and fluorescence excitation light.

4.3 Imaging System

4.3.1 Design of the imaging system

Due to the desired high temporal resolution in combination with the broadband application, an imaging system with minimal group velocity dispersion is necessary. It should also feature a small numerical aperture (large working distance) for signal collimation and a tight signal focusing into the plane of the Kerr gate. The designed imaging optics consists of two silver coated off-axis parabolic mirrors (OAPM) with parental focal lengths of $f_{P1} = 76.2$ mm (OAPM₁, Edmund optics #84-565) for signal collimation and a $f_{P2} = 50.8$ mm (OAPM₂, Edmund optics #47-087) for focusing into the Kerr gate. The off-axis angle was 30°. The arrangement of the mirrors is sketched out in figs. 4.3 and 4.4.

OAPMs are known to show large aberrations (particularly astigmatism and coma, [101]) for light fields, which are not centered at the focus (axially and laterally). Zemax OpticStudio was used to estimate the influence of a finite emitter distribution, excited by a pulse of finite spot size. The imaging properties of the system for three fields emitted by an object (position of the fluorophore, numerical aperture NA = 0.2) into the plane of the OKG were simulated: one centered at the optical axis (F1: $x = 0$ μm , $y = 0$ μm), the others placed off axis (F2: $x = -80$ μm , $y = 0$ μm), (F3: $x = 0$ μm , $y = -80$ μm) and (F4: $x = -80$ μm , $y = -80$ μm). Details are given in appendix C. Additionally the maximum optical path difference along the opening angle of the F1 (sagittal plane) was calculated. All parameters (the positions of the fields, the variation of the object plane and the numerical aperture) were chosen to be larger than in the experiments in order to get an upper limit.

4.3.2 Alignment of the off-axis parabola telescope

One critical aspect of the setup is the accurate alignment of the OAPMs, since even small deviations in their positions or tilts can cause large aberrations, such as coma or astigmatism. Therefore the alignment procedure will be described briefly in this subsection.

First the collimating mirror (OAPM₁ in fig. 4.4) was aligned with the aid of an alignment laser (helium-neon-laser, OAPM₂ was removed for this procedure). The tilt of OAPM₁ was aligned to ensure an angle between the incident and reflected beams of $30 \pm 0.5^\circ$. Subsequently, the beam of the alignment laser was expanded by a telescope towards a beam diameter of approximately 10 mm. The beam profile camera was set to the position of the fluorescence sample and moved axially until the minimum spot diameter of the alignment laser was detected. Afterwards, the lens, used for focusing the excitation pulse was placed into the beam line. Its axial position was optimized by searching the minimum spot size of the excitation pulse on the beam profile camera. Then, OAPM₂ was installed, the beam profile camera was placed at the position of the Kerr gate and a scattering disc was placed at the focal position of the excitation beam ("sample" in fig. 4.4). The tilt of OAPM₂ was optimized by minimizing the spot size of the scattered light in the focus of OAPM₂. In order to find this focus, the beam profile camera was readjusted axially after each optimization step.

4.3.3 Extinction ratio of the polarizers

The extinction ratio r_ϵ (tab. 5.2) of the polarizers is a crucial parameter in terms of efficient background suppression (sect. 3.2.3). The r_ϵ values of three polarizers were investigated: Zeiss polymer thin film polarizer, single layer Edmund optics thin film polarizer (#86-178), and double layer Edmund optics thin film polarizers (#86-178). Therefore, the output of the OPA was set to 532 nm as test wavelength, since this is in the range of the Coumarin153 and the CdS nanostructure fluorescence. The polarization of the laser beam was additionally filtered by a polarizing beam splitter cube. The beam was imaged onto the beam profile camera. For each polarizer, the integrated signal as measurement of the transmitted pulse energy was recorded for parallel and orthogonal orientation of the polarizer with respect to the laser beam polarization. Additionally the background signal (laser blocked) was measured. If necessary, the beam was attenuated by combinations of absorptive neutral density filters (Thorlabs, NE05A, NE10A, NE20A) in order to prevent saturation of the CCD chip.

4.4 Sample preparation and chemical characterization of the investigated Kerr media

An overview over the investigated OKG samples is given in sect. 6.1. Fused silica (F300), N-SF56 glass and ZnS were purchased from Heraeus GmbH, Schott AG and Vitron Spezialwerkstoffe GmbH, respectively. SAL- and Te-glasses were produced using the crucible melting technology according to [102–104] at IPHT. The high purity raw materials (oxides, hydroxides, carbonates) were thoroughly mixed, homogenized and subsequently melted in a covered platinum (SAL-glasses) or gold

crucible (Te-glasses). The temperature range varied for SAL-glasses between 1400 °C and 1650 °C and for Te-glasses between 800 °C and 900 °C in ambient air atmosphere. After several hours of melting, the liquid glass batch (batch size: 20g Te-, 500g SAL-glasses) was cast into preheated moulds and slowly cooled to room temperature (100 K/h).

The homogeneity of SAL-glasses was improved by multistage melting (refining and stirring process). Therefore, the powder pre-melt (first step) was quenched after 8 hours in ultra-pure water to obtain fritted glass particles. The re-melt (second step) of the dried particles at 1650 °C for refining and homogenizing was partly stirred (platinum stirrer) to avoid striae and bubbles.

The chemical glass composition was determined by quantitative electron probe microanalysis (EPMA) using energy dispersive X-ray (EDX) spectrometry on an electron microprobe (JEOL Ltd., JXA-8800L). Glass transition temperatures (T_g) and thermal expansion coefficients (α_{th} at 600 °C) were ascertained by a vertical dilatometer (LINSEIS Messgeraete GmbH, L75V) using a 5 K/min heating rate. The glass densities ρ were determined by the Archimedes' principle in ethanol. The molar volumes V_m were calculated from the ρ values. Finally, the samples were polished to a thickness of 1 mm (SAL-glasses) or 0.7 mm (Te glasses) and cleaned by methanol.

4.5 Setups for measuring the linear and nonlinear optical properties

4.5.1 Linear absorption and transmission measurements

Transmission as well as reflection spectra were acquired by a commercial spectrometer (PerkinElmer, Lambda 900) between 210 nm and 850 nm. For the reflection measurements the samples were placed inside the integrating sphere of the spectrometer. The wavelength dependent absorption and reflection coefficients $\alpha(\lambda)$ and $r(\lambda)$ were retrieved numerically from the obtained spectra (applying "nD Nonlinear System Solver", National Instruments from LabView2011 onto eqs. (3.14)) The linear optical properties of F300, N-SF56 and ZnS were taken from the respective data sheets [84, 105, 106].

4.5.2 Characterization of the nonlinear refractive index

The nonlinear refractive index n_2 of the glasses was determined by the Z-scan technique as proposed in [107]. After the laser pulses, as described in sect. 4.1, had passed a home-built variable attenuator (half wave plate B.Halle, 800 nm, zero order in combination with a thin film polarizer, Layertec article number 107457) the beam was focused by a BK7 lens ($f = 500$ mm) to a $1/e^2$ spot radius $w_0 \approx 40$ μ m. In the far field behind the focus the laser beam passed an aperture of 20 % pulse energy transmission (if sample placed far off the focal plane) onto a photo detector. As a reference, the back reflection from a 0.2 mm thick BK7 cover slip was recorded by a photo diode of the same type. The setup is depicted in fig. 4.1. The sample was moved within the focal region along the laser propagation direction and the transmitted pulse energy recorded for each position. Z-scan signals at different laser

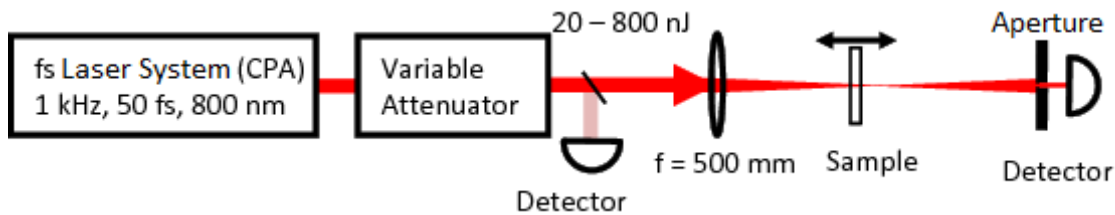


Fig. 4.1: Setup of the Z-scan measurement

pulse energies were recorded. Additionally the Z-scan signal of a reference sample was measured, in order to enable the data analysis as described in [108] using a 0.7 mm thick slab of fused silica with 1200 ppm OH.

In addition to each closed aperture Z-scan measurement, an open aperture measurement was performed. If a significant decrease of the transmitted signal was detected in the open aperture scan, the closed aperture scan was corrected by normalizing to the open one [109]. This was done in order to avoid misleading effects due to nonlinear absorption of the material and was particularly critical, when measuring the Te-glass and ZnS at high intensities.

4.6 Optical Kerr gating setups

4.6.1 Two-color optical Kerr gating setup

For the two-color OKG measurement the OPA output wavelength was set to $\lambda_S = 530$ nm (signal pulse, 1 nJ). A second output of the OPA provided $\lambda_G = 800$ nm pulses (gate pulses). These were coupled into the variable attenuator (sect. 4.5.2, pulse energy: $\mathcal{E}_G = 200$ nJ to 2 μ J) and temporally delayed with respect to the signal pulse ($t_D = -300$ fs to +600 fs). In case of positive t_D , the signal preceded the gate pulse. After rotating the signal beam polarization by 45 degrees (achromatic half wave plate, B. Halle, 460-680nm) the signal and gate pulses were focused into the sample using lenses (BK7) with focal lengths of $f_1 = 250$ mm (gate pulse) and $f_2 = 100$ mm (signal pulse). The experimental setup is shown in fig. 4.2 The spot width of the gate and the signal pulses were measured at the focal plane (Kerr sample removed).

The signal energy transmission of the OKG medium as a function of t_D and E_G was evaluated by integrating the spectrum from 450 nm to 600 nm (polarization integrated signal, PIS). E_G was measured by the photo detector. A virgin spot on the OKG sample was used for every gate pulse energy in order to avoid probing in damaged or photo darkened sample areas. I_G was computed from the pulse duration and the $1/e^2$ radius assuming Gaussian pulses in space and time (chapter 5).

Additionally, the change in signal polarization (polarization selective signal, PSS) was observed by placing an analyzer in front of the spectrometer. Therefore, the linear loss (Fresnel reflection) of the analyzer was evaluated prior to the experiments. This was done by measuring the transmission of the Kerr gate with the analyzer rotated parallel with respect to the laser polarization and without the analyzer. In this case the 530 nm pulses were detected by the photo detector. For this measurement, the output power of the OPA was increased in order to ensure a good signal-to-noise ratio at the detector. The transmission of the OKG sample for parallel orientation

between analyzer and laser polarization and without analyzer amounted to 106 nJ, and 140 nJ, respectively. Thus the linear loss of the polarizer was 25 %. This value was taken into account, when normalizing the PIS with respect to the PSS (sect. 6.5).

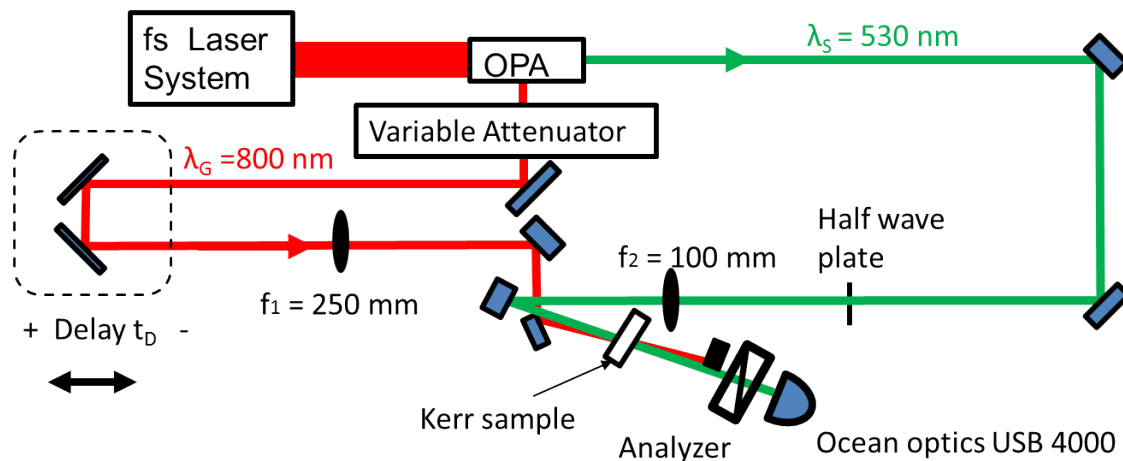


Fig. 4.2: Setup of the two-color OKG measurement: red: beam line of the gate pulse, green: beam line of the signal pulse

4.6.2 White light optical Kerr gating setup

The broad band OKG performance of each individual material was investigated by gating a white light pulse. After rotating its polarization by 45 degrees the pulse at $\lambda_S = 530$ nm was focused ($f = 100$ mm) into a 2 mm quartz crystal (z-cut) generating a white light continuum (WLC, signal pulse). The divergent WLC emission was collimated and focused into the OKG material using the fluorescence imaging optics (sect. 4.3.1). Before entering the sample, the polarization of the WLC was filtered by a thin film polarizer (double layer of thin film polarizers, Edmund optics #86-178, separated by 1 mm). The WLC pulse, collimated by an achromatic lens ($f = 50$ mm) behind the Kerr medium, past an analyzer (polarization rotated by 90° with respect to first polarizer) and was then coupled into the spectrometer (USB4000, Ocean optics) by a microscope objective (Zeiss 20X NA0.4 LP Achroplan). The setup is depicted in fig. 4.3.

Prior to investigating the samples, the spectrally resolved spot size of the WLC at the designated position of the Kerr gate was characterized by the knife edge technique. Therefore an aluminum sheet (thickness $25 \mu\text{m}$) was attached onto a microscope object carrier, which was moved horizontally as well as vertically through the beam at different axial positions near the focal region. The transmitted signal was then detected by the spectrometer (analyzer removed).

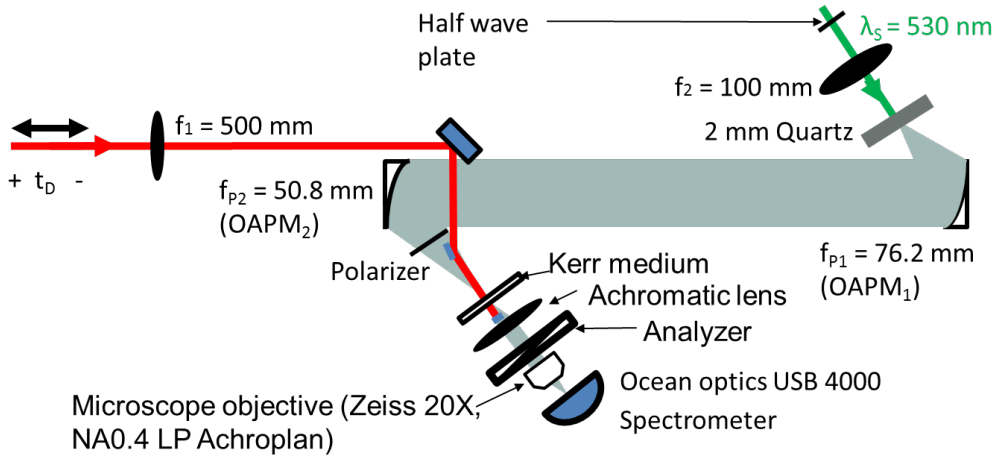


Fig. 4.3: Setup for WLC gating (only the part which is different from the two-color OKG setup), f_{P1} and f_{P2} : parental focal lengths of the parabolic mirrors.

4.6.3 Setup for Kerr gating of axially distributed emission

Principle Kerr gating setup The final setup for analyzing the signals arising from axially distributed emitters upon fs laser excitation is comparable to the gating setup of the white light continuum and depicted in fig. 4.4. The OPA output wavelength was set to $\lambda_{ex} = 440$ nm. The pulse energy was varied by changing internal settings of the OPA (such as frequency doubling or mixing efficiency).

The excitation pulses were focused onto the axially structured sample by a 100 mm fused silica lens. In order to adjust the spot radius and consequently the Rayleigh length of the excitation field, an iris ($Iris_1$) in front of the lens was used to reduce the incident beam diameter (sect. 3.2.1, eq. (3.23)). The spot of the excitation beam in the focal region was characterized by a beam profile camera.

The structured sample (CdS nanostructure layers or double compartment cuvette filled with Coumarin153 solution, cf. paragraph "Sample design" below) was placed onto a linear translation stage in the focal region of the excitation pulse. Epifluorescent light was imaged into the OKG medium using the system as described in sect. 4.3. Additionally an iris ($Iris_2$) was introduced between $OAPM_1$ and $OAPM_2$ in order to define the numerical aperture of the collimation system. For the fluorescence analysis, the diameter of the iris was set to 10 mm, leading to a NA of 0.07 of the detection system. The OKG material was SAL-glass, (SAL4, 25 mol% La_2O_3 , cf. sect. 6.6). The SAL-glass could be laterally and axially shifted with respect to the beam propagation direction. In between the focusing $OAPM_2$ and the SAL-glass, the signal light passed a polarizer (double layer of thin film polarizers, Edmund optics #86-178, separated by 1 mm, cf. sect. 5.3) and entered the detection system (sect. 4.2). The beam line for the gate pulse was the same as for the two-color or the white light setup (using a lens of focal length $f = 500$ mm). The transmitted pulse was blocked by a small beam trap behind the SAL-glass in order to avoid damage inside the microscope objective, the analyzer, the filters or the detection system.

Characterization of the gating system Varying the axial position of the fluorescent object leads to a shift of the fluorescence focal plane at the Kerr gate (appendix C). The influence on this image plane shift was evaluated by placing a scattering disc at varying sample positions (fig. 4.4). At the position of the OKG

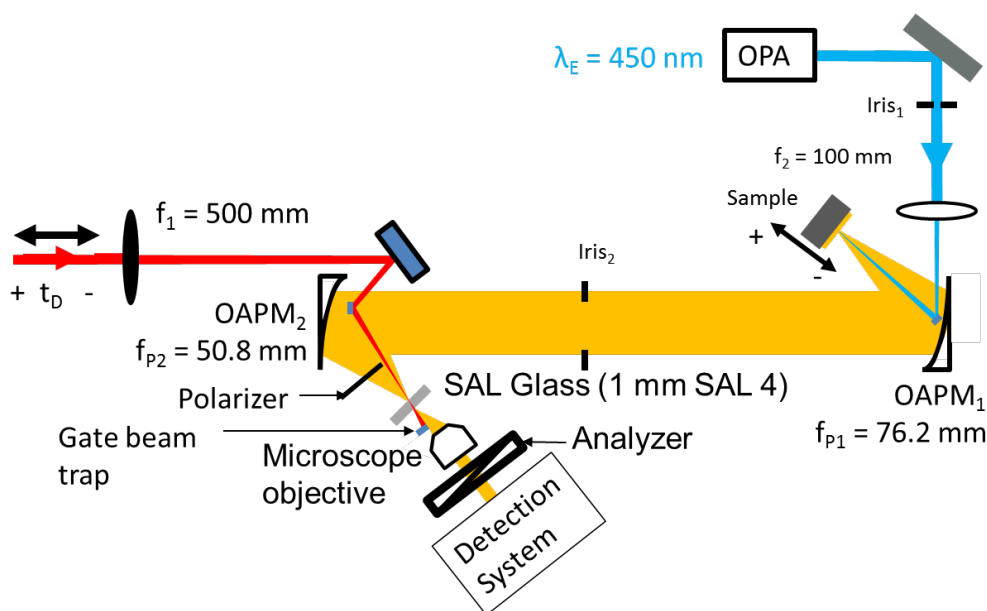


Fig. 4.4: Setup for gating the axially distributed broad band emission

medium the spot size of the scattered light was observed as a function of the scattering disc position. Additionally, the spot size of the pump beam was measured.

Afterwards a time resolved OKG experiment was performed, using SAL-glass (25 mol % La_2O_3) as Kerr medium for different axial positions of the scattering disc. For every position, the transmission of the Kerr gate was recorded as a function of the delay time t_D between the pump and the scattered light. The recorded time traces were fitted by a Gaussian.

Sample design Different configurations of axially distributed emitters were investigated:

- **Axially distributed scattering:** A layered system of a microscope object carrier, double-sided transparent adhesive tape, a 0.7 mm thick slab of fused silica and one layer of double-sided transparent adhesive tape was used as layered scattering sample (fig. 4.5a). The purpose of the cover slide in this case was to simulate the influence of any cuvette wall. The scattered light, transmitting through the Kerr gate was detected as a function of the delay between the pump pulse and the excitation pulse.
- **Single layer CdS nanostructure ensemble:** An ensemble of CdS nanostructures on a silicon substrate provided by the "Institut für Festkörperphysik" of the "Friedrich-Schiller-University" of Jena.
- **Double layer CdS nanostructure imprints:** An imprint of the CdS nanostructures on an ultra thin glass plate (Schott D263[®] T eco Dünnglas, $d = 100 \pm 10 \mu\text{m}$) was produced.
- **Coumarin153 filled double compartment cuvette:** A special cuvette with two distinct compartments filled with a Coumarin153 solution was built. The basic design of the cuvette is depicted in fig. 4.5 (transversal section).

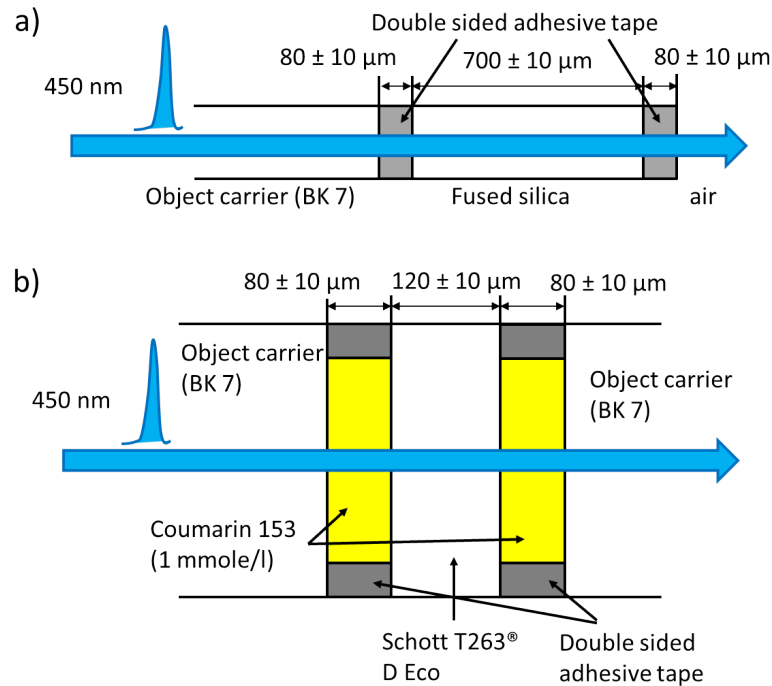


Fig. 4.5: a) Structure to determine axially distributed scattering and propagation direction of the pulse, b) Double compartment cuvette

A 1 mm thick microscope object carrier was cleaned with ethanol. Subsequently, a ring shaped double-sided adhesive tape ($d_{\text{tape}} = 80 \pm 10 \mu\text{m}$) was attached on the object carrier. The inner part of the ring was filled with Coumarin153 solution (Lambdachrome laser dye LC5400, concentration $c = 1 \times 10^{-3}$ mole/l in ethanol). Afterwards, the compartment was closed by an ultra thin glass slab (Schott D263® T eco Dünnglas, $d_{\text{D263}} = 120 \pm 10 \mu\text{m}$) and a second compartment was attached on the other side of the ultra thin glass slab.

Chapter 5

Important setup parameters

In this chapter the experimental parameters of the presented setups are characterized.

5.1 Laser pulse duration and emission spectra

Two-color optical gating The spectrum of the gate pulse is centered around $\lambda_G = 795$ nm exhibiting a bandwidth of $\Delta\lambda_G = 27.5 \pm 0.5$ nm (full-width-half-maximum). The signal pulse for the two-color OKG experiments is centered around $\lambda_S = 530$ nm showing a bandwidth of $\Delta\lambda_S = 12.1 \pm 0.1$ nm (fig. 5.1a). Figure 5.1b depicts the delay time dependent energy transmission of the signal pulse through a 0.7 mm thick slab of fused silica used as OKG material (maximum gate transmission ≈ 5 %). Assuming Gaussian pulses, the bandwidth limited pulse duration of both, the signal and the gate pulses amount to $\Delta\tau_G(\text{min}) \approx \Delta\tau_S(\text{min}) \approx 35$ fs. Therefore, the expected duration of the gated signal is $\Delta\tau_{OKG} = \sqrt{1.5} \times 35$ fs = 43 fs (eq.(3.31)). Nevertheless, the duration of the gated signal is larger, amounting to $\Delta\tau_{OKG} = 90$ fs. Taking into account the temporal walk-off due to the group refractive index mismatch between the signal and gate pulse wavelengths (sect. 6.3.2) and the small angle of 2° between the gate and the signal beams (appendix D), the pulse durations (FWHM) computed from the gated signal are $\Delta\tau_G = 70 \pm 5$ fs and $\Delta\tau_S = 70 \pm 10$ fs. An initial chirp on both pulses is considered to be responsible for their protracted duration. This seems reasonable, since the beam had to pass multiple optical components inside the commercial OPA (lenses, mixing crystals, sapphire slab for creating a white light continuum etc.), before generating the 530 nm signal pulse. Pre-chirping of the IR pulse seeding the OPA was not possible, because the OPA was designed to feature its optimum output (pulse energy and stability) for pulses without pre-chirp.

Excitation pulses for stacked layers The spectrum of the excitation pulse around $\lambda = 440$ nm is shown in fig. 5.2a. It is distorted, but the pulse duration is still short. This was verified by replacing the sample by an aluminum sheet and gating the scattered signal of the excitation pulse using a 1 mm thick slab of SAL4-glass (the same sample was used to gate the fluorescence signal, sect. 6.6). The duration of the gated signal amounts to $\Delta\tau_{OKG} = 150$ fs. The temporal walk-off between the gate pulse and the signal is considered to be the limiting factor of the gating duration in this case (sect. 6.4).

The excitation of the fluorophores, on the other hand, is a linear optical process, thus independent on the pulse duration. Furthermore, for both investigated materials (CdS and Coumarin153) the absorption causes an electronic excitation into

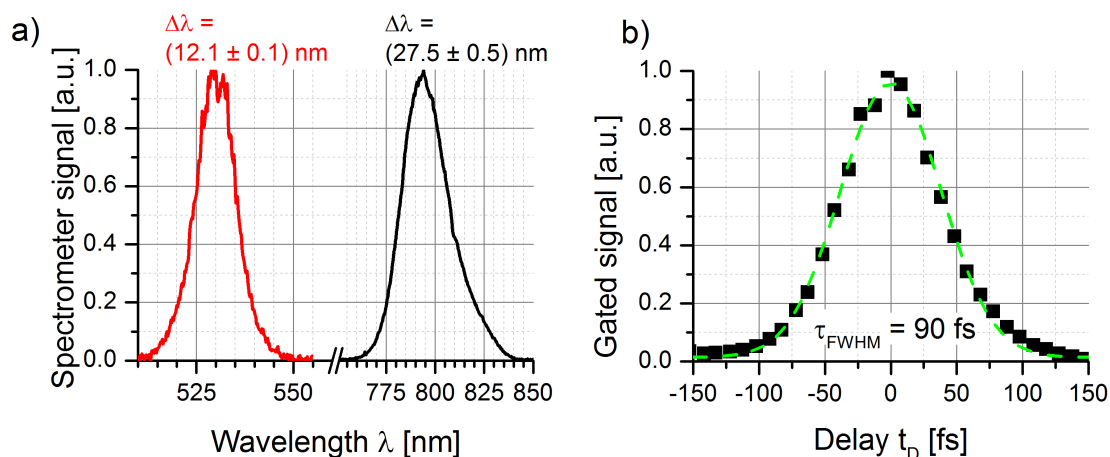


Fig. 5.1: a) Spectra of the signal pulse (red) and the gate pulse (black) for two-color optical Kerr gating b) The delay time dependent trace (amplitude normalized to 1) of the gated signal ($\lambda_S = 530$ nm) using a 0.7 mm thick slab of fused silica as OKG material (Green dashed line: Gaussian fit).

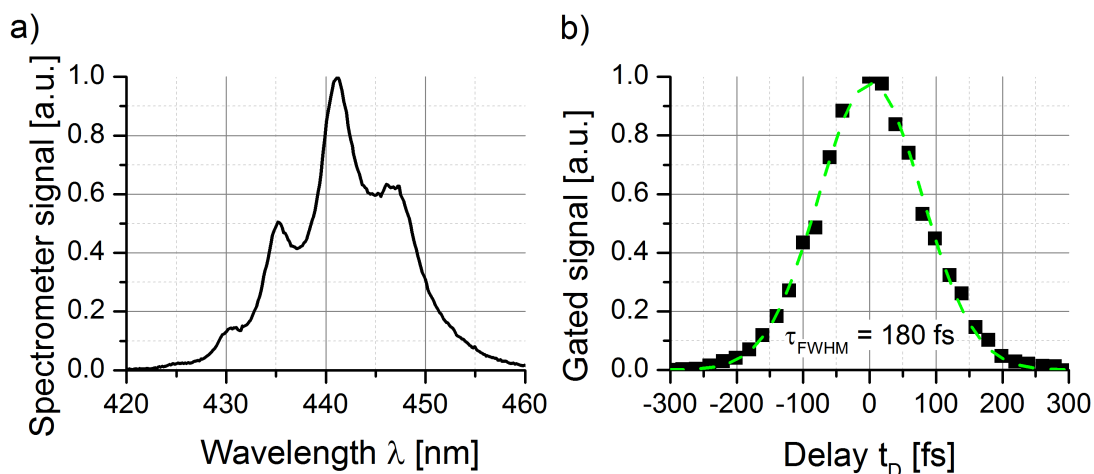


Fig. 5.2: a) Spectrum and b) gated signal of scattered light of the fluorescence excitation pulse ($\lambda_{ex} = 440$ nm and $\lambda_G = 800$ nm)

broad bands (dense vibrational states in Coumarin153 or quasi - continuous states in the conduction band of the CdS). The very fast thermalization of the initial distributions after the excitation makes the actual spectral shape of the excitation pulse play only a minor role.

White light continuum The spectrum of the WLC is depicted in fig. 5.3a. It exhibits a maximum around 530 nm. The WLC intensity is decreasing rapidly towards shorter wavelengths. Towards longer wavelengths up to 750 nm it reaches a more or less constant intensity of around 5 % of its maximum for $\lambda > 600$ nm. Wavelengths above 750 nm were not examined due to the spectral overlay with the pump field.

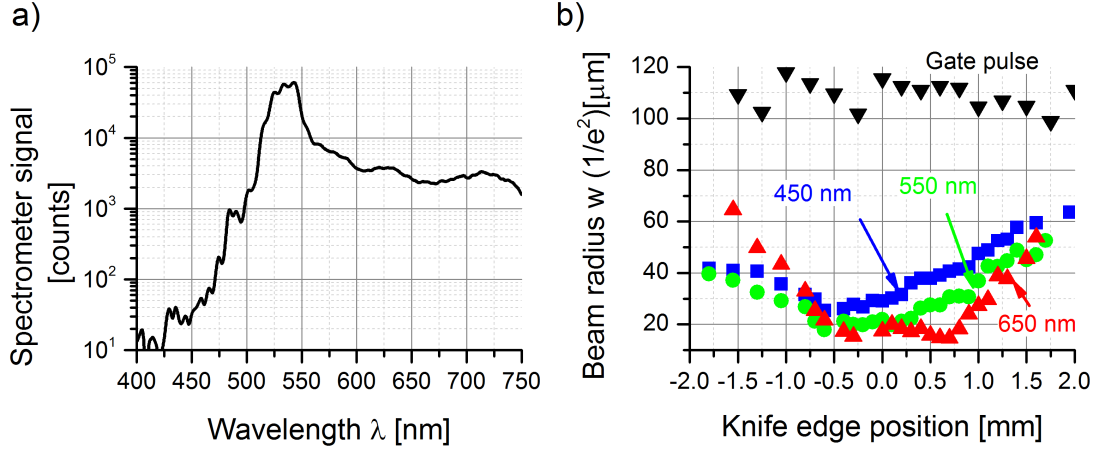


Fig. 5.3: a) Spectrum of the white light continuum, b) $1/e^2$ spot radii of the gate pulse and of selected WLC emission wavelengths around the position of the OKG (determined by knife-edge method, cf. text)

Tab. 5.1: Central wavelength λ , spot radii (horizontal w_H and vertical w_V), Rayleigh length z_R (calculated) as well as FWHM pulse duration $\Delta\tau$ of the signal and the gate pulses for two-color OKG and the excitation pulse of the fluorescence

Pulse	λ [nm]	$w_H(1/e^2)$ [μm]	$w_V(1/e^2)$ [μm]	z_R [mm]	$\Delta\tau$ (FWHM) [fs]
Gate	795	44.2 ± 0.8	46.6 ± 0.8	8.1	70 ± 5
Signal	530	22.2 ± 0.6	26.4 ± 0.6	3.5	70 ± 10
Excitation	440	46.4 ± 0.2	47.6 ± 0.7	15.8	-

5.2 Spot widths

Two-color optical Kerr gating and fluorescence excitation pulse The laser spots for the two-color OKG and the excitation spot of the fluorescence were measured by a beam profile camera. The images of the spots are shown in fig. E.1 in appendix E. Along the horizontal and the vertical axes (with respect to the optical table) the beam profiles were fitted by Gaussians (fig. 5.4a and b). The $1/e^2$ radii are summarized in tab. 5.1. Additionally the Rayleigh lengths z_R (eq.(3.22)) were calculated from the geometrical average of the spot radii, assuming $M^2=1$ (tab. 5.1).

The approximation of collinear beams should be adequate for the used setup. The angle between the gate and the signal beams amounted to 2° and was reduced to a value between 0.8° and 1.5° after entering the sample (Snell's law). Hence the spatial walk-off between both beams was less than $15 \mu\text{m}$ within the sample and thus smaller than the used spot widths.

White light continuum In order to ensure proper focusing of all spectral components of the WLC, its spot around the focal plane was investigated using the knife edge method [110] in combination with spectrally resolved detection (sect. 4.6.2). Figure 5.3b depicts the retrieved $1/e^2$ radii as a result of measurements, where the knife edge was moved horizontally with respect to the optical table. A vertical movement of the knife edge led to comparable results. Evidently the spot radii of the

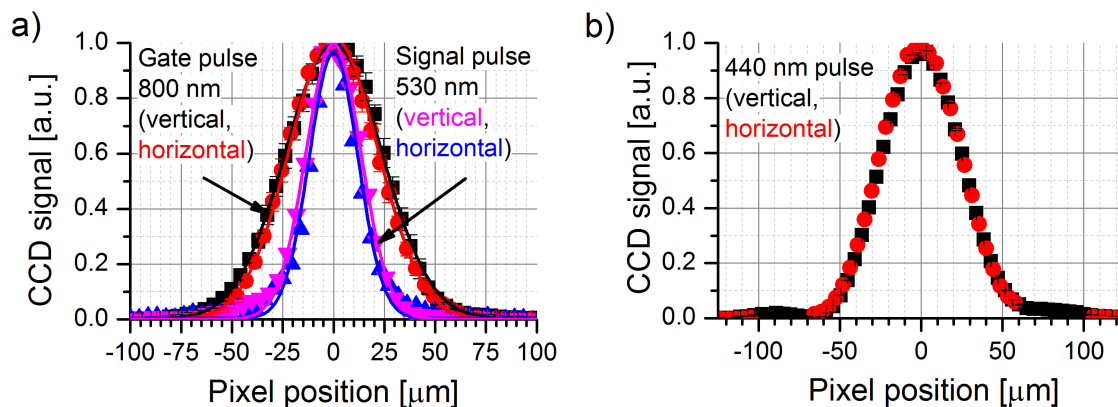


Fig. 5.4: Horizontal and vertical (with respect to the optical table) beam profiles of a) gate pulse ($\lambda_G = 800$ nm) and signal pulse ($\lambda_S = 530$ nm) for the two-color Kerr gating experiments, b) excitation spot of fluorescence ($\lambda = 440$ nm).

different spectral components of the WLC are much smaller than that of the gate pulse over a range before and behind the focal plane being larger than the OKG sample thickness (sect. 6.1). It is pointed out that the gate pulse radii for gating the WLC and for the two-color OKG experiments are different, because lenses of different focal lengths were used (chapter 4).

5.3 Extinction ratio of the polarizers

The extinction ratio r_ϵ (sect. 4.3.3) of the used polarizers was calculated by:

$$r_\epsilon = \frac{T_{\text{para}}}{T_{\text{perp}}} \text{ with } T = (\text{sig} - \text{bckgrd}) \times 10^{\text{OD}}, \quad (5.1)$$

with T_{para} and T_{perp} being the polarizer transmission for parallel or perpendicular orientation with respect to the polarization direction of the laser. The transmissions were computed by subtracting the spatially integrated signals of the CCD chip with ("sig" in eq. (5.1)) and without ("bckgrd") the laser beam and multiplying it with the attenuation of the used neutral density filters (optical density OD).

For the three polarizers the r_ϵ values are summarized in table 5.2.

Tab. 5.2: Extinction ratio r_ϵ of the used polarizers (sect. 4.3.3)

Polarizer	r_ϵ
Edmund optics (#86-178, single)	260
Edmund optics (#86-178, double)	2500
Zeiss	≈ 20000

The double layer polymer polarizer from Edmund optics and the Zeiss polymer polarizer were used as polarizer and analyzer for the OKG setups (chap. 4), respectively.

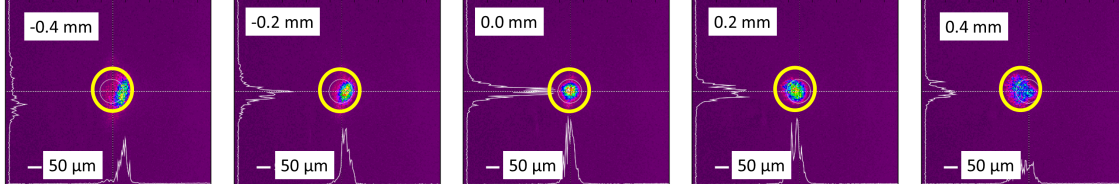


Fig. 5.5: Scattered light in the plane of gate material (different axial positions of the scattering sample), yellow circle: spot size of the gate pulse.

5.4 Characterization of the imaging system

Imaging performance The shift of the image plane when imaging objects from different axial object positions can cause a change in the signal spot size on the surface of the OKG material. This leads to a change in the spatial overlap between the gate pulse and the signal thus varying the gating efficiency (sect. 3.2.3). This will result in an object position dependent amplitude of the gated signal. Hence, this effect used in confocal microscopy, is (initially) counterproductive for depth resolved emitter detection via OKG.

The spot size of the image for different object positions is depicted in fig. 5.5. For comparison, the spot size of the gate pulse is denoted by the yellow circle in fig. 5.5. Shifting the position of the scattering sample for about ± 0.4 mm around the focal position will approximately double the radius of the imaged spot from $w_S \approx 0.5 \times w_G$ to $w_S \approx w_G$. According to fig. 3.2 this leads to a reduction of the maximum gating efficiency by a factor of 2 from $\eta_{max} = 70\%$ ($w_S/w_G = 0.5$) to $\eta_{max} = 35\%$ ($w_S/w_G = 1.0$). These results agree with the results from the simulation (appendix C).

Additionally, the influence of the sample position onto the gating efficiency was evaluated by comparing the maximum amplitude (gating efficiency η) of the gated scattering signal for the different sample positions (fig. 5.6a). Evidently, η only reduces by a factor of around 1.4 (to $\eta = 70\%$ of the maximum) within a range of $\Delta z = \pm 0.5$ mm which is less than expected (fig. 3.2). This is attributed to the thickness of the OKG material. In spite of the shift, the imaging plane remains inside the gate material for small shifts of the object plane (sect. 3.2.3).

The thicknesses of the investigated structures in the present work do not exceed $d_{max} = 260 \mu\text{m}$ (sect. 4.6.3 and chapter 7). The reduction of the gating efficiency in this position range is less than 5 % and therefore neglected. No effect of the object position onto the gating time was observed. This agrees with the results from the simulation. According to the simulation the variation of the object position leads to an optical path difference corresponding to a transit time, which is less than 50 fs, which is much shorter than the gating time (appendix C).

Gating the scattered light pulse ($\lambda_{em} = 440$ nm), imaged by the parabolic mirrors, confirms the absence of imaging optic related temporal distortions of the signal (fig. 5.2b). The broad-band suitability of the designed imaging optic is confirmed by observing the axial beam profile of the WLC at different wavelengths (fig. 5.3b).

Linearity and calibration of the position measurement The linear correlation between the sample position and the delay time t_D was verified by plotting the delay between the maximum of the scattered light signal (cf. previous paragraph) and the maximum of the gate pulse ($t_{D,max}$) as a function of the scattering sample

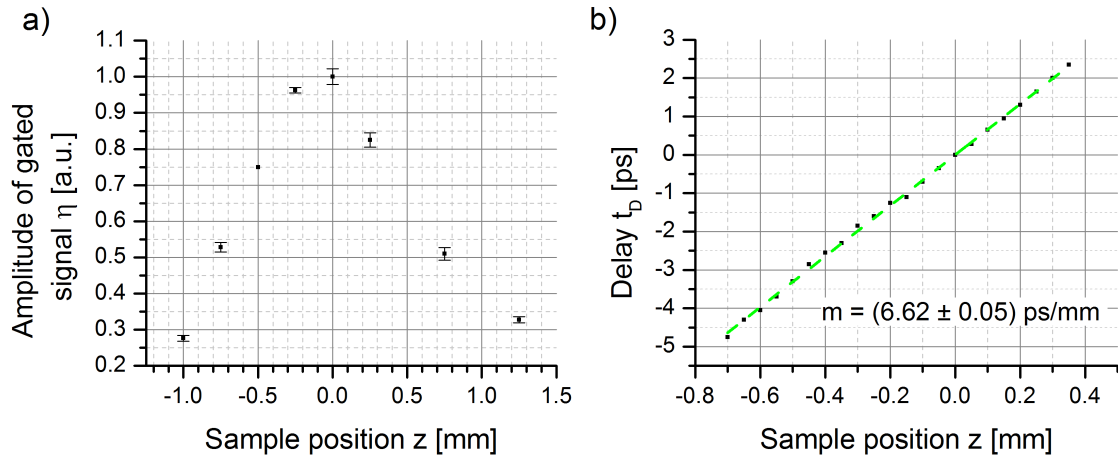


Fig. 5.6: a) Amplitude of gated signal as function of scattering sample position, b) Correlation between delay time t_D (gate and scattered pulse) and position of scattering sample

position (fig. 5.6b). The slope of the linear correlation amounts to $m = 6.62 \pm 0.05$ ps/mm. This confirms the correlation between the propagation time of the light and the position ($t_{D,max} = 2z/c = 6.67z$, sect. 7.1, assuming a refractive index of $n=1$).

Chapter 6

Material evaluation for optical Kerr gating

The quest of analyzing very weak fluorescence signals using rather small gate pulse energies, which are achievable by modern fs oscillators, demands special requirements onto the optical gate material. The designed Kerr setup needs to comprise a

- short gating time,
- large gating efficiency, and
- huge spectral transmission bandwidth.

Commonly used efficient materials show a slow material response [111], thus long gate times. In contrast, fast gating media suffer from inefficient switching [18]. Consequently, a material providing a reasonable compromise of efficiency and speed is required. Therefore in the following section the evaluation of selected promising OKG materials is presented.

At first a brief overview is given regarding selected state of the art OKG material systems. After selecting promising materials for designing an OKG, that fits the challenging requirements, the measured linear and nonlinear optical properties are evaluated with respect to common literature. The impact of dispersion and absorption onto OKG is analyzed. From the results a "Figure of merit" (*FOM*) is deduced to identify the most suited OKG material. The proceeding of this chapter is mapped in fig. 6.1.

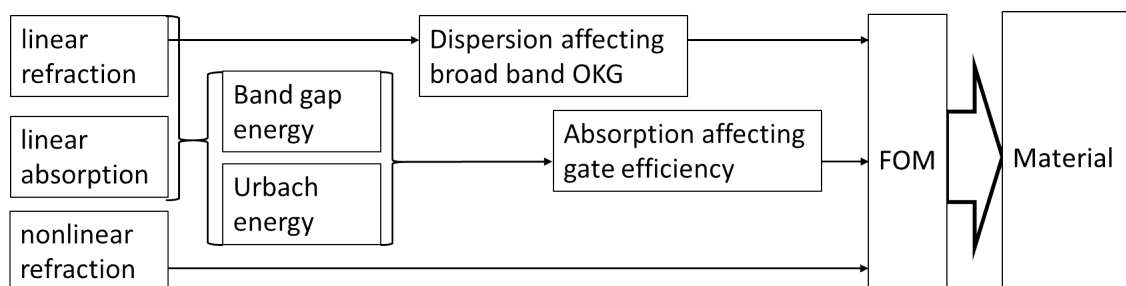


Fig. 6.1: Structure of the present chapter (aim: determine most suited OKG material)

6.1 State-of-the-art of gating materials and their selection

At first sight the gate efficiency η appears to be parallel with the nonlinear refractive index n_2 of the material (sect. 3.2.3). On this account a lot of effort was put into the research of finding materials with very large n_2 values. The traditionally preferred OKG material is carbon disulfide (CS_2) [52–54]. The nonlinear refractive index of CS_2 ranges from $n_2 = 30 \times 10^{-7} \text{ cm}^2/\text{GW}$ up to $n_2 = 400 \times 10^{-7} \text{ cm}^2/\text{GW}$ depending on the pulse duration [40, 112–114]. The large n_2 value of CS_2 is, however, achieved for pulse durations of at least several tens of picoseconds. This is explained by the large contribution of the molecular orientation to the nonlinear refractive index. The reorientation time of the molecules typically amounts to several picoseconds [111, 115]. Different organic liquids such as toluene or nitrobenzene show comparable results [111]. As a consequence the minimum achievable gating time is limited to several picoseconds, which is a drawback. By proposing a double gating technique [116], the gating time was reduced to be twice the gate pulse duration. Thereby the OKG material was irradiated by two gate pulses of perpendicular polarization.

Certain organic molecules such as fullerenes (C_{60}) modified by electron donor groups such as $-\text{NH}_2\text{CN}$ were reported to show a nonlinear refractive index more than 10 times larger than that of CS_2 in the femtosecond range accompanied by response times below 100 fs [35, 114, 117]. Unfortunately, these molecules also show a significant absorption for wavelengths below 600 nm causing signal beam attenuation by both linear and nonlinear absorption.

Deviating from most organic liquids, the contribution of the atomic nuclei in solids (crystalline and amorphous) originates from Raman scattering of the material [118] and not from molecular orientation. Therefore the nuclear response function is much faster and its contribution weaker than that in liquids. In case of fused silica, for example, the nuclear part of the response function is below 20 % of the electronic contribution and it decays exponentially with a time constant of 32 fs [118]. The impact of this decay on the gating time is negligible, compared to the gate pulse duration and effects arising from dispersion (subsect. 6.3.2).

Particularly material systems consisting of light molecular matrices such as alkaline earth silicate glasses or fluoride crystals show a transmission down to the ultraviolet spectral range. Unfortunately these systems only exhibit a very small nonlinear refractive index. In case of fluorides it amounts to $n_2 \approx 1 \times 10^{-7} \text{ cm}^2/\text{GW}$ [119–121]. For alkaline earth silicate glasses the values are slightly larger (in the range of $n_2 = 2 - 3 \times 10^{-7} \text{ cm}^2/\text{GW}$ [122]). In particular the nonlinear refractive index of SiO_2 has been the subject of extensive investigations during the past decades. Its value was measured to lie between $n_2 = 2.3 \times 10^{-7} \text{ cm}^2/\text{GW}$ and $n_2 = 3.25 \times 10^{-7} \text{ cm}^2/\text{GW}$ with an average value of $n_2 = 2.7 \times 10^{-7} \text{ cm}^2/\text{GW}$ [113, 119–128]. The values for crystalline and amorphous SiO_2 are comparable. Certainly, the n_2 value of an individual SiO_2 sample relies on the manufacturing process as well as on the material purity.

In contrast bulk solids composed of heavier atomic constituents show a larger nonlinear refractive index thus being more promising for highly efficient OKG. Most of these materials show a n_2 value exceeding the one for CS_2 (in the limit of short pulse duration). In particular, for germanium or arsenic based chalcogenide glasses (one component systems, binary or ternary) n_2 values as large as $n_2 = 1.4 \times 10^{-4}$

cm^2/GW were reported [129–136]. For CdTe the literature value even amounts to $n_2 = 5.2 \times 10^{-4} \text{ cm}^2/\text{GW}$. These materials have already been used as gate material, although the gating time amounted to several ps [137]. The major drawback of the chalcogenides is their relatively small band gap, leading to transmission breakdowns for wavelengths in the long wavelength visible spectrum (VIS) or even the infrared spectrum. Thus, these materials are inept as gate material for fluorescence analysis.

For the optical gating in the VIS spectral region different material systems showing a larger band gap were suggested. These include heavy flint glasses ($n_2 = 26 - 68 \times 10^{-7} \text{ cm}^2/\text{GW}$, [126, 138]), strontium titanate (SrTiO_3 , $n_2 = 21 \times 10^{-7} \text{ cm}^2/\text{GW}$ [139, 140]), beta-barium borate ($\beta\text{-BaB}_2\text{O}_4$, $n_2 = 5 - 20 \times 10^{-7} \text{ cm}^2/\text{GW}$, [141]), bismuth based glasses ($n_2 \approx 30 \times 10^{-7} \text{ cm}^2/\text{GW}$ [142–145]), lead-phthalocyanine doped glass (n_2 comparable to CS_2 [146]), niobium(V)oxide glasses ($n_2 = 20 - 100 \times 10^{-7} \text{ cm}^2/\text{GW}$) and zinc sulfide (ZnS , $n_2 = 110 \times 10^{-7} \text{ cm}^2/\text{GW}$, [147–149]). A particularly auspicious class of materials is represented by tellurite glasses, which recently have been proposed to be suitable for OKG [60, 150]. Their reported nonlinear refractive indices vary in the range of $n_2 = 5 - 45 \times 10^{-7} \text{ cm}^2/\text{GW}$ [68, 151–157].

The gating times of the presented heavy materials lie between $\Delta\tau_{OKG} = 100$ fs and $\Delta\tau_{OKG} = 1000$ fs, depending on the actual material structure and the spectral relation between the gate pulse and the signal. Due to their fairly short gating time, their nonlinear refractive index is generally assigned to the electronic material response.

Besides bulk material, optical films were investigated in terms of their capability for OKG as well. Giant n_2 values were reported in these material systems. For instance ferroelectric films consisting of complex compounds including TiO_2 or Ta_2O_9 were presented that showed nonlinear refractive indices in the range of $n_2 = 1.9 \times 10^{-3} - 6.1 \times 10^{-5} \text{ cm}^2/\text{GW}$ in the femtosecond region [158–160] or even $n_2 = 3.55 \text{ cm}^2/\text{GW}$ for picosecond gate pulse durations. Greatly enhanced n_2 values were also reported for instance in CuO ($n_2 = -4 \times 10^{-4} \text{ cm}^2/\text{GW}$, [161]) or SrTiO_3 films ($n_2 \approx -1 \times 10^{-3} \text{ cm}^2/\text{GW}$, [162]) as well as in doped (e.g. Ag:BiO_3 , $n_2 \approx 2 \times 10^{-4} \text{ cm}^2/\text{GW}$ [163]) or undoped (e.g. Ag-BaO , $n_2 \approx 2 \times 10^{-4} \text{ cm}^2/\text{GW}$ [164] or Au-SiO_2 $n_2 \approx 1 \times 10^{-2} \text{ cm}^2/\text{GW}$ [165]) composite films. In particular nano structuring of the thin films appears to enhance the absolute value of the nonlinear refractive index, even though it may cause a negative sign. Random (e.g. nano crystalline material [166, 167], nanotubes [168] or embedded nanoparticles [169–171]) and well-arranged nano structures (e.g. metallic grating structure [38, 172] or nanoporous structures [173, 174]) were reported. Confinement effects [166, 174], surface plasmons [163, 172], resonant absorption effects of inter band gap states [162] or Bragg resonances [38] were proposed to be responsible for the extremely enhanced nonlinear refractive index. Also unwanted impurities were explicitly not excluded as an origin of the large n_2 values [174].

At first glance thin film systems seem to be the most promising material system for highly efficient OKG. However, the films show large absorption and scattering losses in particular if they are nanostructured or if interband resonances are responsible for the large n_2 values. Resonant effects furthermore result in long material response times. For that reason bulk materials were chosen to be evaluated in terms of their gating performance. They combine a large nonlinear refractive index value accompanied by a fast response time, a broad transmission bandwidth and the

absence of significant absorption or scattering losses. Five types of bulk materials were investigated in the present work:

- Amorphous SiO₂ (fused silica, Heraeus F300)
- SiO₂-Al₂O₃-La₂O₃ glass (SAL-glass, IPHT fabrication)
- Heavy flint glass (Schott N-SF56)
- Tellurite glass (0.75TeO₂-0.1996ZnO-0.05K₂O-0.0004Er₂O₃, Te-glass, IPHT fabrication)
- Poly-crystalline zinc sulfide (Vitron Spezialwerkstoffe GmbH, ZnS)

Since fused silica has already been investigated exhaustively, it serves as a reference material. Besides the heavy flint glass, the Te-glass and ZnS were reported in the literature to be promising candidates for OKG. The novel SAL glass system was also investigated in terms of its gating capabilities. This system consists of a light glass matrix (SiO₂ and Al₂O₃) where a fraction of the glass maker SiO₂ was replaced by the heavy glass modifier La₂O₃. Although the structural properties of this system have been studied comprehensively during the past [175–182] only little is known about its nonlinear properties [103, 183]. The combination of heavy atoms and a light glass matrix are, however, auspicious in terms of finding a compromise to efficient and fast gating. The composition of the investigated SAL glasses is summarized in tab. 6.1

Tab. 6.1: *Composition of the investigated SAL glasses*

Name	SiO ₂ [mol %]	Al ₂ O ₃ [mol %]	La ₂ O ₃ [mol %]
SAL1	67.4	22.1	10.5
SAL2	65.6	20.1	14.3
SAL3	60.1	21.2	18.7
SAL4	55.7	20.2	24.1

6.2 Linear and nonlinear properties of selected gating materials

The linear and nonlinear material properties are crucial in terms of efficient optical gating (sect. 3.2.3). For that reason the following section aims for examining the linear absorption and refraction as well as the nonlinear refraction of the suggested OKG material. From the linear characteristics the band gap energy and selected material dispersion parameters are derived. Those become particularly important in understanding the complex gating behavior of the materials (sects. 6.4 and 6.5). The results are discussed in the framework of common macroscopic and microscopic theories.

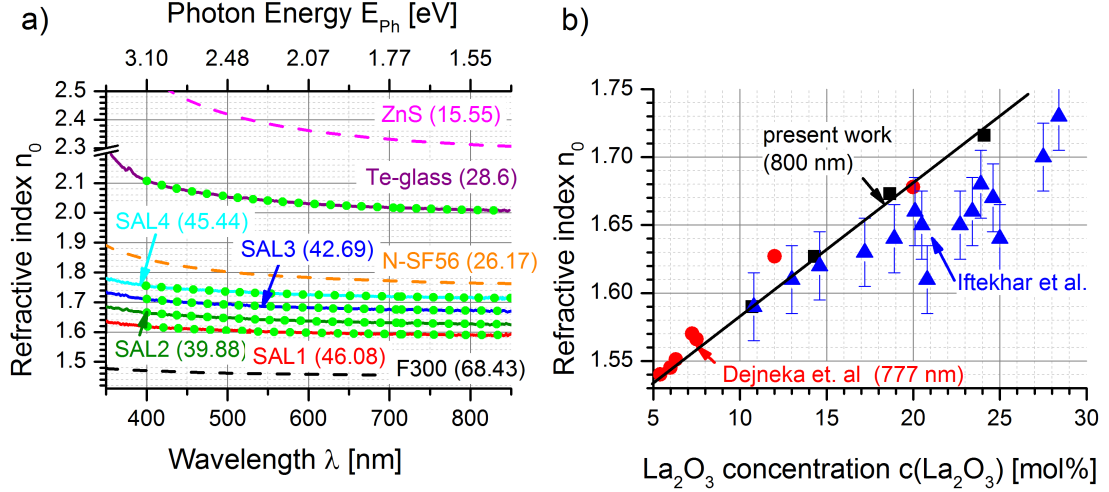


Fig. 6.2: a) Refractive indices n_0 of the investigated materials as function of the wavelength λ and photon energy $E_{Ph} = h\nu$, green lines: fitted Sellmeier curves, brackets: Abbe numbers. b) linear refractive indices n_0 (SAL-glasses) as a function of La_2O_3 concentration, black squares: present work, blue triangles: Iftekhhar et al. [180], red circles: Dejneka et al. [184]

6.2.1 Wavelength dependent linear absorption and refraction

For F300, N-SF56 and ZnS the refractive indices were taken from the literature [84, 105, 106] and the absorption coefficients α (except for F300) were computed from the sample transmission (eq. (3.14)). The required Fresnel reflection coefficients R_F were estimated from n_0 (sect. 3.1.5). In case of the Te-glass and the SAL-glass R_F and the absorption coefficient α were retrieved by numerically solving the set of equations (3.14). The error of the numerical retrieval was estimated to be less than 1 % by comparing the retrieved results when including or excluding the last terms on the right hand side of (3.14). The refractive index $n_0(\lambda)$ was calculated from $R_F(\lambda)$ assuming normally incident light (sect. 3.1.5). The n_0 values as a function of the wavelength λ and the photon energy E_{Ph} are given in fig. 6.2a. The green dashed lines in fig. 6.2a show the fitted Sellmeier curves (eq. (3.2)). The corresponding Sellmeier coefficients are given in tab. 6.4. All investigated materials show normal dispersion. Their Abbe numbers as a scale for the material dispersion are given in brackets in fig. 6.2a and in tab. 6.4. They decrease with increasing refractive index confirming the expected large dispersion for large refractive indices.

The refractive indices of the SAL glasses lie between those of fused silica and of heavy flint glass. The La_2O_3 dependent increase of the linear refractive index n_0 ($\Delta n_0/\Delta c(La_2O_3) = 9.4 \times 10^{-3} \text{ mol}\%^{-1}$) and the glass density ($\Delta \rho/\Delta c(La_2O_3) = 7.9 \times 10^{-2} \text{ gcm}^{-3} \text{ mol}\%^{-1}$, tab. 6.4) in this work are found to be stronger than those recently reported [180]. The relatively steep gradients and the small deviations from the linear dependences in fig. 6.2b are possibly a result of the two-step sample preparation in the present work including a re-melt of a relatively large glass sample. This assumption is supported by the n_0 values obtained at 777 nm from re-melted SAL glasses in ref. [184], which fit the linear regression of the present n_0 values very well in spite of their broad range of Al_2O_3 content from 6 to 20 mol% (fig. 6.2b).

The refractive index and the dispersion of the Te-glass ranges from $n_0 = 2.0$ to $n_0 = 2.3$, thus being much larger than the values of N-SF56. Yet, it is smaller than the refractive index of ZnS. Its fairly large n_0 value and the corresponding

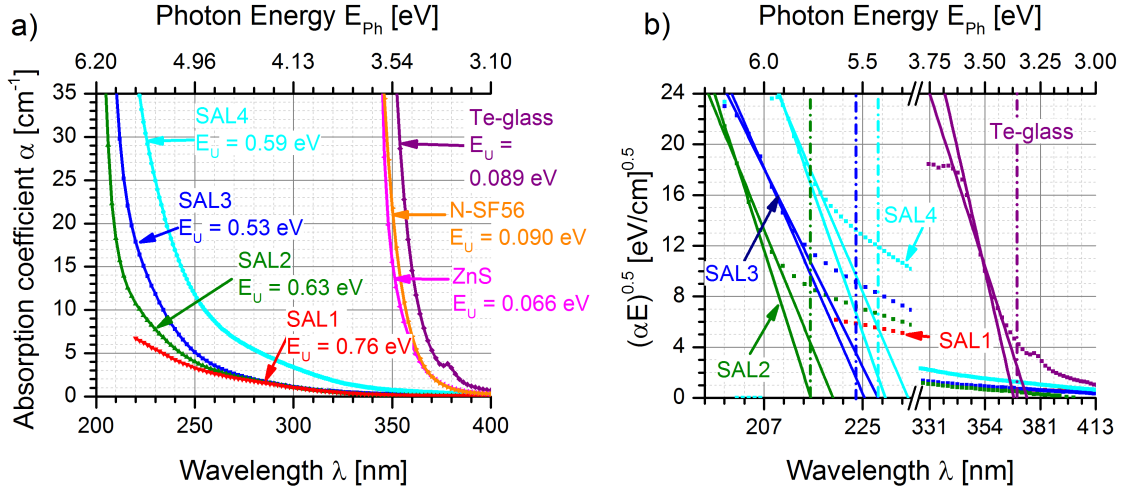


Fig. 6.3: a) Absorption coefficients α as a function of wavelength λ and photon energy E_{Ph} , E_U : Urbach energies b) $\sqrt{\alpha E_{Ph}}$ as a function of wavelength λ and photon energy E_{Ph} , solid lines: linear regressions (different energy /absorption coefficient ranges), dash-dotted lines: estimated band gap energy.

Abbe number of $\nu_d \approx 23$ (tab. 6.4) compare well with known literature values of comparable glass systems with large TeO_2 content [155, 185–188].

In contrast to the refractive indices, the absorption values of the investigated materials group differently (fig. 6.3a). The heavy index materials (N-SF56, Te-glass and ZnS) show a comparable absorption behavior that rapidly increases (from $\alpha = 5 \text{ cm}^{-1}$ to $\alpha = 50 \text{ cm}^{-1}$) between photon energies of $E_{Ph} = 3.3 \text{ eV}$ and $E_{Ph} = 3.6 \text{ eV}$, but the SAL-glasses' absorption rises modestly between $E_{Ph} = 4 \text{ eV}$ and $E_{Ph} = 6 \text{ eV}$. The absorption increases with the La_2O_3 concentration. The absorption spectrum of fused silica was not measured, since it had been subject to intense investigation during the past [189]. The absorption of the F300 should be negligible in the investigated spectral range. From the steepness and the energetic position of the absorption band edges it is possible to estimate the Urbach and the band gap energies. For highly efficient broad band OKG these values are important, particularly in terms of absorption as counter process to the gating (sect. 6.3.1). Thus they will be estimated and discussed in the following section.

6.2.2 Estimate of the Urbach and the band gap energies

The Urbach energy E_U In the low absorption region the absorption coefficient α as a function of the photon energy E_{Ph} was fitted exponentially by [190, 191]:

$$\alpha(E_{Ph}) = \alpha_0 \cdot e^{\frac{E_{Ph}}{E_U}} \quad (6.1)$$

in order to determine the Urbach energy E_U of the respective material. α_0 is the band gap tailing parameter [192]. For the SAL-glasses the E_U values range from 0.53 eV to 0.76 eV. For the high index materials they lie below 100 meV (fig. 6.3a).

The Urbach energy is a characteristic parameter evaluating a materials' structural disorder at a given temperature. [92, 193]. The disorder can be a consequence of defect centers in the materials, impurities, annealing processes or variations in the growth conditions ([190, 193–195]). It is noticeable, that the Urbach energy value

of the present Te-glass is smaller (below 100 meV) than those, mentioned in the literature, which lie in the range of 200 meV to 400 meV ([193, 196–198]). This indicates a low disorder of the Te-glass system that is almost comparable to crystals. Only a few Te-glasses presented in the literature show comparable Urbach energies [152, 186]. A reason for the small disorder might be the Er_2O_3 content which was reported to reduce the Urbach energy in Te-glass [186].

In contrast the Urbach energies of the SAL glasses range from 530 meV to 760 meV and seem to decrease with increasing La_2O_3 content. Hence the glass modifier La_2O_3 is increasing the structural order of the alumino silicate glass. Yet, the Urbach energy is much larger than that of pure fused silica, which is below 0.1 eV [199]. The reason for that might be an increased concentration of non-bridging oxygen ions in the material. Literature values for Urbach energies of SAL-glass structures are not available. However, the presented values are comparable to similar systems, particularly $\text{Li}_2\text{O}-\text{Al}_2\text{O}_3-\text{SiO}_2$ glasses [200]. For all investigated materials the obtained Urbach energies are in the range of amorphous semiconductors ([201]). Of all investigated samples, ZnS shows the smallest value of $E_U = 66$ meV, which is a typical value for a crystalline material [202].

The band gap energy E_{Gap} The Urbach energy is a measure for the density of states (DOS) within the band gap close to the conduction band. This is generally much smaller than the DOS within the conduction band. Hence in order to evaluate (nonlinear) absorption as one counter process for OKG, the energetic position (E_{Gap}) is of much greater interest. Generally, the band gap energy E_{Gap} can be determined by linearly fitting $(\alpha E_{Ph})^{1/2}$ vs. E_{Ph} , (direct transitions) [203–205] for values of the absorption coefficient ranging from $\alpha = 10^3 \text{ cm}^{-1}$ to $\alpha = 10^4 \text{ cm}^{-1}$ [199, 206] (Tauc-plot). The intersection of the fitted curve on the abscissa represents E_{Gap} . The measured absorption coefficients amounted to 60 cm^{-1} at most (only shown up to $\alpha = 35 \text{ cm}^{-1}$ in fig. 6.3a), thus being much smaller than the required values for successfully performing a Tauc-plot. Still, fitting the absorptions according to Tauc et al. [204] may at least give a rough estimate of the actual band gap energy [198, 207, 208]. In order to clearly present the fits for ZnS and N-SF56 are not shown in fig. 6.3b. The values of the band gap energies are depicted in tab. 6.4. Although the values of E_{Gap} are estimates, their error margins were evaluated, by including different data points into the fit. The margins are represented by the zero points of the two lines per absorption curve in fig. 6.3b.

For ZnS, the estimated band gap amounts to 3.43 eV, hence being slightly smaller than the expected value of 3.6 eV [209, 210]. For the Te-glass the value of E_{Gap} is 3.3 eV, which is in the range of the given literature values [205, 206]. Yet, the value of E_{Gap} strongly depends on the exact glass composition. As a first approximation E_{Gap} of the presented Te-glass can be estimated by using the weighted average of its constituents' E_{Gap} values [128, 211]. Consequently, $E_{\text{Gap}}(\text{Te-glass}) \approx 0.75 \times E_{\text{Gap}}(\text{TeO}_2) + 0.2 \times E_{\text{Gap}}(\text{ZnO}) + 0.05 \times E_{\text{Gap}}(\text{K}_2\text{O}) = 0.75 \times 3.79 + 0.2 \times 3.4 + 0.05 \times 2.2 = 3.6$ eV. Besides differences due to obtaining too low absorption coefficients, the deviation between the measured and estimated value may as well arise from nonlinear influences of the different constituents [212]. Furthermore, the given E_{Gap} values are valid for the crystalline materials, yet the Te-glass is an amorphous structure and thus the E_{Gap} values may be slightly different.

Regarding the experimentally estimated E_{Gap} values of the SAL glasses, they range from 5.33 eV to over 6 eV. So far no information about the band gap energies of SAL glasses can be found in the literature. Less information is available on other alumino silicate glasses [195, 200, 213]. The band gaps were determined to approximately 3.46 eV in case of the undoped system, which is quite different from the SAL glass values. Estimating the band gap energy of the SAL-glasses from the weighted average of the constituents' E_{Gap} values (SiO₂: 9 eV [214], Al₂O₃: 7 to 10 eV [215] and La₂O₃: 5.2 eV to 6.2 eV [216–218]) leads to $E_{\text{Gap}} \approx 7.68$ eV for SAL4 and $E_{\text{Gap}} \approx 8.16$ eV for SAL1. These values are larger than those computed from the absorption (tab. 6.4). One reason might be the small absorption coefficient range, that was used for fitting or structural changes in the material due to the glass mixture.

Besides from absorption, E_{Gap} can be estimated from the refractive index of the material. Generally the refractive index scales inversely to the band gap E_{Gap} . In order to evaluate the correlation quantitatively, various (semi-empirical) models were proposed during the past decades [82, 219–222]. They are based on atomic approaches [223] or the oscillator strength [220]. The model of Hervé and Vandamme [222], which takes into account covalent as well as fractional ionic bondings is considered to be accurate for most compound materials. Within the framework of this model, the refractive index n_0 is related to E_{Gap} by:

$$n_0 = \sqrt{1 + \left(\frac{13.6\text{eV}}{E_{\text{Gap}} + 3.4\text{eV}} \right)^2}, \quad (6.2)$$

where n_0 is the refractive index at negligible dispersion.

A different model linking n_0 and E_{Gap} was proposed by Reddy [224]. It is based on Moss' atomic approach [223]. Within the framework of this model, the energy gap is linked to the refractive index by

$$E_{\text{Gap}} e^{n_0} = 36.3\text{eV} \quad (6.3)$$

The E_{Gap} values of the investigated materials computed according to Hervé and Vandamme (eq. (6.2)) and Reddy (eq. (6.3)) are compared in tab. 6.2. To ensure a small dispersion only, the n_0 value at $\lambda = 1 \mu\text{m}$ was extrapolated from the Sellmeier equation for the calculation. The accuracy of n_0 was estimated to be ± 0.1 in order to evaluate the accuracy of the computed E_{Gap} values.

It is conspicuous that both computed E_{Gap} values are larger than the estimated ones except in the case of ZnS. Besides the inaccuracy due to the (semi-)empirical nature of the models, the rough estimate of E_{Gap} from the low absorption coefficients may be the reason. Particularly for the amorphous materials the absorption may still arise from excitation of Urbach states. Nevertheless, the E_{Gap} values of the SAL-glasses seem to lie far above 5 eV, excluding efficient two- and three-photon absorption of the gate pulse for this material system as a counteracting process to OKG.

6.2.3 Nonlinear refraction of the materials

The most important parameter for OKG is the nonlinear refractive index n_2 of the materials, since it ultimately determines the imprinted phase shift (e.g. eq. (3.29)).

Tab. 6.2: Comparison of the estimated band gap values from the absorption (this work) and from the refractive index n_0 according to [222] and [224]

Material	n_0 ($\lambda = 1 \mu\text{m}$)	Estimated from Absorption	Hervé Vandamme	Reddy
SiO ₂	1.45	> 7	10 ± 2.0	8.5 ± 0.9
SAL1	1.587	> 6	8 ± 1.3	7.4 ± 0.8
SAL2	1.623	5.71 ± 0.06	7 ± 1.2	7.2 ± 0.8
SAL3	1.668	5.46 ± 0.05	6.8 ± 1.1	6.8 ± 0.7
SAL4	1.71	5.33 ± 0.05	6.4 ± 0.9	6.6 ± 0.7
SF56	1.73	3.45 ± 0.02	6.2 ± 0.9	6.4 ± 0.7
Te-glass	2.00	3.34 ± 0.04	4.5 ± 0.5	4.9 ± 0.5
ZnS	2.292	3.43 ± 0.04	3.2 ± 0.4	3.7 ± 0.4

Determination of n_2 In the present work n_2 of the materials (except for N-SF56) was measured by the Z-scan technique (sect. 4.5.2). Although the n_2 value can be extracted from a single Z-scan measurement [107] a pulse energy dependent set of Z-scans was recorded for each material (proportional to the pulse intensities) in order to guarantee the absence of higher order nonlinear effects and to improve the accuracy of the measurement.

Exemplary, the Z-scans of SAL1 glass at three different pulse energies are shown in fig. 6.4a. According to Sheik-Bahae et al. [109], the curves were corrected by subtracting a background trace measured at a very low pulse energy in order to eliminate transmission fluctuations due to surface effects (e.g. small scratches).

In the absence of higher order nonlinearities the "Peak-to-Valley" transmission ΔT_{PV} (fig. 6.4a) scales linearly with the imprinted phase shift in the focal plane and consequently with the pulse energy [107, 109, 225]. This is confirmed in fig. 6.4b. Consequently, the ratio $\Delta T_{PV}/E$ is a scale for n_2 . The ratios were determined by linearly fitting the ΔT_{PV} values as functions of the pulse energy (fig. 6.4b). The nonlinear refractive indices of the materials were determined from these ratios by a reference measurement as proposed by Bridges et al. [108] using:

$$(n_2)_s = (n_2)_r \frac{(\Delta T_{PV})_s}{E_s} \frac{E_r}{(\Delta T_{PV})_r} \frac{L_r (1 - R_r)}{L_s (1 - R_s)}, \quad (6.4)$$

with $(n_2)_r$ being the nonlinear refractive index of a reference, L_r and L_s the effective thicknesses, R_r and R_s the reflectivities, $(\Delta T_{PV})_r$ and $(\Delta T_{PV})_s$ the Peak-to-Valley values, and E_r and E_s the pulse energies applied to the reference material (r) and the samples (s). In the absence of linear absorption the effective thickness is equal to the actual geometrical thickness d of each sample. The thicknesses of the samples were chosen to be much smaller than the Rayleigh length of the beam in order to avoid distortions [226]. A 0.7 mm thick slab of fused silica with 1200 ppm OH and $(n_2)_r = (2.7 \pm 0.3) \times 10^{-7} \text{ cm}^2/\text{GW}$ (sect. 6.1) served as reference sample.

The n_2 value may as well be derived from the ΔT_{PV} value directly (without referencing). The accurate determination in this case is, however, tough, since it relies on the exact knowledge of the electric field of the pulse. Although, aberrations of the pulse (e.g. astigmatism) can be corrected by sophisticated measurement techniques [227–229], fluctuations in the pulse duration may cause large errors, particularly for

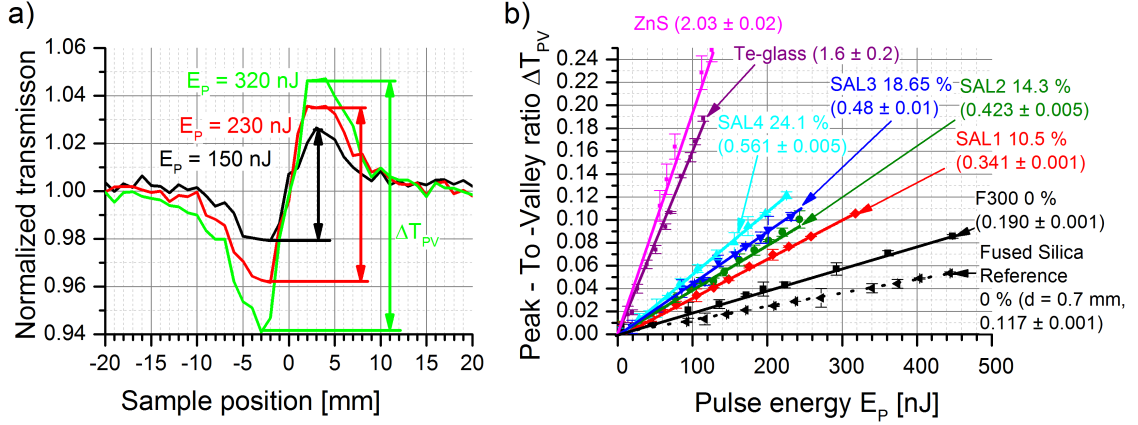


Fig. 6.4: a) Z-Scan traces of the SAL1 10 mol% of La_2O_3 sample at pulse energies E_p , arrows: Peak-To-Valley ratio ΔT_{PV} ; b) ΔT_{PV} values of investigated materials as a function of pulse energy, brackets: slope $\Delta T_{PV}/E$ in 10^{-3} nJ^{-1}

pulse durations below 100 fs. Thus the reference method provides a more accurate determination of the nonlinearity.

The measured nonlinear refractive indices The nonlinear refractive indices of the materials are summarized in tab. 6.4. The n_2 values detected for F300, the Te-glass and ZnS amount to $n_2 = (3.0 \pm 0.1) \times 10^{-7} \text{ cm}^2/\text{GW}$, $n_2 = (50 \pm 5) \times 10^{-7} \text{ cm}^2/\text{GW}$ and $n_2 = (130 \pm 20) \times 10^{-7} \text{ cm}^2/\text{GW}$, respectively. They agree well with the values from literature (sect. 6.1 and [148, 149, 152, 155, 230]). The n_2 value of N-SF56 was taken from the literature [138]. It is conspicuous that the value for F300 is significantly (10 %) larger than that of the fused silica reference. Compared to the reference, F300 possesses only a tiny content of OH (< 1 ppm), which was achieved by adding chlorine to the glass mixture during manufacturing. It is assumed that the increased n_2 value may be due to residual chlorine.

In contrast to the large index material and fused silica only a few studies deal with the nonlinear refractive index of the novel SAL-glass system [103, 183]. The systematic study of this work unravels a linear correlation between the nonlinear refractive index (related to the electric field) n_2^F and the La_2O_3 concentration (fig. 6.5). The correlation between the n_2 value (related to the intensity) and the La_2O_3 concentration can be linearly approximated as well, since the relative linear refractive index variation is small ($n_{\text{SAL1}}/n_{\text{SAL3}} \approx 0.9$, eq. (3.6) in sect. 3.1.2), with the increment amounting to $\Delta n_2/\Delta c(\text{La}_2\text{O}_3) = (0.264 \pm 0.007) \times 10^{-7} \text{ cm}^2/\text{GW mol}\%^{-1}$.

Based on the assumption of one major polarizable constituent in combination with the Lorentz-Lorenz oscillator approach, Boling et al. [231] formulated a well accepted [141, 232] semi-empirical relationship (BGO theory) linking the nonlinear refractive index n_2 to the dispersion (ν_d) and the linear refractive index $n_d = n_0(587.6 \text{ nm})$:

$$n_2^F (10^{-13} \text{ esu}) = \frac{68(n_d - 1)(n_d^2 + 2)^2}{\nu_d \left[1.52 + \frac{(n_d + 1)(n_d^2 + 2)^2}{6n_d} \nu_d \right]^{1/2}}. \quad (6.5)$$

As depicted in fig. 6.5 the measured values of the linear and nonlinear refractive indices agree well with the BGO theory according to eq. (6.5). Additionally, fig. 6.5

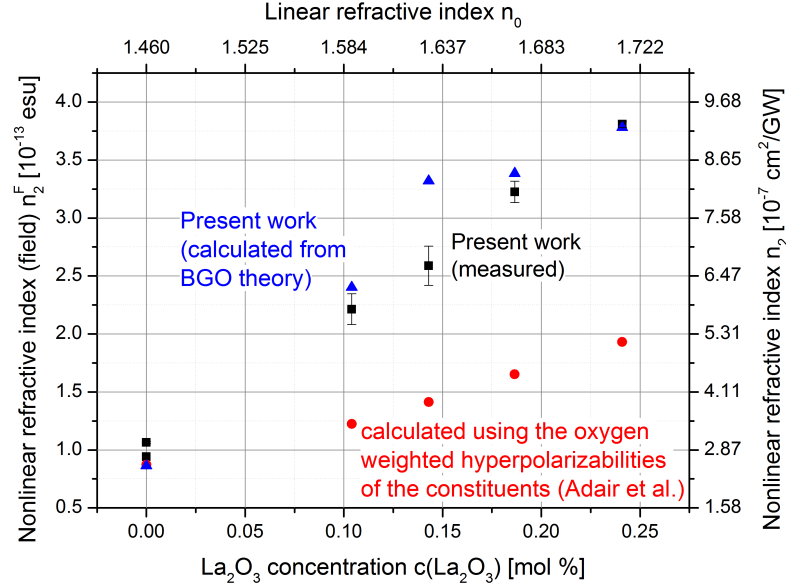


Fig. 6.5: Nonlinear refractive index (n_2^F : cgs units, n_2 : SI units) as a function of La_2O_3 concentration and refractive index ($n_0(800 \text{ nm})$): black squares: measured values, blue triangles: calculated from BGO theory (eq. (6.5)) using measured n_d and ν_d values, red circles: calculated according to eq. (3.8) using only the oxygen hyperpolarizabilities of SiO_2 , Al_2O_3 and La_2O_3 given by Adair et al. [91]

shows the expected nonlinear refractive index, calculated by following the theory given by Adair et al. [91], where only the anion O^{2-} is assumed to contribute to the nonlinear refractive index. This problem will be elucidated in more detail within the next section.

6.2.4 Discussion of the microscopic material properties

In order to provide a base for future optimization of the OKG material, a brief discussion dealing with the linear and nonlinear refractive indices will be given. On the microscopic level, the physical origin of both refractive indices lies in the deformation of the electron cloud of the glass atoms by the incident light wave, i.e. n_0 and n_2 are directly related to the polarizability α_m and the hyperpolarizability γ (sect. 3.1.3). These electronic glass properties are most important in the fs time regime [125], irrespective of counteracting slow processes contributing to n_2 such as the response of the ions or thermal and electrostrictive effects [86].

With the knowledge of the linear or the nonlinear refractive index, the material density and the material composition, values for α_m and γ can be estimated. Generally, the overall polarizability is consisting of contributions from the cation and the anion. The polarizabilities and hyperpolarizabilities of ZnS [91, 233] and various Te-glasses had been studied thoroughly within the past decades [128, 154, 155, 186, 187, 212, 234–236]. Hence a detailed discussion of the (hyper)polarizability is not necessary at this point.

It is, however, remarkable that the n_2 value of the Te-glass is much larger than the value expected from BGO theory ($n_2^F(\text{meas}) = (24 \pm 2) \times 10^{-13}$ esu, $n_2^F(\text{BGO}) = 14 \times 10^{-13}$ esu). This extraordinary large hyperpolarizability may have several reasons. On the one hand, it has been pointed out, that the empty outer d -orbital of

the TeO₂ molecule, that is contributing to the conduction band in combination with a rather small bond length in the range of 2Å is a reason of the large γ -value. On the other hand, the BGO theory relies on the assumption of just one constituent contributing to the nonlinear refractive index. This assumption, however, can be violated, since the Te-glass investigated in the present work additionally possesses a small amount of Er₂O₃, which shows a very large hyperpolarizability [91]. Furthermore, the small content of Er₂O₃ breaks up O-Te-O bonds [205]. Hence there may be an increased concentration of non-bridging oxygen (NBO), which itself contributes to the hyperpolarizability. A too large Er₂O₃ content, however, may also cause an opposite effect, since the O-Te-O bonding was shown to be majorly responsible for the hyperpolarizability [237].

Finally, even if the small Er₂O₃ content (0.04 mol%) would be neglected, the remaining ternary glass structure itself may unravel the reason for its large nonlinearity compared to e.g. binary Te-glass systems ([238]) or single crystalline TeO₂ [236]. On the one hand, the additional component may increase the structural disorder and consequently the concentration of NBO, for instance by breaking the O-Te-O bridge. This effect was shown to be particularly critical in terms of enhancing α_m and even more γ in case of alkali cations, such as K⁺ [212]. Although γ was proven to be more or less independent of the ZnO concentration ([152]), it may change the oxygen packing density still [198], which will effect both, α as well as γ .

Analyzing the origin the linear and nonlinear refractive indices of N-SF56 is much harder than for the other materials, since its composition is not well known. Furthermore it consists of multiple components, which may have comparably large (hyper)polarizabilities, e.g. Nb₂O₅ and TiO₂ [86, 239]. Therefore the basic assumption of only one polarizable constituent, given by Adair et al. and Boling et al. [91, 231] is not valid any further. The large nonlinear refractive index of N-SF56 thus arises from a complex interplay of its components [91].

Compared to the discussed large index glasses only a few studies deal with the (hyper)polarizability of the SAL system [90, 240]. Applying the Clausius-Mosotti equation (3.7) to the measured n_0 values reveals the average polarizability of the SAL-system (α_{meas} in tab. 6.3) representing the weighted average of the molecular polarizabilities of all ions in the glass system. It is considered to be mostly affected by the anions (O²⁻) [125, 241] due to their large volume whereas the polarizability of the cations appears to stay less important. The oxygen polarization follows the relation [192, 241]

$$\alpha_{O^{2-}}(n_0) = \left[\left(\frac{V_m}{2.252} \right) (n_0^2 - 1)/(n_0^2 + 2) - \sum \alpha_i \right] / N_{O^{2-}}, \quad (6.6)$$

with V_m being the molar volume, $\sum \alpha_i = 2x\alpha_{La^{3+}} + y\alpha_{Si^{4+}} + 2(1-x-y)\alpha_{Al^{3+}}$ the molar cation polarizability, and $N_{O^{2-}} = 3x + 2y + 3(1-x-y)$ the number of anions. The cation polarizabilities are taken from Duffy et al. [90]. The anion polarizabilities calculated in the present work are very close to those reported from similar systems by Duffy [90].

The average cation polarizability α_{cat} as shown in tab. 6.3 increases with the La₂O₃ content by more than a factor of two whereas the O²⁻ polarizability $\alpha_{O^{2-}}$ increases due to the O²⁻ volume change by less than 6.5 %. The anion polarizability is, however, generally higher at least by a factor of three. Nevertheless, the sum of both, $\alpha_{cation} + \alpha_{anion}$, is still smaller than the average α_{meas} value (Table 6.3).

Replacing SiO₂ in the SAL system by Al₂O₃ increases the average polarizability by reducing the density of covalent bonds and the generation of a high concentration of non-bridging oxygen (NBO) [180, 182]. As a measure of the NBO concentration an r -value is assigned to the SAL system according to Iftekhar et al. [180].

$$r = \frac{2 + x + (1 - x - y)}{1 - x + (1 - x - y)} = \frac{3 - y}{2 - 2x - y}, \quad (6.7)$$

with x and y being the molar concentrations of La₂O₃ and SiO₂, respectively. The r -values in tab. 6.3 show an increase of about 23 % indicating a significant NBO increase with the La₂O₃ enrichment, which is in agreement with the literature [181]. The exact NBO number is, however, hard to estimate without knowing the fraction of 3-coordinated anions, which is a further necessary parameter to identify the NBO number. Another indicator of a NBO enrichment is the measured increase in the Urbach energy E_U (tab. 6.4), representing the systems' order [195]. In a less ordered system, less oxygen can bind to the cations, leading to more NBO species.

In a simplified consideration of one single polarizable constituent only (La₂O₃ in this case), the hyperpolarizability can be related to the molecular polarizability by $\gamma = Q\alpha_m^2$ [125] with Q being an empirically determined constant. The average hyperpolarizability $\langle\gamma\rangle$ is revealed by the nonlinear refractive index n_2^F by applying the formula

$$\langle\gamma\rangle = \frac{2n_2^F n_0}{f^4 \pi N_m}, \quad (6.8)$$

where f is the Lorentz local field correction factor defined as $f = (n_0^2 + 2)/3$ and N_m is the number density of the glass calculated from the glass density and stoichiometry [91]. Thus the correlation constant Q between the α^2 and γ for the present SAL systems is calculated to $Q = (7.8 \pm 0.6) \times 10^{10} \text{ esu/cm}^6$ (Fig. 6.6a).

As discussed previously, the linear polarizability α is not only affected by the oxygen (due to its large volume and NBO concentration), but also by the increasing content of La³⁺ ions. Thus the La³⁺ content of the glasses should as well affect the hyperpolarizability γ . This appears self-evident, when comparing the measured n_2^F values with those calculated on the basis of the oxygen hyperpolarizabilities given by Adair et al. [91] (Fig. 6.5). Assuming an additive nature of the constituents' hyperpolarizabilities n_2^F [231] can be normalized by the function

$$n_{2 \text{ Norm}} = N_{La_{2/3}O} \gamma_{La_{2/3}O} = \frac{2n_2^F n_0}{f^4 \pi} - N_{Si_{1/2}O} \gamma_{Si_{1/2}O} - N_{Al_{2/3}O} \gamma_{Al_{2/3}O}, \quad (6.9)$$

revealing an upper limit for the La_{2/3}O hyperpolarizability. Here N and γ are the number densities and hyperpolarizabilities of the SAL components. $\gamma_{Si_{1/2}O}$ and $\gamma_{Al_{2/3}O}$ were taken from [91]. The molar fractions normalized to the oxygen were chosen for a direct comparison to the values of $\gamma_{La_{2/3}O}$ given by Adair et al. [91]. Due to the impact of NBO onto γ an exact calculation is not possible, yet. The upper limit can be calculated by fitting $n_{2 \text{ Norm}}$ and the number density of La_{2/3}O linearly. It amounts to $(2.2 \pm 0.2) \times 10^{-36} \text{ esu}$ (fig. 6.6b).

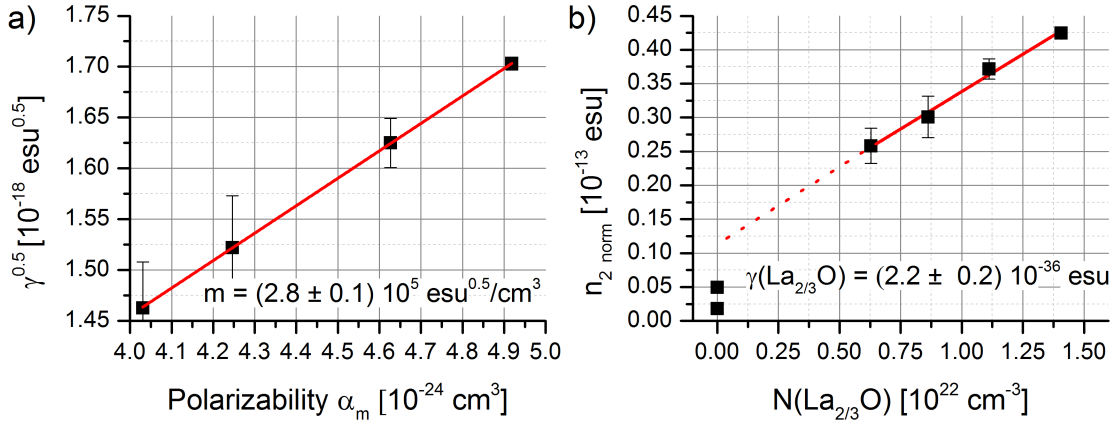


Fig. 6.6: a) Correlation $\gamma = Q\alpha^2$ between hyperpolarizability γ and polarizability α_m , $Q = m^2 = (7.8 \pm 0.6) \times 10^{10} \text{ esu}/\text{cm}^6$ (investigated SAL system), b) Normalized n_2 values (eq. (6.9)) as a function of $\text{La}_{2/3}\text{O}$ number density, upper limit of $\gamma_{\text{La}_2\text{O}_3}$: $(2.2 \pm 0.2) \times 10^{-36} \text{ esu}$.

Finally it should be pointed out, that the linear fits in Figs. 6.6a and 6.6b yield nonzero abscissa scales. This effect is attributed to the approximation of only one polarizable constituent of the glasses given by BGO theory. With decreasing La_2O_3 content, however, this approximation loses its validity: the nonlinear refractive index and hence the hyperpolarizability will increasingly be affected by structural changes such as a decreasing NBO concentration as well as the neglected contributions of the other glass components.

Tab. 6.3: Optical parameters n_2 [$10^{-16} \text{ cm}^2/\text{W}$], n_2^F [10^{-13} esu], $\alpha_{\text{O}^{2-}}$ [\AA^3], α_{Cat} [\AA^3], α_{meas} [\AA^3], $\langle \gamma_{\text{meas}} \rangle$ [10^{-36} esu], and the r value for the SAL glasses and F300

Material	n_2	n_2^F	$\alpha_{\text{O}^{2-}}$	α_{cat}	α_{meas}	$\langle \gamma_{\text{meas}} \rangle$	r
F300	3.0	1.06	1.403 [105]	—	2.971	1.24 ± 0.01	—
SAL1	5.8	2.2	1.621	0.309	4.030	2.1 ± 0.1	2.09
SAL2	6.7	2.6	1.6274	0.439	4.247	2.3 ± 0.2	2.24
SAL3	8.1	3.23	1.695	0.569	4.627	2.64 ± 0.08	2.40
SAL4	9.30	3.81	1.726	0.700	4.919	2.90 ± 0.02	2.58

6.3 Material properties and OKG

After analyzing the optical properties of the suggested OKG materials their impact on the gating process shall be elaborated in this section. Similar to the material analysis, these preliminary considerations are crucial for understanding the complex gating behavior discussed in the subsequent sections.

6.3.1 Absorption

Absorption can limit both, the gate pulse and the signal as they propagate through the material. Even in large band gap media, where linear absorption may be neglected, two-photon absorption may significantly attenuate the gate pulse, as it is of the same nonlinear order as the phase modification, responsible for OKG (subsect.

Tab. 6.4: Properties of investigated OKG samples: Molar concentration of La_2O_3 for the SAL-glasses, Sellmeier coefficients ($C_0, A_i, \tilde{A}_i, B_i$, eqs. (3.2) and (3.3)). Note for ZnS eq. (3.3) was used (A_1, A_i instead of \tilde{A}_i), linear (at 800 nm and 587.6 nm) and nonlinear (for the field in cgs units and the intensity in SI units at 800 nm) refractive indices n_0, n_2 and (n_2^F), the Abbe number ν_d , the group refractive index mismatch between 530 and 800 nm (Δn_G), the Urbach energy E_U , the band gap E_{Gap} estimated from the absorption, the thermal expansion coefficient α_{th} , the glass transition temperature T_G , the density ρ , the molar volume V_m , structural information, group velocity dispersion k'' , dispersion length L_D , sample thickness d and effective thickness for the temporal walk-off d_{eff} , ^a: [105], ^b: [106], ^c: [84]

Material	F300	SAL1	SAL2	SAL3	SAL4	SF56	Te-glass	ZnS
$c(\text{La}_2\text{O}_3)$ [mol %]	—	10.5	14.3	18.7	24.1	—	—	—
C_0	1 ^a	1	1	1	1	1 ^b	1	8.39193 ^c
A_1, \tilde{A}_1	0.6961663 ^a	1.50152	1.61099	1.75686	1.90004	1.73562085 ^b	2.89956	0.14383 ^c
B_1 [μm^2]	0.004679148 ^a	0.01189	0.01473	0.01412	0.01405	0.0129624 ^b	0.03811	0.05861241 ^c
A_2, \tilde{A}_2	0.4079426 ^a	—	—	—	—	0.317487012 ^b	0.02025	4430.99 ^c
B_2 [μm^2]	0.01351206 ^a	—	—	—	—	0.061288428 ^b	0.11102	1347.6241 ^c
A_3, \tilde{A}_3	0.8974794 ^a	—	—	—	—	1.95398203 ^b	—	—
B_3 [μm^2]	97.9340025 ^a	—	—	—	—	161.559441 ^b	—	—
n_0 (800 nm)	1.453	1.591	1.628	1.672	1.715	1.764	2.010	2.313
ν_d	68.43	46.08	39.88	42.69	45.44	26.17	28.60	15.55
n_d (587.6 nm)	1.458	1.599	1.638	1.683	1.727	1.785	2.034	2.368
Δn_G	0.018	0.036	0.049	0.048	0.051	0.098	0.121	0.307
n_2	3.0 ± 0.1^a	5.8 ± 0.4	6.7 ± 0.4	8.1 ± 0.2	9.3 ± 0.1	26 [138]	50 ± 5	130 ± 20
$[10^{-7} \text{ cm}^2/\text{GW}]$	—	—	—	—	—	—	—	[148]
n_2^F [10^{-13} esu]	1.04 \pm 0.04	2.2 ± 0.2	2.6 ± 0.2	3.2 ± 0.1	3.81 ± 0.05	11	24 ± 2	72 ± 11
E_U [eV]	—	0.76 ± 0.01	0.63 ± 0.01	0.53 ± 0.01	0.59 ± 0.01	0.090 ± 0.001	0.089 ± 0.001	0.066 ± 0.003
E_{Gap} [eV]	9[214]	> 6	5.71 ± 0.06	5.46 ± 0.05	5.33 ± 0.05	3.45 ± 0.02	3.34 ± 0.04	3.43 ± 0.04
α_{th} [$10^{-6}/\text{K}$]	0.51	4.3	5.5	5.9	7.0	10 ^b	—	6.5 ^c
T_g [$^\circ\text{C}$]	1120	875	869	861	868	592 ^b	≈ 300	—
ρ [g/cm ³]	2.20	3.21	3.55	3.91	4.28	3.28 ^b	5.6[187]	4.09 ^c
V_m [cm ³]	27.3	30.07	30.17	31.10	31.52	—	25.1	23, 83
Structure	amorphous	amorphous	amorphous	amorphous	amorphous	amorphous	amorphous	poly crystalline ^c
k'' [fs ² / μm]	0.036	0.079	0.104	0.106	0.110	0.185	0.240	0.558
L_D (800 nm) [mm]	9.0	4.1	3.1	3.1	2.9	1.8	1.4	0.58
d [mm]	1	1	1	1	1	0.6	0.7	0.3/1.17
d_{eff} [mm]	1.50	0.75	0.55	0.56	0.53	0.28	0.22	0.088

3.2.3). For high gate pulse intensities even higher order absorption processes may become important as well. Although nonlinear absorption of the signal shall be negligible, it can indirectly be affected by either pump pulse assisted single photon or free carrier absorption [242].

In order to evaluate a material's suitability for OKG in the presence of absorption, Stegeman et al. [135, 243, 244] have developed a well accepted measure (Figure of merit, *FOM*). For most efficient OKG, the phase imprinted onto the signal pulse by the gate pulse should amount to $\phi_{nl} = \pi$. In the absence of any counteracting effects, limiting the gating behavior, this criterion always can be achieved, if the material thickness is large enough (eq. (3.30)). However, if linear or nonlinear absorption of the kind

$$\frac{dI_G}{dz} = -\alpha_k I_G^k \quad (6.10)$$

occurs, where k is the order of the absorption (e.g. $k = 1$ for linear absorption), a finite absorption distance, amounting to $d_{abs} = 1/\alpha_k I_G^{k-1}$ can be defined. Inserting d_{abs} into (3.30) and setting it equal to π defines the *FOM*:

$$FOM = \frac{2n_2}{\lambda\alpha_k I_G^{k-2}}. \quad (6.11)$$

If the *FOM* is larger than 1, the material is considered to be a suitable candidate for OKG. Note, that in the presence of two-photon absorption, the *FOM* is independent of the gate pulse intensity I_G . This *FOM* is only taking the (linear and nonlinear) absorption of the gate pulse into account.

6.3.2 Refraction

Aside from the correlation between the linear and the nonlinear refractive indices or an increased Fresnel reflection at large n_0 -values, refraction itself should not affect the gating process. Its dispersion, however, can cause a walk-off between the gate pulse and the signal on the one hand or gate pulse broadening, hence an intensity reduction on the other hand.

Refractive index mismatch In general, the signal and the gate pulses are traveling through the OKG material at different velocities due to the refractive index mismatch (subsect. 3.1.2). This may be a group- (if the signal is a laser pulse) or a phase index (if the signal is fluorescence light for instance). The mismatch leads to a walk-off between both signals. The delay time t_D introduced in subsection 3.2.3 between the signal and the gate pulse becomes a function of the propagation distance z inside the material [245–247]. In the following t_D is the delay between signal and gate at the entrance surface of the OKG material ($z = 0$). It is particularly pointed out that the signal can be an arbitrary field and does not necessarily need to be a pulse.

In the reference frame of the signal, its phase ϕ_{nl} imprinted by the gate pulse under consideration of a refractive index mismatch (RIM) Δn is given by (eq. (3.30)):

$$\begin{aligned}\phi_{nl}(r, t - t_D, z) &= k_0 n_2 I_G(r) \int_{z=0}^{z=d} e^{-4 \ln 2 (t - t_D + \frac{\Delta n z}{c})^2 / \Delta \tau_G^2} dz \\ &= k_0 n_2 I_G(r) \frac{\sqrt{\pi} \Delta \tau_G c}{2 \sqrt{4 \ln 2} \Delta n} \left[\operatorname{erf} \left(\frac{\sqrt{4 \ln 2}}{\Delta \tau_G} \left(t - t_D + \frac{\Delta n}{c} z \right) \right) \right]_{z=0}^{z=d},\end{aligned}\quad (6.12)$$

where $I_G(r)$ is the lateral function of the gate pulse and $\Delta \tau_G$ is its pulse duration (FWHM). $\Delta n = n(\text{signal}) - n_g(\text{gate})$ is the refractive index mismatch, c is the vacuum speed of light, k_0 is the wave vector of the signal and d is the sample thickness. t_D is the initial delay between the gate pulse and the signal.

In the presence of a RIM the delay between the gate pulse (blue) and the signal changes during the propagation (fig. 6.7). This results in an asymmetrically extended time trace of the imprinted phase and consequently in a larger gating time. Additionally the amplitude of the gated signal is limited and can not be increased by a longer propagation distance (i.e. using a thicker OKG sample). The latter is only possible if $\Delta n_g = 0$, where the phase imprinted on the signal accumulates at $t = t_D$ as it propagates through the sample (red lines in fig. 6.7). The maximum amplitude of the gated signal on the other hand would amount to only 15 % compared to that observed in the absence of RIM. According to Ziólek et al. [245] the impact of the RIM onto the duration of the gate window is characterized by the parameter τ_{GVD} defined as:

$$\tau_{GVD} = \frac{d}{c} \Delta n_g. \quad (6.13)$$

If the signal is a short pulse (duration $\Delta \tau_S$), the temporal broadening due to the RIM causes a broadening of the delay time-dependent trace (DTT). The DTT is the (energy) transmission of the signal through the OKG as a function of the delay time t_D . In this context, the RIM causes e.g. the gate pulse to overtake the signal inside the sample (for $\Delta n_g > 0$) leading to a OKG transmission, although the pulses were not overlapping at the sample entrance (i.e. at $t = t_D$). Consequently the RIM leads to a limited interaction distance d_{eff} between the signal and the gate pulses inside the material. Assuming a second order cross-correlation width $\Delta \tau_{cc} = \sqrt{\Delta \tau_S^2 + 0.5 \Delta \tau_G^2}$ (eq. (3.31) in subsect. 3.2.3) an expression for d_{eff} can be derived from (6.13):

$$d_{eff} = \left| \frac{\tau_{cc} c}{\Delta n} \right|. \quad (6.14)$$

From a different point of view, d_{eff} represents the thickness of the OKG sample at which the optimum gating can be achieved. Smaller thicknesses cause a reduction in efficiency (eq. (3.30)). Larger thicknesses will not improve the gated efficiency anymore but only distort the gated signal due to the larger gating time.

To illustrate the influence of the RIM, the gating time using a pulse with a full-width-half-maximum duration of $\Delta \tau = 50$ fs will be $\Delta \tau_{OKG} = 145$ fs (FWHM) for

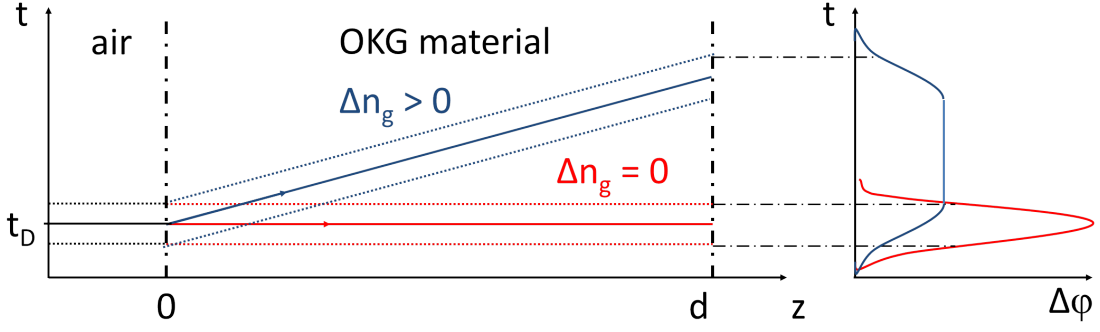


Fig. 6.7: Refractive index mismatch (RIM) affecting the delay between the gate pulse and the signal as function of z , left) phase $\Delta\phi$ imprinted on signal by gate pulse, right) time frame of the signal ($\Delta n_g > 0$ (blue) and the $\Delta n_g = 0$ (red))

$\Delta n_g = 0.05$ at a OKG thickness of $d = 1$ mm. It is in fact a scale for the broadening (but not necessarily the FWHM duration) of the gate window.

Pulse dispersion As the gate pulse travels through the OKG material, it will be broadened by group velocity dispersion. Its influence onto the gating time is negligible compared to the RIM. However, it causes a decrease in the intensity of the gate pulse, influencing the gating efficiency. Even though the thickness of the OKG material was chosen to be smaller than the dispersion lengths L_D (eq. (3.24), except the thick ZnS sample), the gate pulse duration can significantly extend during propagation, affecting I_G . Dispersion related pulse broadening should therefore be taken into account, when evaluating the material's gating efficiency.

In the presence of dispersive pulse broadening the nonlinear phase modification is given as:

$$\phi_{nl}(r, t - t_d, z) = k_0 I_G(r) \int_{z=0}^{z=d} \frac{1}{\sqrt{1 + \left(\frac{z}{L_D}\right)^2}} e^{-\frac{4 \ln 2}{\Delta\tau_G^2} \left(t - t_d + \frac{\Delta n_g z}{c}\right)^2} dz. \quad (6.15)$$

The integration (6.15) cannot be performed analytically. However, for sample thicknesses in the range of L_D , it is adequate to approximate the first term of the integrand by:

$$y_{Disp}(z) = \frac{1}{\sqrt{1 + \left(\frac{z}{L_D}\right)^2}} \approx (1 - y_0) e^{-\left(\frac{z}{\Delta\tau_{Fit}}\right)^2} + y_0 = y_{Fit}(z) \quad (6.16)$$

The dispersion related intensity decrease and its Gaussian fit is shown in fig. 6.8a as a function of the propagation distance z normalized to the dispersion length (3.24) L_D inside the material. The optimum fitting parameter set is a function of the material thickness. Figure 6.8b shows the optimum parameters y_0 and $\Delta\tau_{Fit}$ as

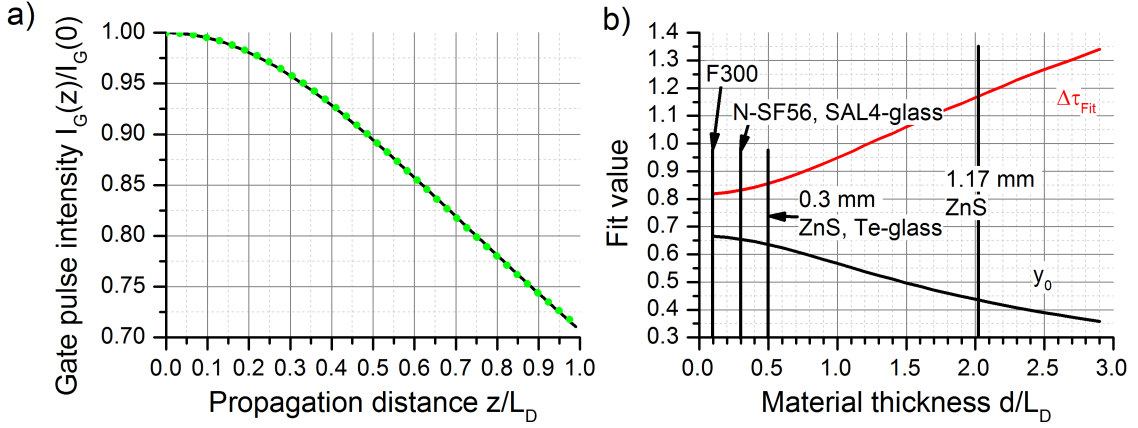


Fig. 6.8: a) black solid line: Gate pulse intensity $I_G(z)/I_G(0)$ as a function of the propagation distance z decreasing due to group velocity dispersion, green dashed line: Gaussian approximation b) parameters $\Delta\tau_{Fit}$ and y_0 of Gaussian fit (eq. (6.16)) as function of the sample thickness d/L_D normalized to L_D , black vertical lines: d/L_D value of investigated samples

function of the sample thickness d (normalized to its dispersion length L_D). The deviation between the original data and the fit was:

$$\delta = \frac{\int_0^d \|y_{Disp}(z) - y_{Fit}(z)\| dz}{\int_0^d (z) dz} < 0.01,$$

for thicknesses $d < 2L_D$.

Employing the approximation (6.16) adds a correction term to the phase shift ϕ_{nl} (6.12) that arises from the pulse broadening:

$$\phi_{nl}(r, t - t_d, z) = k_0 I_G(r) \int_{z=0}^{z=d} \left\{ y_0 e^{-\frac{4 \ln 2}{\Delta\tau_G^2} \left(t - t_d + \frac{\Delta n z}{c}\right)^2} + (1 - y_0) e^{-\frac{4 \ln 2}{\Delta\tau_G^2} \left(t - t_d + \frac{\Delta n z}{c}\right)^2 - \left(\frac{z}{\Delta\tau_{Fit} L_D}\right)^2} \right\} dz. \quad (6.17)$$

6.4 Broad-band OKG performance

One of the major requirements on the optical gate is a satisfactory gating performance over a broad spectral range in the visible region. In this context the suggested OKG materials were tested by gating a spectrally broad white light continuum (sect. 4.6.2 and sect. 5.1).

The spectrally and temporally resolved energy transmission (STRET) of the OKG is displayed in fig. 6.9 for the applied materials (a-e) as well as for two selected thicknesses of ZnS (e,f). For each material and every delay time the corresponding spectrum was divided by the temporally integrated spectrum. Subsequently, the amplitude of the whole STRET signal was normalized.

In case of fused silica the spectral components of the STRET were Gaussian fitted. The corresponding center and the full width half maximum ($\Delta\tau$, dashed lines) as function of the wavelength are depicted as cyan lines in fig. 6.9. The $\Delta\tau$ value stays between 50 fs and 70 fs down to 550 nm and increases up to 120 fs for $\lambda < 550$ nm

(inset in fig. 6.9a). The center of the Gaussian on the other hand shifts from $t_D = 0$ fs at $\lambda = 750$ nm to $t_D = 500$ fs at $\lambda = 500$ nm.

Comparing the STRET signals of the other materials to that of fused silica a temporal broadening of the signal towards larger delay times is observed, while the onset stays constant. For every material the broadening monotonously increases at shorter wavelengths. Additionally it is stronger for materials of larger refractive indices (fig. 6.9a-d) and larger sample thicknesses (fig. 6.9e,f). As a reference, the center and the full width half maximum width of the fused silica values are shown by the cyan lines in fig. 6.9b-f. For 1.17 mm thick ZnS, for instance, the gating time grows from $\Delta\tau = 200$ fs at $\lambda = 700$ nm to $\Delta\tau = 1400$ fs for $\lambda = 500$ nm. (inset in fig. 6.9f).

Simultaneously, the amplitude of every spectral STRET component decreases at shorter signal wavelengths. The decline seems to correlate with the broadening of the signal. Whereas the amplitude of the gated signal using fused silica stays more or less constant over the whole spectral range, it falls by approximately 80 % between $\lambda = 700$ nm and $\lambda = 500$ nm in case of 1.17 mm ZnS.

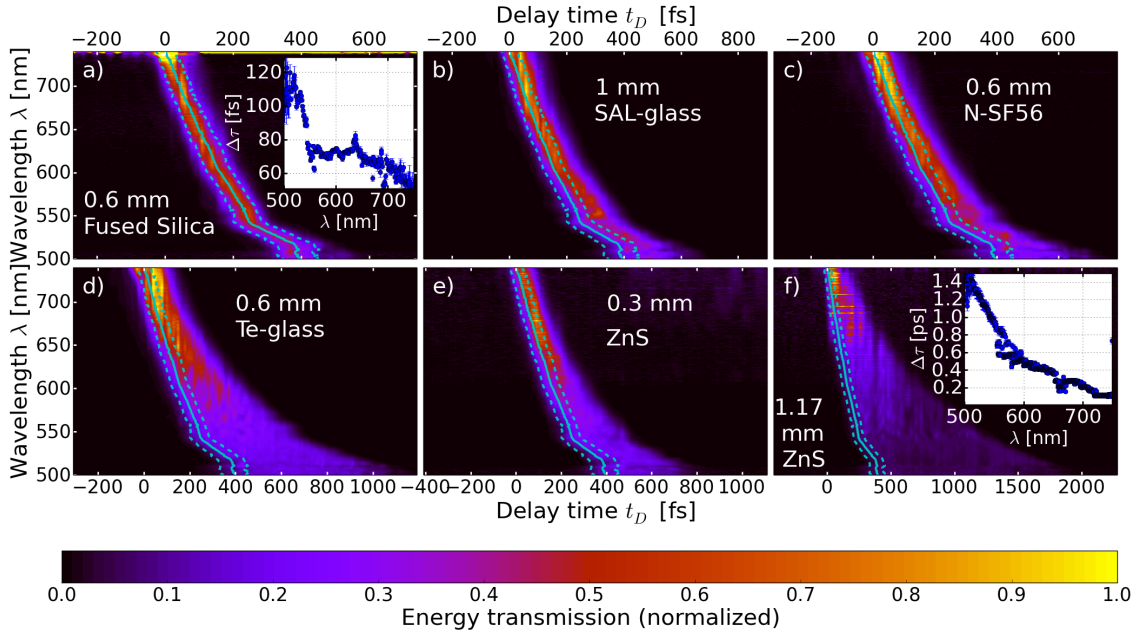


Fig. 6.9: Spectrally and temporally resolved energy transmission (STRET) of the gated WLC pulse, a-e): investigated material e,f) thin and thick ZnS, Cyan lines: center (solid) and FWHM (dashed) of Gaussian fitted fused silica (depicted in all subfigures as guide to the eye).

The temporal walk-off due to the refractive index mismatch (RIM, cf. sect. 6.3.2) between the gating pulse and the WLC signal (sect. 6.3) is suspected to be responsible for the different spectro-temporal behavior of the materials. For all materials the n_g value of the gate pulse is smaller than that for the signal (i.e. normal dispersion, tab. 6.4). This causes broadening towards positive delay times (signal precedes the gate pulse), where the infrared gate pulse can overtake the signal (visible spectral range). Additionally, the monotonous increase of the refractive index towards shorter wavelengths explains the likewise temporal signal broadening. Finally, since the material dispersion parallels the refractive index [248] the broadening is more pronounced for the high refractive index materials. The larger RIM at shorter wavelengths, particularly in high refractive index materials, results in a reduced in-

interaction distance of the gate and the signal inside the material (d_{eff} in eq. (6.14)) leading to smaller amplitudes of short wavelength signals compared to the long wavelength spectral components.

A slow material response as reason for the broadening is excluded, since it would result in broadening towards negative delay times (where the gate pulse precedes the WLC) and should not be a function of the sample thickness.

Due to the very small refractive index mismatch ($\Delta n_g = 0.018$ for $\lambda_G = 800$ nm and $\lambda_S = 530$ nm) of fused silica, the influence of the RIM onto the STRET is negligible compared to the pulse duration ($\tau_{GVD} = 36$ fs $<$ $\Delta\tau_G = 70$ fs). The temporal shift of the gated signal from $t_D = 0$ fs at $\lambda = 750$ nm towards $t_D = 400$ fs at $\lambda = 500$ nm (fig. 6.9a) is attributed to the initial chirp of the WLC.

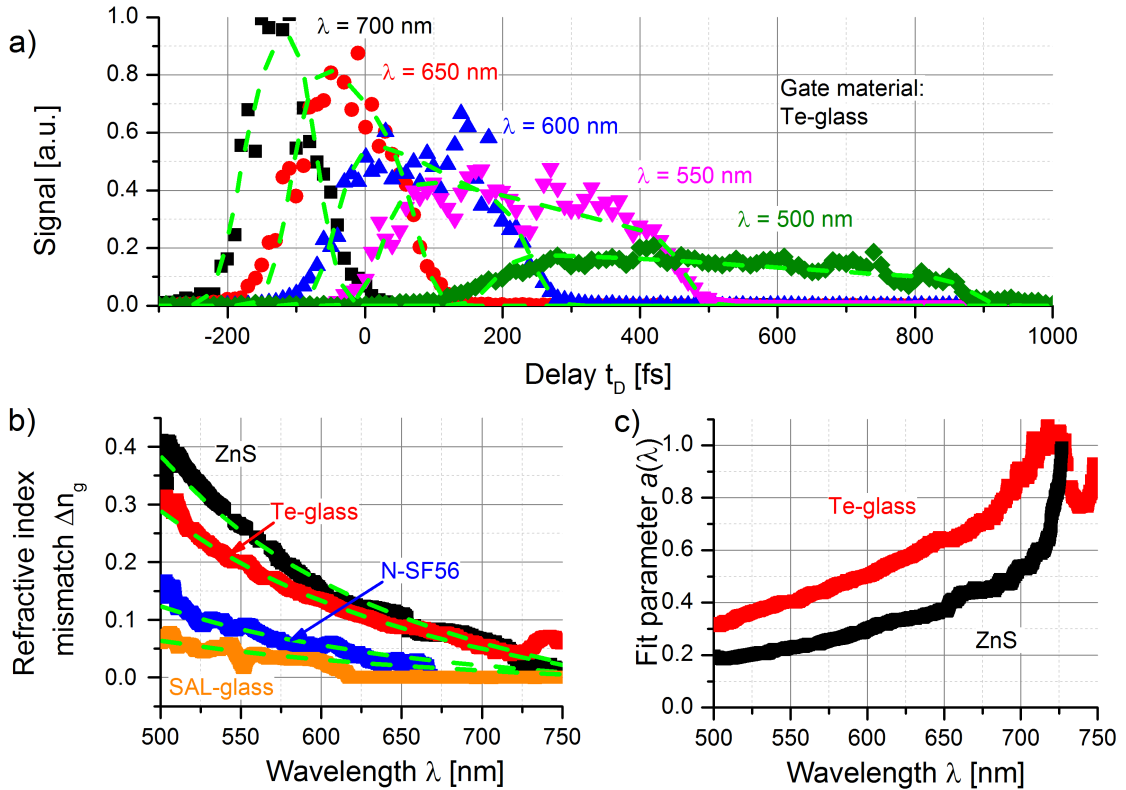


Fig. 6.10: a) Symbols: gated WLC at different wavelengths using Te-glass as OKG medium, dashed lines: fitted by (6.18), b) symbols: fitted values Δn_g , green dashed lines: values for Δn_g derived from Sellmeier equations, c) the fit parameter $a(\lambda)$ from (6.18) (scale for maximum transmission normalized to its maximum in long wavelength region)

The RIM being the reason for the temporal signal broadening is quantitatively supported by fitting the expected gate function to the measured signal. For the selected wavelengths the fitted signal using Te-glass as OKG material is depicted in fig. 6.10a as an example. According to the weak gate pulse intensity approximation (subsect. 3.2.3) the fit function was selected to be the convolution:

$$y(t_D) = aI_S(t_D - t_0) \otimes \phi^2(t_D), \quad (6.18)$$

where $\phi(t)$ is the expression for the phase taking into account the temporal walk-off and a decline of the gate pulse intensity due to dispersion broadening (eq. (6.17)).

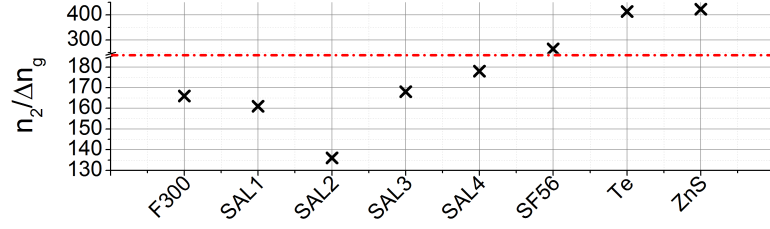


Fig. 6.11: Ratios $n_2/\Delta n_g$ for the investigated materials ($\lambda = 530$ nm)

The necessary dispersion parameters y_0 and $\Delta\tau_{Fit}$ in eq. (6.17) were taken from fig. 6.8b at the related sample thickness normalized to its dispersion length (tab. 6.4). The signal pulse intensity was assumed to be Gaussian shaped. The FWHM duration of the Gaussian was $\Delta\tau_G = \Delta\tau_S = 70$ fs for both the signal pulse $I_S(t_D)$ and the phase $\phi_{nl}(t_D)$.

The parameter a as a scale for the maximum transmission, the refractive index mismatch Δn_g and the temporal position of the white light signal were used as fitting parameters. The latter was necessary, since the temporal position of the WLC at different wavelengths shifts with respect to the delay time t_D due to the WLC chirp (fig. 6.9a).

The fitted RIM Δn_g values are depicted in fig. 6.10b for the applied materials. The green dashed lines represent the Δn_g values computed from the Sellmeier equations (sect. 3.1.2). Evidently, the Δn_g values resulting from the Sellmeier equations and the fits agree very well, in particular for short wavelengths, proving that the RIM is responsible for the temporal broadening. For longer wavelengths and materials exhibiting small refractive indices (e.g. SAL glass at $\lambda > 625$ nm), the Δn_g from the fit differs from that calculated by the Sellmeier equation. This is because at this point the characteristic time related to the RIM τ_{GVD} (eq. (6.13)) is too small compared to the pulse durations $\Delta\tau_G$ and $\Delta\tau_S$. For this spectral regions a Gaussian fit should rather be used to model the OKG transmission and the influence of Δn_g is negligible.

Finally, the fit parameter a is depicted in fig. 6.10c (exemplary for Te-glass and ZnS). It is an indicator for the spectrally dependent transmission of the OKG. Evidently the OKG efficiency η (defined as maximum transmission, cf. next section) is tremendously decreasing towards shorter wavelengths for high refractive index materials. This is a result of a reduced effective interaction length d_{eff} between signal and gate pulse in the OKG material at large Δn_g values. Particularly, when gating spectrally very broad signals (such as fluorescence) the spectrally dependent OKG transmission may cause spectral distortions in the detected signal amplitude and so has to be taken into account.

Furthermore the question is, if the larger nonlinear refractive index of these materials is able to compensate the reduction of the interaction distance inside the sample. Inserting d_{eff} into the equation for the imprinted phase (3.30) leads to:

$$\phi_{nl} \propto \frac{n_2}{\Delta n_g}. \quad (6.19)$$

These ratios are shown in fig. 6.11 for a signal wavelength of $\lambda_S = 530$ nm. This comparison proves that Te-glass and ZnS still exhibit superior gating capabilities

even though they suffer from the strongest refractive index mismatch. Although possessing a much smaller nonlinear refractive index, the gating capability of Te-glass is comparable to that of ZnS. It is particularly interesting, that SAL glass with a small content of La_2O_3 shows worse gating capabilities than fused silica, whereas SAL glass with large La_2O_3 content is better suited for OKG than fused silica.

6.5 Efficiency analysis using two-color OKG

Although the large n_2 values of the high refractive index materials compensate their reduction of d_{eff} the only possibility to increase the gating efficiency is to increase the gate pulse intensity I_G due to the basic limitation of d_{eff} . For gating the WLC pulse (cf. previous section) I_G was kept low, to ensure the validity of the weak gate pulse approximation in the data analysis. It is *a priori* not clear, if the high refractive index materials remain superior in their gating performance for increasing gate pulse intensities (in a range that is easily accessible by modern high repetition rate fs laser systems). The systematic study described in the following section aims for comparing the maximum achievable gating efficiency η of the different materials in a gate pulse intensity range of $0 \text{ GW/cm}^2 < I_G < 700 \text{ GW/cm}^2$. Therefore a weak signal pulse ($\lambda_S = 530 \text{ nm}$) was gated using a strong gate pulse ($\lambda_G = 800 \text{ nm}$) of variable peak intensity (sect. 5.1). Plane waves were assumed for both pulses while propagating through the samples. This is adequate, since the Rayleigh lengths of the signal and the gate beams are much larger than the sample thicknesses (tabs. 5.1 and 6.4).

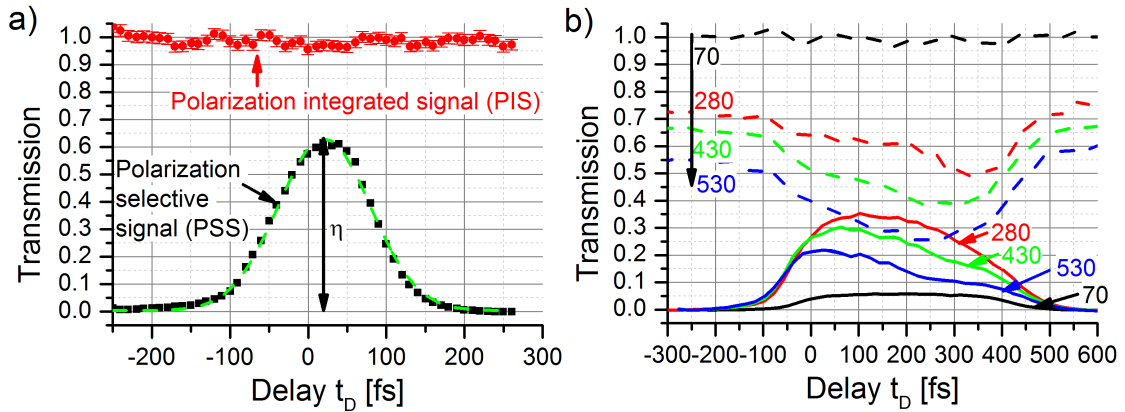


Fig. 6.12: a) Signals of the SAL4-glass (normalized to PIS, $I_G = 0.50 \text{ TW/cm}^2$): black: polarization selective time trace (PSS), red: polarization integrated time trace (PIS), maximum of PSS emission = gating efficiency η , b) OKG measurements using Te-glass at different gating intensities I_G (values in GW/cm^2): solid lines: normalized PSS trace, dashed lines: normalized PIS trace

6.5.1 Qualitative comparison of the materials

For each material at every gate pulse intensity a polarization integrated signal (PIS) and a polarization selective signal (PSS) was recorded as function of the delay time t_D between gate pulse and signal pulse (sect. 4.6.1). Both signals were normalized to the averaged PIS value at very low gate pulse peak intensity I_G and large delay

times t_D (where the signal preceded the gate pulse). The transmission maximum of the normalized PSS was defined as gating efficiency η . The different time traces and the definition of η are exemplified for SAL-glass (SAL4) at $I_G = 500 \text{ GW/cm}^2$ in fig. 6.12a. Figures 6.13a and b show the measured efficiency values η as function of I_G for all investigated materials (in case of ZnS: thick sample).

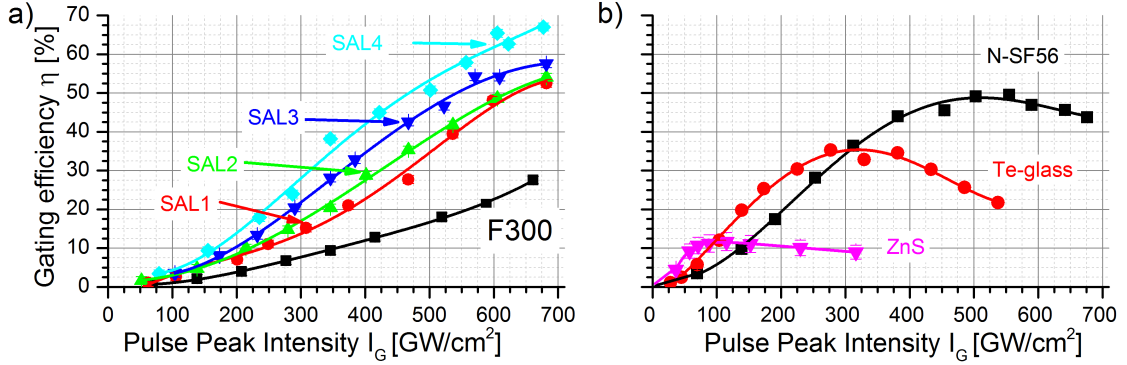


Fig. 6.13: OKG efficiency η as a function of gate pulse intensity I_G : a) the SAL-glasses and fused silica, b) materials of large nonlinear refractive index (ZnS: thick sample)

The different material classes (small n_2 materials and large n_2 materials) show qualitatively as well as quantitatively different dependences of η on I_G . All glasses in fig. 6.13a exhibit a monotonous increase in their efficiencies with increasing I_G up to a maximum η_{\max} that lies between 50 % and 70 % for the SAL-glasses at the highest applied gate pulse intensity of 650 GW/cm², while η_{\max} of F300 stays below 30 %.

In fig. 6.13b η of the high index materials grows much faster with increasing I_G for low gate intensities than for high ones. However, after reaching a maximum efficiency η_{\max} at a characteristic $I_{G,\max}$ value, η decreases again. Among the high index materials, N-SF56 shows the largest maximum efficiency of $\eta_{\max} \approx 50 \%$, as opposed to the maximum efficiency of ZnS only amounting to $\eta_{\max} \approx 12 \%$. The maximum achievable efficiencies η_{\max} seem to decrease with increasing nonlinear refractive index n_2 . Despite their large n_2 values, the high refractive index materials show an inferior gate efficiency compared to the SAL-glasses for large gate pulse intensities $I_G > 450 \text{ GW/cm}^2$.

In order to achieve more insight into the complex OKG behavior of the high n_2 materials, delay time traces of the PIS and the PSS at different I_G values are depicted in fig. 6.12b for the Te-glass as a representative for its class. The PIS shows permanent absorption (PA) which increases with increasing I_G values and is readily detectable in the PIS signals recorded at large delay times (e.g. $t_D > 500 \text{ fs}$ for Te-glass). In addition a transient absorption (TA) around $t_D = 0 \text{ fs}$ is observed. It parallels the PSS and becomes asymmetric for large I_G values. Both kinds of absorption are solely observed in the high refractive index materials (PA in N-SF56 and Te-glass, TA in all high index materials). They limit the amplitude of the PSS and consequently the maximum gating efficiency of these materials.

The permanent absorption is attributed to photo-darkening of the material. Due to an increase in intensity, even small multiphoton absorption of the gate pulse may cause an accumulation of defect centers within the glass, leading to single photon

absorption of the signal pulse. [39, 249]. The origin of the photo-darkening in the glasses is still unknown and requires more research.

The transient absorption, on the other hand, is assigned to combined multiphoton absorption (CMPA) of the signal and the gate pulses (sect. 3.1.4). If both pulses overlap, the strong gate field supports single photon absorption of the signal field. Absorption due to free carriers seeded by the gate pulse (FCA), as alternate origin for the transient absorption is considered to play a minor role. FCA typically shows lifetimes of several hundreds of femtoseconds to several hundreds of picoseconds [242]. Hence a significant absorption at negative delay times $t_D < 0$ fs (where the gate pulse precedes the signal pulse) would be observed in the presence of FCA. The transient signal at these delay times is, however, zero for $t_D < 100$ fs.

Besides the RIM caused broadening, the PSS shows, however, an asymmetry that is more pronounced at larger I_G values (fig. 6.12b). This asymmetry leads to a shift in the maximum of the gating amplitude towards $t_D = 0$ fs. An increasing CMPA at increasing positive delay times as a consequence of the interplay between self-focusing and the temporal walk-off is suspected to be the origin of the asymmetry [250, 251]. More precisely, self-focusing of the gate beam leads to an increase of I_G deeper in the sample due to a decrease in the spot radius w_G . The self-focusing distances d_{SF} as a function of the incident I_G value are depicted in fig. 6.14a (computed according to eq. (3.26) using the material constants given in tab. 6.4). Thus self-focusing will particularly be critical for the high refractive index materials (ZnS, Te-glass, and N-SF56), where d_{SF} is very close to (Te-glass, N-SF56) or even below the material thickness (thick ZnS, above 100 GW/cm²). The increase of I_G at the rear side of the sample leads to an increase of CMPA. The temporal walk-off, on the other hand, leads to an interaction of the signal pulse and the gate pulse deep inside the sample for large delay times (sect. 6.3.2). Consequently, the transient absorption at large delay times t_D is larger than that at $t_D \approx 0$.

6.5.2 Quantitative analysis of the transient absorption

The permanent and transient transmission values (referring to PA and TA) for the different high refractive index materials are compared in fig. 6.14b as a function of I_G . For thick ZnS, Te-glass and N-SF56 the transient transmission decreases about 60 %, 75 % and 40 % within 100 GW/cm², 530 GW/cm² and 670 GW/cm², respectively. The permanent transmission in N-SF56 and Te-glass decreases about 15 % and 40 % respectively. In contrast, no PA was observed in ZnS.

The transient absorption (at $t_D = 0$ fs) was fitted numerically by calculating the sample transmission in the presence of CMPA and absorption due to photo-darkening (eqs. (3.12) and (3.11)) with the nonlinear absorption coefficient α_k being the fit parameter. For all materials the fit was performed for $k = 2$ (two-photon CMPA: absorption of one gate photon and one signal photon, solid lines in fig. 6.14b) and $k = 3$ (three-photon CMPA: absorption of two gate photons and one signal photon, dashed lines in fig. 6.14b). For N-SF56 and Te-glass the influence of the intensity dependent permanent absorption (photo-darkening) was empirically approximated by a parabolic function prior to fitting (dash-dotted lines in fig. 6.14b). Details regarding the fitting procedure are explained in appendix F.

Although neither transient nor permanent absorption was observed in SAL-glass and fused silica, an upper limit for α_3 (pure three-photon CMPA, no photo-darkening)

was estimated by assuming a transmission decline of 5 %, corresponding to the noise of the PSS (fig. 6.12a) at the maximum gate pulse intensity ($I_G = 750 \text{ GW/cm}^2$). The absorption coefficients resulting from the fits are summarized in table 6.5.

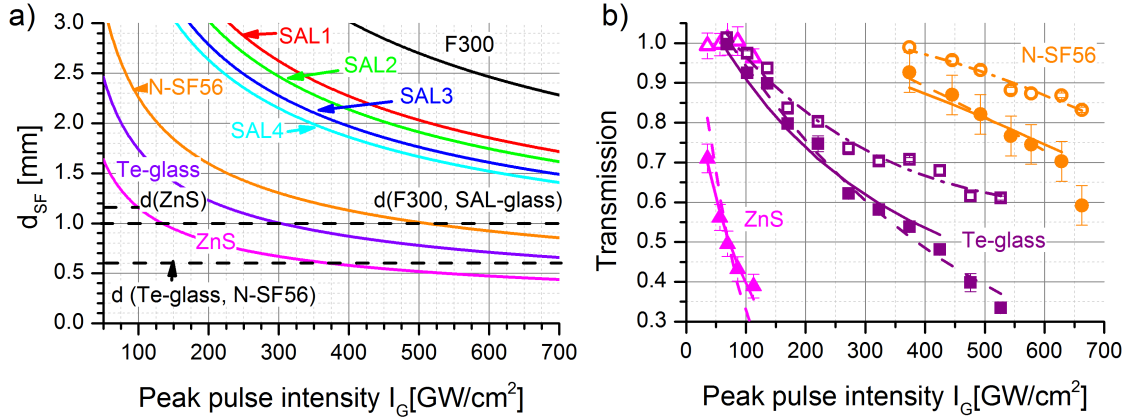


Fig. 6.14: a) Self focusing distances $d_{SF}(I_G)$ of investigated Kerr materials according to (3.26) as a function of the gate pulse intensity, horizontal dashed lines: sample thicknesses; b) symbols: transient (filled) and permanent (empty) transmission of ZnS (pink), Te-glass (purple), and N-SF56 (orange), lines: fitted curves (cf. text) for two-photon CMPA (solid), three-photon CMPA (dashed) and photo-darkening (empirical, dash-dotted)

Evidently, two-photon CMPA seems to be the mechanism, causing the absorption in ZnS, since the fitted data agree much better than in the case of three-photon CMPA. This was expected, because the band gap energy of ZnS ($E_{Gap} \approx 3.4 \text{ eV}$, tab. 6.4) is smaller than the sum of the photon energies of the signal and the probe beams ($E_{ph,S} + E_{ph,G} = 3.89 \text{ eV}$). For Te-glass and N-SF56 both absorption mechanisms seem possible within the error margins. However, three-photon CMPA appears to fit the data better than two-photon CMPA. Particularly for Te-glass, the fitted two-photon CMPA seems only eligible for gate pulse intensities $I_G < 400 \text{ GW/cm}^2$. Although the estimated energy gaps E_{Gap} of both materials are comparable to that of ZnS (tab. 6.4), the slope of the absorption edge of Te-glass and N-SF56 is conspicuously smaller than that of ZnS (fig. 6.3a). A larger concentration of Urbach states (sect. 6.2.2) in the amorphous glasses compared to that of crystalline ZnS may be an explanation for that difference. As discussed in sect. 6.2.2 the E_{Gap} value is a rough estimate only, since the maximum measured absorption coefficient amounted to $\alpha = 60 \text{ cm}^{-1}$. Hence the E_{Gap} value of the glasses could be larger, even exceeding the sum of the photon energies of the gate and the signal beams (3.89 eV). Therefore the multiphoton absorption might consist of two parts: A two-photon CMPA into the Urbach states and a three-photon CMPA into the conduction band of the material. The reliable identification of the CMPA origin requires more experimental data.

The E_{Gap} values of the SAL-glasses and fused silica exceed the necessary energy for three-photon CMPA ($E_{ph,S} + 2 \times E_{ph,G} = 5.44 \text{ eV}$, fig. 6.3a and tab. 6.4). Additionally the Urbach state absorption below 5.44 eV is very low ($\alpha < 30 \text{ cm}^{-1}$), preventing efficient two- or three-photon CMPA. Consequently, absorption is not limiting the OKG efficiency in the given intensity range. This is consistent with a maximum efficiency $\eta_{max} = 70 \%$, which is the maximum possible value at the given ratio of the beam radii amounting to $w_S/w_G = 0.5$ (sects. 3.2.3 and 5.1).

Tab. 6.5: Estimated CMPA coefficients for two- (α_2) and three- (α_3) photon absorption

Material	α_2 [10^{-3} cm/GW]	α_3 [10^{-5} cm ³ /GW ²]
ZnS	160 ± 20	(400)
Te-glass	20 ± 2	9.5 ± 0.9
N-SF56	7 ± 1	2.1 ± 0.2
SAL-glass	–	< 0.1

6.6 The optimum gating material

Comparing the switching performance of the investigated materials, SAL glass with a large content of La_2O_3 is the most suitable candidate for highly efficient OKG at gate pulse intensities $500 \text{ GW/cm}^2 < I_G < 1000 \text{ GW/cm}^2$. In this intensity range SAL-glasses show efficiencies as large as $\eta_{\max} = 70 \%$ limited by the spatial overlay of the pulses, only. A large La_2O_3 content causes a large nonlinear refractive index n_2 enabling more efficient gating compared to other low index materials, such as fused silica.

On the other hand, its glass matrix mostly consisting of light molecules (SiO_2 , Al_2O_3) causes a relatively large band gap $E_{\text{Gap}} > 5.5 \text{ eV}$ compared to high refractive index materials such as Te-glasses, N-SF56 or ZnS. This prevents nonlinear absorption as a counteracting process for OKG, particularly in the region of short wavelengths of the visible spectrum ($\lambda_S < 550 \text{ nm}$). This spectral range is, however, of great importance for investigating fluorescence signals arising from molecules of biological or medical interest, such as NADH. For small gate pulse intensities $I_G < 500 \text{ GW/cm}^2$, however, large refractive index materials, (N-SF56, Te-glass or ZnS) should be preferred for OKG. In all cases a maximum sample thickness depending on the (group) refractive indices of the gate pulse and the signal should not be exceeded in order to avoid signal broadening by temporal walk-off.

In order to quantify the evaluation a "figure of merit" is defined, following the discussion of Stegeman et al. [135, 243, 244] (eq. (6.11)). A problem of the commonly used *FOM* is that only absorption effects on the gate pulse are taken into account. Gate pulse induced single photon absorption of the signal beam in contrast to gate pulse attenuation was, however, found to be the major effect diminishing the OKG efficiency. The temporal walk-off between the gate pulse and the signal is as well limiting η .

Hence, a more adequate *FOM* resulting from the OKG transmission (eq. (3.28)) is desired. It can be given by:

$$FOM_{\text{new}} = (1 - \cos(k_0 n_2 I_G d_{\text{eff}})) \times e^{-\alpha(I_G) d_{\text{eff}}}, \quad (6.20)$$

where d_{eff} is the effective interaction length inside the OKG material (sect. 6.3.2). $\alpha(I_G)$ is an absorption coefficient that describes the linear and nonlinear attenuation of the signal (eq. (3.10)). For the nonlinear losses only gate pulse assisted multiphoton absorption (CMPA) is considered, since the signal intensity is assumed to be weak.

The first term on the right hand side in eq. (6.20) describes the transmission through the Kerr gate (eq. (3.28)), the second describes the signal attenuation by the induced absorption (subsect. 3.1.4). It is pointed out that the new FOM is not taking into account gate pulse attenuation.

The new FOM_{new} will not only be a function of the material, but also of selected experimental parameters, particularly the pulse duration and the wavelength difference between the gate pulse and the signal (implicitly in d_{eff} , eq. (6.14)).

For the investigated high refractive index materials and the SAL4-glass the new figures of merit are depicted in fig. 6.15. In order to estimate the absorption of the materials, only CMPA using the coefficients given in 6.5 was taken into account. Photo-darkening was neglected.

In qualitative agreement with the experimental results (fig. 6.13) the new FOM_{new} predicts the superior gating behavior of the large refractive index material at low intensities and of SAL4 at high I_G values. Furthermore, the novel FOM_{new} indicates a larger achievable OKG transmission (efficiency η) of the SAL-glass compared to that of the high index materials. The comparably small FOM_{new} of ZnS is due to its strong nonlinear absorption (two-photon CMPA). The decrease of the FOM_{new} for Te-glass, N-SF56, and SAL4-glass at large intensities is, however, related to the sinusoidal behavior of the OKG transmission (eq. (3.29)) and not so much to the counteracting CMPA. The much smaller ratio of the maximum FOM_{new} of the SAL4- and Te-glass, and the SAL4- and N-SF56-glasses, compared to the maximum efficiency ratios $\eta_{max}(SAL4) : \eta_{max}(Te-glass)$ and $\eta_{max}(SAL4) : \eta_{max}(N-SF56)$ (fig. 6.13) are a result of additional photo-darkening in the high index material. This absorption was not taken into account in the FOM_{new} .

Additionally, the spot radius ratio w_S/w_G of the signal and the gate pulses are not taken into account in the definition of FOM_{new} . Hence the maximum predicted gate efficiency amounts to $\eta_{max} \approx 100\%$ instead of $\eta_{max} \approx 70\%$ (exemplary for SAL-glass).

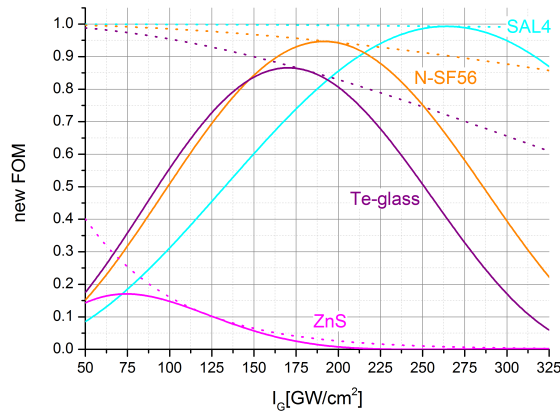


Fig. 6.15: FOM_{new} as a function of the gate pulse peak intensity I_G taking the temporal walk-off into account, dotted lines: transmission limit due to CMPA (the absorption length is the interaction length d_{eff} , eq. (6.20)).

The finite ratio between the spot radii and the durations of the gate and the signal pulses might be the reason for the difference in the predicted and detected gate pulse intensity for most efficient gating (figs. 6.13 and 6.15). The I_G value in eq. (6.20) refers to the peak gate pulse intensity (on axis and at the temporal center of the

gate pulse). At an finitely extended signal pulse, however, peripheral components will be gated at different efficiencies. The optimum gating of those components will occur at higher I_G values. The measured gate pulse intensity for maximum gating efficiency of the whole signal pulse is an average of the I_G values referring to central and peripheral gating.

Eventually, the result of the presented modified FOM_{new} agrees with the experimental findings and the quantitative analysis above, evaluating the SAL4 glass to be the most suitable candidate for OKG experiments at moderate gate pulse intensities I_G . Therefore this SAL glass was used as OKG medium for all experiments presented in the second part of this work. The sample thickness of the SAL is selected to be $d = 1$ mm. This is larger than d_{eff} of the SAL4 glass (tab. 6.4). Hence temporal broadening of the gate signal is observed (fig. 6.9b), which however is not critical for the following experiments.

Chapter 7

Detection of axially distributed emitters

Having discussed the optimization of the optical gating setup comprehensively, this chapter focuses on its application in order to detect the axial distribution of a fluorophore. One major problem of using the time-of-flight (ToF) method for resolving the axial distribution of a given emitter is the ambiguity of the measured delay dependent time trace (DTT). On the one hand, the axial distribution of the fluorophores is encoded in the time trace. On the other hand, it depicts the temporal behavior of the emission upon laser irradiation. The problem is basically discussed by Gräfe et al. [16]. They retrieved the axial distribution by fitting superposed \sin^2 shaped fluorophore distributions, which leads to satisfying results. It is, however, related to computational effort, which may be susceptible to noise and of course limits the spatial resolution to the width of the base function (\sin^2).

In the following chapter the problem of spatio-temporal coupling is disentangled by investigating the spatio-temporal properties on the DTT separately. This is achieved by analyzing the temporal response of spatially distributed materials, showing different temporal emission characteristics. After elucidating the correlation between the emitter spatial distribution and the detected DTT, the temporal response of axially distributed scattering (fast instantaneous response) is discussed. Subsequently, the impact of a complex temporal response onto the spatial resolution is investigated by analyzing the temporally resolved emission of cadmium sulfide (CdS) nanostructures arranged as a thin single layer and as a thin, distinct double layer. Finally the time trace of two 80 μm thick layers of Coumarin153 dissolved in ethanol and separated by a 120 μm thick glass plate is investigated.

7.1 Spatial and temporal relations in the time-of-flight method

In the ToF method the geometric axial position z_O^G of an object is determined by measuring the time elapsed between the emission of an excitation light pulse at a reference position $z_r^G \stackrel{!}{=} 0$ and the detection of the object's optical response upon this light pulse. This time is given by:

$$t'(z_O) = \frac{n_1}{c} z_O^G + \frac{n_2}{c} z_O^G = \frac{2z_O}{c}, \quad (7.1)$$

with n_1 and n_2 being the refractive indices at the wavelengths λ_1 and λ_2 of the exciting light pulse and the the object's optical response, respectively. c is the

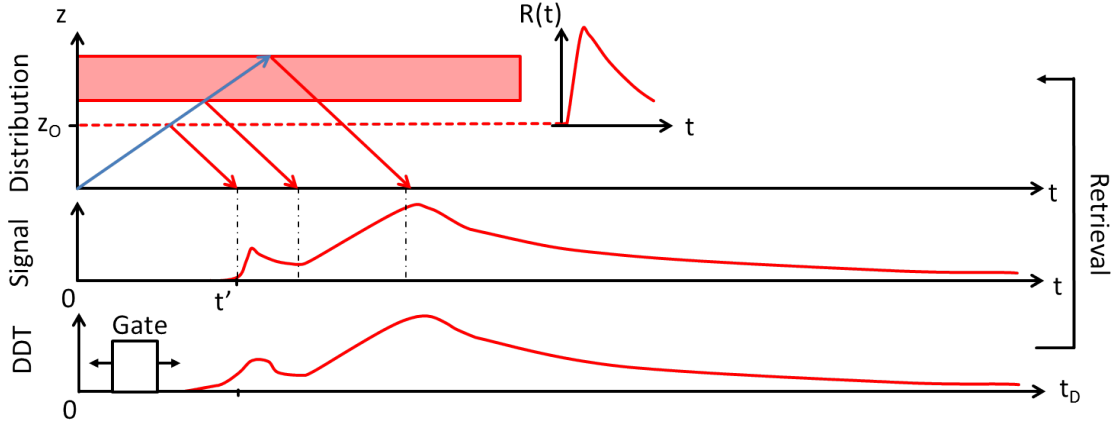


Fig. 7.1: ToF method: upper graph: distribution of objects (dashed line: thin object, solid field: extended object distribution on optical path length z), path of the excitation light (blue) and the object's optical response R (red), R is highlighted in the inset, lower graphs: resulting signal as function of t and measured delay dependent time trace (DDT) as function of t_D

vacuum speed of light. For convenience the optical path $z = n \times z^G$ will be referred to from here on, rather than the geometrical z^G .

The generally extended temporal emission behavior of the object leads to superposition of the temporal signals from different layers in time. Let $R(t)$ be the temporal response of a layer when excited at time $t' = 0$ (thus at the position $z_O = 0$). Hence the signal arising from distributed distinct layers is given by:

$$S(t) = \sum_i a_i R(t - t'_i), \quad (7.2)$$

with a_i being the amplitude of the response from layer i . For a continuous distribution $a(t')$ the sum changes into an integral, hence the signal $S(t)$ is the convolution of the distribution $a(t'(z))$ and the temporal response $R(t)$:

$$S(t) = \int a(t') R(t - t') dt' = (a \otimes R)(t). \quad (7.3)$$

The emission is excited by an excitation pulse $E(t)$ and gated. Thus the convolved signal $E \otimes S(t)$ is analyzed by the OKG with gate function $G(t - t_D)$ (signal field $I_S(r, t)$ in eq. (3.28) in subsect. 3.2.3). Consequently, the signal $sig(t_D)$ detected by the OKG is

$$sig(t_D) = \left(\overbrace{E \otimes G \otimes R \otimes a}^{r(t_D)} \right)_{sys(t_D)}(t_D), \quad (7.4)$$

This is consistent with the findings of Gräfe et al. [16]. When using the OKG in order to analyze a temporal structure the time t , which is the time coordinate of the signal field transfers to the delay time t_D between the signal field and the gate pulse. Generally the zero delay time $t_D = 0$ is a parameter that can be freely chosen, due to the arbitrary selection of the reference point z_r . In this context, the ToF method is mostly suited to measure optical distances between two layers. As a consequence

the zero delay can always be chosen in a way, that $t_D = t$. The correlation between axial position z and the detected signal $sig(t_D)$ is illustrated in fig. 7.1.

The system function $sys(t_D) = (E \otimes G)(t_D)$ in eq. (7.4) is the resulting DTT, if the (Gaussian shaped) excitation pulse was gated directly. Thus $sys(t_D)$ is assumed to be Gaussian shaped with a duration (FWHM) $\Delta\tau_{eff}$.

The convolution (7.4) shows that the measured axial profile of the emitters is distorted by the system response function $r(t_D)$ (eq. (7.4)). In this context $r(t_D)$ seems to be analogous to the point-spread function in microscopy (one dimensional case). Thus, comparable methods to those used for image retrieval might be used to determine $a(z_O)$ from a DTT. The influence of the long temporal response function is unclear. The following sections aim for investigating its impact on the measurement.

7.2 Axially distributed scattering

As a preliminary step the DTT of axially distributed scattering was investigated. In this case the temporal emission behavior $R(t)$ of the object is very fast ($R(t) \approx \delta(t)$). The DTT representing the response of a scattering stack (design: fig. 4.5a) yields four distinct peaks (fig. 7.2) which were fitted by Gaussian functions. The peaks are attributed to the four interfaces of the scattering test sample (BK7 - adhesive tape (AT), AT - SiO₂, SiO₂ - AT, AT - air, fig. 4.5a). The separations between the peaks and the FWHM values of the Gaussians are shown in fig. 7.2 (optical path z and delay time t_D). The inaccuracies given arise from the fitting procedure. The distances between the peaks represent the optical layer thicknesses. Thus the material thickness can be calculated by simply dividing the distances by the group refractive index n_G of each material at the respective wavelengths. Particularly its value for fused silica is very well known [105]. For the adhesive tape only the phase refractive index is known ($n = 1.48$) [252]. The calculated geometrical thicknesses d_G are compared to the d_M values determined by a gauge in tab. 7.1. Particularly the derived thickness values for the fused silica slab and the second adhesive tape layer agree very well with the independently determined sample properties (within 1.5 % error limit). This error is attributed to the accuracy of the gauge, which amounts to $\pm 10 \mu\text{m}$. In case of the adhesive tape, the vague knowledge of the refractive index contains a second cause of error. This was taken into account in tab. 7.1 by tremendously varying the refractive index value by ± 0.1 . The result for the first layer thickness, however, greatly diverges from the expected measured value. The origin for that is not clear, yet. It is noticeable, that this layer is in between the two glass slabs, which might cause compression effects of the adhesive tape or the glue. Also refractive index and thickness variations or structural changes resulting in a permanent refractive index modification may have occurred, since the tape (polypropylene spacer as well as the glue) might be photo sensitive to light around 440 nm. Nonlinearities in the measurement system, as observed e.g. in self-interference experiments [27] are, however, excluded, since the linearity was shown already at the characterization of the setup (fig. 5.6b).

Additionally, the measured FWHM values of the peaks range from $\delta t = 150 fs$ up to $\delta t = 270 fs$. The lower limit of δt agrees well with the temporal resolution of the Kerr gate under consideration of the temporal walk-off in the OKG material (SAL4-glass, sect. 6.4). The longer δt values can be a consequence of a finite distribution

of the scattering samples (thickness variation of the glue) or non-ballistic scattering inside the system.

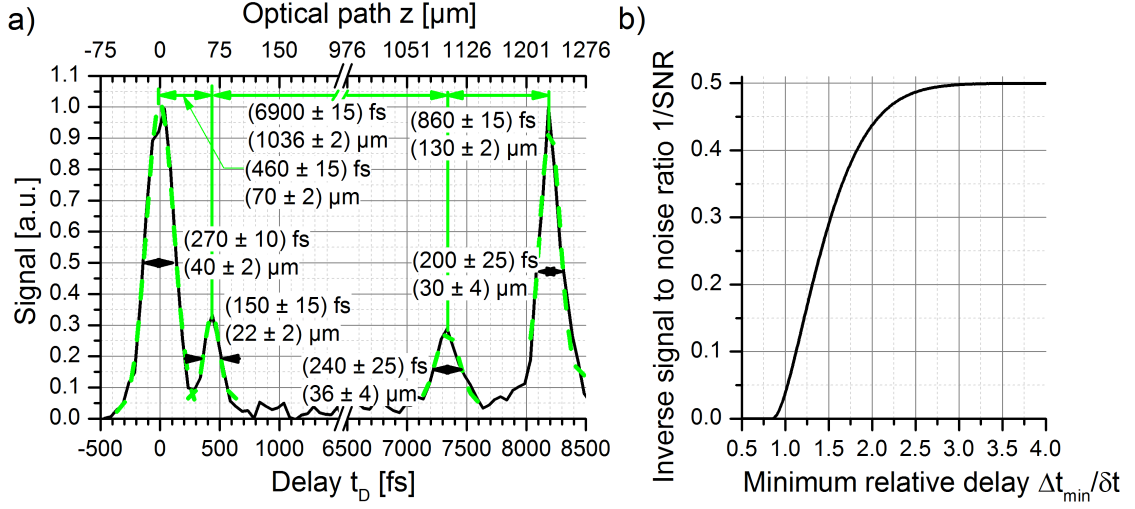


Fig. 7.2: a) Scattered signal of stacked system (adhesive tape and fused silica, fig. 4.5a), green dashed lines: Gaussian fits, b) distance at which two peaks can still be resolved (units of the peak width δt) as a function of the SNR (derived from Sparrow criterion [253])

Tab. 7.1: The delays and distances of the peaks in fig. 7.2 Δt and Δz , the group velocity refractive index n_G , the calculated thickness d_C and the thickness measured by a gauge d_M of the respective layer

Δt [fs]	Δz [μm]	n_G (440 nm)	d_C [μm]	d_M [μm]	
460 ± 15	70 ± 2	1.48 ± 0.1	47 ± 3	80	tape
6900 ± 15	1036 ± 2	1.500	691 ± 1	700	SiO ₂
860 ± 15	130 ± 2	1.48 ± 0.1	87 ± 5	80	tape

The smaller amplitudes of the center peaks compared to the outer ones indicate less efficient scattering at the AT-SiO₂ interface than at the AT-BK7 and the AT-air interfaces.

The noise amplitude (which is equal to the inverse signal-to-noise ratio, since the maximum peak height was normalized to 1) in gating the scattered light amounts to approximately $N = 5\%$ of the maximum signal (fig. 7.2, $800 \text{ fs} < \Delta t < 7000 \text{ fs}$). This enables to define the axial resolution $\Delta t_{\min} = c/2\Delta z_{\min}$ of two distinct layers using the present system. It seems appropriate to claim that two separate peaks can still be identified, if the local minimum between them is larger than twice the noise of the signal. This is a modification of the "Sparrow" criterion known from microscopy. In the absence of noise, the minimum distance amounts to $\Delta t_{\min} = \delta t/(\sqrt{2\ln 2})$ for Gaussian pulses. For a given signal-to-noise ratio (SNR) the Δt_{\min} is depicted in fig. 7.2b. Thus the temporal resolution of the present system for identifying two separate layers amounts to $\Delta t_{\min} \approx \delta t = 150 \text{ fs} \hat{=} 22 \mu\text{m}$.

Note that the resolution given above is a scale for the minimum distance at which two peaks still can be identified. The accuracy of measuring the distance between two well distinct peaks is, however, much higher, amounting to $\Delta \Delta z = \pm 2 \mu\text{m}$. This is because more data points can be used per peak when finding the position of one distinct peak, compared to trying to detect two very close peaks.

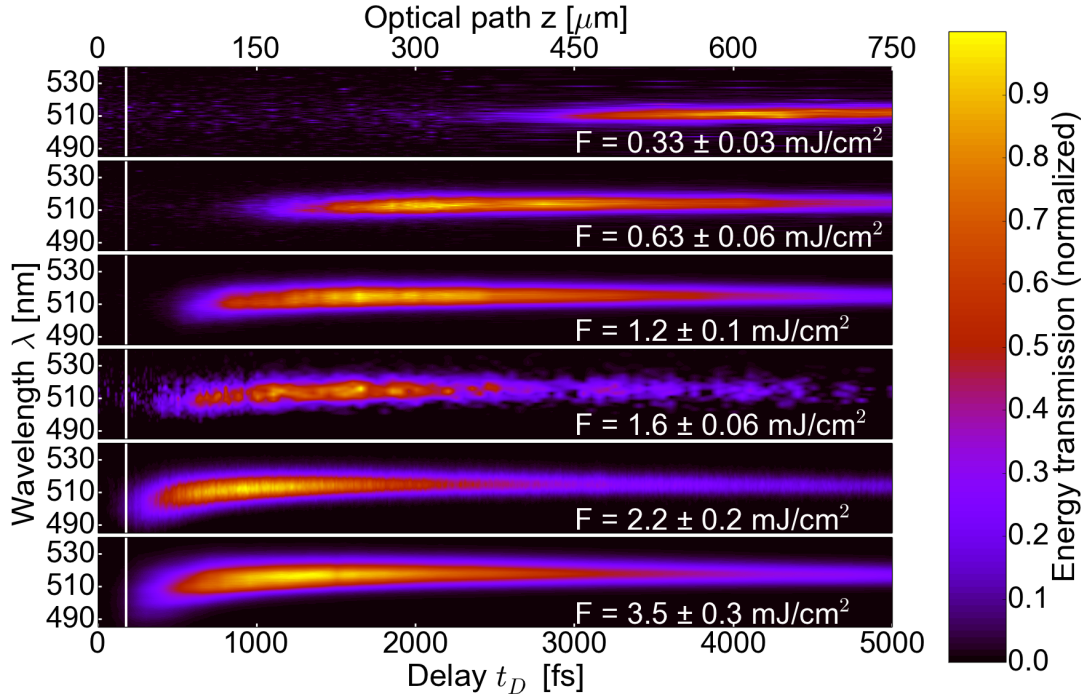


Fig. 7.3: Spectral temporal response of the CdS ensemble upon femtolaser pulse excitation ($\lambda_{ex} = 440$ nm central wavelength) as a function of excitation fluence F

7.3 Identifying the axial distribution of thin layers showing a finite temporal response

When investigating the axial distribution of emitters that show a complex temporal behavior (such as fluorophores) their temporal response function may affect the axial resolution of the detection system, which is explained in the following sections. In order to avoid convolution effects due to the axial extent of the emitters (eq. (7.3)) very thin distinct layers were investigated in a first step. An ensemble of cadmium sulfide (CdS) nanostructures was used as test samples, since they possess a strong emission and can be deposited as very thin layers (only a few hundred nm). Its emission lies around $\lambda_{em} = 510$ nm [254], which is in the range of the fluorescence from important biological molecules such as NADH ([14, 99]).

7.3.1 Emission of a single CdS nanostructure layer

Appendix G depicts an electron microscopic image of the CdS nanostructures grown on a silicon substrate provided by "Institut für Festkörperphysik" of the University of Jena [255].

The spectrally and temporally resolved response of the CdS nanostructure ensemble upon fs laser pulse irradiation at 440 nm central wavelength is depicted in fig. 7.3. The excitation pulse fluences ranged from $F = 0.33$ mJ/cm² to $F = 3.5$ mJ/cm². For each fluence, the amplitude of the signal was normalized to 1. The white line at $t_D = 180$ fs represents the duration $\Delta\tau_{eff}$ of the system function $sys(t)$, which was determined by detecting the 440 nm light scattered by the silicon substrate. This is an upper limit of $\Delta\tau_{eff}$, since the gating time for the nanostructure

emission signal should be shorter due to a reduced temporal walk-off ($\lambda_{ex} \approx 440 \text{ nm} < \lambda_{em} \approx 530 \text{ nm}$, subsect. 6.3.2).

At large fluences above $F > 1.6 \text{ mJ/cm}^2$ the emission signal of the CdS ensemble starts within 500 fs after the excitation pulse. In contrast, at smaller fluences the emission is delayed up to $t_D = 2.5 \text{ ps}$ with respect to the excitation at the lowest investigated fluence value of $F = 0.33 \text{ mJ/cm}^2$. The delayed onset is highlighted in fig. 7.4a, where the temporal behavior of the spectrally integrated emission signal is compared for different excitation fluences. Besides the onset time, the rise- and the lifetimes of the CdS emission increase with decreasing excitation pulse fluence.

Besides a fast emission, a broadening of the emission spectrum is observed for large excitation fluences. In this case the temporal characteristics of the emission strongly depends on the emission wavelength λ_{em} (fig. 7.4b). At the lower wavelength limit around $\lambda_{em} = 500 \text{ nm}$ the emission increases very fast and reaches its maximum within the first 500 fs after the laser pulse. The rise of the signal at large wavelengths is slower. In case of an excitation fluence of $F = 3.5 \text{ mJ/cm}^2$, for instance, the emission at $\lambda_{em} = 525 \text{ nm}$ reaches its maximum approximately 1.5 ps after the excitation. The signal lifetime also depends on the emission wavelength. At $\lambda_{em} = 500 \text{ nm}$ and $\lambda_{em} = 511 \text{ nm}$ it shows a biexponential decay with time constants of $\tau_{F,1} = 240 \pm 10$ and $\tau_{F,2} = 10000 \pm 2000 \text{ fs}$ (500 nm) and $\tau_{F,1} = 700 \pm 20$ and $\tau_{F,2} = 4900 \pm 400 \text{ fs}$ (511 nm). The decay at $\lambda_{em} = 525 \text{ nm}$ is single exponential, showing a lifetime of $\tau_F = 1450 \pm 30 \text{ fs}$.

The difference in the time constants (emission build-up and lifetime) for different spectral components of the emission leads to a shift in the centroid of the spectrum λ_c (fig. 7.4c). The emission spectrum is blue shifted for short time delays ($t_D < 1000 \text{ fs}$) and red shifted for long time delays ($t_D > 1000 \text{ fs}$). For very large time delays $t_D > 16000 \text{ fs}$ λ_c strives toward the value of small excitation fluences.

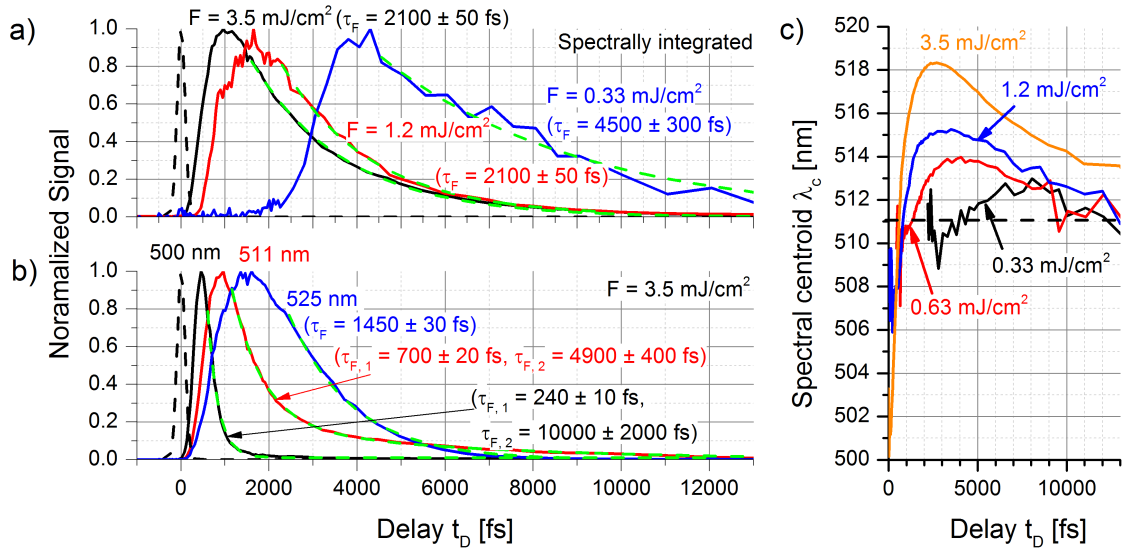


Fig. 7.4: a) Spectrally integrated delay time (t_D) dependent CdS emission signal for different excitation fluences, b) delay time dependent CdS emission for different emission wavelengths ($F = 3.5 \text{ mJ/cm}^2$), dashed lines: apparatus function (gated scattering signal), c) spectral centroid of the CdS emission as a function of the delay time t_D (different excitation fluences), dashed line: centroid of very weak excitation fluences (large t_D values)

7.3.2 Interpretation of the CdS ensemble emission

Cadmium sulfide (CdS) is a well investigated direct II-VI semiconductor [95, 256–260]. At room temperature the band gap energy of the CdS nanostructures was reported to be $E_{Gap} = 2.4$ eV [261–264]. Its emission upon photo excitation is attributed to the recombination of free excitons (Wannier-Mott type [265]) [258, 259, 266, 267]. At large excitation fluence the large number density of excitons can result in an electron-hole-plasma [268–270]. The spontaneous fluorescence of CdS nanostructures is exhibiting a lifetime of at least several hundred ps [263, 270]. At excitation fluences in the range of several tens of $\mu\text{J}/\text{cm}^2$ amplified spontaneous emission (ASE, subsect. 3.1.6) was observed. ASE dramatically reduces the emission lifetime to at least several tens of ps [254, 270]. For excitation fluences above $F > 100$ $\mu\text{J}/\text{cm}^2$ nanostructure lasing was reported [146, 255, 266, 267]. Due to the large excitation fluences applied at the sample and the short emission lifetime of $\tau_F < 10$ ps, the signal observed in this work is attributed to a stimulated emission. This attribution is supported by the observed delayed onset of the emission [269, 271]: In order to enable a population inversion in the excitonic states, the initial highly excited electron and hole distributions in the conduction band (CB) and the valence band (VB) after photo excitation have to thermalize. This is related to a time constant τ_r (subsect. 3.1.6). In agreement with the presented results the time required for sufficiently populating the excitonic states decreases with increasing excitation fluence. In contrast, fluorescence (spontaneous emission) would be observable simultaneously besides the excitation pulse. It is pointed out that spontaneous fluorescence is not excluded as an emission process. Its peak power is, however, much lower compared to that of the stimulated emission and hence below the noise level of the measurement. The origin of the stimulated emission (ASE, lasing) is not clear, although due to the strong fluence lasing is the most likely process. Single nanostructure lasing is generally identified by sharp lines in the emission spectrum due to the Fabry-Perot properties of the nanostructure, which serves as lasing cavity [255]. In case of an ensemble, however, this effect should vanish due to a broad distribution of the nanostructure lengths and hence the Fabry-Perot-resonances. Collective or random lasing, which possesses a broad emission spectrum is, however, also possible [272, 273]. Finally, the observed signal may be a combination of (fast) lasing and (slower) ASE, which would explain the biexponential decay.

Besides the delayed and short emission, the observed dynamic spectral shift at large fluences is impressive (fig. 7.4). The blue shift at short delay times is attributed to the dynamic Burstein-Moss effect (BME, also known as band-filling effect [262, 274–279]). At high electron and hole concentrations (due to large fluences), the CB and the VB fill up (the CB with electrons, the VB with holes), enabling carrier recombination (stimulated or spontaneously) at energies larger than E_{Gap} .

In addition, high electron and hole concentrations in the CB and the VB, respectively, lead to a reduction of the band gap (band gap renormalization, BGR) [94, 160, 262, 269]. Above a critical concentration the band edges are at lower energies than the excitonic states and cause a red shift in the emission. For BGR the electrons (holes) have to relax to the bottom (top) of the conduction (valence) band. Hence this process is slower than BME. Regarding the emission wavelength BGR counteracts BME. This explains the blue shift at short delay times and the red shift at large delay times. At very large delay times, the carrier concentration

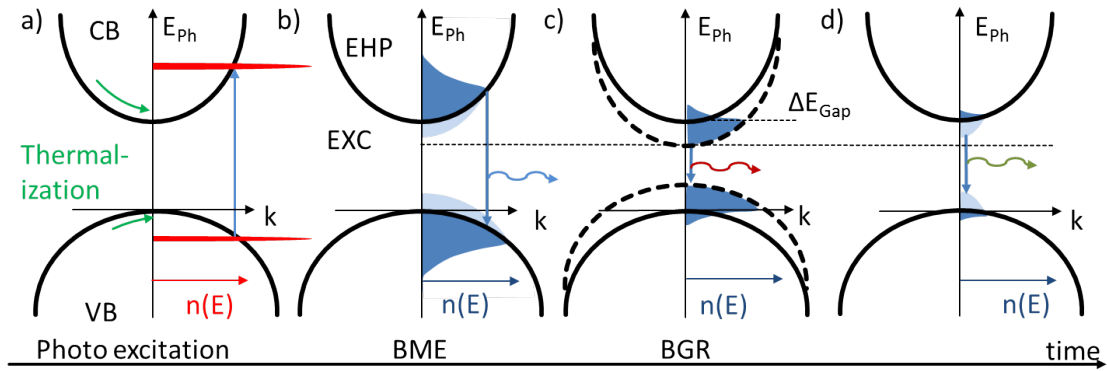


Fig. 7.5: Processes leading to complex spectral temporal response of the CdS nanostructures (large excitation fluences): a) Distribution of electron (holes) in the conduction (valence) band (CB, VB) upon photo excitation, b) electron-hole-plasma (EHP) and excitonic states (EXC) after thermalization causing Burstein-Moss effect (BME), c) huge exciton density causes band gap renormalization (BGR), d) almost relaxed system (no BM and no BGR effects)

in the CB (VB) has reduced, so that the band edge of the CB (VB) is at higher (lower) energies than the excitonic states and the emission spectrum equals that of small fluence excitation. For an overview, the processes are summarized in fig. 7.5.

7.3.3 Emission from a stacked CdS nanostructure system

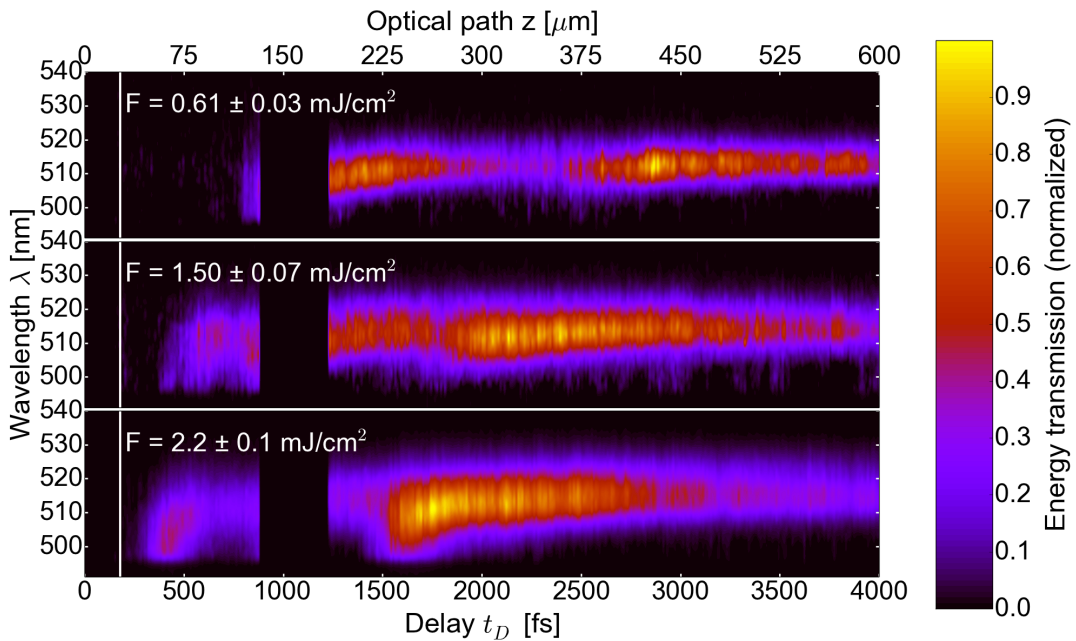


Fig. 7.6: Spectrally and temporally resolved emission of an imprinted CdS double layer (front and back surface of a 100 μm thick glass slide) upon fs laser irradiation ($\lambda_{ex} = 440 \text{ nm}$, variable fluence), signal around $t_D = 0 \text{ fs}$ and $t_D = 1000 \text{ fs}$ suppressed (cf. text)

In order to examine the performance of the OKG setup for depth resolution of a thin layer system showing a complex temporal response, a double layer structure of a CdS nanostructure imprint on the front and the back surfaces of a 100 μm thick glass slab was produced (paragraph 4.6.3). The spectrally and temporally resolved

signal is shown in fig. 7.6. At delay times around $t_D = 0$ fs and $t_D = 1000$ fs, a strong signal was observed, which is attributed to residual light from the long wavelength edge of the excitation pulse (scattering from the glass slide or the CdS nanostructures, suppressed in fig. 7.6, dark bars). In the single layer ensemble measurement such residual signals were not detected, because the CdS emission of the ensemble was much stronger than that of the imprints.

For all investigated fluences, the signal seems to show a comparable spectro-temporal behavior (spectral broadening, delayed onset of the emission as a function of the fluence) as the single layer ensemble emission. The emission onset varies between 300 fs at 2.2 mJ/cm² and 1000 fs at 0.61 mJ/cm². At delay times between $t_D = 1500$ fs and $t_D = 2500$ fs the signal evidently increases again, showing a comparable spectral broadening compared to short delay times. The second signal increase is attributed to emission originating from the rear CdS layer.

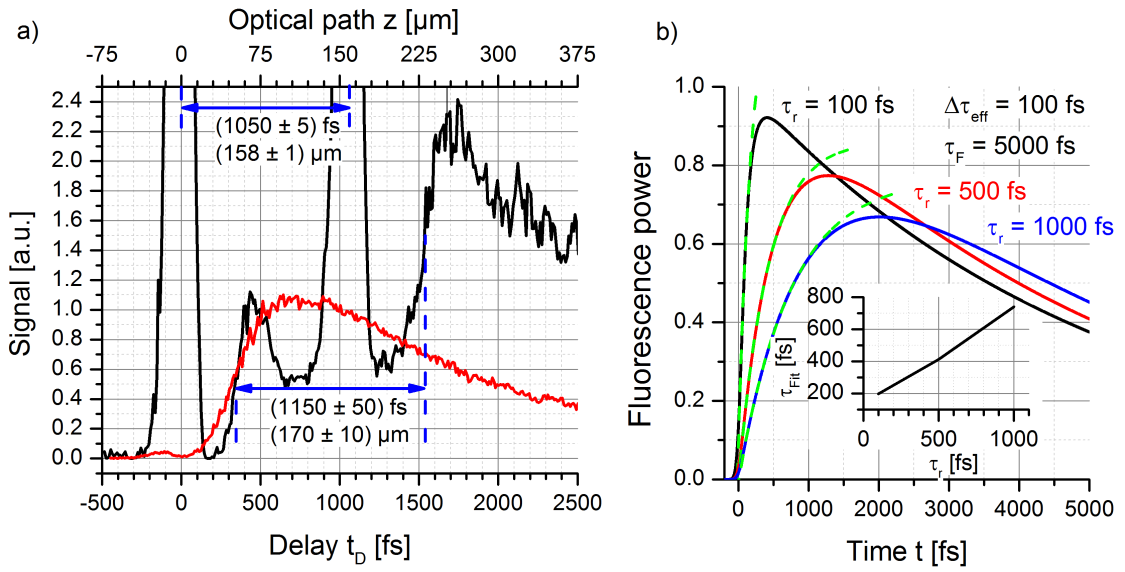


Fig. 7.7: a) Spectrally integrated signal of red: single layer, black: double layer measurement ($F = 2.2$ mJ/cm²), b) simulated temporal behavior of fluorescence for different thermalization times τ_r ($\Delta\tau_{eff} = 100$ fs, $\tau_F = 5$ ps), green dashed lines: fits according to eq. (7.5), inset: correlation between τ_{fit} and τ_r

Comparing the spectrally integrated signals, however, reveals differences between the single and the double layer systems, as shown in fig. 7.7a for $F = 2.2$ mJ/cm² (normalized DTT). Compared to the single layer emission the double layer signal increases very fast (within 100 fs). Its onset, on the other hand, is delayed longer than that of the single layer (approximately 200 fs). Furthermore, the signal lifetime, particularly of the emission from the first layer seems to be much shorter. A different CdS nanostructure density might explain the different temporal characteristics of the single and the double layer emission: Due to the large density in the ensemble, photons may additionally stimulate emission in the neighboring wires, supporting the emission build-up. Although stimulated emission from neighboring wires should be present in the imprints as well, the effect should be less pronounced due to their lower density. Additionally, random lasing as one possible origin for the emission (subsect. 7.3.2) will be stronger for higher nanostructure densities. Additional

experiments are necessary in order to identify the origin of the different emission characteristics.

In order to investigate the performance of the OKG for depth resolution it is, however, sufficient to have a closer look to the double layer signal only. The peaks caused by the scattered light of the excitation pulse at delay times $t_D = 0$ fs and $t_D \approx 1000$ fs are attributed to the front and rear surfaces of the glass slide. Their centers are separated by $\delta t = 1050 \pm 5$ fs, which correlates to $\delta z^G = 105 \pm 0.5 \mu\text{m}$ using eq. (7.1) and assuming a refractive index of the glass of $n = 1.5$. Thus the δz^G - value agrees very well with the thickness of the glass slide, which was measured to be $d = 100 \pm 10 \mu\text{m}$. The onset of the emission signal is, however, separated by $\delta t = 1150 \pm 50$ fs (measured at 50 % of the respective slope). This will be discussed in more detail in sect. 7.3.5.

7.3.4 Data analysis

In this section the data analysis for quantitative evaluation of the CdS nanostructure emission (double layers) is presented.

Model of the CdS emission build-up kinetics and data fitting The temporal emission characteristics of a CdS single layer ($R(t)$ in eq.(7.4)) of nanostructures is empirically modeled by a simple three level dynamics as presented in eq. (3.16) with thermalization time τ_r and fluorescence lifetime τ_F . The observed delayed onset time of the CdS emission with respect to the excitation pulse (sect. 7.3.1) is modeled by the parameter t_0 in eq. (3.16). For successful fitting the number of fit parameters should stay at a minimum. Therefore, the convolution with the system function $sys(t)$ is not incorporated in the fit. Additionally the emission lifetime τ_F in eq.(3.16) is considered to be infinity. This leads to a fit function for the emission build-up of a single layer:

$$y = a \left(1 - e^{-(t-t_{0,fit})/\tau_{fit}} \right), \quad (7.5)$$

where τ_{fit} , a and $t_{0,fit}$ are the fit parameters. The eligibility approximations become obvious when fitting simulated data (fig. 7.7b). In the simulation, a signal with a finite emission lifetime $\tau_F = 5000$ fs convolved with a Gaussian shaped system function $sys(t)$ (FWHM: $\Delta\tau_{eff} = 100$ fs) was calculated for different thermalization constants τ_r . Due to the linear correlation between τ_r and the fit parameter τ_{fit} the latter can be used as a scale for the build-up time (inset in fig. 7.7b).

The parameter $t_{0,fit}$ approximates the detected onset of the emission upon the laser excitation pulse. If the emission arises from a thin layer at a position z_O it combines the respective time $t'(z_O)$ (sect. 7.1) and the delayed emission onset t_0 (sect. 7.3.1):

$$t_{0,fit} \approx t'(z_O) + t_0. \quad (7.6)$$

It is *a priori* not clear, how the fit parameter $t_{0,fit}$ is affected by the parameters (τ_r and τ_F), the system function ($\Delta\tau_{eff}$) and the fitted data range. This has been investigated by measuring $t_{0,fit}$ as a function of the thermalization time for different configurations of the respective parameters. An object position $z_O = 0 \mu\text{m}$ and a emission delay $t_0 = 0$ fs was assumed. Hence the deviation from $t_{0,fit} = 0$ fs is a

scale for the fitting accuracy. The results are depicted in fig. 7.8. Fig 7.8a shows the fit results of $t_{0,fit}$ for a variation of the data range (signal rise from 10 % to 90 % (black), 20 % to 80 % (red) and 30 % to 70 % (blue)). Obviously using a smaller range leads to smaller deviations. In the presence of noisy data however, fitting within a smaller range causes larger statistical error. The fitting error is also increasing with smaller emission lifetimes τ_F (fig. 7.8b), particularly for small values of τ_r . The variation $t_{0,fit}$ due to the system function's duration $\Delta\tau_{eff}$ is larger than that caused by τ_F or the data range (fig. 7.8c). It however stays well below the $\Delta\tau_{eff}$, hence below the achievable resolution (cf. next paragraph) even for small τ_r values.

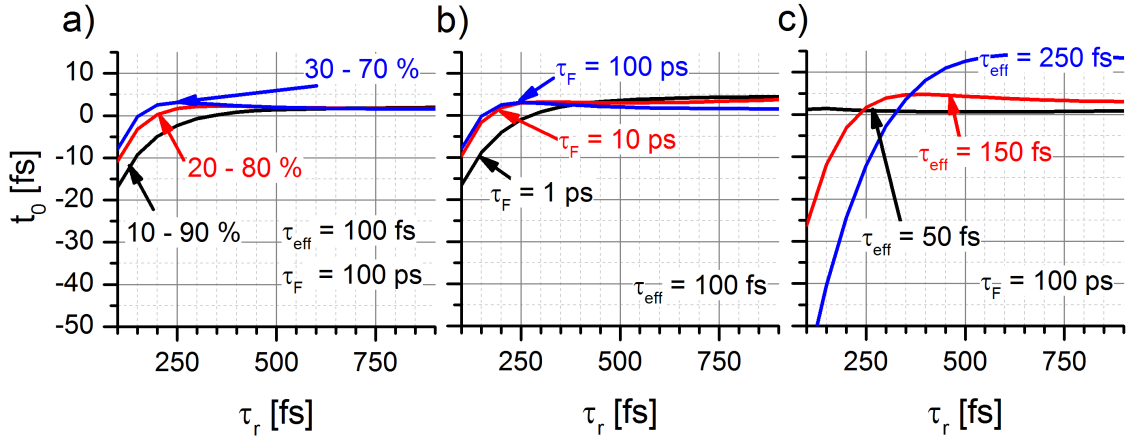


Fig. 7.8: Influence of a) the range of the fitted data (the number represents the rise between the minimum and the maximum of the fluorescence signal as shown in fig. 7.7b), b) the fluorescence lifetime $\Delta\tau_{eff}$ and c) the time constant of the Gaussian shaped apparatus function $\Delta\tau_{eff}$ onto the fit parameter t_0 as a function of the thermalization constant τ_r .

Parallels to microscopy For an instantaneous response of the emitters upon fs laser irradiation the measured DTT can be analyzed in analogy to methods known from lateral microscopy (sect. 7.2). In this context the Sparrow resolution criterion can be used in order to define the axial resolution.

A slow and asymmetric response function $R(t)$ (eq.(7.4)) marks, however, an essential difference between microscopy and the ToF method, because the latter depends on the investigated system. The emission lifetime τ_F is generally much larger than the light propagation time Δt , which is supposed to be measured. The build-up time τ_r , on the other hand, might be in that range or even shorter.

Investigating the limiting case of very fast build-up and very slow response ($\tau_r \rightarrow 0$ fs and $\tau_F \rightarrow \infty$) shows that $R(t)$ causes an integration of the signal (inserting a step function for $R(t)$ into eq. (7.4)). Therefore a derivation of the DTT seems plausible. For an exponential build-up behavior, which is typical for a fluorescence signal (eq. (7.5)) the derivative results in a single exponential decay, additionally convolved with the (Gaussian) system function $sys(t_D)$. A simulated DTT (time in units of the system time constant $\Delta\tau_{eff}$) of a double layer structure and its derivative is shown in fig. 7.9a. Based on the Sparrow criterion (sect. 7.2) a comparable resolution criterion can be defined taking the slow response into account: Two layers can be identified as separate ones, if the derivative of their DTT shows a local minimum

deeper than twice its noise ratio $2N = 2/SNR$. This is illustrated in fig. 7.9a. The limiting effect of the SNR onto the resolution is also known in microscopy [280]. The correlation between τ_r , $1/SNR$ and Δt_{min} is illustrated in fig. 7.9b. It is noteworthy that for very small noise levels ($1/SNR < 0.05$) the minimum resolution is not much affected by τ_r .

It is pointed out that another important difference between the system response function $r(t_D) = (sys \otimes R)(t_D)$ in eq. (7.4) and the response function known from lateral microscopy (known as "point spread function") is the absence of a limitation in the Fourier transform of the former one.

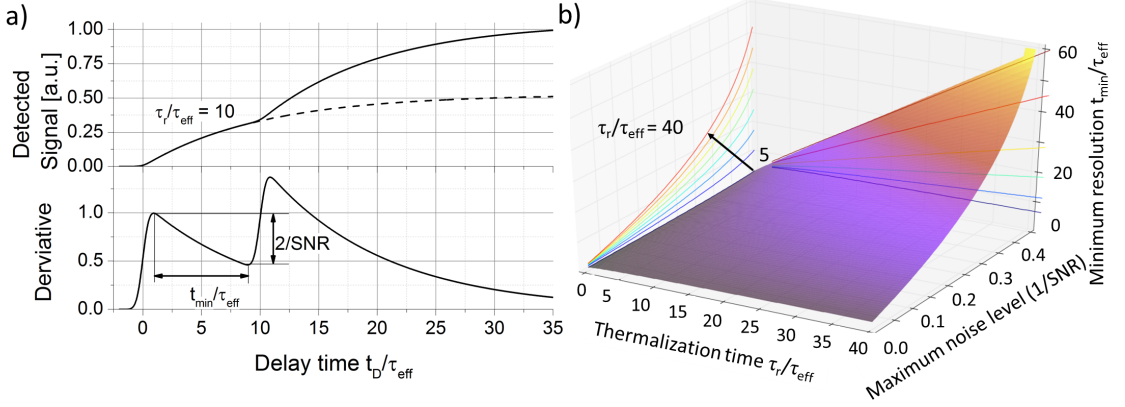


Fig. 7.9: a) Simulated DTT of a fluorescing double layer structure ($\tau_r/\Delta\tau_{eff} = 10$). b) correlation between noise ($1/SNR$) of the derivative, τ_r and the resolution t_0

Data smoothing and its impact on the derivative When calculating the derivative of a measured data set even a small amount of noise will cause tremendous fluctuations. Hence proper data smoothing is necessary. Besides the computation of the derivative adequate smoothing will also facilitate the data fitting by minimizing mutual dependences in the fitting parameters.

In frequency space, the system function is Gaussian shaped with a FWHM frequency of $\Delta\omega_{FWHM} = 8 \ln 2 / \Delta\tau_{eff} = 3.0 \times 10^{-2} \text{ fs}^{-1}$ ($\Delta\tau_{eff} = 180 \text{ fs}$) and centered at $\omega_0 = 0$. Consequently it acts as a low pass filter with a cut-off frequency $\omega_{g,sys}$. The signal noise, on the other hand, can be considered to be additive white noise. Effective data smoothing should therefore be possible by appropriate low pass filtering the signal. The cut-off frequency ω_g of the low pass filter has to be larger than $\Delta\omega_{FWHM}$, as too small ω_g values cause signal distortion. It is noted that a slow material response $R(t)$ acts as additional low pass filter. It is, however, sufficient to define the cut-off frequency ω_g for the filter with respect to $\Delta\omega_{FWHM}$. For a smaller cut-off frequency arising from $R(t)$ ω_g is an upper limit not causing any signal distortions. For large values, on the other hand (fast response), $\Delta\omega_{FWHM}$ limits the maximum detectable frequency.

The data smoothing is exemplified on the DTT of the spectrally integrated double layer system at an excitation fluence $F = 2.2 \text{ mJ/cm}^2$. Fig. 7.10a shows the original DTT of the signal and that smoothed by different low pass filters (cut-off frequencies ω_g , color coded). The respective derivatives are depicted in fig. 7.10b. The difference in the maximum and the minimum of the derivative within the delay time range of $3000 \text{ fs} < \Delta t < 4500 \text{ fs}$ was used as noise level of the derivative. The SNR as a

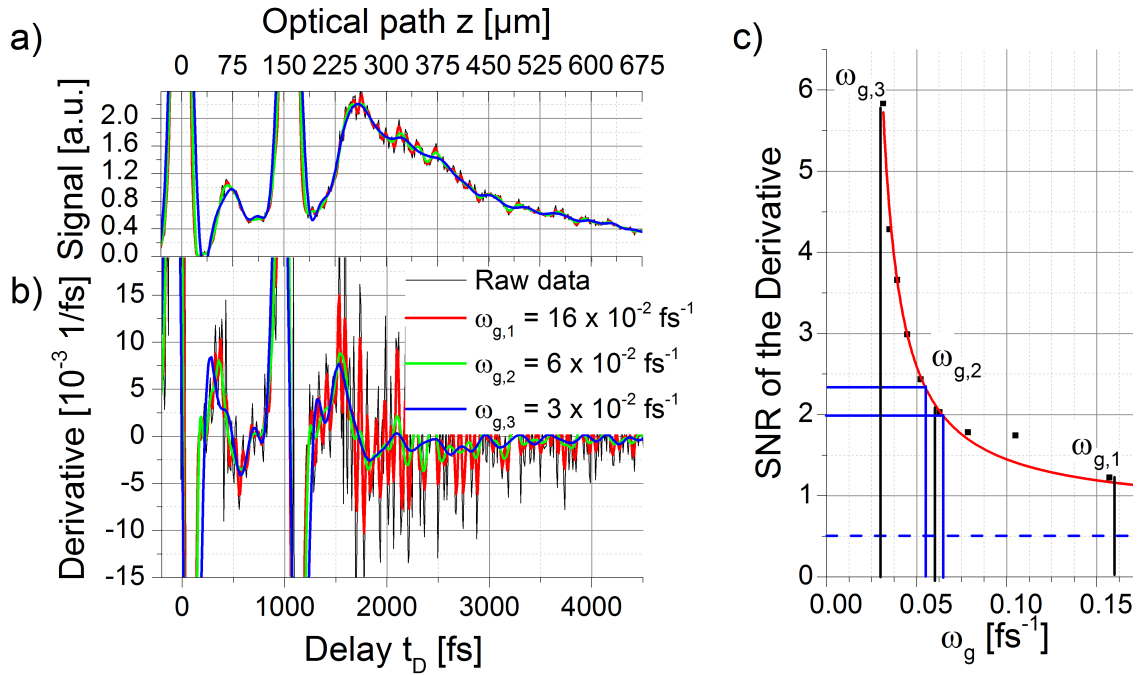


Fig. 7.10: Effect of low pass filtering onto signal derivative, a) spectrally integrated CdS emission signal (double layer, $F = 2.2 \text{ mJ/cm}^2$), smoothed by different low pass filters (cut-off frequencies ω_g). b) related derivatives, c) signal-to-noise ratio SNR of derivative as a function of ω_g , red line: hyperbolic fit, blue dashed line: SNR of the raw data, blue solid lines: limits of the SNR due to the resolution criterion ($\text{SNR} > 2$) and due to the apparatus function, black lines: SNR for the different ω_g values)

function of the smoothing cut-off frequency ω_g is depicted in fig. 7.10c. The dashed blue line represents the SNR of derivative computed from the raw data. Evidently, the SNR as a function of ω_g follows a hyperbolic shape. This is empirically expected, since very small cut-off frequencies will lead to zero noise (everything is smoothed) causing the SNR to limit at infinity. If ω_g converges towards infinity, on the other hand, the signal will not be smoothed at all and the SNR is that of the raw data.

A minimum $\text{SNR} = 2$ was defined to be necessary to successfully resolve two maxima (sect. 7.2) defining the maximum value for ω_g . In the present case this amounts to a maximum cut-off-frequency of $\omega_g = 6.5 \times 10^{-2} \text{ fs}^{-1}$. Its minimum value, on the other hand, is defined by $\omega_g = 1.5 \omega_{FWHM,sys} = 5.5 \times 10^{-2} \text{ fs}^{-1}$ which correlates to a $\text{SNR} = 2.4$ (fig. 7.10c). Smaller cut-off frequencies lead to signal distortions.

This is additionally emphasized by comparing the data set and its derivative upon smoothing at different ω_g values in figs. 7.10a and b, respectively. Whereas the smoothed data fit the raw data well for cut-off frequencies $\omega_{g,1}$ and $\omega_{g,2}$, the value $\omega_{g,3}$ causes significant signal distortions. In contrast, no clear maximum in the derivative can be assigned to the signal at the large cut-off frequency $\omega_{g,3}$. Only the $\omega_{g,2}$ smoothed signal satisfies both criteria and therefore should be used for optimum data smoothing.

7.3.5 Identifying the layers of the stacked CdS system

When axially resolving two layers, two important parameters are considered. First, the accuracy $\Delta\Delta z$ at which the distance between two distinct layers can be measured and second the minimum resolution, i.e. the minimum distance Δz_{min} at which two layers can still be detected as separate ones. In the following subsection, the former will be investigated by applying the fitting function given in eq. (7.5) to the smoothed data sets. The latter will be rated by applying the Sparrow criterion onto the derivative of the data set.

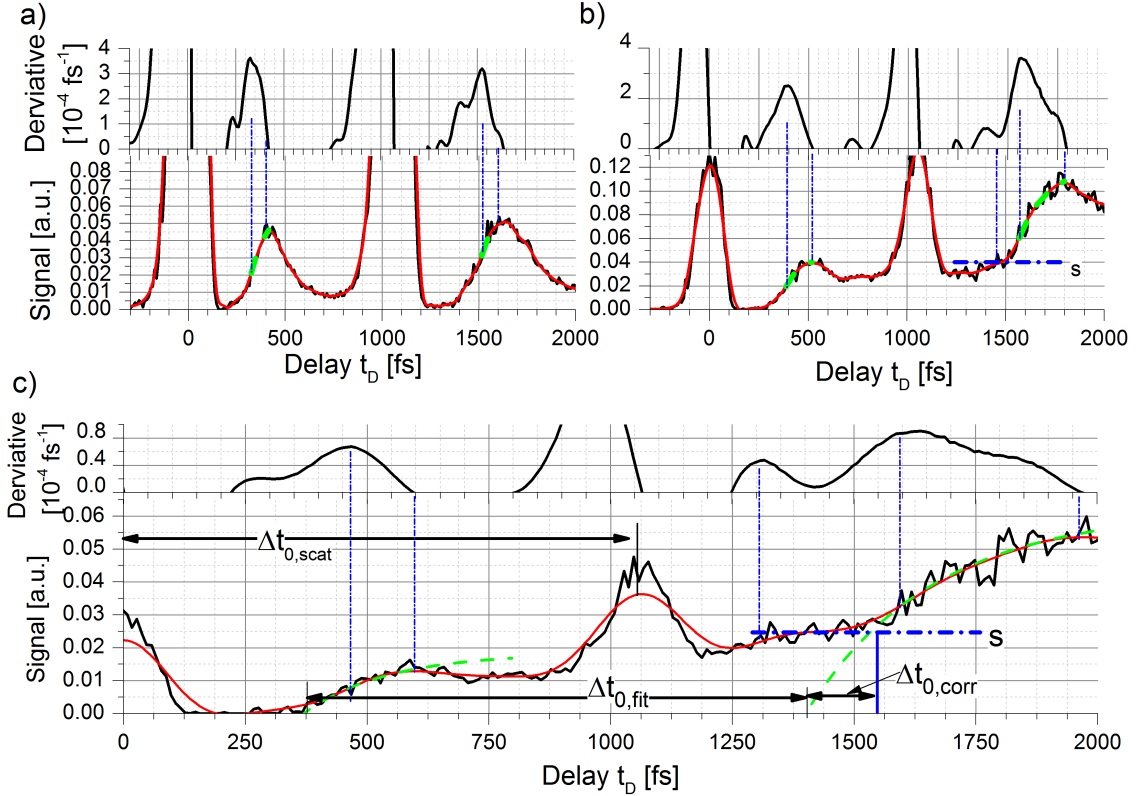


Fig. 7.11: Delay time dependent traces at a) 500 nm b) 511 nm and c) 520 nm of the double layer CdS emission ($F = 2.2 \text{ mJ/cm}^2$), red lines: smoothed signal, upper graphs: derivatives of smoothed signal, green dashed lines: fitted build-up, s : background of at fit from other layer, $\Delta t_{0,scat}$, $\Delta t_{0,fit}$ and $\Delta t_{0,corr}$: delay time distance (cf. text)

Measuring the distance between two distinct layers Measuring the distance between two distinct layers with the current system was evaluated by comparing the signals at three different emission wavelengths ($\lambda_{em,1} = 500 \text{ nm}$, $\lambda_{em,2} = 511 \text{ nm}$ and $\lambda_{em,3} = 520 \text{ nm}$, fig. 7.11) amongst each other and with respect to scattering signals from the interfaces. The delay time range for applying the fit (7.5) was identified by computing the derivative of the DTT. It was chosen to be between the maximum and the subsequent zero point of the derivative (dashed blue lines in 7.11). In addition, the signals arising from scattered excitation light were Gaussian fitted (distinct peaks in fig. 7.11). The fitted parameters are summarized in tab. 7.2. The distance between the centers of the two Gaussians amounts to $\Delta t = 1060 \text{ fs}$ for each wavelength. This correlates to an optical path of $\Delta z = 160 \mu\text{m}$ or a

geometrical path of $\Delta z_G = 106 \mu\text{m}$, which represents the thickness of the glass slab between the two layers (sect. 4.6.3, paragraph "Sample design").

Retrieving the position z_O of each layer requires the analysis of the parameter $t_{0,fit}$ which encodes $t'(z_O)$ (sect. 7.3.4). Evidently, the difference between the fitted $\Delta t_{0,fit}$ is a function of the emission wavelength (tab.7.2). Both parameters contributing to $t_{0,fit}$ (object position $t'(z_O)$ and emission onset t_0) should however be independent of λ_{em} . The wavelength dependence is attributed to a longer emission lifetime τ_F at larger wavelengths λ_{em} causing an offset s for the onset of the second signal rise (at delay time $t_{0,fit,2}$, fig. 7.11c). For $s > 0$ the distance between the fitted t_0 values of the two layers is larger compared to $s = 0$ (tab. 7.2).

Tab. 7.2: Fitting parameters τ_{fit} , $t_{0,fit}$ and a (τ and a of second signal only) of the DTT according to the fit function (7.5). The indices indicate the layer. s is the offset of the second signal (cf. text) and $\Delta t_{0,scat}$ the distance of the scatter peaks. and layer distances of the spectrally resolved double layer emission.

λ [nm]	500	511	520
$t_{0,fit,1}$ [fs]	290 ± 10	350 ± 10	370 ± 10
$t_{0,fit,2}$ [fs]	1470 ± 5	1470 ± 5	1400 ± 10
a_2 [a.u.]	-	0.189 ± 0.002	0.0618 ± 0.0005
$\tau_{fit,2}$ [fs]	55 ± 5	140 ± 5	260 ± 10
s [a.u.]	0	0.04 ± 0.01	0.024 ± 0.003
$\Delta t_{0,fit} = t_{0,fit,2} - t_{0,fit,1}$ [fs]	1180 ± 15	1120 ± 15	1030 ± 15
$\Delta t_{0,scat}$ [fs]	1060 ± 5	1055 ± 5	1060 ± 5
$\Delta t_{0,corr}$ [fs]	1160 ± 15	1170 ± 10	1180 ± 15

Interestingly, no decay of the signal arising from the first layer is observed at $\lambda_{em} = 511 \text{ nm}$ and $\lambda_{em} = 520 \text{ nm}$. Instead for 520 nm emission the signal increases slowly between the scattering peak assigned to the second surface and the appendant CdS emission (at delay times $1000 \text{ fs} < t_D < 1400 \text{ fs}$). The origin of this growth is not clear and requires further investigations. Presumably, it may be attributed to stimulated emission processes in the second surface caused by emitted light from the first layer.

Taking the offset into account allows to compute a corrected distance between the fitted signal onsets:

$$\Delta t_{0,corr} = t_{0,fit,2} - t_{0,fit,1} - \tau_{fit,2} \ln \left(1 - \frac{s}{a} \right) \quad (7.7)$$

The offset s was determined by using the signal value assigned to the minimum value in the derivative before the signal grows due to the second layer emission. The relation between $\Delta t_{0,scat}$, $\Delta t_{0,fit}$ and $\Delta t_{0,corr}$ is shown in fig. 7.11 c ($\lambda_{em} = 520 \text{ nm}$).

Using the correction term leads to comparable results of the computed difference for all investigated wavelengths. The values differ less than 1% amongst each other (tab. 7.2). This deviation is within the error margins arising from the fit. It is noteworthy that even a large uncertainty in the offset parameter (up to 25 % in the present case) causes only small inaccuracies of the computed layer distance. The major part of the position uncertainty still arises from the fitting accuracy of the parameter $t_{0,fit}$. Consequently the accuracy for measuring the distance between

two layers amounts to $\Delta\Delta z = \pm 2 \mu\text{m}$. It is comparable with the results for the scattered signals and is not significantly affected by the temporal response behavior of the emitters.

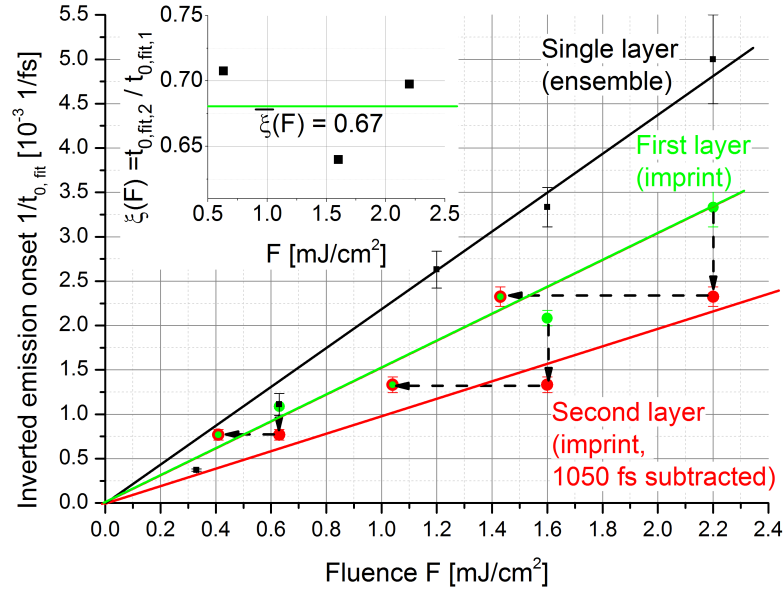


Fig. 7.12: Inverse onset times of emission as a function of the excitation fluence F for black: single layer ensemble, green: first, red: second layer from double layer imprints, red-green: corrected inverse onset times of second layer, inset: ratio of onset times as function of F .

Comparing the temporal distance of the scattered layers ($\Delta t_{0,scat}$) and that of the thin layers ($\Delta t_{0,corr}$) it is remarkable that $\Delta t_{0,corr} = 1170 \pm 15 \text{ fs}$ is significantly larger than $\Delta t_{0,scat} = 1060 \pm 5 \text{ fs}$. This is attributed to the fluence dependence of the emission onset t_0 as one component in $t_{0,fit}$. t_0 converges towards 0 for large fluences and towards infinity for very small fluences (sect. 7.3.1). Before exciting the second layer, the excitation pulse is however attenuated by absorption and scattering of the first layer or Fresnel reflection at the interfaces. Consequently, the emission onset of the second layer and hence $t_{0,fit,2}$ is expected to shift towards larger delay times t_D . When applying the ToF method to investigate axially distributed emitters, this would lead to wrong conclusions regarding the emitter positions.

In order to analyze the effect quantitatively the correlation between F and t_0 is empirically modeled by a hyperbolic. The inverted onset time $1/t_{0,fit}$ of the single layer (ensemble) and the double layer (imprints) are plotted as a function of the fluence in fig. 7.12 for the spectrally integrated emission signals (black: single layer ensemble, green: signal assigned to the first layer imprint, red: signal assigned to the second layer imprint). From values regarding the second layer ($t_{0,fit,2}$) the distance between the scattering signals ($1060 \pm 5 \text{ fs}$) was subtracted in order to correct the propagation time through the glass slab. The linear correlation between F and $1/t_{0,fit}$ validates the hyperbolic model. The difference in the slopes assigned to the signals of the single layer (ensemble) and the first of the double layer (imprint) is attributed to the larger nanostructure density of the ensemble and resulting effects (sect. 7.3.3). Comparing the signals assigned to first and the second of the double layer imprint their averaged ratio of the inverse onset times and consequently the excitation fluences amounts to $\bar{\xi} = \overline{t_{0,fit,2}/t_{0,fit,1}} = 67 \%$ (inset and red-green symbols in fig. 7.12). Thus, the attenuation of the excitation fluence amounts to $\Delta F/F = 33$

%. Estimating the attenuation due to Fresnel reflection by assuming a refractive index of CdS of $n = 2.8$ (at $\lambda = 510$ nm) [281] and a stacked system of bulk CdS - glass ($n = 1.5$) - homogeneous CdS leads to a beam attenuation of $\Delta F/F = 31$ % (normal incidence). This agrees well with the value estimated from the delayed onset.

Resolution in case of thin distinct layers The minimum distance Δt_{min} at which two thin layers can still be identified as separate ones is investigated by analyzing the derivatives of the DTT. For two excitation fluences ($F = 2.2$ mJ/cm² and $F = 1.6$ mJ/cm²) the smoothed signals (black dashed lines) and the corresponding derivatives (red solid lines) are shown in fig. 7.13.

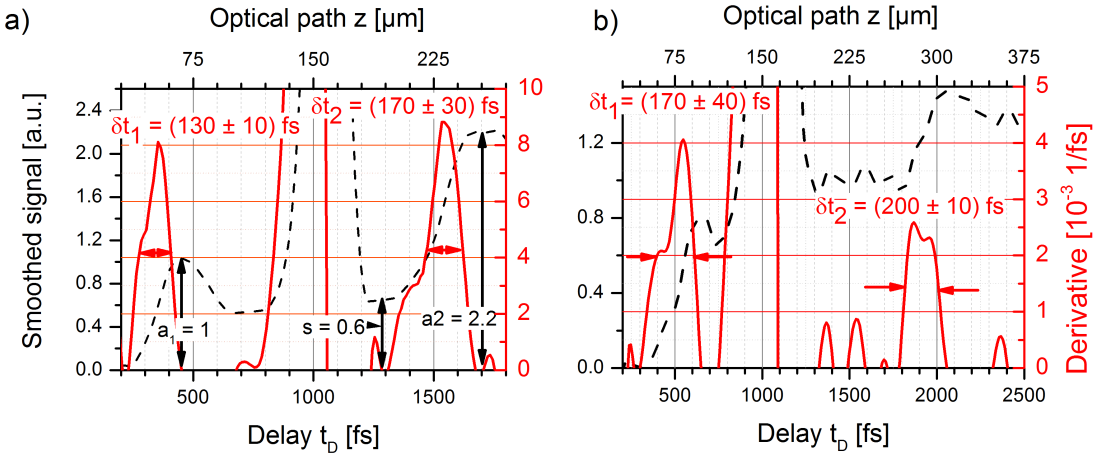


Fig. 7.13: Black dashed lines: smoothed signal ($\omega_g = 0.06$ fs⁻¹), red solid lines: derivative of double layer structure: a) $F = 2.2$ mJ/cm², b) $F = 1.6$ mJ/cm². a_i and s : signal amplitudes at different delay times (first maximum was normalized to $a_1 = 1$)

The expected exponential decay of the derivatives (sect. 7.3.4) is, however, not observed. Instead, the derivative decreases quickly showing distinct peaks. This is attributed to the short emission lifetime τ_F in the picosecond time range and a very short emission build-up time τ_r that is in the range of the pulse duration.

Yet, the impact of τ_r onto the resolution is observable quantitatively. The FWHM durations of the peaks of the derivatives assigned to the respective layers range from $\delta t = 130 \pm 20$ fs (first layer at $F = 2.2$ mJ/cm²) up to $\delta t = 200 \pm 30$ fs (second layer $F = 1.6$ mJ/cm²). The larger δt are attributed to larger τ_r values of the emission. Due to the peak-like behavior of the derivatives, the criterion as presented in sect. 7.2 can be applied to estimate the spatial resolution. The average peak duration $\overline{\delta t} = 0.5(\delta t_1 + \delta t_2)$ of both layers and the correlation between the noise level N and the ratio $\Delta t_{min}/\delta t$ as shown in fig. 7.2) are used in order to estimate the axial resolution at the given excitation pulse energy. An overview over the important parameters and the resolution is given in tab.7.3. It is remarkable that the δt values are larger for signals attributed to the second layers. The attenuated excitation pulse fluence at the second layer ($\Delta F/F \approx 67$ %, cf. previous paragraph) is assumed to be the reason, since the time for the CdS emission to increase is a function of the excitation fluence (sect. 7.3.1). This assumption is supported by the comparable δt

Tab. 7.3: Estimation of the axial resolution Δt_{min} and Δz_{min} , respectively for detecting the CdS double layer structure excited at different pulse fluences F . (average peak duration $\bar{\delta t} = 0.5(\delta t_1 + \delta t_2)$, noise level N)

F [mJ/cm ²]	$\bar{\delta t}$ [fs]	N [%]	Δt_{min} [fs]	Δz_{min} [μ m]
1.6	185	25	260	40
2.2	150	12	170	26

values for the second and the first layer at $F = 2.2$ mJ/cm² and $F = 1.6$ mJ/cm², respectively.

7.3.6 Nanostructure density of the layers

The amplitudes of the spectrally integrated signal as shown in fig. 7.13a are a scale for the nanostructure concentration of the individual imprint. Assuming a comparable emission yield of the nanostructures in both layers and a linear correlation between the maximum emission signal and the excitation fluence the concentration ratio of both layers can be estimated by computing the ratio, weighted with the fluence attenuation of 33 %:

$$R_c = \frac{c_{CdS}[1]}{c_{CdS}[2]} \approx \frac{(1 - 0.33)a_1}{a_2 - s} = 0.40, \quad (7.8)$$

where $c_{CdS}[i]$ is the nanostructure concentration of the layer i , a_i is the amplitude of the signal assigned to the respective layer and s is the offset of the second layers' signal due to the emission lifetime of the first one (fig. 7.13a). Thus, the nanostructure density at the second layer is roughly double the concentration of the first one. This however is only an estimate, since the linear correlation between F and the amplitude is a first approximation and the offset s as well as the fluence attenuation are estimates. A more detailed study, particularly regarding the correlation between excitation fluence, nanostructure density and emission amplitude is necessary in order to acquire more accurate results. Using a double layer system with a well defined concentration (sect. 7.4) is thus a better test structure to evaluate the capability of the presented measurement system for investigating the fluorophore concentration.

7.4 The temporal response of thick distributed emitter layers

In case of thin distinct layers, the detected signal can be analyzed separately for every layer. As a consequence the identification of the layer position is independent on the emission build-up time. Hence assuming a thin distinct distribution facilitates the data analysis a lot. This assumption might be adequate when applying the measurement method to investigate the NADH distribution in the retina, since it is known to be distinctly distributed [19, 20]. However, this generally limits the applicability of the system. In addition locally agglomerated NADH in the human retina is not precluding a continuous distribution (of lower density).

Retrieving a continuous distribution of a given DTT is however more challenging compared to identifying distinct layers, because the sum (7.2) changes to the convolution (7.3) linking the distribution $a(t'(z))$ and the response $R(t)$. In a first approach Gräfe et al. [16] retrieved the distribution by iteratively reconstructing the distribution on the base of \sin^2 functions. They found the thermalization time τ_r to be a crucial parameter for the distribution retrieval.

In this section, the DTT signal arising from two thick layers of Coumarin153 (C153) dissolved in ethanol (sect. 4.6.3) will be investigated. The C153 emission wavelength of about 530 nm [282] is comparable to that of the CdS nanostructures (sect. 7.3) and NADH ([14, 99]).

The thermalization constant upon fs excitation at $\lambda_{ex} = 440$ nm, the relative fluorophore concentration of each layer and the minimum distance Δz_{min} for successfully resolving the layers will be estimated. Finally two alternative approaches to that given by Gräfe et al. are analyzed with respect to their stability against uncertainties of the emission build-up time (thermalization time τ_r).

7.4.1 Delay time dependent signal of the fluorophore

The normalized emission signal of the C153 solution from the double compartment cuvette is shown in fig. 7.14 (black symbols). From a delay time $t_D = 0$ fs it steadily increases up to 55 % of its final value within approximately 1000 fs. Subsequently, the signal stays constant for 900 fs and rises up to 100 % within another 1000 fs (cf. black dashed lines). Each build-up is attributed to light originating from one compartment. The intermediate plateau is assigned to the excitation light propagation through the glass spacer.

The blue lines in fig. 7.14 indicate the known fluorophore distribution with the respective refractive indices n . For the fluorophore solution n was approximated by the value for ethanol ($n = 1.36$, [283]). The refractive index of the glass was $n = 1.5$. Evidently, the signal keeps rising at delay times t_D which exceed the propagation time for the cuvette thickness ($t'(d = 80 \mu\text{m}, n = 1.36) = 725$ fs) of the fluorophore by approximately 300 fs.

7.4.2 Evaluation of the thermalization time constant τ_r , the fluorophore concentration and the temporal resolution

The protracted signal build-up is attributed to the thermalization of the vibrations of the electronically excited molecules upon fs laser irradiation in C153, which is characterized by τ_r (sect. 3.1.6). This is confirmed by simulating the DTT for different values of τ_r (red lines in fig. 7.14). Smaller or larger τ_r values cause a faster or slower emission increase, respectively. $t_D = 0$ fs was defined as the delay after which a significant increase of the measured signal was observed. The position of the compartments (first compartment at $t_D = -250$ fs) was determined by determining the optimum fit between the simulated and the measured data. Details, regarding the simulation are explained in appendix H. The best fit between the simulated and the measured data is achieved for $\tau_r = 600$ fs. In contrast to the expectations based on the literature [16] tremendously varying the thermalization constant by about 25 % will, however, not result in a critical deviation of the simulated from the measured data. The value for the thermalization constant agrees well with those

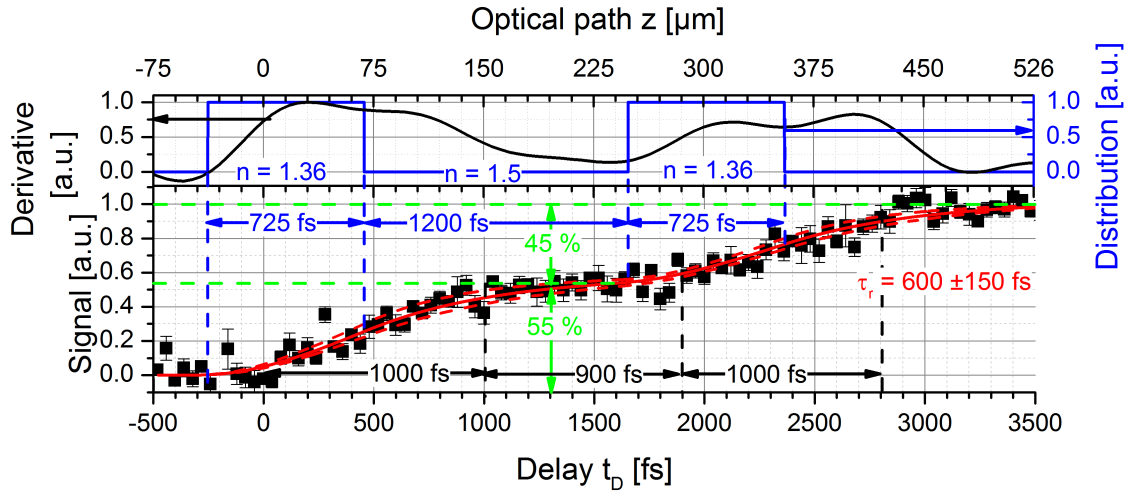


Fig. 7.14: black symbols and line: time resolved signal and derivative (after data smoothing) of Coumarin 153 (dissolved in ethanol) in double compartment cuvette ($\lambda_{ex} = 440$ nm), red lines: simulated DTT ($\tau_r = 600 \pm 150$ fs, dashed lines indicate error margins), blue lines: fluorophore distribution and refractive indices (glass spacer and fluorophore distribution)

reported in the literature for C153 dissolved in ethanol or methanol ($\tau_r \approx 500$ fs [284, 285]). Generalizing τ_r is, however, very hard, since it does not only depend on the fluorophore, but also strongly on the solvent.

Determining the absolute value of the fluorophore concentration from the measured DTT is challenging, since it depends on many parameters. The concentration ratio between the two compartments, denoted by:

$$R_c = \frac{c_{C153}[1]}{c_{C153}[2]} = \frac{a_1}{a_2} \quad (\text{appendix H}) \quad (7.9)$$

can on the other hand be determined easily by investigating the plateau between the two build-ups. Varying R_c leads to $R_c = 1 \pm 0.2$, which is expected, since both compartments contained the same fluorophore solution. The large error of 20 % is a consequence of the large noise on the measured data. Excitation pulse absorption in the compartments is the reason for the plateau being at 55 % instead at 50 % of the entire signal (appendix H).

The minimum distance Δt_{min} at which two thick layers can still be identified is determined analogously to the case for thin layers showing a complex temporal response by investigating the derivative of the signal (subsect. 7.3.4 paragraph "Parallels to microscopy"). It was calculated after smoothing the data set and is depicted in the top most graph of fig. 7.14 (amplitude normalized to 1). The noise level of the derivative amounts to $1/SNR = N = 0.3$. Applying the resolution criterion in the presence of noise (fig. 7.9b), the resolution is $\Delta t_{min} \approx 5\Delta\tau_{eff} = 900$ fs. This correlates to an optical path difference between the two layers of $\Delta z_{min} \approx 130$ μm ($\Delta z^G = 90$ fs, if $n = 1.5$). The major reason for the poor resolution in this case is the large noise level of 30 %. Reducing N could improve the resolution by a factor of 5 ($\Delta t_{min} = \Delta\tau_{eff} = 180$ fs). An even better resolution requires shorter gating times.

7.4.3 Retrieval of the emitter distribution

Certainly, the fluorophore distribution is generally unknown and supposed to be determined. Identifying an arbitrary distribution $a(t'(z))$ requires the deconvolution of the DTT (eq. (7.3)).

The deconvolution is a mathematically challenging process, since even small signal noise will cause tremendous noise in the deconvolved signal. Typically either direct methods based on matrix regularization or iterative methods are applied to successfully deconvolve noisy data. Two methods of retrieving the fluorophore distribution are compared. In the first approach the convolution integral (7.3) was solved by applying the "Wiener" deconvolution method [286], where an approximated distribution function $\hat{a}(t)$ was computed by introducing a regularization parameter ϵ related to the noise of the signal. As for the second method an iterative algorithm was applied. An initial guessed distribution was randomly varied in order to fit its convolution with the response function to the data points. Both techniques are elucidated in more detail in appendix I.

An approach similar to the second method was already applied by Gräfe et al. [16]. There the fluorophore distribution was fitted by superposing \sin^2 -functions. The spatial resolution in that work amounted to about a hundred microns. This algorithm did, however, depend strongly on the exact knowledge of the thermalization time constant τ_r . Another drawback appears to be an insufficient reconstruction of the fluorophore amplitude at layer distances as thin as $150 \mu\text{m}$ (fig. 5 in [16]).

The iterative algorithm presented in this work was tested by reconstructing a modeled fluorophore distribution from a simulated DTT ($\tau_r^{sim} = 500 \text{ fs}$). The algorithm was shown to satisfyingly reconstruct the distribution even in case of a strong deviation $\Delta\tau_r$ between the assumed thermalization constant and τ_r^{sim} up to $\Delta\tau_r = \pm 300 \text{ fs}$. It also shows good results in the presence of noise (appendix I). A disadvantage of the presented algorithm is the fairly large noise of the retrieved signal due to the random variation. This however can be smoothed by applying a low pass filter (subsect. 7.3.4). The results of the fluorophore distribution retrieved from the measured data set using the "Wiener" deconvolution method and the iterative fit are depicted in figs. 7.15a and b. The retrieved distributions are represented by the black solid lines in the upper graph ($\tau_r = 600 \text{ fs}$), whereas the red dashed lines represent the original distribution. The black dashed lines in the upper graph of fig. 7.15 show the retrieved signals by varying the thermalization constant about $\pm 300 \text{ fs}$ (50 %). Comparing the retrieved distributions for the different thermalization constants shows that its accurate knowledge is not as crucial as pointed out by Gräfe et al.. This agrees with the test results of the evolutionary algorithm (appendix I).

Regardless of the applied method the retrieved fluorophore distributions are blurred compared to the original one. This is attributed to the low pass filtering due to the convolution of distribution $a(z(t_D))$ with the Gaussian shaped system function and the fluorescence response function. The green dashed line in fig. 7.15b (at $\tau_r = 600 \text{ fs}$) indicates the effect of the low pass filter onto the fluorophore distribution. Evidently, the result of the iterative algorithm agrees fairly well with the filtered original distribution. The deviation of the distribution computed by the "Wiener" deconvolution is attributed to the regularization parameter, hence the SNR. This parameter reduces the data noise but may lead to distortions in the retrieved result [287].

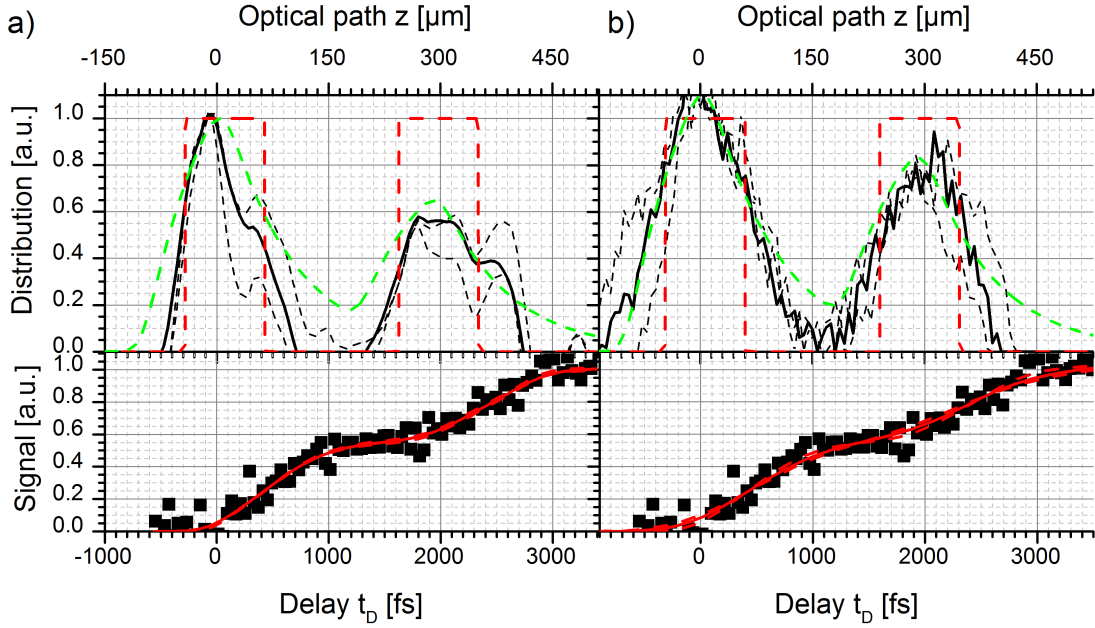


Fig. 7.15: upper graph: retrieved fluorophore distributions (black solid lines) by a) Wiener deconvolution method, b) iterative algorithm ($\tau_r = 600 \pm 300$ fs, dashed black lines indicate fluctuation), red dashed lines: original distribution, green dashed lines: distribution low pass filtered by apparatus function ($r(t)$ in eq. (7.4)), lower graph: black squares: original data, red lines: retrieved time trace (dashed lines indicate fluctuation).

The lower graphs in fig. 7.15a and b show the measured DTT (black squares) and the signals arising from the convolution of the retrieved distribution (a: Wiener deconvolution, b: iterative algorithm) with the response function (red, solid: $\tau_r = 600$ fs, dashed: $\tau_r = 600 \pm 300$ fs). Within the deviation of the data points, the DTT assigned to the recovered distributions fit well for both reconstruction algorithms. In order to acquire a more accurate fit, a better SNR of the original data would be necessary.

The retrieved distribution is a scale for the fluorophore concentration in each layer. The difference in the concentration peak amplitude assigned to the first (a_1) and the second (a_2) compartment is attributed to the absorption of the excitation pulse, which was not taken into account in the deconvolution algorithm. The average pulse attenuation per compartment amounts to approximately 12 % (appendix H). Hence the ratio of the amplitudes was estimated to amount to $R_c = a_1/a_2 = 1.14$. For reconstructing the distribution using the "Wiener" deconvolution it is, however, $R_c \approx 2$. For the iterative algorithm, on the other hand, it amounts to $R_c = 1.25$ %.

Due to the better retrieval of the signal amplitudes, the iterative method is considered to be the superior deconvolution method. Deducing the axial resolution (i.e. Δt_{min}) that can be achieved by the presented reconstruction algorithms requires further experiments, because it is not clear how very close vicinal extended fluorophore distributions will affect the reconstruction. As a first estimate, the distance between the signals at which the amplitude falls below the noise level can be taken. This amounts to $\Delta z_{min} \approx 70 \mu\text{m}$. This is smaller than the resolution given in subsect. 7.4.2, because the derivative was not necessary to calculate. The derivative greatly reduces the SNR and thus the resolution. A better signal-to-noise ratio should also improve the data reconstruction due to a smaller regularization parameters.

Chapter 8

Summary

Measuring the propagation time difference of the light emitted from different deep layers in a system ("time-of-flight" method, ToF) in order to investigate the axial distribution of fluorophores on the 10 μm scale requires an ultrafast gating technique with about 100 fs time resolution. Particularly its anticipated application as a diagnostic tool for three dimensional functional retina examination poses tremendous demands on the optical gating technique (chapt. 1).

For such an application all optical Kerr gating (OKG) has been identified as most suitable. It combines a high temporal resolution, the possibility of single photon gating over a broad spectral range and stability with respect to signal perturbations by scattering. Particularly the latter can be critical for competing interferometric techniques.

In order to identify the most suited OKG material, different material classes were investigated in terms of their optical properties and OKG performance. As representatives for low nonlinear refractive index materials, fused silica and novel $\text{SiO}_2\text{-Al}_2\text{O}_3$ -glasses (SAL-glass) were examined. Tellurite glass, heavy flint glass and poly crystalline ZnS were analyzed as materials of large nonlinear refractive index. The materials' gating performances for broad-band OKG were investigated by switching a super continuum pulse and a signal pulse at $\lambda_S = 530$ nm using a gate pulse at $\lambda_G = 800$ nm.

The band gap energies of the investigated OKG materials were estimated from absorption coefficients using a Tauc plot. They were found to generally be smaller than the values expected from common theoretical models [222, 224]. This was attributed to the low absorption region used for fitting.

The correlation between the linear and nonlinear refractive indices of SAL glass was found to fit well in the theoretical framework given by Boling et al. (BGO theory). The large values of n and n_2 were ascribed to an increasing content of La^{3+} ions, increasing oxygen (hyper)polarizability and increasing amount of non-bridging oxygen at increasing La_2O_3 content. An upper limit for the hyperpolarizability of the $\text{La}_{2/3}\text{O}$ molecule was found to be $\gamma_{max} = 2.2 \pm 0.2 \times 10^{-36}$ esu.

Due to the dispersion related temporal walk-off between the gate pulse and the signal an optimum OKG sample thickness d_{eff} was found for broad-band gating. Using thicker samples causes an increase in the gating duration, but does not enhance the efficiency. For a sample thickness d_{eff} dispersion related broadening of the gate pulse did not have a significant influence onto the gating time. It however affected the gate efficiency due to the reduction of the peak intensity as the gate pulse is broadened. Additionally, the gating efficiency was found to be potentially reduced by gate pulse induced single photon absorption of the signal (CMPA).

SAL-glass showed the largest OKG efficiency $\eta_{max} > 65\%$ at an intensity $I_{G,max} \approx 650 \text{ GW/cm}^2$. In comparison the high index materials exhibited a superior gating performance at low gate intensities. However, their maximum efficiency was found to be significantly smaller than that of SAL-glass and decreasing with increasing n_2 value.

The superior gating performance of SAL-glass at moderately high intensities was attributed to its large band gap energy ($E_{Gap} > 5.3 \text{ eV}$) in combination with its relatively large nonlinear refractive index ($n_2 = 9.1 \times 10^{-7} \text{ GW/cm}^2$). The large E_{Gap} prevented CMPA in the SAL glass, which in contrast was found to be critical for large n_2 materials (small E_{Gap}).

A novel "Figure of Merit" (FOM) was deduced from the findings, taking into account both, the OKG sample thickness limitation due to the temporal walk-off and the signal attenuation by gate pulse induced absorption (CMPA). The new FOM quantitatively confirmed the superiority of SAL-glass for moderately high gate pulse intensities and of high nonlinear refractive index materials for low gate pulse intensities, respectively.

Besides performing a comprehensive OKG material study, a well suited imaging optics system for the emission was designed, consisting of two off-axis parabolic mirrors. It was shown to image a white light continuum without temporal distortions caused by dispersion.

The optimized OKG setup enabled the investigation of stacked emitter systems. The axial distribution of the emitters (in units of propagation time) and their temporal response were found to be linked by a convolution. This allowed to analyze the ToF time trace in analogy to methods known from microscopy. A resolution criterion in order to identify distinct layers was deduced from the Sparrow criterion [253] taking into account the signal-to-noise ratio (SNR) of the measurement. A substantial difference to microscopy was, however, the dependence of the system response function on parameters of the investigated sample (emission build-up time τ_r and emission lifetime τ_F).

In order to examine the influence of these parameters, three layered systems were measured using the optimized set-up:

- **Thin layers with fast response:** Using the defined criterion, the resolution for detecting distinct scattering layers was identified to be $\Delta z_{min} = 22 \mu\text{m}$. It was limited mainly by the gating time and the duration of the scattered pulse. A reduction of the resolution due to noise was found to become significant for noise levels $N > 5\%$ of the maximum signal amplitude. The accuracy of detecting the distance between two well distinct layers amounted to $\Delta\Delta z = \pm 2 \mu\text{m}$. This was rationalized by the larger number of data points, hence larger accuracy, when fitting two distinct signals, compared to the case of two very close peaks.
- **Thin layers with complex temporal response:** Thin distinct layers of cadmium sulfide (CdS) nanostructures acted as a test system. Their strong and fast emission signal enabled the spectrally resolved detection of the gated signal. Their complex spectral temporal response allowed to comprehensively study the influence of the emission build-up time and the emission lifetime onto the spatial resolution.

The accuracy of measuring the distance between two layers was determined by fitting the signal build-up. It amounted to $\Delta\Delta z = \pm 2 \mu\text{m}$. This was comparable to the results from the distinct scattering layers. In the presence of a long emission lifetime, the signal from deeper layers was superposed by background signals from more shallow layers. This had to be taken into account when fitting the build-up. The accuracy of the distance measurement was found to be insensitive to uncertainties of the background.

In order to estimate the depth resolution in the presence of a complex temporal behavior it was shown that the developed resolution criterion can be applied onto the derivative of the detected time trace. The resolution ranged from $\Delta z_{min} = 26 \mu\text{m}$ to $\Delta z_{min} = 40 \mu\text{m}$ and depended on the emission build-up time. It was found to be strongly affected by the low SNR of the signal derivative. However, a simulation showed that the temporal resolution should become independent of the emission build-up characteristics for large SNR values of the measured time traces' derivative. This of course is limited by the dynamics of the detection system.

- **Thick layers with complex temporal response:** A spatially extended fluorophore distribution (Coumarin153 in ethanol) exhibiting a long emission lifetime of $\tau_F = 5 \text{ ns}$ was investigated. Based on the knowledge of the fluorophore distribution the emission build-up time could be estimated to amount to $\tau_r = 600 \pm 150 \text{ fs}$. By exploiting the previously developed resolution criterion, the axial resolution for the thick layer measurements was found to amount to $\Delta z_{min} = 130 \mu\text{m}$ and to be strongly affected by the poor SNR of the signal derivative.

With the knowledge of τ_r the retrieval of the broad fluorophore distribution based on methods known from optical microscopy was fathomed. A direct regularized deconvolution method ("Wiener" deconvolution) and an iterative algorithm, based on a random optimization approach were compared. Both methods were found to work comparably well in reconstructing the spatial distribution of the fluorophore system even at large variations (up to 50 %) of the emission build-up time. Regarding the reconstruction of the local fluorophore concentration, the iterative algorithm showed superior results.

Although not being combined with single photon detection yet, no evidence indicating a limitation to a minimum signal power was found. Substantially, the technique is limited to a signal power that ensures the emission of photons within the gating time.

Using the CdS nanostructures as test sample for the OKG setup did not only proof the capability to discriminate thin distinct layers, but also revealed novel insight in the physical mechanisms of this nanostructure system upon fs laser excitation at fluences between $F = 0.33 \text{ mJ/cm}^2$ and $F = 3.5 \text{ mJ/cm}^2$. Due to the delayed onset and the short emission lifetime, the observed luminescence is attributed to stimulated emission. It is, however, not clear if it is amplified spontaneous emission or collective lasing. The spectral emission of the CdS nanostructures showed a blue shift on the 0 ps – 1 ps time scale and a red shift on the 1 ps – 10 ps time scale. The spectral shifts were found to be more pronounced at large excitation fluences. They are attributed to a complex interplay between band gap renormalization (red shift) and band filling processes (blue shift) in the CdS nanostructures.

Chapter 9

Conclusion and outlook

The successful broad-band detection of an axial fluorophore distribution by measuring the light propagation time using an optical Kerr gate (OKG) was shown for the first time in this work. Employing this method, a spatial resolution of $\Delta z = 26 \mu\text{m}$ was achieved, which is sufficient to resolve individual retinal layers. Hence the present work paves the way to further develop the ToF method in combination with OKG towards three dimensional functional *in vivo* diagnostics of the human retina.

For the design of the OKG care has to be taken in the selection and the design of the Kerr sample in order to satisfy the tremendous demands on the gate (chapt. 1). The novel $\text{SiO}_2\text{-Al}_2\text{O}_3\text{-La}_2\text{O}_3$ -glass (SAL-glass) offers the opportunity to tailor the gating material by optimizing the ratio between SiO_2 and La_2O_3 contents. This allows to maximize the nonlinear phase modulation at a given intensity on the one hand and to minimize nonlinear counter processes (e.g. nonlinear absorption) on the other hand.

The large gating efficiency of SAL-glass as OKG material at moderate gate pulse intensities enables the application of commercially available femtosecond laser oscillators for gating at repetition rates $f_{rep} = 5 \text{ MHz}$ [288]. As an example, scanning a three dimensional image of $100 \times 100 \times 50$ pixels (1000 averages per pixel) would only take 100 s. This is still an adequate detection time even for *in vivo* diagnostics. Utilizing high refractive index materials even allows the use of oscillators that work at $f_{rep} = 80 \text{ MHz}$ [289] at the expense of gating efficiency.

Highly efficient gating using fs laser oscillators requires, however, strong focusing of the gate and signal beams down to spot radii of $w_0 \approx 30 \mu\text{m}$. This prohibits efficient gating of wide field images.

The axial resolution of the analyzed method is higher than that of confocal microscopy at a small numerical aperture of $NA < 0.1$. Compared to self-interference of fluorescence microscopy (SIFM), on the other hand, the resolution of the current ToF system is presently smaller. Improving the SNR should, however, lead to a spatial resolution which exceeds the one of SIFM. This can be achieved by optimizing several aspects of the measurement system:

- **Repetition rate of the laser system:** Further optimization of the gating material allows the use of femtosecond laser oscillators (repetition rate $f_{rep} \gg 1 \text{ MHz}$) rather than amplified systems ($f_{rep} = 1 \text{ kHz}$). Consequently, averaging over several thousand pulses without significant prolongation of the experimental time becomes possible.
- **Detection method:** In addition to its high efficiency at high pulse repetition rates, the lock-in technique can further be improved by modulating both, the

gate and the fluorescence excitation pulse trains. A SNR up to 10^5 was shown by applying this method [290].

Additionally, the background due to fluorescence light leaking through the polarizers can be reduced by applying very fast electronic detectors that reach a temporal resolution down to 20 ps and still enable single photon counting [17, 28].

- **Improved sampling:** Due to the parallelism of the presented ToF method to optical microscopy the common sampling rules defined e.g. for laser scanning microscopy [291, 292] may be transferred to optimize the ToF signal recording in order to reduce the noise and the detection time.
- **Imaging system:** Although the designed imaging system presented in this work is very well suited for imaging of the broad-band fluorescence light without significant temporal or spatial distortions, it can be improved by rotating one mirror about 90° . This would reduce the still existing astigmatism, hence enabling tighter focusing and thus a larger gate efficiency [101].

Besides the SNR, the gate and the fluorescence excitation pulse durations are the limiting factors for improving the axial resolution. Consequently, using shorter pulses will significantly improve the resolution. Since the temporal walk-off ultimately limits the maximum OKG sample thickness at a given time resolution shorter pulses (at a fixed intensity) will automatically lead to a reduction in the gating efficiency (eq. (6.14)). Although the possibility of acquiring sub 10 fs time resolution using pulses as long as 1 ps by ptychographic technologies was shown [293] these methods cannot be applied for ultrafast fluorescence detection, since coherent light is necessary.

Using gate pulses at longer wavelengths seems to be a promising idea. Thereby the gate pulse assisted single photon absorption (CMPA), which was identified to be the limiting factor in applying high refractive index materials as OKG material, could be reduced.

Finally, further work is necessary, in order to optimize the method for retrieving the fluorophore distribution from the measured time trace. Due to its analogy, known and well developed methods should be adapted from microscopy. Since the emission build-up time is mostly completely unknown it seems promising to employ methods, which are based on blind reconstruction approaches [294].

List of abbreviations and symbols

Abbreviations

AMD	Age related macular degeneration
ASE	Amplified spontaneous emission
BGR	Bandgap renormalization
BGO	Theory from N. Boling, A. Glass, and A. Owyong
BME	Burnstein-Moss effect
CB	Conduction band
CdS	Cadmium sulfide
CFM	Confocal microscopy
CMPA	Combined multi-photon absorption
DTT	Delay time dependent time trace
EHP	Electron-hole plasma
FAD	Flavin adenine dinucleotide
FCA	Free carrier absorption
FLIM	Fluorescence lifetime imaging
FMN	Flavin mononucleotide
FOM	Figure of merit
LIDAR	Light detection and ranging
NA	Numerical aperture
NADH	Hydrogenated nicotinamide adenine dinucleotide
OAPM	Off-axis parabolic mirror
OCT	Optical coherence tomography
OKG	Optical Kerr gating
OPA	Optical parametric amplification / amplifier
PA	Permanent absorption
PD	Photo darkening
PIS	Polarization integrated DTT
PSS	Polarization selective DTT
RIM	Refractive index mismatch
SAL-Glass	SiO ₂ -Al ₂ O ₃ -La ₂ O ₃ glass
SFG	Sum frequency generation
SIFM	Self interference of fluorescence microscopy
SNR	Signal-to-noise ratio
STRET	Spectrally and temporally resolved energy transmission
TA	Transient absorption
TBR	Transmission-to-background ratio
Te-glass	Tellurite glass
ToF	Time-of-flight (method)
VB	Valence band
VIS	Visible spectral range
WLC	White light continuum

Greek symbols

α	Absorption coefficient
α_k	Nonlinear absorption coefficient (order k)
α_m	Molar polarizability
α_{PD}	Absorption coefficient related to photo-darkening
α_{Th}	Thermal expansion coefficient
γ	Hyperpolarizability
Δn	Refractive index mismatch
ΔT_{PV}	Peak-to-Valley ratio for the z-scan measurements
$\Delta\tau_{cc}$	Cross correlation width (FWHM)
$\Delta\tau_{eff}$	Width of the system function $sys(t_D)$ (FWHM)
$\Delta\tau_{Fit}$	Broadening parameter of the dispersion model function
$\Delta\tau_G$	Gate pulse width (FWHM)
$\Delta\tau_{OKG}$	OKG width (FWHM)
$\Delta\tau_P$	Pulse width (FWHM)
$\Delta\tau_S$	Signal pulse width (FWHM)
$\Delta\omega, \Delta\lambda$	Spectral bandwidth (in units of frequency or wavelength)
$\Delta z, \Delta t$	Distance between two peaks (in units of space, or time) for layer resolution (G indicates geometrical path, min indicates minimum)
δ	Deviation between fitted and computed curve for modeling of dispersion broadening
$\delta z, \delta t$	Peak width/duration (in units of space or time) for layer resolution
η	OKG efficiency (maximum OKG transmission)
η_{eff}	Effective system efficiency
η_F	Fluorescence quantum yield
η_w	Spot width related efficiency
ϵ	Molar decadic extinction coefficient
λ	Wavelength
λ_c	Centroid wavelength
λ_{em}	Emission wavelength
λ_{ex}	Excitation wavelength
ν_d	Abbe number
τ_F	Emission life time
τ_r	Emission build-up time (thermalization time)
τ_{GVD}	Characteristic walk-off time between signal and gate pulse
τ_{Fit}	Fitted emission build-up time
ϕ_{NL}	Phase of the signal imprinted by the gate pulse
$\chi^{(i)}$	Electric susceptibility (order i)
ω_g	Cut-off frequency for low pass filter

Latin symbols

$A_i, \widetilde{A}_i, B_i, C_i$	Sellmeier coefficients
a_i	Signal amplitude referring to layer i (\propto Emitter concentration of layer i)
$a(t'(z))$	Emitter distribution function
d	Material thickness
d_{eff}	Interaction distance between signal and gate pulses in the material
d_{sf}	Self-focusing distance
\mathcal{E}_0	Pulse energy
$E(t)$	Emitter excitation pulse function
E_{Gap}	Band gap energy
E_{Ph}	Photon energy
E_U	Urbach energy
F	Pulse energy fluence
f	Local-field correction factor ($= (n_0^2 + 2)/3$)
$G(t)$	Gate function
I_G	Gate pulse (peak) intensity
I_S	Signal intensity
k''	Group velocity dispersion
L_D	Dispersion length
L_{NL}	Nonlinear interaction length
M_m	Molar mass
n_0, n	Linear refractive index
n_2	Nonlinear refractive index referring to the intensity in SI units (cm^2/GW)
n_2^F	Nonlinear refractive index referring to the electric field in cgs units (esu)
n_g	Linear group refractive index
N	Noise level
N_m	Number density of molecules
P_{cr}	Critical power for self-focusing
$R(t)$	Temporal response function of the emitters
R_c	Emitter density ratio of two layers
R_F	Reflection coefficient
$r(t_D)$	Response function for emission ($= (E \otimes G \otimes R)(t_D)$)
r_ϵ	Extinction ratio of the polarizers
t_0	Onset time of the emission
$t_{0,fit}$	Fitted emission onset time
t_D	Delay time between signal and gate pulse
T	Transmission
T_g	Glass transition temperature
s	Background arising from signals of other layers
$S_F(t)$	Power of the emission
$sys(t_D)$	System function for emission excitation ($= (E \otimes G)(t_D)$)
V_m	Molar volume
w	$1/e^2$ spot radius
z_r	Rayleigh length

Fields

\vec{E}	Electric field
\vec{P}	Polarization field
\vec{D}	Electric displacement field

Fundamental physical constant

ϵ_0	Vacuum permittivity ($\approx 8.854 \times 10^{-12}$ As/Vm)
c	Speed of light (= 0.299792458 $\mu\text{m}/\text{fs}$)
\hbar	Planck constant ($\approx 6.582 \times 10^{-16}$ eVs)
N_A	Avogadro constant ($\approx 6.022 \times 10^{23}$ mol ⁻¹)

Appendix A

In this appendix a detailed analysis of the OKG process is described.

The electric field of the linearly polarized signal is given by:

$$\vec{E}_S(x, y, t) = \frac{E_0}{\sqrt{2}} f(x, y) g(t) \begin{pmatrix} e^{-i\phi_x} \\ e^{-i\phi_y} \end{pmatrix} + c.c., \quad (\text{A.1})$$

where $f(x, y)$ is the spatial (lateral) component and $g(t)$ the temporal component. Their maximum amplitudes are normalized to 1. The last factor describes the phase of the signal for the lateral components.

The signal intensity is given by:

$$I_S(x, y, t) = I_{S,0} I_{S,r}(x, y) I_{S,t}(t) = c\epsilon_0 \left\langle \left| \vec{E}_S \right|^2 \right\rangle_t = 2c\epsilon_0 E_0^2 f^2(x, y) g^2(t), \quad (\text{A.2})$$

with c being the vacuum speed of light and ϵ_0 the vacuum permittivity. Note that $I_{S,r}(x, y) = f^2(x, y)$ and $I_{S,t} = g^2(t)$

In the presence of a strong (linearly polarized) gate field the phase term in eq. (A.1) will be modulated by a nonlinear component:

$$\begin{pmatrix} e^{-i\phi_x} \\ e^{-i\phi_y} \end{pmatrix} = \begin{pmatrix} \cos \alpha e^{-ik_0 n_0 z} e^{-i\phi_{nl}(x,y,t)} \\ \sin \alpha e^{-ik_0 n_0 z} \end{pmatrix}, \quad (\text{A.3})$$

where α is the angle between the gate and the signal field polarization. $k_0 = 2\pi/\lambda_S$ is the wave vector of the signal field (in vacuum) and n_0 is the linear refractive index. ϕ_{nl} is the imprinted phase modulation by the gate field as both fields travel through the OKG material.

Behind the OKG material the signal field passes an analyzer that blocks the non-modulated field, since it is rotated about 90° with respect to the polarization of the incident signal.

In case of the nonlinear modulation of the signal phase the electric field behind the analyzer is given by:

$$\begin{aligned} \vec{E}_{out}(x, y, t) &= \hat{J} \vec{E}_S \\ &= \frac{E_0}{\sqrt{2}} f(x, y) g(t) \begin{pmatrix} + \cos \alpha e^{ik_0 d + \phi_{nl}(x,y,t)} - \sin \alpha e^{ik_0 d + \phi_{nl}(x,y,t)} \\ - \cos \alpha e^{ik_0 d + \phi_{nl}(x,y,t)} + \sin \alpha e^{ik_0 d + \phi_{nl}(x,y,t)} \end{pmatrix} + c.c., \end{aligned} \quad (\text{A.4})$$

with \hat{J} being the Jones matrix, which describes the analyzer:

$$\hat{J} = \frac{1}{2} \begin{bmatrix} 1 & -1 \\ -1 & 1 \end{bmatrix} \quad (\text{A.5})$$

Assuming an angle between the polarization of the signal and the gate fields of $\alpha = 45^\circ$, the signal field intensity behind the analyzer is:

$$\begin{aligned} I_{out} &= c\epsilon_0 \left\langle \left| \vec{E}_{out} \right|^2 \right\rangle_t \\ &= c\epsilon_0 E_0^2 f^2(x, y) g^2(t) (1 - \cos(\phi_{nl}(x, y, t))) = \frac{I_S}{2} (1 - \cos(\phi_{nl}(x, y, t))) \end{aligned} \quad (\text{A.6})$$

Evidently, the above derivation is in the signal's temporal frame of reference. If the gate field can variably be delayed with respect to the signal, it is worth to introduce the variable delay as separate coordinate t_D . A detector behind the analyzer measures the energy. This can be calculated by integrating the intensity (assuming spatially cylindrical symmetry):

$$\mathcal{E}(t_D) = \pi \int_{-\infty}^{+\infty} \int_0^{+\infty} I_S(r, t) r (1 - \cos \phi_{nl}(r, t - t_D)) dr dt, \quad (\text{A.7})$$

Assuming $\phi_{nl}(r, t - t_D) = \phi_{nl,r}(r) \phi_{nl,t}(t - t_D)$ (which is adequate particularly for Gaussian pulses) and developing the \cos function results in:

$$\begin{aligned} \mathcal{E}(t_D) &= \pi \int_{-\infty}^{+\infty} \int_0^{+\infty} I_S(r, t) r \left(\sum_{j=1}^{\infty} (-1)^{j-1} \frac{\phi_{nl}^{2j}(r, t - t_D)}{(2j)!} \right) dr dt \\ &= \pi \sum_{j=1}^{\infty} \frac{(-1)^{j-1}}{(2j)!} I_{S,0} \int_0^{+\infty} I_{S,r}(r) r \phi_{nl,r}^{2j}(r) dr \int_{-\infty}^{+\infty} I_{S,t}(t) \phi_{nl,t}^{2j}(t) dt \end{aligned} \quad (\text{A.8})$$

Assuming a Gaussian spot shape for the gate and the signal pulses, $\phi_{nl,r}(r)$ and $I_{S,r}(r)$ are given by:

$$\begin{aligned} \phi_{nl,r}(r) &= \phi_{nl,0} e^{-2(r/w_G)^2} \\ I_{S,r}(r) &= e^{-2(r/w_S)^2}, \end{aligned}$$

with w_G and w_S being the $1/e^2$ radii of the gate pulse and the signal (intensity), respectively. It is pointed out that no prefactor is necessary for $I_{S,r}(r)$, since it is already normalized. Consequently, the transmitted energy is given by:

$$\begin{aligned} \mathcal{E}(t_D) &= \pi \sum_{j=1}^{\infty} \frac{(-1)^{j-1}}{2j} I_{S,0} \int_{-\infty}^{+\infty} I_{S,t}(t) \phi_{nl,t}^{2j}(t) dt \int_0^{+\infty} r e^{-(4j/w_G^2 + 2/w_S^2)r^2} dr \\ &= \pi \sum_{j=1}^{\infty} \frac{(-1)^{j-1}}{2j} I_{S,0} \int_{-\infty}^{+\infty} I_{S,t}(t) \phi_{nl,t}^{2j}(t) dt \frac{w_G^2 w_S^2}{8j w_S^2 + 4w_G^2} \end{aligned} \quad (\text{A.9})$$

Hence for the weak gate pulse approximation (i.e. the $j = 1$ term of the sum only), the transmitted energy as a function of the spot widths is given by:

$$\mathcal{E}(w_S, w_G) = A \frac{w_S^2}{1 + 2 \frac{w_S^2}{w_G^2}}, \quad (\text{A.10})$$

with A containing the constants and the temporal characteristics of the transmitted signal energy \mathcal{E} . It is pointed out that the presented derivation requires that the spatial and the temporal components of ϕ_{nl} and I_S can be separated. This is true for Gaussian shaped collimated beams (Signal and Gate). In case of a large divergence within the sample this is, however, not eligible anymore.

Appendix B

In this appendix the computation of the "Transmission-to-Background" ratio TBR of the OKG is elucidated. For simplicity a rectangularly shaped gate function with an efficiency η and a time duration $\Delta\tau_G$ as well an exponential signal function, possessing a decay constant τ_F and a maximum amplitude P_{0S} is assumed (fig. B.1).

The energy of the fluorescence signal is given by:

$$E_F = \int_0^{\infty} P_{Sig}(t)dt = P_{0S}\tau_F \quad (\text{B.1})$$

At a given polarizer extinction r_ϵ , the background of the detected signal can be estimated by:

$$B = r_\epsilon P_{0S}\tau_F. \quad (\text{B.2})$$

Gating the signal at time t_0 leads to a transmission that can be estimated by:

$$T(t_0) = \eta \int_{t_0}^{t_0+\Delta\tau_G} P_{Sig}(t)dt = \eta\tau_F P_{0S} \left(e^{-\frac{t_0+\Delta\tau_G}{\tau_F}} - e^{-\frac{t_0}{\tau_F}} \right) \approx \eta P_{0S}\Delta\tau_G = \eta E_F \frac{\Delta\tau_G}{\tau_F}. \quad (\text{B.3})$$

The last two terms in (B.3) are a good approximation, if the signal is gated around its onset time.

Finally the TBR can be defined as:

$$\frac{T}{B} = \frac{\eta\Delta\tau_G}{r_\epsilon\tau_F}. \quad (\text{B.4})$$

Besides the TBR of the gated signal, the transmitted energy may be of great interest as well. The expected value generally will be very small. Therefore it is expressed as number of transmitted photons n :

$$n = \frac{1.57\eta_{eff}F_{ex}w_0^2\lambda_S\Delta\tau_G}{hc\tau_F}, \quad (\text{B.5})$$

where F_{ex} is the excitation fluence of the signal, η_{eff} the effective efficiency of the system (the product of the gating efficiency, the transmission of the imaging system and the quantum efficiency of the fluorescence), λ_S the signal wavelength, w_0 the spot

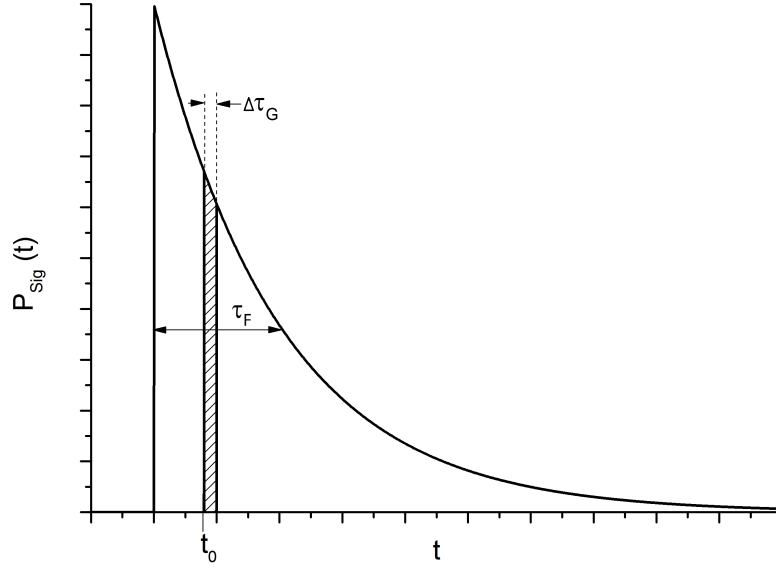


Fig. B.1: Scheme for estimating the signal background of a Kerr gate

diameter of the signal excitation, h the Planck constant, c the vacuum speed of light, $\Delta\tau_G$ the gate pulse duration and τ_F the signal decay time constant, respectively.

It is pointed out that for a more realistic approach it is adequate to take the emission build-up time into account as presented in eq. (3.16). The maximum signal is achieved at

$$t_{max} = \frac{\tau_F \tau_r \ln(\tau_F / \tau_r)}{\tau_F - \tau_r}, \quad (\text{B.6})$$

with τ_r being the emission build-up time, respectively. The maximum gated signal can be estimated by:

$$T_{max} = P_{0,S} \eta \int_0^{\infty} (e^{-t/\tau_F} - e^{-t/\tau_r}) e^{-2(2\sqrt{\ln 2}(t-t_{max})/\Delta\tau_G)^2} dt \quad (\text{B.7})$$

This leads to a maximum of gated photons given by:

$$\begin{aligned} n_{max} = & \frac{1.57 \eta_{eff} F_{ex} w_0^2 \lambda_S}{hc \tau_F} \frac{\sqrt{\pi} \Delta\tau_G}{4\sqrt{2 \ln 2}} \left[e^{\frac{\Delta\tau_G^2 (1 - 4\tau_F t_{max} 8 \ln 2 / \Delta\tau_G^2)}{32 \ln 2 \tau_F^2}} \right. \\ & \times \operatorname{erf} \left(\frac{\Delta\tau_G (16 \ln 2 \frac{\tau_F t_{max}}{\Delta\tau_G^2} + 1)}{4\sqrt{2 \ln 2} \tau_F} + 1 \right) - e^{\frac{\Delta\tau_G^2 (1 - 4\tau_r t_{max} 8 \ln 2 / \Delta\tau_G^2)}{32 \ln 2 \tau_r^2}} \\ & \left. \times \operatorname{erf} \left(\frac{\Delta\tau_G (16 \ln 2 \frac{\tau_r t_{max}}{\Delta\tau_G^2} + 1)}{4\sqrt{2 \ln 2} \tau_r} + 1 \right) \right] \quad (\text{B.8}) \end{aligned}$$

Appendix C

In this appendix the simulation results for the imaging system using "Zemax Op-
ticStudio" are shown in fig. C.1. The imaging properties of three fields emitted by
an object (position of the fluorophore) into planes close to the focal plane (position
of the Kerr gate) were simulated: one centered at the optical axis (F1: $x = 0 \mu\text{m}$, $y = 0 \mu\text{m}$), the other placed off-axis (F2: $x = -80 \mu\text{m}$, $y = 0 \mu\text{m}$), (F3: $x = 0 \mu\text{m}$, $y = -80 \mu\text{m}$) and (F4: $x = -80 \mu\text{m}$, $y = -80 \mu\text{m}$). The positive direction of the plane
means the image or the object is moved away from the respective mirror. The focal
shift is observed. Hence care has to be taken in the proper selection of the OKG
material thickness.

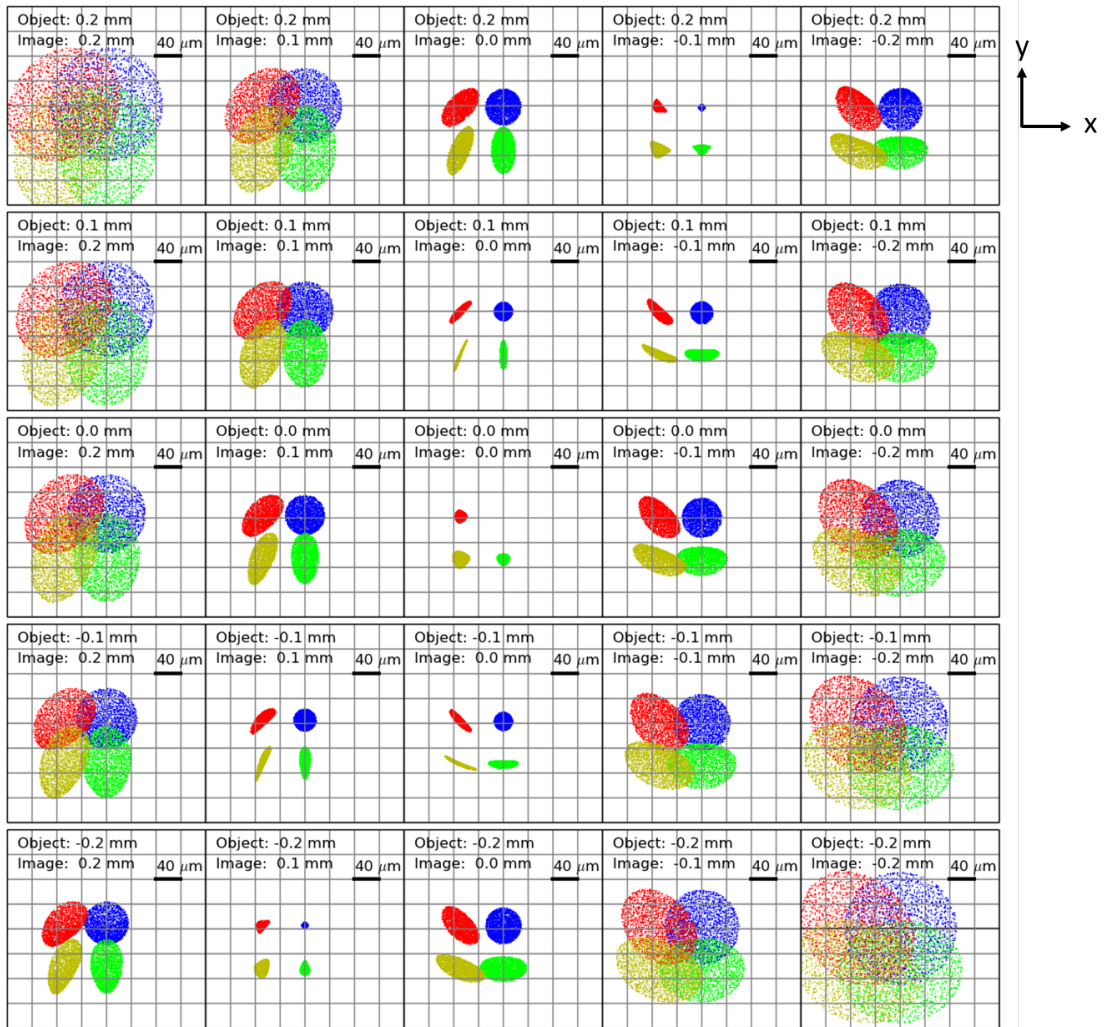


Fig. C.1: simulated imaging properties for the fields F1 (blue), F2 (red), F3 (green) and F4 (yellow): rows: object plane fixed, image plane moving, columns: object plane moving, image plane fixed, positive direction: image or object moved away from the respective mirror

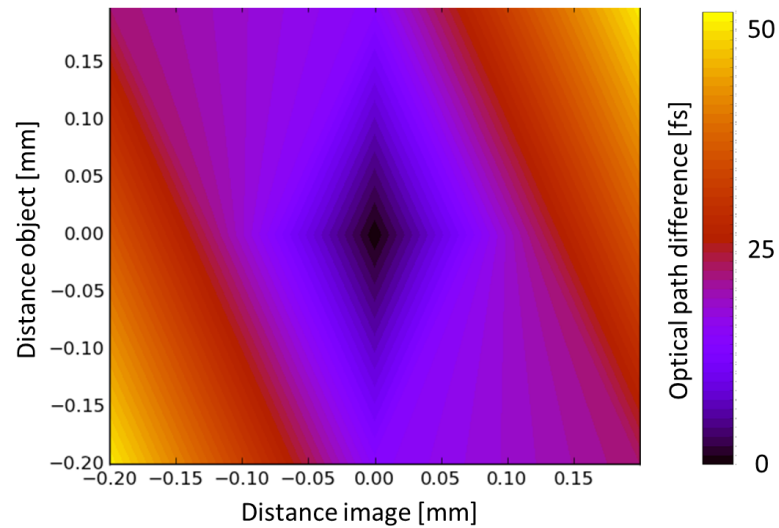


Fig. C.2: maximum optical path difference OPD (F1, in the sagittal plane, $NA = 0.2$) as a function of the object and the image distances.

Additionally the maximum optical path difference (OPD) between the center of each field and the outer part (numerical aperture $NA = 0.2$) was calculated. As a representative the correlation for F1 (sagittal plane) is shown in fig. C.2. The correlations for the other fields and the tangential planes are comparable. The OPD is not exceeding 50 fs.

Appendix D

The influence of the angle between the signal and the gate beams onto the temporal resolution of a Kerr gating experiment is analyzed by using a simple geometrical approach. Assuming a Gaussian shaped gate pulse, with a $1/e^2$ spot radius w_G and a *FWHM* pulse duration $\Delta\tau_G$, the effective pulse duration of this gate pulse with respect to a signal pulse with a propagation direction tilted about an angle α with respect to the propagation direction of the gate pulse is given by (fig. D.1):

$$\Delta\tau_G^* = \Delta\tau_G \cos \alpha + \frac{\sqrt{2 \ln 2} w_G}{c_0} \sin \alpha \approx \Delta\tau_G + \alpha \frac{\sqrt{2 \ln 2} w_G}{c_0}, \quad (\text{D.1})$$

where c_0 is the speed of light. If α is sufficiently small, the effective pulse duration $\Delta\tau_G^*$ can be considered to be composed of the original pulse duration $\Delta\tau_G$ and an additional part from the radial component. In case of a gate pulse with a spot radius of $w_G = 44 \mu\text{m}$ and an angle $\alpha = 2^\circ$, $\Delta\tau_G^*$ amounts to approximately $\Delta\tau_G + 6 \text{ fs}$.

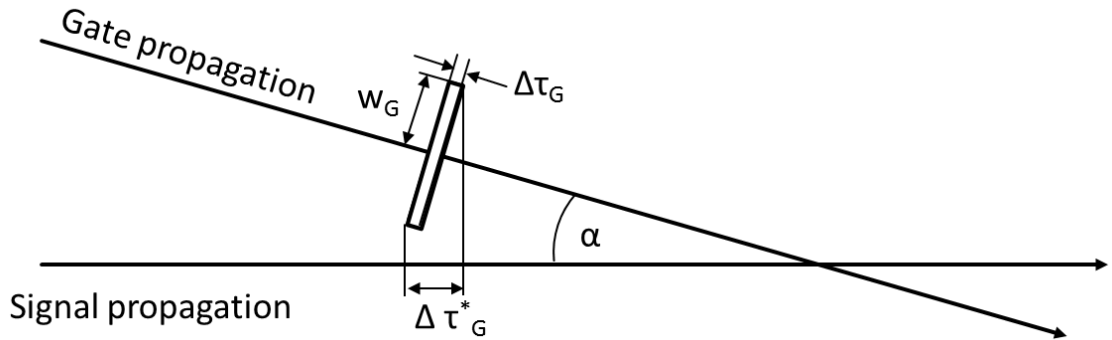


Fig. D.1: Schematic elucidation of the composition of $\Delta\tau_G^*$

Appendix E

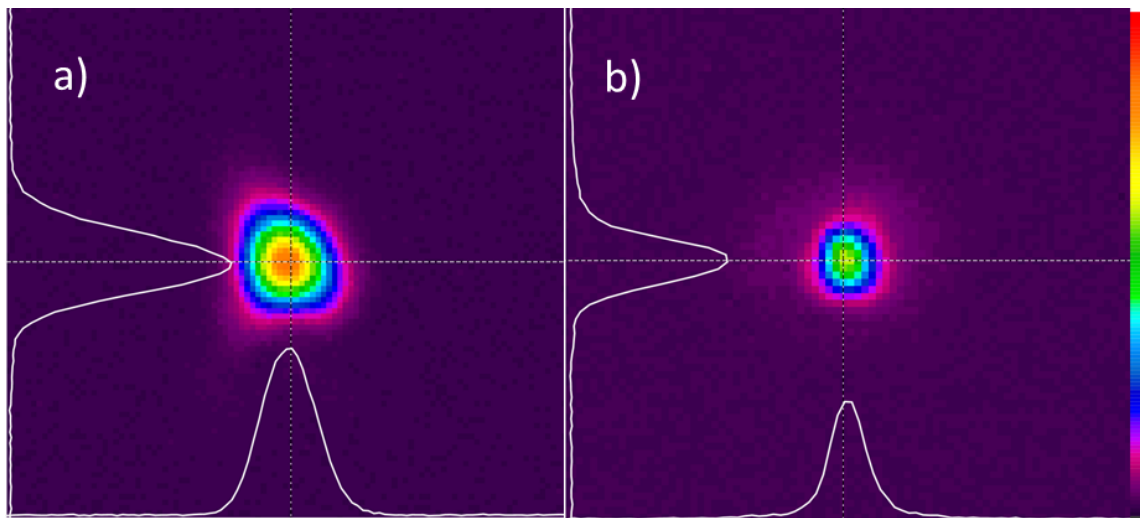


Fig. E.1: CCD images of the spots in the focal plane of the two-color OKG experiment: a: Gate beam ($\lambda_G = 800$ nm), b: a: Signal beam ($\lambda_S = 530$ nm), cf. fig. 5.4 for spot sizes

Appendix F

The fitting procedure that was applied in order to acquire the combined multiphoton absorption coefficients in subsect. 6.5.2 is explained.

Linear absorption of the signal beam (e.g. due to photo-darkening) and combined multiphotonabsorption (CMPA, assuming a very weak signal pulse that only experiences single photon absorption) depend on the gate pulse intensity. The transmitted signal intensity is given by (eq. (3.11)):

$$I_S = I_0 e^{-(\alpha_{PD}d + \alpha_k I_G^{k-1} d_{eff})(1-R_P)}, \quad (\text{F.1})$$

where α_{PD} is a generally unknown function of the gate pulse intensity I_G . It describes the absorption coefficient, related to the photo-darkening. α_k is the absorption coefficient related to CMPA. k represents the order of the CMPA ($k = 2$: one gate and one signal photon absorption, $k = 3$: two gate and one signal photon absorption).

The signal beam transmission is given by (eq.(3.12)):

$$T(t_D) = \frac{\int_{-\infty}^{\infty} \int_{-\infty}^{\infty} I_S(t, t_D, r) dr dt}{\mathcal{E}_0}, \quad (\text{F.2})$$

with \mathcal{E}_0 being the signal pulse energy.

For the numerical data analysis two Gaussian pulses (gate and signal) were assumed, propagating collinearly with the pulse parameters given in tab. 5.1. In case of Te-glass and N-SF56, where significant photo-darkening was observed, the signal transmission for the permanent absorption (empty symbols in fig. 6.14b) was fitted using the empirical function

$$\alpha_{PD} = aI_G^2 + bI_G + c \quad (\text{F.3})$$

and computing the transmitted pulse energy by numerical integration (in space and time). The CMPA was set to be zero in this case ($\alpha_k = 0$). a , b and c were the fitting parameters.

Subsequently, the CMPA coefficient was determined by fitting the transient absorption (filled symbols in fig. 6.14b), using the previously determined $\alpha_{PD}(I_G)$ values. The effective interaction lengths as defined by eq. (6.14) in subsect. 6.3.2 was used to determine the interaction distance for the CMPA (eq. (F.1)).

The integral $T(t_D)$ was again solved numerically. α_k was the fitting parameter. The error of α_k resulted from varying the used parameters in (3.11) within their error margins (spot widths, pulse durations, fitting parameters from (F.3))

Appendix G

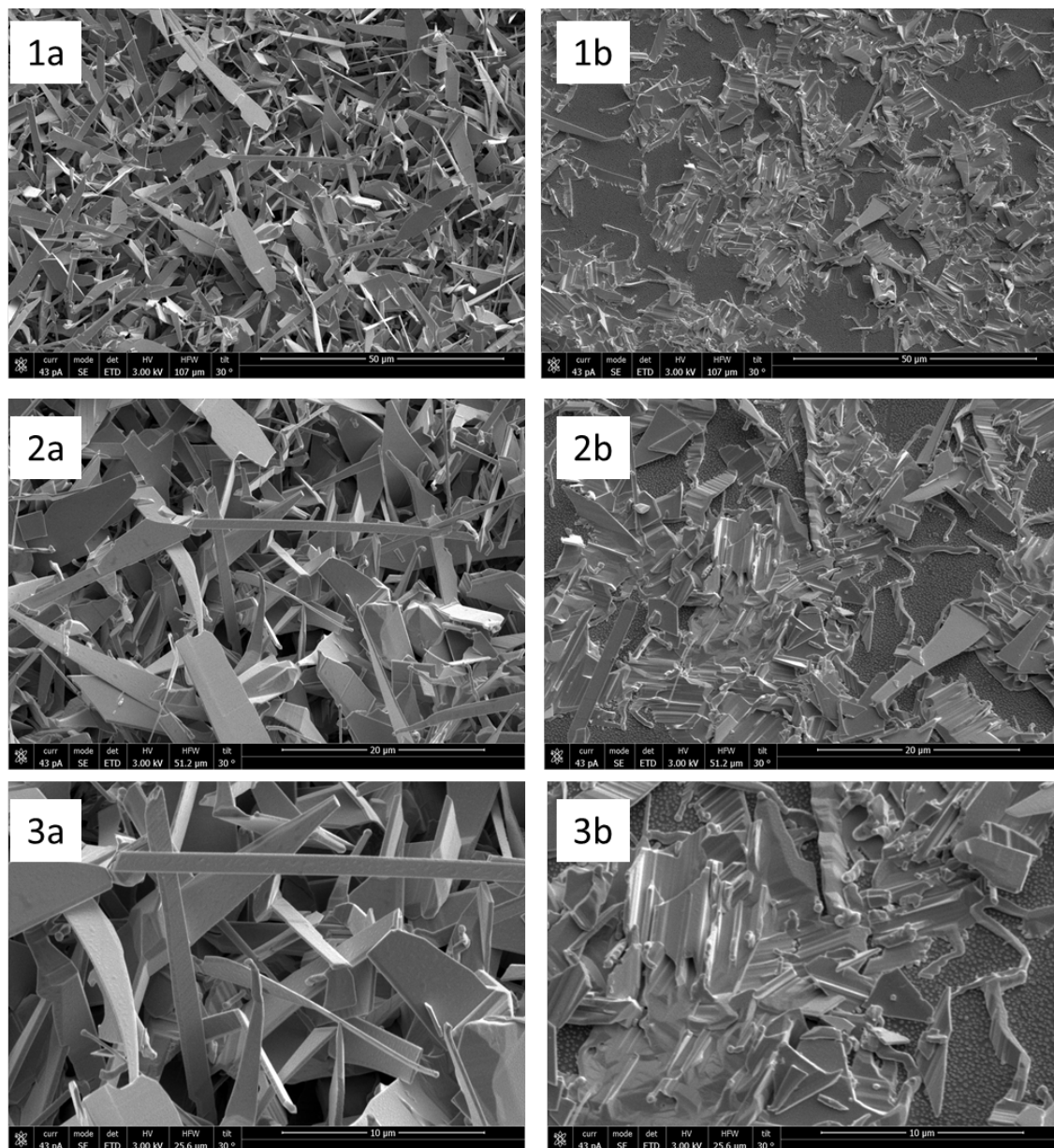


Fig. G.1: Scanning electron microscopic images of the CdS ensemble grown on a silicon substrate recorded at different magnifications (1, 2, 3) and at different positions on the sample (a, b)

Figure G.1 shows scanning electron microscopic images of the CdS nanowire ensemble on the silicon substrate for different magnifications (1,2,3) and at different areas of the sample (a, b). The density of the CdS nanostructures in fig. G.1a

is much larger than in G.1b. The ensemble measurements in the present work were performed at a position of high particle density. The CdS particle density of the imprints is considered to be comparable to that in fig G.1b. The electron microscopic images were provided by R. Röder ("Institut für Festkörperphysik", Friedrich-Schiller-Universität, Jena).

Appendix H

In this appendix the simulation of the delay time dependent trace DTT for the double cuvette filled with Coumarin 153 dissolved in ethanol is described. The geometrical relations are shown in fig. H.1. d^G is the geometrical thickness of the compartments and z is the optical path. The dye compartments are located between $z_1 = 0 \mu\text{m}$ and $z_2 = 109 \mu\text{m}$ as well as between $z_3 = 290 \mu\text{m}$ and $z_4 = 398 \mu\text{m}$. These refer to propagation times t'_1 to t'_4 (sect. 7.1, eq. (7.1)). For the compartments a constant fluorophore concentration is assumed. In the glass spacer the fluorescence concentration is $a(z) = 0$ (fig. H.1). Hence the distribution function describing the fluorophore concentration (sect. 7.1) in units of time is:

$$a = \begin{cases} 0 & t' < t'_1 \\ a_1 & t'_1 < t' < t'_2 \\ 0 & t'_2 < t' < t'_3 \\ a_2 & t'_3 < t' < t'_4 \\ 0 & t'_4 < t' \end{cases} \quad (\text{H.1})$$

with a_1 and a_2 representing the fluorophore concentrations in the respective compartments. The temporal response of the fluorophore located at a position $z_O \hat{=} t'$ (fig. 7.1) is modeled by (eq. (3.16), assuming an infinitely long fluorescence lifetime τ_F):

$$R(t) = \left[1 - e^{-(t-t')/\tau_r} \right] \Theta(t - t'), \quad (\text{H.2})$$

where $\Theta(t - t')$ is the Heaviside step function.

When propagating through a compartment the excitation pulse is attenuated by absorption, which is characterized by an absorption coefficient $\alpha_z^G = \ln 10 \epsilon c_{C153}$. ϵ is the molar decadic extinction coefficient. In units of time t' the absorption is $\alpha_t = \epsilon c_{C153} \ln 10 \frac{c}{2n}$. c_{C153} is the molar concentration. The parameters affecting the excitation beam absorption amount to:

- $\epsilon = 1.5 \times 10^{-4} \text{ l}\cdot\text{mole}^{-1}\text{cm}^{-1}$ [295]
- $c_{C153} = 1 \times 10^{-3} \text{ mole/l}$.

Fresnel reflections at the fluorophore-glass interfaces are negligible due to the small difference in the refractive index.

On the base of the response function $R(t)$, the fluorophore distribution ($a(t)$) and

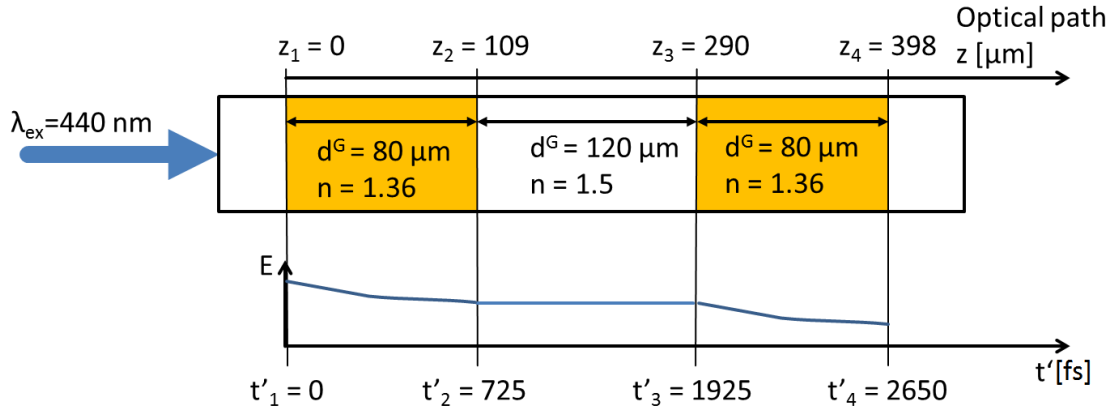


Fig. H.1: Design of the double compartment cuvette. The spatial coordinate z : optical path. d^G : geometrical thickness of the compartments, n : refractive indices, E is the energy of the excitation pulse as a function of z (or t')

the absorption characterized by α_t , the expected fluorescence signal as a function of time from the double compartment cuvette can be modeled:

$$\begin{aligned}
 S_F(t) = a_0 \int_{t'_1}^{t'_2} e^{-\alpha_t t'} \left(1 - e^{-(t-t')/\tau}\right) \Theta(t-t') dt' \\
 + a_0 \int_{t'_3}^{t'_4} e^{-\alpha_t (t'-t'_3+t'_2)} \left(1 - e^{-(t-t')/\tau}\right) \Theta(t-t') dt'.
 \end{aligned} \tag{H.3}$$

Consequently, the signal detected by the OKG system will be

$$sigt_D = (sys \otimes S_F)(t_D). \tag{H.4}$$

sys is the Gaussian shaped system function (sect. 7.1) with a FWHM duration of $\Delta\tau_{eff} = 150$ fs.

Appendix I

In this appendix the different methods for retrieving the continuous distribution of emitters out of a given signal are elucidated. As explained in the text the measured signal is a convolution of the distribution and the response function of the emitter.

$$S_F(t) = \int (a(t')R(t-t'))dt' = (a \otimes R)(t) \quad (\text{I.1})$$

Particularly in the presence of noise the deconvolution, hence the retrieval of a is not straightforward. One option that was investigated in the present work is the application of the "Wiener" deconvolution.

In this case the distribution a can be estimated by:

$$\hat{a}(t) \approx \mathcal{F}^{-1} \left\{ \frac{\mathcal{S}(\omega)}{\mathcal{R}(\omega)} \left[\frac{|\mathcal{R}(\omega)|^2}{|\mathcal{R}(\omega)|^2 + \epsilon(\omega)} \right] \right\}. \quad (\text{I.2})$$

The calligraphic letters indicate the fourier transform of the respective variable. \mathcal{F}^{-1} indicates the inverse Fourier transform. ϵ is a regularization parameter. It can be estimated by the inverse signal-to-noise ratio $\epsilon = 1/SNR$. Although ϵ is generally a function of the frequency ω it is considered to be constant in the present case. Thus white noise is assumed. The python code, used to compute the Wiener deconvolution is displayed below.

```
def wiener_decon(data,resp, epsilon):
    DAT = np.fft.fft(data);
    RES = np.fft.fft(resp);
    dist = np.fft.ifft(DAT/RES*(np.absolute(RES)**2/
                                (np.absolute(RES)**2+epsilon)))
    return(np.real(dist))
```

A different approach that was used in this work was to fit the distribution directly by an iterative algorithm. An initial distribution was guessed. It was chosen to be an equipartition. Its magnitude amounted to the average of the measured data points. Subsequently a random point out of the distribution was varied randomly (maximum variation about 0.5 %). The squared distances between the measured data and the signals arising from the old and the varied distribution were compared. If the squared distance of the varied distribution was smaller than the one of the old distribution the variation was retained. Otherwise it was discarded. The python source code of the algorithm is depicted below.

```
def evo_algorithm(t, data, resp, max_gen):
```

```

#initial distribution
dist = data*0+np.sum(data)/np.size(data);
generation = np.arange(0,max_gen,1)

#calculate the signal of the distribution
old_data = create_result(dist, resp)

#squared distance between estimated and original data
abweichung_old = np.sum((old_data-data)**2);

for i in generation:
    # random value for mutation
    mut = np.random.rand(np.size(data))-0.5

    # grab arbitrary point in the distribution
    index = np.random.randint(0,np.size(dist));

    #mutate point
    mut = mut*0.005*dist[index]+dist;

    #the new distribution must not contain negative values
    mut = mut*(mut>0);

    #compute new signal
    new_data = create_result(mut, resp)

    #compute squared distance between new signal and original data
    abweichung_new = np.sum((new_data-data)**2);

    #keep mutated point if the new signal is a better estimate
    if abweichung_new < abweichung_old:
        dist = mut;
        abweichung_old = abweichung_new;
        old_data = new_data;
return dist

```

Although the retrieved distribution of this algorithm delivers fairly noisy signals it is quite stable with respect to inaccuracies of the thermalization constant τ_r and noise (fig. I.1). As a test a thermalization constant of $\tau_r = 500$ fs was chosen. The response function was a convolution of a Gaussian (FWHM: $\Delta\tau_{eff} = 150$ fs) and the fluorescence build-up function (eq. (7.5), $\tau_r = 500$ fs). The signal was created by convolving the original distribution and the response function and normalizing it to one. In case of the noisy signal, normally distributed random values with a variance of 0.1 were added to the normalized signal.

For the retrieval test, τ_r of the assumed response function was varied between 200 fs and 800 fs. The retrieved distributions were smoothed by a low pass filter ($f_g = 2.5 \times 10^{-3}$ fs $^{-1}$).

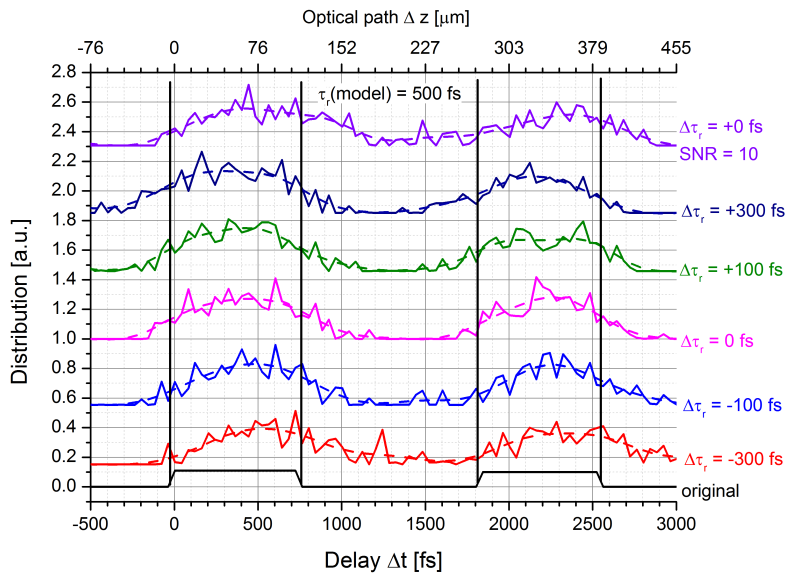


Fig. I.1: Original (black) and retrieved distributions of a test function using the evolutionary algorithm. The thermalization constant of the response function for the algorithm was varied.

Bibliography

- [1] World health organization. Global report on diabetes. <http://www.who.int/diabetes/global-report/en/>. Accessed: 2016-04-14.
- [2] R. D. Jager, W. F. Mieler, and J. W. Miller. Age-Related Macular Degeneration. *N. Engl. J. Med.*, 358(24):2606–2617, 2008.
- [3] E. A. Ellis, B. M. Grant, F. T Murray, M. B. Wachowski, D. L. Guberski, B. S. Kubilis, and G. A. Luty. Increased NADH oxidase activity in the retina of the BBZ/Wor diabetic rat. *Free Radic Biol. Med.*, 24(1):111–120, 1998.
- [4] V. L. Bonilha. Age and disease-related structural changes in the retinal pigment epithelium. *Clin. Ophthalmol.*, 2(2):413–424, 2008.
- [5] A. Mayevsky and G. G. Rogattsky. Mitochondrial function in vivo evaluated by NADH fluorescence: from animal models to human studies. *Am. J. Physiol. Cell Physiol.*, 292(2):C615–C640, 2007.
- [6] M. Hammer, D. Schweitzer, L. Leistritz, M. Scibor, K.-H. Donnerhacke, and J. Strobel. Imaging spectroscopy of the human ocular fundus in vivo. *J. Biomed. Opt.*, 2(4):418–425, 1997.
- [7] M. Hammer, E. Königsdörffer, C. Liebermann, C. Framme, G. Schuch, D. Schweitzer, and J. Strobel. Ocular fundus auto-fluorescence observations at different wavelengths in patients with age-related macular degeneration and diabetic retinopathy. *Graefes Arch. Clin. Exp. Ophthalmol.*, 246(1):105–114, 2008.
- [8] D. Schweitzer, E. R. Gaillard, J. Dillon, R. F. Mullins, S. Russel, B. Hoffmann, S. Peters, M. Hammer, and C. Biskup. Time-Resolved Autofluorescence Imaging of Human Donor Retina Tissue from Donors with Significant Extramacular Drusen. *Invest. Ophthalmol. Vis. Sci.*, 53(7):3376–3386, 2012.
- [9] D. Schweitzer, M. Hammer, F. Schweitzer, R. Anders, T. Doebbecke, S. Schenke, and E. R. Gaillard. In vivo measurement of time-resolved autofluorescence at the human fundus. *J. Biomed. Opt.*, 9(6):1214–22, 2004.
- [10] D. Schweitzer, M. Hammer, and E. R. Gaillard. Comparison of Autofluorescence Lifetimes: In vivo Measurements at the Fundus versus Co-enzymes and Metabolic By-products. *Invest. Ophthalmol. Vis. Sci.*, 44(13):3615–3615, 2003.

- [11] J. R. Lakowicz, H. Szmajcinski, N. Kazimierz, and M. L. Johnson. Fluorescence lifetime imaging of free and protein-bound NADH. *Proc. Natl. Acad. Sci. U. S. A.*, 89(4):1271–1275, 1992.
- [12] M. C. Skala, K. M. Riching, A. Gendron-Fitzpatrick, J. Eickhoff, K. W. Eliceiri, J. G. White, and N. Ramanujam. In vivo multiphoton microscopy of NADH and FAD redox states, fluorescence lifetimes, and cellular morphology in precancerous epithelia. *Proc. Natl. Acad. Sci. U S A*, 104(49):19494–9, 2007.
- [13] J. Blackwell, K. M. Katika, L. Pilon, K. M. Dipple, S. R. Levin, and A. Nouvong. In vivo time-resolved autofluorescence measurements to test for glycation of human skin. *J. Biomed. Opt.*, 13(1):014004, 2008.
- [14] Innovative Optische Messtechnik GmbH. Documentation No. 5: Fluorescence spectrum of NADH measured with LF401Lambda. www.iom-berlin.de/pdfs/Documentation_5_NADH_spectrum.pdf. Accessed: 2016-04-11.
- [15] WEBVISION The Organization of the Retina and Visual System. <http://webvision.med.utah.edu/>. Accessed: 2016-04-14.
- [16] M. G. O. Gräfe, A. Hoffmann, and C. Spielmann. Ultrafast fluorescence spectroscopy for axial resolution of fluorophore distributions. *Appl. Phys. B*, 117(3):833–840, 2014.
- [17] W. Becker. *The bh TCSPC Handbook*. Becker & Hickl GmbH, Berlin, 4th edition, 2010.
- [18] B. Schmidt, S. Laimgruber, W. Zinth, and P. Gilch. A broadband Kerr shutter for femtosecond fluorescence spectroscopy. *Appl. Phys. B*, 76(8):809–814, 2003.
- [19] M. Cobcroft, T. Vaccaro, and J. Mitrofanis. Distinct patterns of distribution among NADPH-diaphorase neurones of the guinea pig retina. *Neurosci. Lett.*, 103(1):1–7, 1989.
- [20] S. Darius, G. Wolf, P. L. Huang, and M. C. Fishman. Localization of NADPH-diaphorase/nitric oxide synthase in the rat retina: an electron microscopic study. *Brain Research*, 690(2):231–235, 1995.
- [21] C. Weikamp. *Lidar - range-resolved optical remote sensing of the atmosphere*. Springer, New York, 2005.
- [22] F. Takashi. *Laser remote sensing*. CRC Press / Taylor & Francis, Boca Raton, 2005.
- [23] G. Cox and C. J. Sheppard. Practical limits of resolution in confocal and nonlinear microscopy. *Microsc. Res. Tech.*, 63(1):18–22, 2004.
- [24] G. Cox. *Optical Imaging Techniques in Cell Biology*. CRC Press / Taylor & Francis Group, Boca Raton, 2012.

- [25] S. Wilhelm, B. Gröbler, M. Gluch, and H. Heinz. Die konfokale Laser Scanning Mikroskopie. http://www.cai.hhu.de/fileadmin/redaktion/Fakultaeten/Mathematisch-Naturwissenschaftliche_Fakultaet/CAI/Literatur/Die_konfokale_Laser_Scanning_Mikroskopie.pdf. Accessed: 2016-04-14.
- [26] W. Drexler, U. Morgner, R. K. Ghanta, F. X. Kärtner, J. S. Schuman, and J. G. Fujimoto. Ultrahigh-resolution ophthalmic optical coherence tomography. *Nat. Med.*, 7(4):502–507, 2001.
- [27] M. de Groot, C. L. Evans, and J. F. de Boer. Self-interference fluorescence microscopy: three dimensional fluorescence imaging without depth scanning. *Opt. Express*, 20(14):15253–15262, 2012.
- [28] J. Toussaint, S. Dochow, I. Latka, A. Lukic, T. May, H. G. Meyer, K. Il'in, M. Siegel, and J. Popp. Proof of concept of fiber dispersed Raman spectroscopy using superconducting nanowire single-photon detectors. *Opt. Express*, 23(4):5078–5090, 2015.
- [29] Hamamatsu. Guide to streak cameras. http://www.hamamatsu.com/resources/pdf/sys/SHSS0006E_STREAK.pdf. Accessed: 2016-04-11.
- [30] E. Hillinger. *Optisches Schalten mit Elektroabsorptionsmodulatoren*. PhD thesis, Technische Universität Berlin, 2003.
- [31] M. Mero, A. J. Sabbah, J. Zeller, and W. Rudolph. Femtosecond dynamics of dielectric films in the pre-ablation regime. *Appl. Phys. A*, 81(2):317–324, 2005.
- [32] J. Zeller, A. J. Sabbah, M. Mero, P. M. Alsing, J. McIver, and W. Rudolph. Femtosecond dynamics of highly excited dielectric thin films. In *Proc. SPIE: Laser-Induced Damage in Optical Materials: 2003*, volume 5273, pages 515–526, 2003.
- [33] U. Keller, K. J. Weingarten, F. X. Kärtner, D. Kopf, B. Braun, I. D. Jung, R. Fluck, C. Hönniger, N. Matuschek, and J. Aus der Au. Semiconductor Saturable Absorber Mirrors (SESAM's) for Femtosecond to Nanosecond Pulse Generation in Solid-State Lasers. *IEEE J. Sel. Top. Quantum Electron.*, 2(3):435–453, 1996.
- [34] M. A. M. Versteegh and J. I. Dijkhuis. Ultrafast all-optical shutter based on two-photon absorption. *Opt. Lett.*, 36(15):2776–2778, 2011.
- [35] Q. Gong, X. Y. Hu, H. Yang, and S. Wang. Ultrafast organic nonlinear optical molecules and the realization of mesoscopic photonic devices. *Chin. Sci. Bull.*, 55(20):2111–2117, 2010.
- [36] H. Ju, S. Zhang, D. Lenstra, H. de Waardt, E. Tangdiongga, G. Khoe, and H. Dorren. SOA-based all-optical switch with subpicosecond full recovery. *Opt. Express*, 13(3):942–947, 2005.

- [37] H. Nakamura, Y. Sugimoto, K. Kanamoto, N. Ikeda, Y. Tanaka, Y. Nakamura, S. Ohkouchi, Y. Watanabe, K. Inoue, H. Ishikawa, and K. Asakawa. Ultra-fast photonic crystal/quantum dot all-optical switch for future photonic networks. *Opt. Express*, 12(26):6606–6614, 2004.
- [38] X. Hu, Y. Zhang, Y. Fu, H. Yang, and Q. Gong. Low-Power and Ultrafast All-Optical Tunable Nanometer-Scale Photonic Metamaterials. *Adv. Mater.*, 23(37):4295–4300, 2011.
- [39] J. D. Musgraves, K. Richardson, and H. Jain. Laser-induced structural modification, its mechanisms, and applications in glassy optical materials. *Opt. Mat. Express*, 1(5):921–935, 2011.
- [40] M. Reichert, H. Hu, M. R. Ferdinandus, M. Seidel, P. Zhao, T. R. Ensley, D. Peceli, J. M. Reed, D. A. Fishman, S. Webster, D. J. Hagan, and E. W. Van Stryland. Temporal, spectral, and polarization dependence of the nonlinear optical response of carbon disulfide. *Optica*, 1(6):436–445, 2014.
- [41] E. Williams, M. J. Soileau, and E. W. Van Stryland. Optical switching and n_2 measurements in CS_2 . *Opt. Commun.*, 50(4):256–260, 1984.
- [42] H. Zhan, Z. Zhou, A. Lin, J. Cheng, L. Yan, J. Si, F. Chen, and X. Hou. Chirp structure measurement of a supercontinuum pulse based on transient lens effect in tellurite glass. *J. Appl. Phys.*, 113(11):113106, 2013.
- [43] T. Xia, D. J. Hagan, M. Sheik-Bahae, and E. W. Van Stryland. Eclipsing Z-scan measurement of $\lambda/10^4$ wave-front distortion. *Opt. Lett.*, 19(5):317–319, 1994.
- [44] A. C. Bhasikuttan, M. Suzuki, S. Nakashima, and T. Okada. Ultrafast Fluorescence Detection in Tris(2,2'-bipyridine)ruthenium(II) Complex in Solution: Relaxation Dynamics Involving Higher Excited States. *J. Am. Chem. Soc.*, 124(28):8398–8405, 2002.
- [45] X.-X. Zhang, C. Würth, L. Zhao, U. Resch-Genger, N. P. Ernsting, and M. Sajadi. Femtosecond broadband fluorescence upconversion spectroscopy: Improved setup and photometric correction. *Rev. Sci. Instrum.*, 82:063108, 2011.
- [46] C. H. Kim and T. Joo. Ultrafast time-resolved fluorescence by two photon absorption excitation. *Opt. Express*, 16(25):20742–20747, 2008.
- [47] P. Fita, Y. Stepanenko, and C. Radzewicz. Femtosecond transient fluorescence spectrometer based on parametric amplification. *Appl. Phys. Lett.*, 86(2):021909, 2005.
- [48] X. Han, X. Chen, Y. Weng, and J. Zhang. Ultrasensitive femtosecond time-resolved fluorescence spectroscopy for relaxation processes by using parametric amplification. *J. Opt. Soc. Am. B*, 24(7):1633–1638, 2007.
- [49] D. F. Underwood, T. Kippeny, and S. J. Rosenthal. Ultrafast Carrier Dynamics in CdSe Nanocrystals Determined by Femtosecond Fluorescence Upconversion Spectroscopy. *J. Phys. Chem. B*, 105(2):436–443, 2000.

- [50] J. Xu and J. R. Knutson. Ultrafast Fluorescence Spectroscopy via Upconversion: Applications to Biophysics. *Methods Enzymol.*, 450:159–183, 2008.
- [51] J.-C. Diels and W. Rudolph. *Ultrashort Laser Pulse Phenomena Fundamentals, Techniques, and Applications on a Femtosecond Time Scale*. Elsevier, Amsterdam, 2nd edition, 1996.
- [52] M. A. Duguay and J. W. Hansen. An ultrafast light gate. *Appl. Phys. Lett.*, 15(6):192–194, 1969.
- [53] E. P. Ippen and C. V. Shank. Picosecond response of a high - repetition - rate CS₂ optical Kerr gate. *Appl. Phys. Lett.*, 26(3):92–93, 1975.
- [54] E. P. Ippen, C. V. Shank, and A. Bergman. Picosecond recovery dynamics of malachite green. *Chem. Phys. Lett.*, 38(3):611–614, 1976.
- [55] E. P. Ippen, C. V. Shank, and R. L. Woerner. Picosecond dynamics of azulene. *Chem. Phys. Lett.*, 46(1):20–23, 1977.
- [56] Y. Kanematsu, H. Ozawa, I. Tanaka, and S. Kinoshita. Femtosecond optical Kerr-gate measurement of fluorescence spectra of dye solutions. *JOL*, 87-89(0):917–919, 2000.
- [57] R. Nakamura, N. Hamada, H. Ichida, F. Tokunaga, and Y. Kanematsu. Double-gated spectral snapshots for biomolecular fluorescence. *JOL*, 122-123(0):297–300, 2007.
- [58] S. Arzhantsev and M. Maroncelli. Design and Characterization of a Femtosecond Fluorescence Spectrometer Based on Optical Kerr Gating. *Appl. Spectrosc.*, 59(2):206–220, 2005.
- [59] S. Kinoshita, H. Ozawa, Y. Kanematsu, I. Tanaka, N. Sugimoto, and S. Fujiwara. Efficient optical Kerr shutter for femtosecond time-resolved luminescence spectroscopy. *Rev. Sci. Instrum.*, 71(9):3317–3322, 2000.
- [60] H. Zhang, Z. Zhou, A. Lin, J. Cheng, H. Liu, J. Si, F. Chen, and X. Hou. Efficient optical Kerr gate of tellurite glass for acquiring ultrafast fluorescence. *J. Opt. A*, 14(6):065201, 2012.
- [61] S. P. Laptinok, P. Nuernberger, A. Lukacs, and M. H. Vos. *Fluorescence Spectroscopy and Microscopy: Methods and Protocols, Methods in Molecular Biology*, volume 1076, chapter 13 Subpicosecond Kerr-Gate Spectrofluorometry. Springer, New York, 2014.
- [62] L. Gundlach and P. Piotrowiak. Ultrafast Spatially Resolved Carrier Dynamics in Single CdSSe Nanobelts. *J. Phys. Chem. C*, 113(28):12162–12166, 2009.
- [63] J. Blake, J. Nieto-Pescador, Z. Li, and L. Gundlach. Ultraviolet femtosecond kerr-gated wide-field fluorescence microscopy. *Opt. Lett.*, doc. ID 260480, posted 22 April 2016, in press.

- [64] D. J. Kane and R. Trebino. Characterization of arbitrary femtosecond pulses using frequency-resolved optical gating. *IEEE J. Quant. Electron.*, 29(2):571–579, 1993.
- [65] J. Tong, W. Tan, J. Si, F. Chen, W. Yi, and X. Hou. High Time-Resolved Imaging of Targets in Turbid Media Using Ultrafast Optical Kerr Gate. *Chin. Phys. Lett.*, 29(2):024207, 2012.
- [66] L. M. Wang, P. P. Ho, and R. R. Alfano. Double-stage picosecond Kerr gate for ballistic time-gated optical imaging in turbid media. *Appl. Opt.*, 32(4):535–540, 1993.
- [67] L. Wang, P. P. Ho, C. Liu, G. Zhang, and R. R. Alfano. Ballistic 2-D Imaging Through Scattering Walls Using an Ultrafast Optical Kerr Gate. *Science*, 253(5021):769–771, 1991.
- [68] W. Tan, Z. Zhou, A. Lin, J. Si, J. Tong, and X. Hou. Femtosecond nonlinear optical property of a $\text{TeO}_2\text{-ZnO-Na}_2\text{O}$ glass and its application in time-resolved three-dimensional imaging. *Opt. Commun.*, 291:337–340, 2013.
- [69] W. Tan, Z. Zhou, A. Lin, J. Tong, J. Si, and X. Hou. Instantaneous three-dimensional imaging using supercontinuum and ultrafast optical Kerr gate of tellurite glass. *Opt. Eng.*, 53(4):043108, 2014.
- [70] T. Yasui, K. Minoshima, and H. Matsumoto. Three-dimensional shape measurement of a diffusing surface by use of a femtosecond amplifying optical Kerr gate. *Appl. Opt.*, 39(1):65–71, 2000.
- [71] D. R. Symes, U. Wegner, H. C. Ahlswede, M. J. V. Streeter, P. L. Gallegos, E. J. Divall, R. A. Smith, P. P. Rajeev, and D. Neely. Ultrafast gated imaging of laser produced plasmas using the optical Kerr effect. *Appl. Phys. Lett.*, 96(1):011109, 2010.
- [72] S. K. Sahoo, S. Umaphathy, and A. W. Parker. Time-Resolved Resonance Raman Spectroscopy: Exploring Reactive Intermediates. *Appl. Spectrosc.*, 65(10):1087–1115, 2011.
- [73] I. Johansson, B. Zachhuber, M. Nordberg, and H. Östmark. Rejection of fluorescence from Raman spectra of explosives by picosecond optical Kerr gating. In *Proc. SPIE: Chemical, Biological, Radiological, Nuclear, and Explosives (CBRNE) Sensing XIV*, volume 8710, pages 87100R–8, 2013.
- [74] P. Matousek, M. Towrie, and A. W. Parker. Fluorescence background suppression in Raman spectroscopy using combined Kerr gated and shifted excitation Raman difference techniques. *J. Raman Spectrosc.*, 33(4):238–242, 2002.
- [75] M. D. Morris, P. Matousek, M. Towrie, A. W. Parker, A. E. Goodship, and E. R. C. Draper. Kerr-gated time-resolved Raman spectroscopy of equine cortical bone tissue. *J. Biomed. Opt.*, 10(1):014014–014017, 2005.

- [76] M. C. H. Prieto, P. Matousek, M. Towrie, A. W. Parker, M. Wright, A. W. Ritchie, and N. Stone. Use of picosecond Kerr-gated Raman spectroscopy to suppress signals from both surface and deep layers in bladder and prostate tissue. *J. Biomed. Opt.*, 10(4):044006, 2005.
- [77] R. Baker, P. Matousek, K. L. Ronayne, A. W. Parker, K. Rogers, and N. Stone. Depth profiling of calcifications in breast tissue using picosecond Kerr-gated Raman spectroscopy. *Analyst*, 132(1):48–53, 2007.
- [78] N. Stone, R. Baker, M. H. C. Prieto, and P. Matousek. Novel Raman signal recovery from deeply buried tissue components. In *Proc. SPIE: Biomedical Optical Spectroscopy*, volume 6853, 2008. 0N-15.
- [79] G. Jonusauskas, J. Oberlé, E. Abraham, and C. Rullière. "Fast" amplifying optical Kerr gate using stimulated emission of organic non-linear dyes. *Opt. Commun.*, 137(1-3):199–206, 1997.
- [80] D. Meschede. *Optics, Light and Lasers. The Practical Approach to Modern Aspects of Photonics and Laser Physics*. Wiley-VCH, Weinheim, 2007.
- [81] R. W. Boyd. *Nonlinear Optics*. Academic Press, Amsterdam, 2008.
- [82] G. Ghosh. Sellmeier coefficients and dispersion of thermo-optic coefficients for some optical glasses. *Appl. Opt.*, 36(7):1540–1546, 1997.
- [83] B. Tatian. Fitting refractive-index data with the Sellmeier dispersion formula. *Appl. Opt.*, 23(24):4477–4485, 1984.
- [84] Vitron Spezialwerkstoffe GmbH. VITRON CVD Zinc Sulfid. <http://www.vitron.de/datasheets/VITRON%20CVD%20ZnS%20Datenblatt%20Jan%202015.pdf>. Accessed: 2016-04-11.
- [85] R. Paschotta. *Encyclopedia of Laser Physics and Technology*. Wiley-VCH, Weinheim, 2008.
- [86] R. L. Sutherland. *Handbook of nonlinear optics*. Marcel Dekker, Inc., New York, Basel, Hong Kong, 1996.
- [87] H. Fritzsche. Optical anisotropies in chalcogenide glasses induced by band-gap light. *Phys. Rev. B*, 52(22):15854–15861, 1995.
- [88] A. Zakery and S. R. Elliott. Optical properties and applications of chalcogenide glasses: a review. *J. Non-Cryst. Solids*, 330(1-3):1–12, 2003.
- [89] S. R. Elliott and V. K. Tikhomirov. Vectorial and scalar photoinduced effects in chalcogenide glasses. *J. Non-Cryst. Solids*, 198:669–674, 1996.
- [90] J. A. Duffy. Polarisability and polarising power of rare earth ions in glass: an optical basicity assessment. *Phys. Chem. Glasses: Eur. J. Glass Sci. Technol. B.*, 46(1):1–6, 2005.
- [91] R. Adair, L. L. Chase, and S. A. Payne. Nonlinear refractive index of optical crystals. *Phys. Rev. B*, 39(5):3337–3350, 1989.

- [92] F. Urbach. The Long-Wavelength Edge of Photographic Sensitivity and of the Electronic Absorption of Solids. *Phys. Rev.*, 92(5):1324–1324, 1953.
- [93] B. E. Sernelius. Intraband relaxation time in highly excited semiconductors. *Phys. Rev. B.*, 43(9):7136–7137, 1991.
- [94] C. F. Klingshirn. *Semiconductor Optics*. Springer, Berlin, 3rd edition, 2007.
- [95] C. Klingshirn and H. Haug. Optical Properties of Highly Excited Direct Gap Semiconductors. *Phys. Rep.*, 70(5):315–398, 1981.
- [96] H. Fujisaki and J. E. Straub. Vibrational energy relaxation in proteins. *Proc. Natl. Acad. Sci. U. S. A.*, 102(19):6726–6731, 2005.
- [97] K. Rurack and M. Spielers. Fluorescence Quantum Yields of a Series of Red and Near-Infrared Dyes Emitting at 600-1000 nm. *Anal. Chem.*, 83(4):1232–1242, 2011.
- [98] T. S. Blacker, Z. F. Mann, J. E. Gale, M. Ziegler, A. J. Bain, G. Szabadkai, and M. R. Duchon. Separating NADH and NADPH fluorescence in live cells and tissues using FLIM. *Nat. Commun.*, 5:3936, 2014.
- [99] A. Baici, R. Joppich-Kuhn, P. L. Luisi, A. Olomucki, M. O. Monneuse-Doublet, and F. Thome-Beau. Fluorescence Properties of Reduced Thionicotinamide - Adenine Dinucleotide and of Its Complex with Octopine Dehydrogenase. *Eur. J. Biochem.*, 83:601–607, 1978.
- [100] Hamamatsu Photonics K.K. Photomultiplier Tubes Basics and Applications, 3rd edition. https://www.hamamatsu.com/resources/pdf/etd/PMT_handbook_v3aE.pdf. Accessed: 2016-04-11.
- [101] Prof. H. Gross, 2014. Personal communication, Jena.
- [102] K. Schuster, D. Litzkendorf, S. Grimm, J. Kobelke, A. Schwuchow, A. Ludwig, M. Leich, S. Jetschke, J. Dellith, J. L. Auguste, S. Leparmentier, G. Humbert, and G. Werner. Study of lanthanum aluminum silicate glasses for passive and active optical fibers. In *Proc. SPIE: Optical Components and Materials X*, volume 8621, pages 86210Q–12, 2013.
- [103] D. Litzkendorf, S. Grimm, K. Schuster, J. Kobelke, A. Schwuchow, A. Ludwig, J. Kirchhof, M. Leich, S. Jetschke, J. Dellith, J.-L. Auguste, and G. Humbert. Study of Lanthanum Aluminum Silicate Glasses for Passive and Active Optical Fibers. *Int. J. Appl. Glass Sci.*, 3(4):321–331, 2012.
- [104] J. S. Wang, E. M. Vogel, and E. Snitzer. Tellurite glass: a new candidate for fiber devices. *Opt. Mater.*, 3(3):187–203, 1994.
- [105] Heraeus. Quartz Glass for Optics - Data and Properties. http://heraeus-quarzglas.com/media/webmedia_local/downloads/broschren_mo/DataandProperties_Optics_fusedsilica.pdf. Accessed: 2016-04-14.

- [106] Schott AG. N-SF56 Datenblatt.
http://www.schott.com/advanced_optics/german/abbe_datasheets/schott-datasheetinquiryglass-n-sf56.pdf. Accessed: 2016-04-11.
- [107] M. Sheik-Bahae, A. A. Said, and E. W. Van Stryland. High-sensitivity, single-beam n_2 measurements. *Opt. Lett.*, 14(17):955–957, 1989.
- [108] R. E. Bridges, G. L. Fischer, and R. W. Boyd. Z-scan measurement technique for non-Gaussian beams and arbitrary sample thicknesses. *Opt. Lett.*, 20(17):1821–1823, 1995.
- [109] M. Sheik-Bahae, A. A. Said, T. H. Wei, D. J. Hagan, and E. W. Van Stryland. Sensitive measurement of optical nonlinearities using a single beam. *IEEE J. Quant. Electron.*, 26(4):760–769, 1990.
- [110] M. A. de Araújo, R. Silva, E. de Lima, D. P. Pereira, and P. C. de Oliveira. Measurement of Gaussian laser beam radius using the knife-edge technique: improvement on data analysis. *Appl. Opt.*, 48(2):393–396, 2009.
- [111] S. Kedenburg, A. Steinmann, R. Hegenbarth, T. Steinle, and H. Giessen. Nonlinear refractive indices of nonlinear liquids: wavelength dependence and influence of retarded response. *Appl. Phys. B*, 117(3):803–816, 2014.
- [112] R. A. Ganeev, A. I. Ryasnyansky, M. Baba, M. Suzuki, N. Ishizawa, M. Turu, S. Sakakibara, and H. Kuroda. Nonlinear refraction in CS_2 . *Appl. Phys. B*, 78(3):433–438, 2004.
- [113] S. Couris, M. Renard, O. Faucher, B. Lavorel, R. Chaux, E. Koudoumas, and X. Michaut. An experimental investigation of the nonlinear refractive index (n_2) of carbon disulfide and toluene by spectral shearing interferometry and z-scan techniques. *Chem. Phys. Lett.*, 369(3-4):318–324, 2003.
- [114] H. S. Nalwa. Organic Materials for Third-Order Nonlinear Optics. *Adv. Mater.*, 5(5):341–358, 1993.
- [115] W. T. Lotshaw, D. McMorro, C. Kalpouzos, and G. A. Kenney-Wallace. Femtosecond dynamics of the optical Kerr effect in liquid nitrobenzene and chlorobenzene. *Chem. Phys. Lett.*, 136(3-4):323–328, 1987.
- [116] G. Jonusauskas, R. Gadonas, and C. Rulliere. "Fast" optical Kerr gate with "slow" nonlinearity. *Opt. Commun.*, 112(1-2):80–84, 1994.
- [117] S. Wang, W. Huang, R. Liang, Q. Gong, H. Li, H. Chen, and D. Qiang. Enlarged ultrafast optical Kerr response of C_{60} with attached multielectron donors. *Phys. Rev. B*, 63(15):153408, 2001.
- [118] G. P. Agrawal. *Nonlinear Fiber Optics*. Academic Press, Amsterdam, 5th edition, 2013.
- [119] C. Nagura, A. Suda, H. Kawano, M. Obara, and K. Midorikawa. Generation and characterization of ultrafast white-light continuum in condensed media. *Appl. Opt.*, 41(18):3735–3742, 2002.

- [120] E. T. J. Nibbering, M. A. Franco, B. S. Prade, G. Grillon, C. Le Blanc, and A. Mysyrowicz. Measurement of the nonlinear refractive index of transparent materials by spectral analysis after nonlinear propagation. *Opt. Commun.*, 119(5-6):479–484, 1995.
- [121] K. Dota, J. A. Dharmadhikari, D. Mathur, and A. K. Dharmadhikari. Third-order nonlinear optical response in transparent solids using ultrashort laser pulses. *Appl. Phys. B*, 107(3):703–709, 2012.
- [122] M. Grehn, T. Seuthe, W. Tsai, M. Höfner, A. W. Achtstein, A. Mermillod-Blondin, M. Eberstein, H. J. Eichler, and J. Bonse. Nonlinear absorption and refraction of binary and ternary alkaline and alkaline earth silicate glasses. *Opt. Mater. Express*, 3(12):2132–2140, 2013.
- [123] D. Milam. Review and Assessment of Measured Values of the Nonlinear Refractive-Index Coefficient of Fused Silica. *Appl. Opt.*, 37(3):546–550, 1998.
- [124] D. Blömer, A. Szameit, F. Dreisow, T. Schreiber, S. Nolte, and A. Tünnermann. Nonlinear refractive index of fs-laser-written waveguides in fused silica. *Opt. Express*, 14(6):2151–2157, 2006.
- [125] R. Adair, L. L. Chase, and S. A. Payne. Nonlinear refractive-index measurements of glasses using three-wave frequency mixing. *J. Opt. Soc. Am. B*, 4(6):875–881, 1987.
- [126] S. Santran, M. Martinez-Rosas, L. Canioni, L. Sarger, L. N. Glebova, A. Tirpak, and L. B. Glebov. Nonlinear refractive index of photo-thermo-refractive glass. *Opt. Mater.*, 28(4):401–407, 2006.
- [127] D. Milam, M. J. Weber, and A. J. Glass. Nonlinear refractive index of fluoride crystals. *Appl. Phys. Lett.*, 31(12):822–825, 1977.
- [128] V. Dimitrov and S. Sakka. Linear and nonlinear optical properties of simple oxides. II. *J. Appl. Phys.*, 79(3):1741–1745, 1996.
- [129] H. Guo, C. Hou, F. Gao, A. Lin, P. Wang, Z. Zhou, M. Lu, W. Wei, and B. Peng. Third-order nonlinear optical properties of GeS₂-Sb₂S₃-CdS chalcogenide glasses. *Opt. Express*, 18(22):23275–23284, 2010.
- [130] X. F. Wang, Z. W. Wang, J. G. Yu, C. L. Liu, X. J. Zhao, and Q. H. Gong. Large and ultrafast third-order optical nonlinearity of GeS₂-Ga₂S₃-CdS chalcogenide glass. *Chem. Phys. Lett.*, 399(1-3):230–233, 2004.
- [131] T. Wang, X. Gai, W. Wei, R. Wang, Z. Yang, X. Shen, S. Madden, and B. Luther-Davies. Systematic z-scan measurements of the third order nonlinearity of chalcogenide glasses. *Opt. Mater. Express*, 4(5):1011–1022, 2014.
- [132] B. Qiao, F. Chen, Y. Huang, P. Zhang, S. Dai, and Q. Nie. Investigation of mid-infrared optical nonlinearity of Ge₂₀Sn_xSe_{80-x} ternary chalcogenide glasses. *Mater. Lett.*, 162:17–19, 2016.

- [133] M. Asobe, T. Kanamori, and K. Kubodera. Applications of highly nonlinear chalcogenide glass fibers in ultrafast all-optical switches. *IEEE J. Quant. Electron.*, 29(8):2325–2333, 1993.
- [134] H. Kobayashi, H. Kanbara, M. Koga, and K. Kubodera. Third-order nonlinear optical properties of As₂S₃ chalcogenide glass. *J. Appl. Phys.*, 74(6):3683–3687, 1993.
- [135] G. Lenz, J. Zimmermann, T. Katsufuji, M. E. Lines, H. Y. Hwang, S. Spälter, R. E. Slusher, S. W. Cheong, J. S. Sanghera, and I. D. Aggarwal. Large Kerr effect in bulk Se-based chalcogenide glasses. *Opt. Lett.*, 25(4):254–256, 2000.
- [136] G. Dong, H. Tao, S. Chu, S. Wang, X. Zhao, Q. Gong, X. Xiao, and C. P. Lin. Study on the structure dependent ultrafast third-order optical nonlinearity of GeS₂-In₂S₃ chalcogenide glasses. *Opt. Commun.*, 270(2):373–378, 2007.
- [137] M. Asobe, T. Ohara, I. Yokohama, and T. Kaino. Low power all-optical switching in a nonlinear optical loop mirror using chalcogenide glass fiber. *Electron. Lett.*, 32(15):1396–1397, 1996.
- [138] S. R. Friberg and P. W. Smith. Nonlinear optical glasses for ultrafast optical switches. *IEEE J. Quant. Electron.*, 23(12):2089–2094, 1987.
- [139] L. Yan, S. Jia, J. Si, S. Matsuo, F. Chen, and X. Hou. Application of Optical Kerr Gate with SrTiO₃ Crystal in Acquisition of Gated Spectra from a Supercontinuum. *Chin. Phys. Lett.*, 29(7):074207, 2012.
- [140] S. Qibing, L. Hongjun, H. Nan, W. Zhaolu, L. Shaopeng, and H. Jing. Highly efficient nonlinear ellipse rotation in bulk SrTiO₃ crystal and its applications. *Laser Phys.*, 25(12):125403, 2015.
- [141] M. Bache, H. Guo, B. Zhou, and X. Zeng. The anisotropic Kerr nonlinear refractive index of the beta-barium borate (β -BaB₂O₄) nonlinear crystal. *Opt. Mater. Express*, 3(3):357, 2013.
- [142] J. Tong, W. Tan, J. Si, Y. Yang, W. Yi, F. Chen, and X. Hou. Elimination of the coherent effect in the optical Kerr measurement of bismuth glass using supercontinuum. *J. Appl. Phys.*, 109(12):123104, 2011.
- [143] L. Yan, J. Yue, J. Si, and X. Hou. Influence of self-diffraction effect on femtosecond pump-probe optical Kerr measurements. *Opt. Express*, 16(16):12069–12074, 2008.
- [144] L. Yan, J. Si, F. Chen, S. Jia, Y. Zhang, and X. Hou. Pump power dependence of Kerr signals in femtosecond cross pump-probe optical Kerr measurements. *Opt. Express*, 17(24):21509–21514, 2009.
- [145] B. L. Yu, A. B. Bykov, T. Qiu, P. P. Ho, R. R. Alfano, and N. Borrelli. Femtosecond optical Kerr shutter using lead-bismuth-gallium oxide glass. *Opt. Commun.*, 215(4-6):407–411, 2003.

- [146] H. Liu, W. Tan, J. Si, and X. Hou. Acquisition of gated spectra from a supercontinuum using ultrafast optical Kerr gate of lead phthalocyanine-doped hybrid glasses. *Opt. Express*, 16(17):13486–13491, 2008.
- [147] Y. Wu, M. Ren, Z. Wang, W. Li, Q. Wu, S. Yi, X. Zhang, and J. Xu. Optical nonlinear dynamics in ZnS from femtosecond laser pulses. *AIP Adv.*, 4(5):057107, 2014.
- [148] T. D. Krauss and F. W. Wise. Femtosecond measurement of nonlinear absorption and refraction in CdS, ZnSe, and ZnS. *Appl. Phys. Lett.*, 65(14):1739–1741, 1994.
- [149] M. Dabbicco, A. M. Fox, G. von Plessen, and J. F. Ryan. Role of $\chi^{(3)}$ anisotropy in the generation of squeezed light in semiconductors. *Phys. Rev. B*, 53(8):4479–4487, 1996.
- [150] Y. Xiong, L. Yan, Z. Zhou, W. Yi, A. Lin, J. Si, F. Chen, and X. Hou. Efficient optical Kerr gating property of fluorotellurite glass. *Optik*, 125(3):1444–1447, 2014.
- [151] A. Jha, X. Liu, A. K. Kar, and H. T. Bookey. Inorganic glasses as Kerr-like media. *Curr. Opin. Solid State Mater. Sci.*, 5(6):475–479, 2001.
- [152] E. Yousef, M. Hotzel, and C. Rüssel. Effect of ZnO and Bi₂O₃ addition on linear and non-linear optical properties of tellurite glasses. *J. Non-Cryst. Solids*, 353(4):333–338, 2007.
- [153] T. Oliveira, D. Manzani, E. Falcao-Filho, Y. Messaddeq, G. Boudebs, K. Fedus, and C. de Araújo. Near-infrared nonlinearity of a multicomponent tellurium oxide glass at 800 and 1064 nm. *Appl. Phys. B*, 116(1):1–5, 2014.
- [154] M. E. Lines. Oxide glasses for fast photonic switching: A comparative study. *J. Appl. Phys.*, 69:6876 – 6885, 1991.
- [155] E. Yousef, M. Hotzel, and C. Rüssel. Linear and non-linear refractive indices of tellurite glasses in the system TeO₂-WO₃-ZnF₂. *J. Non-Cryst. Solids*, 342(1-3):82–88, 2004.
- [156] T. Xu, F. Chen, S. Dai, X. Shen, X. Wang, Q. Nie, C. Liu, K. Xu, and J. Heo. Glass formation and third-order optical nonlinear properties within TeO₂-Bi₂O₃-BaO pseudo-ternary system. *J. Non-Cryst. Solids*, 357(11-13):2219–2222, 2011.
- [157] K. Kato, T. Hayakawa, Y. Kasuya, and P. Thomas. Influence of Al₂O₃ incorporation on the third-order nonlinear optical properties of Ag₂O-TeO₂ glasses. *J. Non-Cryst. Solids*, 431:97–102, 2016.
- [158] F. W. Shi, X. J. Meng, G. S. Wang, J. L. Sun, T. Lin, J. H. Ma, Y. W. Li, and J. H. Chu. The third-order optical nonlinearity of Bi_{3.25}La_{0.75}Ti₃O₁₂ ferroelectric thin film on quartz. *Thin Solid Films*, 496(2):333–335, 2006.

- [159] B. Gu, Y. Wang, W. Ji, and J. Wang. Observation of a fifth-order optical nonlinearity in $\text{Bi}_{0.9}\text{La}_{0.1}\text{Fe}_{0.98}\text{Mg}_{0.02}\text{O}_3$ ferroelectric thin films. *Appl. Phys. Lett.*, 95:041114, 2009.
- [160] S. W. Liu, J. Xu, D. Guzun, G. J. Salamo, C. L. Chen, Y. Lin, and M. Xiao. Nonlinear optical absorption and refraction of epitaxial $\text{Ba}_{0.6}\text{Sr}_{0.4}\text{TiO}_3$ thin films on (001) MgO substrates. *Appl. Phys. B*, 82(3):443–447, 2005.
- [161] A. Chen, G. Yang, H. Long, F. Li, Y. Li, and P. Lu. Nonlinear optical properties of laser deposited CuO thin films. *Thin Solid Films*, 517(15):4277–4280, 2009.
- [162] Y. Deng, Y. L. Du, M. S. Zhang, J. H. Han, and Z. Yin. Nonlinear optical properties in SrTiO_3 thin films by pulsed laser deposition. *Solid State Commun.*, 135(4):221–225, 2005.
- [163] P. Zhou, G. J. You, Y. G. Li, T. Han, J. Li, S. Y. Wang, L. Y. Chen, Y. Liu, and S. X. Qian. Linear and ultrafast nonlinear optical response of $\text{Ag}:\text{Bi}_2\text{O}_3$ composite films. *Appl. Phys. Lett.*, 83(19):3876–3878, 2003.
- [164] Q. F. Zhang, W. M. Liu, Z. Q. Xue, J. L. Wu, S. F. Wang, D. L. Wang, and Q. H. Gong. Ultrafast optical Kerr effect of Ag-BaO composite thin films. *Appl. Phys. Lett.*, 82(6):958–960, 2003.
- [165] I. Tanahashi, Y. Manabe, T. Tohda, S. Sasaki, and A. Nakamura. Optical nonlinearities of Au/ SiO_2 composite thin films prepared by a sputtering method. *J. Appl. Phys.*, 79(3):1244–1249, 1996.
- [166] Q. Wang, S. Wang, W. Huang, Q. Gong, B. Yang, and J. Shi. Ultrafast and large third-order optical nonlinearity of porous nanosized poly-crystal LiNbO_3 film. *J. Phys. D: Appl. Phys.*, 35(5):430–432, 2002.
- [167] H. Long, A. Chen, G. Yang, Y. Li, and P. Lu. Third-order optical nonlinearities in anatase and rutile TiO_2 thin films. *Thin Solid Films*, 517(19):5601–5604, 2009.
- [168] G. Lu, B. Cheng, H. Shen, Y. Chen, T. Wang, Z. Chen, H. Lu, K. Jin, Y. Zhou, and G. Yang. Large optical third-order nonlinearity of composite thin film of carbon nanotubes and BaTiO_3 . *Chem. Phys. Lett.*, 407(4-6):397–401, 2005.
- [169] A. S. Akbar, P. B. Bisht, B. S. Kalanoor, A. Patra, and S. Kasiviswanathan. Enhanced short wave IR third order nonlinearity of gold nanoparticle embedded ZnO thin films. *J. Opt. Soc. Am. B*, 30(8):2226–2232, 2013.
- [170] R. Lopez, R. F. Haglund, L. C. Feldman, L. A. Boatner, and T. E. Haynes. Optical nonlinearities in VO_2 nanoparticles and thin films. *Appl. Phys. Lett.*, 85(22):5191–5193, 2004.
- [171] P. Kumbhakar, M. Chattopadhyay, and A. K. Mitra. Nonlinear optical properties of ZnS nanoparticles. *Int. J. Nanosci.*, 10(01n02):177–180, 2011.

- [172] C. Min, P. Wang, C. Chen, Y. Deng, Y. Lu, H. Ming, T. Ning, Y. Zhou, and G. Yang. All-optical switching in subwavelength metallic grating structure containing nonlinear optical materials. *Opt. Lett.*, 33(8):869–871, 2008.
- [173] V. Gayvoronsky, A. Galas, E. Shepelyavyy, Th. Dittrich, V. Y. Timoshenko, S. A. Nepijko, M. S. Brodyn, and F. Koch. Giant nonlinear optical response of nanoporous anatase layers. *Appl. Phys. B*, 80(1):97–100, 2005.
- [174] H. W. Lee, J. K. Anthony, H.-D. Nguyen, S. Mho, K. Kim, H. Lim, J. Lee, and F. Rotermund. Enhanced ultrafast optical nonlinearity of porous anodized aluminum oxide nanostructures. *Opt. Express*, 17(21):19093–19101, 2009.
- [175] R. Weber, S. Sen, R. E. Youngman, R. T. Hart, and C. J. Benmore. Structure of High Alumina Content $\text{Al}_2\text{O}_3\text{-SiO}_2$ Composition Glasses. *J. Phys. Chem. B*, 112(51):16726–16733, 2008.
- [176] P. Florian, N. Sadiki, D. Massiot, and J. P. Coutures. ^{27}Al NMR Study of the Structure of Lanthanum- and Yttrium-Based Aluminosilicate Glasses and Melts. *J. Phys. Chem. B*, 111(33):9747–9757, 2007.
- [177] S. Tanabe, K. Hirao, and N. Soga. Elastic Properties and Molar Volume of Rare-Earth Aluminosilicate Glasses. *J. Am. Ceram. Soc.*, 75(3):503–506, 1992.
- [178] I. Pozdnyakova, N. Sadiki, L. Hennet, V. Cristiglio, A. Bytchkov, G. J. Cuello, J. P. Coutures, and D. L. Price. Structures of lanthanum and yttrium aluminosilicate glasses determined by X-ray and neutron diffraction. *J. Non-Cryst. Solids*, 354(18):2038–2044, 2008.
- [179] S. Iftekhhar, E. Leonova, and M. Edén. Structural characterization of lanthanum aluminosilicate glasses by ^{29}Si solid-state NMR. *J. Non-Cryst. Solids*, 355(43-44):2165–2174, 2009.
- [180] S. Iftekhhar, J. Grins, and M. Edén. Composition-property relationships of the $\text{La}_2\text{O}_3\text{-Al}_2\text{O}_3\text{-SiO}_2$ glass system. *J. Non-Cryst. Solids*, 356(20-22):1043–1048, 2010.
- [181] A. Aronne, S. Esposito, and P. Pernice. FTIR and DTA study of lanthanum aluminosilicate glasses. *Mater. Chem. Phys.*, 51(2):163–168, 1997.
- [182] N. J. Clayden, S. Esposito, A. Aronne, and P. Pernice. Solid state ^{27}Al NMR and FTIR study of lanthanum aluminosilicate glasses. *J. Non-Cryst. Solids*, 258(1-3):11–19, 1999.
- [183] A. V. Kiryanov, M. C. Paul, Y. O. Barmenkov, S. Das, M. Pal, and L. Escalante-Zarate. Yb^{3+} Concentration Effects in Novel Yb Doped Lanthano-Alumino-Silicate Fibers: Experimental Study. *IEEE J. Quant. Electron.*, 49(6):528–544, 2013.
- [184] M. J. Dejneka, B. Z. Hanson, S. G. Crigler, L. A. Zenteno, J. D. Minelly, D. C. Allan, W. J. Miller, and D. Kuksenkov. $\text{La}_2\text{O}_3\text{-Al}_2\text{O}_3\text{-SiO}_2$ Glasses for

- High-Power, Yb³⁺-Doped, 980-nm Fiber Lasers. *J. Am. Ceram. Soc.*, 85(5):1100–1106, 2002.
- [185] R. F. Souza, M. A. R. C. Alencar, J. M. Hickmann, R. Kobayashi, and L. R. P. Kassab. Femtosecond nonlinear optical properties of tellurite glasses. *Appl. Phys. Lett.*, 89(17):171917, 2006.
- [186] R. El-Mallawany, M. D. Abdalla, and I. A. Ahmed. New tellurite glass: Optical properties. *Mater. Chem. Phys.*, 109(2-3):291–296, 2008.
- [187] S. Balaji, A. D. Sontakke, and K. Annapurna. Yb³⁺ ion concentration effects on 1 μ m emission in tellurite glass. *J. Opt. Soc. Am. B*, 29(7):1569–1579, 2012.
- [188] K. Sae-Hoon, T. Yoko, and S. Sakka. Nonlinear Optical Properties of TeO₂-Based Glasses: La₂O₃-TeO₂ Binary Glasses. *J. Am. Chem. Soc.*, 76(4):865–869, 1993.
- [189] R. Kitamura, L. Pilon, and M. Jonasz. Optical constants of silica glass from extreme ultraviolet to far infrared at near room temperature. *Appl. Opt.*, 46(33):8118–33, 2007.
- [190] S. Zaynobidinov, R. G. Ikramov, and R. M. Jalalov. Urbach energy and the tails of the density of states in amorphous semiconductors. *J. Appl. Spectrosc.*, 78(2):223–227, 2011.
- [191] I. T. Godmanis, A. N. Trukhin, and K. Hübner. Exciton-phonon interaction in crystalline and vitreous SiO₂. *phys. stat. sol. (b)*, 116(1):279–287, 1983.
- [192] M. Abdel-Baki, F. A. Abdel-Wahab, A. Radi, and F. El-Diasty. Factors affecting optical dispersion in borate glass systems. *J. Phys. Chem. Solids*, 68(8):1457–1470, 2007.
- [193] I. S. Mustafa, H. M. Kamari, W. M. D. Yusoff, S. A. Aziz, and A. A. Rahman. Structural and Optical Properties of Lead-Boro-Tellurite Glasses Induced by Gamma-Ray. *Int. J. Mol. Sci.*, 14(2):3201–3214, 2013.
- [194] S. C. Cheng. The measurements of frozen-in disorder and thermal disorder of fused silica by electron energy loss spectroscopy. *Phys. Chem. Glasses: Eur. J. Glass Sci. Technol. B.*, 50(5):329–331, 2009.
- [195] F. El-Diasty, F. A. Abdel Wahab, and M. Abdel-Baki. Optical band gap studies on lithium aluminum silicate glasses doped with Cr³⁺ ions. *J. Appl. Phys.*, 100(9):093511, 2006.
- [196] H. A. A. Sidek, S. Rosmawati, Z. A. Talib, M. K. Halimah, and W. M. Daud. Synthesis and Optical Properties of ZnO-TeO₂ Glass System. *Am. J. Appl. Sci.*, 6(8):148–1494, 2009.
- [197] H. M. Oo, H. Mohamed-Kamari, and W. M. D. Wan-Yusoff. Optical Properties of Bismuth Tellurite Based Glass. *Int. J. Mol. Sci.*, 13(4):4623–4631, 2012.

- [198] P. Gayathri Pavani, K. Sadhana, and V. Chandra Mouli. Optical, physical and structural studies of boro-zinc tellurite glasses. *Physica B Condens. Matter*, 406(6-7):1242–1247, 2011.
- [199] K. Saito and A. J. Ikushima. Absorption edge in silica glass. *Phys. Rev. B*, 62(13):8584–8587, 2000.
- [200] M. S. Shakeri and M Rezvani. Optical band gap and spectroscopic study of lithium alumino silicate glass containing Y^{3+} ions. *Spectrochim. Acta Mol. Biomol. Spectrosc.*, 79:1920–1925, 2011.
- [201] N. F. Mott and E. A. Davis. *Electronic Processes in Non-Crystalline Materials*. Clarendon Press, Oxford, 2nd edition, 1979.
- [202] R. Bhatt, I. Bhaumik, S. Ganesamoorthy, A. K. Karnal, M. K. Swami, H. S. Patel, and P. K. Gupta. Urbach tail and bandgap analysis in near stoichiometric $LiNbO_3$ crystals. *phys. stat. sol. (a)*, 209(1):176–180, 2012.
- [203] D. B. Buchholz, J. Liu, T. J. Marks, M. Zhang, and R. P. H. Chang. Control and Characterization of the Structural, Electrical, and Optical Properties of Amorphous Zinc-Indium-Tin Oxide Thin Films. *ACS Appl. Mater. Interfaces*, 1(10):2147–2153, 2009.
- [204] J. Tauc, R. Grigorovici, and A. Vancu. Optical Properties and Electronic Structure of Amorphous Germanium. *phys. stat. sol. (b)*, 15(2):627–637, 1966.
- [205] Z. A. S. Mahraz, M. R. Sahar, and S. K. Ghoshal. Band gap and polarizability of boro-tellurite glass: Influence of erbium ions. *J. Mol. Struct.*, 1072:238–241, 2014.
- [206] M. Farahmandjou and S. A. Salehizadeh. The optical band gap and the tailing states determination in glasses of TeO_2 - V_2O_5 - K_2O system. *Glass Phys. Chem*, 39(5):473–479, 2013.
- [207] F. Funabiki, T. Kmiya, and H. Hosono. Doping effects in amorphous oxides. *J. Ceram. Soc. Jpn.*, 120(11):447–457, 2012.
- [208] M. N. Azlan, M. K. Halimah, S. Z. Shafinas, and W. M Daud. Polarizability and optical basicity of Er^{3+} ions doped tellurite glasses. *Chalcogenide Lett.*, 11(7):319–335, 2014.
- [209] G. Wang, B. Huang, Z. Li, Z. Lou, Z. Wang, Y. Dai, and M. Whangbo. Synthesis and characterization of ZnS with controlled amount of S vacancies for photocatalytic H_2 production under visible light. *Sci. Rep.*, 5:8544, 2015.
- [210] E. D. Palik. *Handbook of optical constants of solids II*. Academic Press, San Diego, 1998.
- [211] R. D. Eithiraj, G. Jaiganesh, and G. Kalpana. Electronic structure and ground-state properties of alkali-metal oxides- Li_2O , Na_2O , K_2O and Rb_2O : A first-principles study . *Physica B, Condens. Matter*, 396:124–131, 2007.

- [212] O. Noguera and S. Suehara. High nonlinear optical properties in TeO₂-based glasses: A modifier's influence study from the localized hyperpolarizability approach. *J. Non-Cryst. Solids*, 354(2-9):188–192, 2008.
- [213] A. Novatski, A. Steimacher, A. N. Medina, A. C. Bento, M. L. Baesso, L. H. C. Andrade, S. M. Lima, Y. Guyot, and G. Boulon. Relations among nonbridging oxygen, optical properties, optical basicity, and color center formation in CaO-MgO aluminosilicate glasses. *J. Appl. Phys.*, 104(9):094910, 2008.
- [214] A. Q. Wu, I. H. Chowdhury, and X. F. Xu. Femtosecond laser absorption in fused silica: Numerical and experimental investigation. *Phys. Rev. B*, 72(8):085128, 2005.
- [215] F. S. Ohuchi, S. Ghose, M. H. Engelhard, and D. R. Baer. Chemical bonding and electronic structures of the Al₂SiO₅ polymorphs, andalusite, sillimanite, and kyanite: X-ray photoelectron- and electron energy loss spectroscopy studies. *Amer. Mineral.*, 91:740–746, 2006.
- [216] S. Ohmi, C. Kobayashi, I. Kashiwagi, C. Ohshima, H. Ishiwara, and H. Iwai. Characterization of La₂O₃ and Yb₂O₃ Thin Films for High-k Gate Insulator Application. *J. Electrochem. Soc.*, 150(7):F134–F140, 2003.
- [217] Q. Liu, Z. Fang, T. Ji, S. Liu, Y. Tan, J. Chen, and Y. Zhu. Band Alignment and Band Gap Characterization of La₂O₃ Films on Si Substrates Grown by Radio Frequency Magnetron Sputtering. *Chin. Phys. Lett.*, 31(2):027702, 2014.
- [218] J. Robertson, K. Xiong, and S. J. Clark. Band gaps and defect levels in functional oxides. *Thin Solid Films*, 496(1):1–7, 2006.
- [219] A. Haralampieva, I. Simeonova-Lozanova, and V. Dimitrov. Optical properties and structure of BaO-V₂O₅ and Fe₂O₃-BaO-V₂O₅ Glasses. *J. Chem. Technol. Metall.*, 47(4):392–397, 2012.
- [220] S. H. Wemple. Optical oscillator strengths and excitation energies in solids, liquids, and molecules. *J. Chem. Phys.*, 67(5):2151, 1977.
- [221] N. M. Ravindra, P. Ganapathy, and J. Choi. Energy gap-refractive index relations in semiconductors - An overview. *Infrared Phys. Technol.*, 50(1):21–29, 2007.
- [222] P. Hervé and L. K. J. Vandamme. General relation between refractive index and energy gap in semiconductors. *Infrared Phys. Technol.*, 35(4):609–615, 1994.
- [223] T. S. Moss. Relations between the Refractive Index and Energy Gap of Semiconductors. *phys. stat. sol. (b)*, 131(2):415–427, 1985.
- [224] R. R. Reddy and S. Anjaneyulu. Analysis of the Moss and Ravindra relations. *phys. stat. sol. (b)*, 174(2):K91–K93, 1992.

- [225] B. Gu, J. Chen, Y. Fan, J. Ding, and H. Wang. Theory of Gaussian beam Z scan with simultaneous third- and fifth-order nonlinear refraction based on a Gaussian decomposition method. *J. Opt. Soc. Am. B*, 22(12):2651–2659, 2005.
- [226] W. Zang, J. Tian, Z. Liu, W. Zhou, F. Song, and C. Zhang. Analytic solutions to Z-scan characteristics of thick media with nonlinear refraction and nonlinear absorption. *J. Opt. Soc. Am. B*, 21(1):63–66, 2004.
- [227] G. Tsigaridas, M. Fakis, I. Polyzos, P. Persephonis, and V. Giannetas. Z-scan technique for elliptic Gaussian beams. *Appl. Phys. B*, 77(1):71–75, 2003.
- [228] Y. L. Huang and C. K. Sun. Z-scan measurement with an astigmatic Gaussian beam. *J. Opt. Soc. Am. B*, 17(1):43–47, 2000.
- [229] S. M. Mian, B. Taheri, and J. P. Wicksted. Effects of beam ellipticity on Z-scan measurements. *J. Opt. Soc. Am. B*, 13(5):856–863, 1996.
- [230] M. J. Weber. *Handbook of Optical Materials*. CRC Press, Boca Raton, 2003.
- [231] N. Boling, A. Glass, and A. Owyong. Empirical relationships for predicting nonlinear refractive index changes in optical solids. *IEEE J. Quant. Electron.*, 14(8):601–608, 1978.
- [232] K. Tanaka. Optical nonlinearity in photonic glasses. *J. Mater. Sci. Mater. Electron.*, 16(10):633–643, 2005.
- [233] V. Ramamurthy and R. K. Nagabhushana. *Polarizabilities of a few semiconductors: molecular vibration approach*. Electrical and Optical Behaviour of Solids: Proceedings of National Conference on Electrical and Optical Properties held during March 26-28, 1987 at the Department of Physics. Mittal Publications, Delhi, 1989.
- [234] S. Suehara, P. Thomas, A. P. Mirgorodsky, T. Merle-Méjean, J. C. Champarnaud-Mesjard, T. Aizawa, S. Hishita, S. Todoroki, T. Konishi, and S. Inoue. Localized hyperpolarizability approach to the origin of nonlinear optical properties in TeO₂-based materials. *Phys. Rev. B*, 70(20):205121, 2004.
- [235] B. Jeansannetas, S. Blanchandin, P. Thomas, P. Marchet, J. C. Champarnaud-Mesjard, T. Merle-Méjean, B. Frit, V. Nazabal, E. Fargin, G. Le Flem, M. O. Martin, B. Bousquet, L. Canioni, S. Le Boiteux, P. Segonds, and L. Sarger. Glass Structure and Optical Nonlinearities in Thallium(I) Tellurium(IV) Oxide Glasses. *J. Solid State Chem.*, 146(2):329–335, 1999.
- [236] M. B. Yahia, E. Orhan, A. Beltrán, O. Masson, T. Merle-Méjean, A. Mirgorodski, and P. Thomas. Theoretical Third-Order Hyperpolarizability of Paratellurite from the Finite Field Perturbation Method. *J. Phys. Chem. B*, 112(35):10777–10781, 2008.

- [237] M. Soulis, T. Merle-Méjean, A. P. Mirgorodsky, O. Masson, E. Orhan, P. Thomas, and M. B. Smirnov. Local molecular orbitals and hyper-susceptibility of TeO₂ glass. *J. Non-Cryst. Solids*, 354(2-9):199–202, 2008.
- [238] K. Sae-Hoon and Y. Toshinobu. Nonlinear Optical Properties of TeO₂-Based Glasses: MO_x-TeO₂ (M = Sc, Ti, V, Nb, Mo, Ta, and W) Binary Glasses. *J. Am. Ceram. Soc.*, 78(4):1061–1065, 1995.
- [239] T. Cardinal, E. Frargin, G. Le Flem, M. Couzi, L. Canioni, P. Segonds, L. Sarger, A. Ducasse, and F. Adamietz. Nonlinear optical properties of some niobium (V) oxide glasses. *Eur. J. Solid State Inorg. Chem.*, 33:597–605, 1996.
- [240] X. Zhao, X. Wang, H. Lin, and Z. Wang. Electronic polarizability and optical basicity of lanthanide oxides. *Physica B Condens. Matter*, 392(1-2):132–136, 2007.
- [241] V. Dimitrov and T. Komatsu. An interpretation of optical properties of oxides and oxide glasses in terms of the electronic ion polarizability and average single bond strength. *J. Chem. Technol. Metall.*, 45(3):219–250, 2010.
- [242] I. H. Chowdhury, A. Q. Wu, X. F. Xu, and A. M. Weiner. Ultra-fast laser absorption and ablation dynamics in wide-band-gap dielectrics. *Appl. Phys. A*, 81(8):1627–1632, 2005.
- [243] G. I. Stegeman and E. M. Wright. All-optical waveguide switching. *Opt. Quant. Electron.*, 22(2):95–122, 1990.
- [244] M. Bala Murali Krishna, L. Giribabu, and D. Narayana Rao. Ultrafast third order nonlinear optical properties of water soluble zinc-octacarboxy-phthalocyanine. *JPP (Journal of Porphyrins and Phthalocyanines)*, 16(09):1015–1023, 2012.
- [245] M. Ziólek, M. Lorenc, and R. Naskrecki. Determination of the temporal response function in femtosecond pump-probe systems. *Appl. Phys. B*, 72(7):843–847, 2001.
- [246] R. A. Negres, J. M. Hales, A. Kobayakov, D. J. Hagan, and E. W. Van Stryland. Experiment and analysis of two-photon absorption spectroscopy using a white-light continuum probe. *IEEE J. Quant. Electron.*, 38(9):1205–1216, 2002.
- [247] A. N. Naumov and A. M. Zheltikov. Cross-Phase Modulation in Short Light Pulses as a Probe for Gas Ionization Dynamics: The Influence of Group-Delay Walk-off Effects. *Laser Phys.*, 10(4):923–926, 2000.
- [248] H. Ticha and L. Tichy. Semiempirical relation between non-linear susceptibility (refractive index), linear refractive index and optical gap and its application to amorphous chalcogenides. *J. Optoelectron. Adv. M.*, 4:381–386, 2002.

- [249] S. Manning, H. Ebendorff-Heidepriem, and T. M. Monro. Ternary tellurite glasses for the fabrication of nonlinear optical fibres. *Opt. Mater. Express*, 2(2):140, 2012.
- [250] L. Yan, S. Jia, J. Si, F. Chen, W. Yi, and X. Hou. Influence of self-focusing effect on femtosecond collinear nondegenerate optical Kerr measurements. *Optik*, 123(8):722–725, 2012.
- [251] S. Jia, L. Yan, J. Si, W. Yi, F. Chen, and X. Hou. Self-focusing in two-color collinear optical Kerr measurements. *Opt. Commun.*, 283(21):4346–4349, 2010.
- [252] Tesa Product information.
http://www.tesa.com/industry/electronics/assortment_overview/functional_tapes/optically_clear_adhesive/tesa_69404,i.html.
Accessed: 2016-04-11.
- [253] R. Barakat. Application of Apodization of Increase Two-Point Resolution by the Sparrow Criterion. I. Coherent Illumination. *J. Opt. Soc. Am.*, 52(3):276–283, 1962.
- [254] X. Xu, Y. Zhao, E. J. Sie, Y. Lu, B. Liu, S. A. Ekahana, X. Ju, Q. Jiang, J. Wang, H. D. Sun, T. Sum, C. H. A. Huan, Y. P. Feng, and Q. H. Xiong. Dynamics of Bound Exciton Complexes in CdS Nanobelts. *ACS Nano*, 5(5):3660–3669, 2011.
- [255] S. Geburt, A. Thielmann, R. Röder, C. Borschel, A. McDonnell, M. Kozlik, J. Kühnel, K. A. Sunter, F. Capasso, and C. Ronning. Low threshold room-temperature lasing of CdS nanowires. *Nanotechnology*, 22(365204):1–6, 2012.
- [256] N. B. Kinding and W. E. Spicer. Band Structure of Cadmium Sulfide - Photoemission Studies. *Phys. Rev.*, 138(2A):A561 – A576, 1965.
- [257] D. Magde and H. Mahr. Exciton-Exciton interaction in CdS, CdSe, and ZnO. *Phys. Rev. Lett.*, 24(16):890–893, 1970.
- [258] T. Fischer and J. Bille. Recombination processes in highly excited CdS. *J. Appl. Phys.*, 45(9):3937–3942, 1974.
- [259] S. W. Koch, H. Haug, G. Schmieder, W. Bohnert, and C. Klingshirn. Stimulated Intrinsic Recombination Processes in II-VI Compounds. *phys. stat. sol. (b)*, 89:431–440, 1978.
- [260] K. Saito and E. O. Göbel. Picosecond spectroscopy of highly excited CdS. *Phys. Rev. B*, 31(4):2360–2369, 1985.
- [261] R. Röder, T. P. H. Sidiropoulos, C. Tessarek, S. Christiansen, R. F. Oulton, and C. Ronning. Ultrafast Dynamics of Lasing Semiconductor Nanowires. *Nano Lett.*, 15(7):4637–4643, 2015.
- [262] J. Puthussery, A. Lan, T. H. Kosel, and M. Kuno. Band-Filling of Solution-Synthesized CdS Nanowires. *ACS Nano*, 2(2):357–367, 2008.

- [263] S. Liang, M. Li, J. H. Wang, X. L. Liu, Z. H. Hao, L. Zhou, X. F. Yu, and Q. Q. Wang. Silica-coated and annealed CdS nanowires with enhanced photoluminescence. *Opt. Express*, 21(3):3253–3258, 2013.
- [264] A. L. Pan, D. P. Liu, R. B. Liu, F. Wang, X. Zhu, and B. Zou. Optical Waveguide through CdS Nanoribbons. *Small*, 1(10):980–983, 2005.
- [265] I. Pelant and J. Valenta. *Luminescence Spectroscopy of Semiconductors*, chapter 7: Luminescence of excitons. Oxford University Press, 2012.
- [266] B. Liu, R. Chen, X. L. Xu, D. H. Li, Y. Y. Zhao, Z. X. Shen, Q. H. Xiong, and H. D. Sun. Exciton-Related Photoluminescence and Lasing in CdS Nanobelts. *J. Phys. Chem. C*, 115(26):12826–12830, 2011.
- [267] R. Agarwal, C. J. Barrelet, and C. M. Lieber. Lasing in Single Cadmium Sulfide Nanowire Optical Cavities. *Nano Lett.*, 5(5):917–920, 2005.
- [268] J. C. Johnson, H.-J. Choi, K. P. Knutsen, R. D. Schaller, P. Yang, and R. J. Saykally. Single gallium nitride nanowire lasers. *Nat. Mater.*, 1(2):106–110, 2002.
- [269] J. K. Song, U. Willer, J. M. Szarko, S. R. Leone, S. Li, and Y. Zhao. Ultrafast Upconversion Probing of Lasing Dynamics in Single ZnO Nanowire Lasers. *J. Phys. Chem. C*, 112(5):1679–1684, 2008.
- [270] A. Pan, R. B. Liu, Q. Yang, Y. C. Zhu, G. Yang, B. Zou, and K. Chen. Stimulated Emissions in Aligned CdS Nanowires at Room Temperature. *J. Phys. Chem.*, 109(51):24268–24272, 2005.
- [271] Y. H. Leung, W. M. Kowk, A. B. Djuricic, D. L. Phillips, and W. K. Chan. Time-resolved study of stimulated emission in ZnO tetrapod nanowires. *Nanotechnology*, 16:579–582, 2005.
- [272] K. Appavoo, X. Liu, V. Menon, and M. Y. Sfeir. Excitonic Lasing in Solution-Processed Subwavelength Nanosphere Assemblies. *Nano Letters*, 16(3):2004–2010, 2016.
- [273] H. Y. Yang, S. F. Yu, G. P. Li, and T. Wu. Random lasing action of randomly assembled ZnO Nanowires with MgO coating. *Opt. Express*, 18(13):13647–13654, 2010.
- [274] Y. Rosenwaks, M. C. Hanna, D. H. Levi, D. M. Szmyd, R. K. Ahrenkiel, and A. J. Nozik. Hot-carrier cooling in GaAs: Quantum wells versus bulk. *Phys. Rev. B*, 48(19):14675–14678, 1993.
- [275] A. J. Nozik. Spectroscopy and hot electron relaxation dynamics in semiconductor quantum wells and quantum dots. *Annu. Rev. Phys. Chem.*, 52(1):193–231, 2001.
- [276] S. Schmitt-Rink, D. S. Chemla, and D. A. B. Miller. Linear and nonlinear optical properties of semiconductor quantum wells. *Adv. Phys.*, 38(2):89–188, 1989.

- [277] J. M. A. Gilman, A. Hamnett, and R. A. Batchelor. Franz-Keldysh and band-filling effects in the electroreflectance of highly doped p-type GaAs. *Phys. Rev. B*, 46(20):13363–13370, 1992.
- [278] M. Feneberg, S. Osterburg, K. Lange, C. Lidig, B. Garke, R. Goldhahn, E. Richter, C. Netzel, M. D. Neumann, N. Esser, S. Fritze, H. Witte, J. Bläsing, A. Dadgar, and A. Krost. Band gap renormalization and Burstein-Moss effect in silicon- and germanium-doped wurtzite GaN up to 10^{20}cm^{-3} . *Phys. Rev. B*, 90(7):075203, 2014.
- [279] B. Arnaudov, D. S. Domanevskii, S. Evtimova, Ch. Ivanov, and R. Kakanakov. Band-filling effect on the light emission spectra of InGaN/GaN quantum wells with highly doped barriers. *Microelectron. J.*, 40(2):346–348, 2009.
- [280] E. H. K. Stelzer. Contrast, resolution, pixelation, dynamic range and signal-to-noise ratio: fundamental limits to resolution in fluorescence light microscopy. *J. Microsc.*, 189(1):15–24, 1998.
- [281] T. M. Bieniewski and S. J. Czyzak. Refractive Indexes of Single Hexagonal ZnS and CdS Crystals. *J. Opt. Soc. Am.*, 53(4):496–497, 1963.
- [282] M. Maroncelli and G. R. Fleming. Picosecond solvation dynamics of coumarin 153: The importance of molecular aspects of solvation. *J. Chem. Phys.*, 86(11):6221–6239, 1987.
- [283] S. Kedenburg, M. Vieweg, T. Gissibl, and H. Giessen. Linear refractive index and absorption measurements of nonlinear optical liquids in the visible and near-infrared spectral region. *Opt. Mater. Express*, 2(11):1588–1611, 2012.
- [284] B. Lang, G. Angulo, and E. Vauthey. Ultrafast Solvation Dynamics of Coumarin 153 in Imidazolium-Based Ionic Liquids. *J. Phys. Chem. A*, 110(22):7028–7034, 2006.
- [285] T. Gustavsson, L. Cassara, V. Gulbinas, G. Gurzadyan, J.-C. Mialocq, S. Pommeret, M. Sorgius, and P. v.d.Meulen. Femtosecond Spectroscopic Study of Relaxation Processes of Three Amino-Substituted Coumarin Dyes in Methanol and Dimethyl Sulfoxide. *J. Phys. Chem. A*, 102(23):4229–4245, 1998.
- [286] E. Sekko, G. Thomas, and A. Boukrouche. A deconvolution technique using optimal Wiener filtering and regularization. *Signal Processing*, 72(1):23–32, 1999.
- [287] F. Mucha, 2015. Personal communication, Jena.
- [288] Spectra Physics. Femtosource XL: High Pulse energy ultrafast Ti:Sapphire Oscillators. <http://www.spectra-physics.com/documents/datasheets/Femtosource%20XL%20Data%20Sheet.pdf>. Accessed: 2016-04-11.
- [289] Coherent Inc. Chameleon Ultra Family: Widely Tunable, Hands-Free, Modelocked Ti:Sapphire Lasers. <http://>

[//www.coherent.com/downloads/ChameleonUltra_DS_160216_F.pdf](http://www.coherent.com/downloads/ChameleonUltra_DS_160216_F.pdf).
Accessed: 2016-04-11.

- [290] J. Vollmann, D. M. Profunser, and J. Dual. Sensitivity improvement of a pump-probe set-up for thin film and microstructure metrology. *Ultrasonics*, 40(1-8):757–763, 2002.
- [291] T. Damm. and B. Wilhelmi. Optimum recording conditions in scanning microscopes. *J. Microsc.*, 165(1):71–80, 1992.
- [292] T. Damm. *Optimierung und Anwendung von laser-rastermikroskopischen Verfahren zur Untersuchung und Beeinflussung von mikro-elektronischen Bauelementen*. PhD thesis, Friedrich-Schiller-Universität Jena, 1990.
- [293] D. Spangenberg, P. Neethling, E. Rohwer, M. H. Brüggemann, and T. Feurer. Time-domain ptychography. *Phys. Rev. A*, 91:021803, 2015.
- [294] M. S. C. Almeida and M. A. T. Figueiredo. Parameter Estimation for Blind and Non-Blind Deblurring Using Residual Whiteness Measures. *IEEE Transactions on Image processing*, 22(7):2751–2763, 2013.
- [295] U. Brackmann. *Lambdachrome Laser Dyes*. Lambda Physik, Göttingen, 2000.

List of Figures

1.1	Excitation of the NADH auto-fluorescence in the fundus of the human eye and the NADH emission spectrum (Spectrum from [14], scheme from [15])	1
3.1	a) Carrier dynamics in a solid upon irradiation: left: electron-hole pair generation in the conduction band (CB) and the valence band (VB), respectively: I) single photon absorption, II) two photon absorption, III) combined two photon absorption; right: relaxation process: thermal disequilibrium (DE), thermalization (TH), electron-phonon interaction (E-Ph), hole-phonon interaction (H-Ph) and exciton (EXC) generation b) Excitation of molecules: (right, $ 0 \rangle$: electronic ground state, $ 1 \rangle$: excited electronic state, $ 1_e \rangle$: excited vibrational state of $ 1 \rangle$). τ_r and τ_F are the different relaxation time constants (cf. text)	12
3.2	Efficiency η_w of the OKG as a function of the spot width ratio w_S/w_G (weak gating intensity)	18
4.1	Setup of the Z-scan measurement	23
4.2	Setup of the two-color OKG measurement: red: beam line of the gate pulse, green: beam line of the signal pulse	24
4.3	Setup for WLC gating (only the part which is different from the two-color OKG setup), f_{P1} and f_{P2} : parental focal lengths of the parabolic mirrors.	25
4.4	Setup for gating the axially distributed broad band emission	26
4.5	a) Structure to determine axially distributed scattering and propagation direction of the pulse, b) Double compartment cuvette	27
5.1	a) Spectra of the signal pulse (red) and the gate pulse (black) for two-color optical Kerr gating b) The delay time dependent trace (amplitude normalized to 1) of the gated signal ($\lambda_S = 530$ nm) using a 0.7 mm thick slab of fused silica as OKG material (Green dashed line: Gaussian fit).	29
5.2	a) Spectrum and b) gated signal of scattered light of the fluorescence excitation pulse ($\lambda_{ex} = 440$ nm and $\lambda_G = 800$ nm)	29
5.3	a) Spectrum of the white light continuum, b) $1/e^2$ spot radii of the gate pulse and of selected WLC emission wavelengths around the position of the OKG (determined by knife-edge method, cf. text)	30
5.4	Horizontal and vertical (with respect to the optical table) beam profiles of a) gate pulse ($\lambda_G = 800$ nm) and signal pulse ($\lambda_S = 530$ nm) for the two-color Kerr gating experiments, b) excitation spot of fluorescence ($\lambda = 440$ nm).	31

5.5	Scattered light in the plane of gate material (different axial positions of the scattering sample), yellow circle: spot size of the gate pulse. . .	32
5.6	a) Amplitude of gated signal as function of scattering sample position, b) Correlation between delay time t_D (gate and scattered pulse) and position of scattering sample	33
6.1	Structure of the present chapter (aim: determine most suited OKG material)	34
6.2	a) Refractive indices n_0 of the investigated materials as function of the wavelength λ and photon energy $E_{Ph} = h\nu$, green lines: fitted Sellmeier curves, brackets: Abbe numbers. b) linear refractive indices n_0 (SAL-glasses) as a function of La_2O_3 concentration, black squares: present work, blue triangles: Iftekhar et al. [180], red circles: Dejneka et al. [184]	38
6.3	a) Absorption coefficients α as a function of wavelength λ and photon energy E_{Ph} , E_U : Urbach energies b) $\sqrt{\alpha E_{Ph}}$ as a function of wavelength λ and photon energy E_{Ph} , solid lines: linear regressions (different energy /absorption coefficient ranges), dash-dotted lines: estimated band gap energy.	39
6.4	a) Z-Scan traces of the SAL1 10 mol% of La_2O_3 sample at pulse energies E , arrows: Peak-To-Valley ratio ΔT_{PV} ; b) ΔT_{PV} values of investigated materials as a function of pulse energy, brackets: slope $\Delta T_{PV}/E$ in 10^{-3} nJ^{-1}	43
6.5	Nonlinear refractive index (n_2^F : cgs units, n_2 : SI units) as a function of La_2O_3 concentration and refractive index ($n_0(800 \text{ nm})$): black squares: measured values, blue triangles: calculated from BGO theory (eq. (6.5)) using measured n_d and ν_d values, red circles: calculated according to eq. (3.8) using only the oxygen hyperpolarizabilities of SiO_2 , Al_2O_3 and La_2O_3 given by Adair et al. [91]	44
6.6	a) Correlation $\gamma = Q\alpha^2$ between hyperpolarizability γ and polarizability α_m , $Q = m^2 = (7.8 \pm 0.6) \times 10^{10} \text{ esu/cm}^6$ (investigated SAL system), b) Normalized n_2 values (eq. (6.9)) as a function of $\text{La}_{2/3}\text{O}$ number density, upper limit of $\gamma_{\text{La}_2\text{O}_3}$: $(2.2 \pm 0.2) \times 10^{-36} \text{ esu}$	47
6.7	Refractive index mismatch (RIM) affecting the delay between the gate pulse and the signal as function of z , left) phase $\Delta\phi$ imprinted on signal by gate pulse, right) time frame of the signal ($\Delta n_g > 0$ (blue) and the $\Delta n_g = 0$ (red))	51
6.8	a) black solid line: Gate pulse intensity $I_G(z)/I_G(0)$ as a function of the propagation distance z decreasing due to group velocity dispersion, green dashed line: Gaussian approximation b) parameters $\Delta\tau_{Fit}$ and y_0 of Gaussian fit (eq. (6.16)) as function of the sample thickness d/L_D normalized to L_D , black vertical lines: d/L_D value of investigated samples	52
6.9	Spectrally and temporally resolved energy transmission (STRET) of the gated WLC pulse, a-e): investigated material e,f) thin and thick ZnS, Cyan lines: center (solid) and FWHM (dashed) of Gaussian fitted fused silica (depicted in all subfigures as guide to the eye).	53

6.10	a) Symbols: gated WLC at different wavelengths using Te-glass as OKG medium, dashed lines: fitted by (6.18), b) symbols: fitted values Δn_g , green dashed lines: values for Δn_g derived from Sellmeier equations, c) the fit parameter $a(\lambda)$ from (6.18) (scale for maximum transmission normalized to its maximum in long wavelength region)	54
6.11	Ratios $n_2/\Delta n_g$ for the investigated materials ($\lambda = 530$ nm)	55
6.12	a) Signals of the SAL4-glass (normalized to PIS, $I_G = 0.50$ TW/cm ²): black: polarization selective time trace (PSS), red: polarization integrated time trace (PIS), maximum of PSS emission = gating efficiency η , b) OKG measurements using Te-glass at different gating intensities I_G (values in GW/cm ²): solid lines: normalized PSS trace, dashed lines: normalized PIS trace	56
6.13	OKG efficiency η as a function of gate pulse intensity I_G : a) the SAL-glasses and fused silica, b) materials of large nonlinear refractive index (ZnS: thick sample)	57
6.14	a) Self focusing distances $d_{SF}(I_G)$ of investigated Kerr materials according to (3.26) as a function of the gate pulse intensity, horizontal dashed lines: sample thicknesses; b) symbols: transient (filled) and permanent (empty) transmission of ZnS (pink), Te-glass (purple), and N-SF56 (orange), lines: fitted curves (cf. text) for two-photon CMPA (solid), three-photon CMPA (dashed) and photo-darkening (empirical, dash-dotted)	59
6.15	FOM_{new} as a function of the gate pulse peak intensity I_G taking the temporal walk-off into account, dotted lines: transmission limit due to CMPA (the absorption length is the interaction length d_{eff} , eq. (6.20).	61
7.1	ToF method: upper graph: distribution of objects (dashed line: thin object, solid field: extended object distribution on optical path length z), path of the excitation light (blue) and the object's optical response R (red), R is highlighted in the inset, lower graphs: resulting signal as function of t and measured delay dependent time trace (DTT) as function of t_D	64
7.2	a) Scattered signal of stacked system (adhesive tape and fused silica, fig. 4.5a), green dashed lines: Gaussian fits, b) distance at which two peaks can still be resolved (units of the peak width δt) as a function of the SNR (derived from Sparrow criterion [253])	66
7.3	Spectral temporal response of the CdS ensemble upon femtolaser pulse excitation ($\lambda_{ex} = 440$ nm central wavelength) as a function of excitation fluence F	67
7.4	a) Spectrally integrated delay time (t_D) dependent CdS emission signal for different excitation fluences, b) delay time dependent CdS emission for different emission wavelengths ($F = 3.5$ mJ/cm ²), dashed lines: apparatus function (gated scattering signal), c) spectral centroid of the CdS emission as a function of the delay time t_D (different excitation fluences), dashed line: centroid of very weak excitation fluences (large t_D values)	68

- 7.5 Processes leading to complex spectral temporal response of the CdS nanostructures (large excitation fluences): a) Distribution of electron (holes) in the conduction (valence) band (CB, VB) upon photo excitation, b) electron-hole-plasma (EHP) and excitonic states (EXC) after thermalization causing Burstein-Moss effect (BME), c) huge exciton density causes band gap renormalization (BGR), d) almost relaxed system (no BM and no BGR effects) 70
- 7.6 Spectrally and temporally resolved emission of an imprinted CdS double layer (front and back surface of a 100 μm thick glass slide) upon fs laser irradiation ($\lambda_{ex} = 440 \text{ nm}$, variable fluence), signal around $t_D = 0 \text{ fs}$ and $t_D = 1000 \text{ fs}$ suppressed (cf. text) 70
- 7.7 a) Spectrally integrated signal of red: single layer, black: double layer measurement ($F = 2.2 \text{ mJ/cm}^2$), b) simulated temporal behavior of fluorescence for different thermalization times τ_r ($\Delta\tau_{eff} = 100 \text{ fs}$, $\tau_F = 5 \text{ ps}$), green dashed lines: fits according to eq. (7.5), inset: correlation between τ_{fit} and τ_r 71
- 7.8 Influence of a) the range of the fitted data (the number represents the rise between the minimum and the maximum of the fluorescence signal as shown in fig. 7.7b), b) the fluorescence lifetime $\Delta\tau_{eff}$ and c) the time constant of the Gaussian shaped apparatus function $\Delta\tau_{eff}$ onto the fit parameter t_0 as a function of the thermalization constant τ_r 73
- 7.9 a) Simulated DTT of a fluorescing double layer structure ($\tau_r/\Delta\tau_{eff} = 10$). b) correlation between noise ($1/\text{SNR}$) of the derivative, τ_r and the resolution t_0 74
- 7.10 Effect of low pass filtering onto signal derivative, a) spectrally integrated CdS emission signal (double layer, $F = 2.2 \text{ mJ/cm}^2$), smoothed by different low pass filters (cut-off frequencies ω_g). b) related derivatives, c) signal-to-noise ratio SNR of derivative as a function of ω_g , red line: hyperbolic fit, blue dashed line: SNR of the raw data, blue solid lines: limits of the SNR due to the resolution criterion ($\text{SNR} > 2$) and due to the apparatus function, black lines: SNR for the different ω_g values) 75
- 7.11 Delay time dependent traces at a) 500 nm b) 511 nm and c) 520 nm of the double layer CdS emission ($F = 2.2 \text{ mJ/cm}^2$), red lines: smoothed signal, upper graphs: derivatives of smoothed signal, green dashed lines: fitted build-up, s : background of at fit from other layer, $\Delta t_{0,scat}$, $\Delta t_{0,fit}$ and $\Delta t_{0,corr}$: delay time distance (cf. text) 76
- 7.12 Inverse onset times of emission as a function of the excitation fluence F for black: single layer ensemble, green: first, red: second layer from double layer imprints, red-green: corrected inverse onset times of second layer, inset: ratio of onset times as function of F 78
- 7.13 Black dashed lines: smoothed signal ($\omega_g = 0.06 \text{ fs}^{-1}$), red solid lines: derivative of double layer structure: a) $F = 2.2 \text{ mJ/cm}^2$, b) $F = 1.6 \text{ mJ/cm}^2$. a_i and s : signal amplitudes at different delay times (first maximum was normalized to $a_1 = 1$) 79

7.14	black symbols and line: time resolved signal and derivative (after data smoothing) of Coumarin 153 (dissolved in ethanol) in double compartment cuvette ($\lambda_{ex} = 440$ nm), red lines: simulated DTT ($\tau_r = 600 \pm 150$ fs, dashed lines indicate error margins), blue lines: fluorophore distribution and refractive indices (glass spacer and fluorophore distribution)	82
7.15	upper graph: retrieved fluorophore distributions (black solid lines) by a) Wiener deconvolution method, b) iterative algorithm ($\tau_r = 600 \pm 300$ fs, dashed black lines indicate fluctuation), red dashed lines: original distribution, green dashed lines: distribution low pass filtered by apparatus function ($r(t)$ in eq. (7.4)), lower graph: black squares: original data, red lines: retrieved time trace (dashed lines indicate fluctuation).	84
B.1	Scheme for estimating the signal background of a Kerr gate	98
C.1	simulated imaging properties for the fields F1 (blue), F2 (red), F3 (green) and F4 (yellow): rows: object plane fixed, image plane moving, columns: object plane moving, image plane fixed, positive direction: image or object moved away from the respective mirror	99
C.2	maximum optical path difference OPD (F1, in the sagittal plane, $NA = 0.2$) as a function of the object and the image distances.	100
D.1	Schematic elucidation of the composition of $\Delta\tau_G^*$	101
E.1	CCD images of the spots in the focal plane of the two-color OKG experiment: a: Gate beam ($\lambda_G = 800$ nm), b: a: Signal beam ($\lambda_S = 530$ nm), cf. fig. 5.4 for spot sizes	102
G.1	Scanning electron microscopic images of the CdS ensemble grown on a silicon substrate recorded at different magnifications (1, 2, 3) and at different positions on the sample (a, b)	104
H.1	Design of the double compartment cuvette. The spatial coordinate z : optical path. d^G : geometrical thickness of the compartments, n : refractive indices, E is the energy of the excitation pulse as a function of z (or t')	107
I.1	Original (black) and retrieved distributions of a test function using the evolutionary algorithm. The thermalization constant of the response function for the algorithm was varied.	110

List of Tables

5.1	Central wavelength λ , spot radii (horizontal w_H and vertical w_V), Rayleigh length z_R (calculated) as well as FWHM pulse duration $\Delta\tau$ of the signal and the gate pulses for two-color OKG and the excitation pulse of the fluorescence	30
5.2	Extinction ratio r_e of the used polarizers (sect. 4.3.3)	31
6.1	Composition of the investigated SAL glasses	37
6.2	Comparison of the estimated band gap values from the absorption (this work) and from the refractive index n_0 according to [222] and [224]	42
6.3	Optical parameters n_2 [10^{-16} cm ² /W], n_2^F [10^{-13} esu], α_{O2-} [\AA^3], α_{Cat} [\AA^3], α_{meas} [\AA^3], $\langle\gamma_{meas}\rangle$ [10^{-36} esu], and the r value for the SAL glasses and F300	47
6.4	Properties of investigated OKG samples: Molar concentration of La ₂ O ₃ for the SAL-glasses, Sellmeier coefficients (C_0 , A_i , \tilde{A}_i , B_i , eqs. (3.2) and (3.3). Note for ZnS eq. (3.3) was used (A_1 , \tilde{A}_i instead of A_i), linear (at 800 nm and 587.6 nm) and nonlinear (for the field in cgs units and the intensity in SI units at 800 nm) refractive indices n_0 , n_2 and (n_2^F), the Abbe number ν_d , the group refractive index mismatch between 530 and 800 nm (Δn_G), the Urbach energy E_U , the band gap E_{Gap} estimated from the absorption, the thermal expansion coefficient α_{th} , the glass transition temperature T_G , the density ρ , the molar volume V_m , structural information, group velocity dispersion k'' , dispersion length L_D , sample thickness d and effective thickness for the temporal walk-off d_{eff} , a : [105], b : [106], c : [84]	48
6.5	Estimated CMPA coefficients for two- (α_2) and three- (α_3) photon absorption	60
7.1	The delays and distances of the peaks in fig. 7.2 Δt and Δz , the group velocity refractive index n_G , the calculated thickness d_C and the thickness measured by a gauge d_M of the respective layer	66
7.2	Fitting parameters τ_{fit} , $t_{0,fit}$ and a (τ and a of second signal only) of the DTT according to the fit function (7.5). The indices indicate the layer. s is the offset of the second signal (cf. text) and $\Delta t_{0,scat}$ the distance of the scatter peaks. and layer distances of the spectrally resolved double layer emission.	77
7.3	Estimation of the axial resolution Δt_{min} and Δz_{min} , respectively for detecting the CdS double layer structure excited at different pulse fluences F . (average peak duration $\overline{\delta t} = 0.5(\delta t_1 + \delta t_2)$, noise level N)	80

List of Publications

First author

- C. Karras, C. Mühlig, W. Paa, T. Zeuner, W. Triebel and H. Stafast, "Femtosecond relaxation kinetics of highly excited MNa^{**} states in CaF_2 at 3.2 eV and 4.7 eV", *Appl. Phys. B.*, 104(01):17-20 (2011)
- C. Karras, D. Litzkendorf, S. Grimm, K. Schuster, W. Paa and H. Stafast, "Nonlinear refractive index study on $SiO_2-Al_2O_3-La_2O_3$ glasses", *Opt. Mat. Express*, 4(10):2066-2077 (2014)
- C. Karras, D. Litzkendorf, S. Grimm, K. Schuster, W. Paa and H. Stafast, " $SiO_2-Al_2O_3-La_2O_3$ glass - a superior medium for optical Kerr gating at moderate pump intensity", *Opt. Mat. Express*, 6(1):125-130 (2016)

Conference Proceedings

- C. Karras, Z. Sun, D. Nguyen, L. Emmert, W. Rudolph, "The impact ionization coefficient in dielectric materials revisited", *Proc. SPIE: Laser-Induced Damage in Optical Materials: 2011*, volume: 8190, 819028 (2011)
- C. Karras, C. Mühlig, W. Paa, H. Stafast, W. Triebel, T. Zeuner, "Population kinetics of the fluorescing MNa center state in CaF_2 upon fs laser excitation at 392 nm and 262 nm", *Proc. SPIE: Laser-Induced Damage in Optical Materials: 2010*, volume 7842, 78421R (2010)
- W. Rudolph, L. Emmert, D. Nguyen, C. Karras, Z. Sun, R. Weber, "Sub-picosecond laser breakdown in optical thin films", *Proc. SPIE: Pacific Rim Laser Damage 2011: Optical Materials for High Power Lasers*, volume 8206, 82060D (2011)
- Ch. Mühlig, H. Stafast, W. Triebel, Th. Zeuner, Ch. Karras, M. Letz, "Influence of Na-related defects on DUV nonlinear absorption in CaF_2 : nanosecond versus femtosecond laser pulses", *Proc. SPIE: Laser-Induced Damage in Optical Materials: 2009*, volume 7504, 75040I (2009)

Presentations

Talks

- " $SiO_2-Al_2O_3-La_2O_3$ Glass - A Superior Medium for Optical Kerr Gating at Moderate Pump Intensity", *OSA topical meeting on nonlinear optics*, Kauai, Hawaii, 2015
- "Temporal walk-off affecting optical Kerr gating in the sub - ps time range", *OSA topical meeting on nonlinear optics*, Kauai, Hawaii, 2015

Posters

- "Temporal walk-off affecting optical Kerrgating in the sub-ps time range", *IONS conference of OSA*, Karlsruhe, 2014
- "Kerr gating efficiency of tellurite glasses as a function of their composition", *DPG Frühjahrstagung*, Dresden 2014

Curriculum Vitae

Personal information

Name: Christian Karras
Date of Birth: May 24, 1986
Place of Birth: Meiningen
Nationality: German

Education

07/2010 Graduation from university (Diploma in physics), Jena
09/2009 - 06/2010 Diploma thesis at the "Institute of Photonic Technology",
Title: " M_{Na} -Defektzentren in CaF_2 -Einkristallen: Kombinierte fs-Laserpulsanregung bei 785 nm, 392 nm und 262 nm"
09/2004 - 07.2010 Study of Engineering Physics (Technische Physik) at the
"Friedrich-Schiller-Universität", Jena
06/2004 Abitur
08/1996 - 06/2004 Henfling Gymnasium, Meiningen

Academic career

since 01/2012 PhD student at "(Leibniz) Institute of Photonic Technology",
Jena
11/2011-01/2012 Research assistant at "Institute of Photonic Technology",
Jena
09/2010-10/2011 Research assistant of Prof. Wolfgang Rudolph at University
of New Mexico, Albuquerque, New Mexico, USA
09/2008-03/2009 Research assistant at GRINTECH GmbH, Jena
01/2008-04/2008 Research assistant of Prof. Brian King at McMaster University,
Hamilton, Ontario, Canada

Jena, April 27, 2016

Christian Karras

Thesen

1. Laufzeitunterschiede von Licht (ToF = Time of Flight) in Schichtsystemen kann zur tiefenaufgelösten Systemcharakterisierung genutzt werden. Beispielsweise liefert LIDAR (Light Detection and Ranging) dreidimensionale Profile ausgewählter Atmosphärenbestandteile.
2. Zur funktionellen molekülspezifischen Systemanalyse lässt sich die Technik auf lumineszierende Schichtsysteme anwenden.
3. Sehr dünne Schichtsysteme wie der Augenhintergrund mit Schichtdicken im Bereich von $10\ \mu\text{m}$ erfordern eine Zeitauflösung von $10^{-13}\ \text{s}$ bei der Anregung und der Detektion. Dies lässt sich durch Abtasten des Lichtsignals mit einem optischen Kerrschalter (OKG) nach Femtosekunden (fs)-Laseranregung realisieren.
4. Bei der Messung von Lumineszenz auf der ultrakurzen Zeitskala können viele sonst vernachlässigbare Effekte die Zeitauflösung und die Sensitivität des Systems beeinflussen. Beispiele dafür sind Dispersion, Multiphotonenabsorption, Relaxation im OKG-Material oder das zeitliche Emissionsverhalten der Schichtsysteme.
5. Mit dem entwickelten Detektionssystem bestehend aus einem optimierten OKG-Material und einem dispersionsfreien Abbildungssystem wurden Ortsauflösungen bis zu $\Delta z = 2\ \mu\text{m}$ möglich und an ausgewählten Testsystemen nachgewiesen.
6. $\text{SiO}_2\text{-Al}_2\text{O}_3\text{-La}_2\text{O}_3$ (SAL) Glas zeigt einen Wirkungsgrad von $\eta > 50\ \%$ beim Schalten mit moderaten Schaltintensitäten im Bereich $I_G = 500\ \text{GW}/\text{cm}^2$, die mit kommerziellen fs-Laseroszillatoren bei Repetitionsraten im MHz Bereich realisierbar sind.
7. Die axiale Auflösung der Messung wird hauptsächlich durch die Schaltzeiten (Anregung und Detektion) und das Signal-zu-Rauschverhältnis (SNR) bestimmt. Bei hohem SNR ist die Auflösung des Systems nahezu unabhängig von dem zeitlichen Emissionsverhalten der vermessenen Strukturen.
8. Zum Ermitteln der Auflösung und zur Rekonstruktion der örtlichen Emitterverteilung aus dem zeitaufgelösten Signal können aus der Mikroskopie bekannte Verfahren verwendet werden.
9. Die zeitliche Entwicklung der stimulierten Emission von Cadmiumsulfid-(CdS) Nanostrukturen, einem verwendeten Testsystem, liegt im Bereich von $0.1\ \text{ps}$ und $5\ \text{ps}$. Diese Entwicklung ist abhängig von der Anregungsfluenz.
10. Das komplexe spektral-zeitliche Emissionsverhalten der CdS-Nanostrukturen ist eine Folge gekoppelter Relaxationsprozesse nach der fs-Laseranregung.

Theses

1. Measuring the propagation time differences of light (ToF = Time of Flight) enables the depth resolved analysis of layered systems. This is for instance used to image three-dimensional profiles of selected atmospheric constituents (LIDAR, light detection and ranging).
2. For a functional molecule specific analysis, this technique can be applied to luminescent layered structures.
3. For analyzing very thin structured layers such as the human retina, showing layer thicknesses in the range of $10\ \mu\text{m}$, a temporal resolution in the range of $10^{-13}\ \text{s}$ is required for both, excitation and detection. This can be achieved by temporally scanning the emission upon femtosecond (fs)-laser excitation using an optical Kerr gate.
4. Many effects, which are generally negligible, can crucially affect the temporal resolution and the sensitivity of the detection system, when measuring the luminescence on the ultrashort time scale. Examples are dispersion, nonlinear absorption, relaxation processes in the OKG material or the temporal emission behavior of the layered system.
5. The developed detection system consists of an optimized OKG material and a dispersion optimized imaging system. Spatial resolutions down to $\Delta z = 2\ \mu\text{m}$ were achieved, when investigating different test systems.
6. $\text{SiO}_2\text{-Al}_2\text{O}_3\text{-La}_2\text{O}_3$ (SAL) glass is the most suitable OKG material for the present application showing an efficiency $\eta > 50\ \%$ for moderate gate pulse intensities $I_G \approx 500\ \text{GW}/\text{cm}^2$. These can be achieved by commercial fs-laser oscillators with pulse repetition rates of several MHz.
7. The axial resolution of the measurement is mostly determined by the gating time, the pulse duration for the luminescence excitation and the signal-to-noise ratio (SNR). At large SNR values, the resolution is almost independent of the temporal emission behavior of the layers.
8. In order to determine the system resolution and to reconstruct the spatial emitter distribution from a measured time signal, methods known from microscopy can be employed.
9. Stimulated emission of cadmium sulfide (CdS) nanostructures shows a complex build-up characteristic between $0.1\ \text{ps}$ and $5\ \text{ps}$. It depends on the excitation fluence.
10. The intricate spectro-temporal emission characteristics of CdS nanostructures is a consequence of complex relaxation processes upon fs-laser excitation.

Danksagung

Die vorliegende Doktorarbeit ist in der Arbeitsgruppe "‘Lasertiagnostik’" am Leibniz Institut für Photonische Technologien (IPHT) in Jena entstanden. An dieser Stelle möchte ich meinen persönlichen Dank an all jene richten, die zum erfolgreichen Abschluss beigetragen haben.

Besonderer Dank gilt an dieser Stelle

- **Prof. Dr. Herbert Stafast** für die ausgezeichnete Betreuung über die gesamte Promotionszeit und die vielen nützlichen Diskussionen zum Thema,
- **Prof. Dr. Christian Spielmann** für das Erstellen eines Zweitgutachtens der Arbeit, sowie nützliche Diskussionen,
- **Prof. Dr. Patrick Nürnberger** für das Erstellen eines Drittgutachtens der Arbeit,
- **Prof. Dr. Jürgen Popp** für die Finanzierung während der Arbeit durch das IPHT,
- **Prof. Dr. Hartmut Bartelt** für die Bereitschaft zur ersatzweisen Betreuung der Arbeit, sowie für nützliche Diskussionen zum Thema,
- **Dr. Wolfgang Paa** für die aufgeschlossene Aufnahme in die Arbeitsgruppe sowie allzeitiger kompetenter Hilfe bei Problemen und Fragen,
- **Prof. Dr. Wolfgang Triebel** für die ausführliche Beantwortung von Fragen zu physikalischen Hintergründen und viele hilfreiche Tipps,
- **Doz. Dr. Dietrich Schweitzer** und **Dr. Martin Hammer** für die Diskussionen bezüglich der Anwendung des vorgestellten Messsystems für den Augenhintergrund,
- **Prof. Dr. Carsten Ronning** und **Robert Röder** (Institut für Festkörperphysik, Friedrich-Schiller Universität Jena) für die Bereitstellung der CdS Nanostrukturen und für fruchtbare Diskussion bezüglich dieser,
- **Doris Litzkendorf, Stephan Grimm** und **Dr. Kay Schuster** für die Bereitstellung der ZnS und der N-SF56 Proben, für die Präparation und die Bereitstellung und die Charakterisierung (Glasübergangstemperatur, Dichte und thermischer Ausdehnungskoeffizient) der SAL- und Tellurit-Glasproben sowie für nützliche Diskussionen bezüglich der Glasseigenschaften,
- **Dr. Thomas Zeuner** für die kompetente Unterstützung bei Problemen mit dem verwendeten Femtosekundenlasersystem,
- **Matthias Arnz** für die Bearbeitung der Glass- und der ZnS-Proben,
- **Kokila Egodage** für die Englischkorrektur,
- **den Mitarbeitern der Werkstatt** (insbesondere Didi, Fabian und Micha) für die schnelle und professionelle Bearbeitung der Werkstattaufträge,

- **Per Heisel, Dr. Christian Mühlig, Dr. Thomas Zeuner** sowie **Dr. Frank Garwe** für die freundschaftliche Büroatmosphäre, allzeitige Unterstützung sowie lustige und ernste Gespräche über physikalische und nicht-physikalische Angelegenheiten,
- **Ronny Förster, Prof. Dr. Herbert Gross** und **Dr. Joachim Bergmann** für nützliche Diskussionen bezüglich Mikroskopie und Optik,
- **Felix Mucha** für nützliche Diskussionen bezüglich Entfaltungsalgorithmen,
- **Dirk Müller, Andreas Nagel** und **Michael Teupser** für die Unterstützung bei Problemen mit der Rechentechnik,
- den übrigen Mitglieder der Arbeitsgruppe für ihr offenes Ohr bei allen Fragen, den angenehmen und unkomplizierten Arbeitsalltag.

Besonderer Dank gilt an letzter Stelle meinen Freunden in Jena, (Raum) Meinigen und in Albuquerque, sowie meinen Eltern, meinen Großeltern, meiner Schwester mit Familie und meiner Cousine, allgemein für die Unterstützung und speziell dafür, dass sie immer ein offenes Ohr für meine Probleme hatten, sich (vor allem im letzten Teil der Arbeit) mein "Gejammer" angehört, mein "Gemecker" ertragen und mich dann wieder aufgemuntert haben, und natürlich für die entspannende Zeit am Ernst-Häckel-Platz in Jena.

Erklärung der Selbstständigkeit

Ich, Christian Karras erkläre, dass ich die vorliegende Arbeit selbständig verfasst und keine anderen als die angegebenen Quellen und Hilfsmittel benutzt habe. Die aus anderen Quellen direkt oder indirekt übernommenen Daten und Konzepte sind unter Angabe der Quelle gekennzeichnet. Weder habe ich Hilfe von anderen, außer den in der Danksagung benannten Personen, erhalten, noch habe ich die Hilfe eines Promotionsberaters in Anspruch genommen. Niemand hat von mir geldwerte Leistungen im Zusammenhang mit dem Inhalt der vorgelegten Dissertation erhalten. Ich habe die Dissertation nicht als Prüfungsarbeit für eine staatliche oder wissenschaftliche Prüfungsarbeit oder als Dissertationsarbeit (auch nur in Teilen) an einer anderen Hochschule eingereicht.

Seitens des Verfassers bestehen keine Einwände, die vorliegende Dissertation für die öffentliche Nutzung in der Thüringer Universitäts- und Landesbibliothek zur Verfügung zu stellen.

Declaration of authorship

I, Christian Karras, hereby declare, that this thesis and the work presented in it are my own and have been generated by me as the result of my own original research. I confirm that I have quoted from the work and/or acknowledged of others, the source is always given. With the exception of such quotations, this thesis is entirely my own work. I have not taken any help of any qualified consultant. I have not directly nor indirectly received any monetary benefit from third parties in connection to this research thesis. Furthermore, I certify that this research thesis or any part of it has not been previously submitted for a degree or any other qualification at the University of Jena or any other institution in Germany or abroad.